Weak Gravitational Lensing and Galaxy Bias

Dissertation

zur

Erlangung des Doktorgrades (Dr. rer. nat.)

der

Mathematisch-Naturwissenschaftlichen Fakultät

der

Rheinischen Friedrich-Wilhelms-Universität Bonn

vorgelegt von

Patrick Simon

aus

Landsberg/Lech

Bonn 2005

Angefertigt mit Genehmigung der Mathematisch-Naturwissenschaftlichen Fakultät der Rheinischen Friedrich-Wilhelms-Universität Bonn.

1. Referent: Prof. Dr. Peter Schneider
2. Referent: Prof. Dr. Pavel Kroupa

Tag der Promotion: 16. Juni 2005

CONTENTS

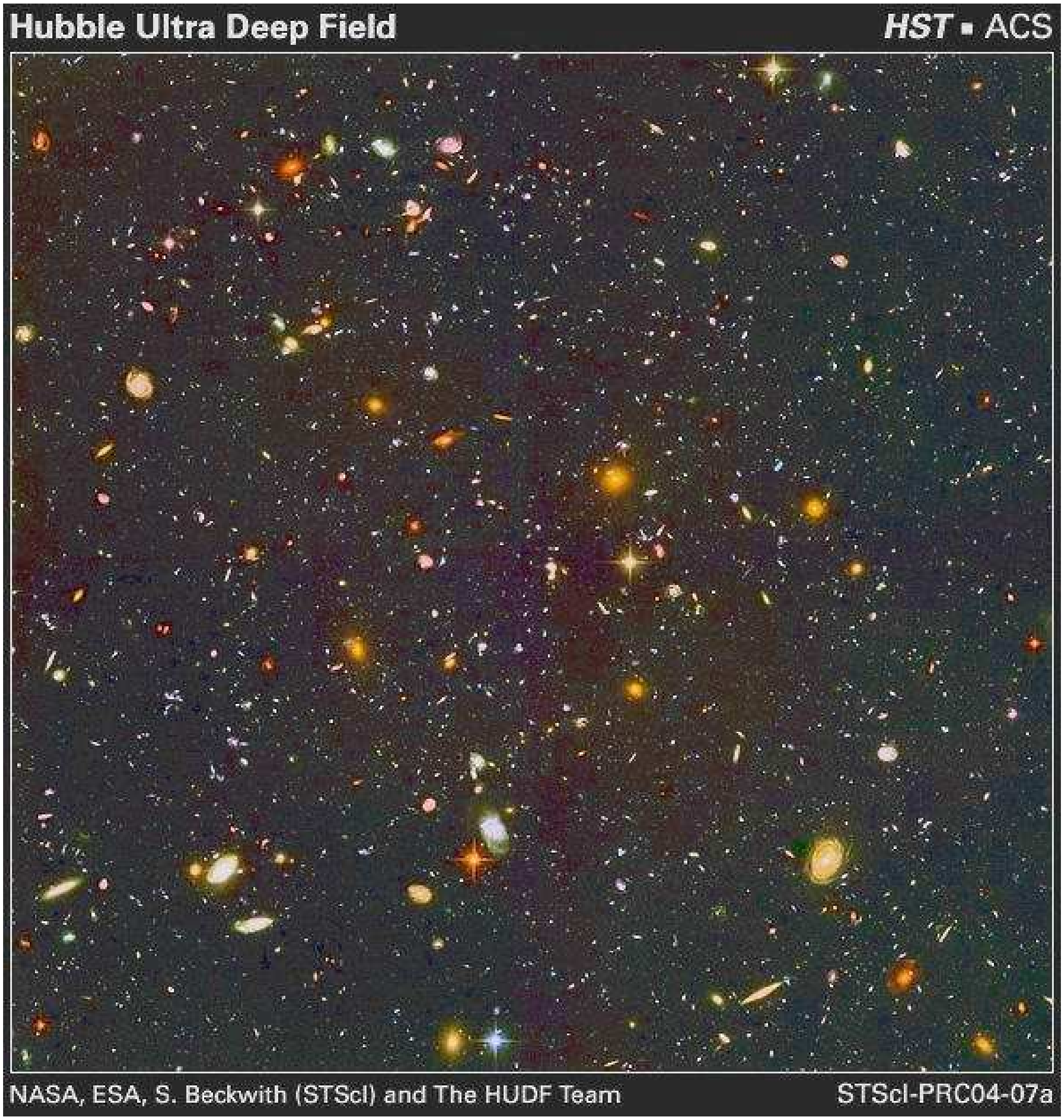

The Hubble Ultra Deep Field is an roughly one million seconds exposure of a virtually star-empty area in the sky taken by the Hubble space telescope (ACS). This picture exhibits the deepest view into the visible Universe ever taken. Although of a size of just one-tenth of the apparent diameter of the full moon, it still hosts about 10,000 galaxies of various sizes, shapes and colours. Some of the galaxies may belong to the very first generation of galaxies formed in Universe.

Introduction and overview

Cosmology studies the distribution, dynamics and origin of matter on the largest scales known in nature. The basic building blocks of structure are galaxies. Billions of galaxies fill the observable Universe forming a network of filaments, galaxy clusters and voids, the so-called cosmic web. Galaxies are, compared to cosmic scales, compact and isolated objects comprising millions to billions of stars. However, they are not all alike. Today a confusing wealth of different types of galaxies are known.

Except for very thin gas the vast space between galaxies appears at first sight to be empty. The observed dynamics of large-scale objects have led most cosmologists to the conclusion that there is, distributed inside and between galaxies, a lot more matter, *dark matter*, in the Universe than seen as stars, galaxies or gas. As J. Silk remarked, galaxies are just "the cream on the chocolate pie". In the modern paradigm of cosmology, dark matter is the main driver for the formation of cosmic structure. Within this paradigm, we now understand fairly well the basics of the formation of structure on cosmological scales, but have been less successful in explaining the diversity in morphology, mass, chemistry and colour of galaxies. How can an initially quite featureless Universe, as seen in the cosmic microwave background, evolve to give galaxies, still further, to produce such a diversity in galaxy properties? The main underlying physical processes seem to be identified: the primordial baryonic matter, left-over from the Big Bang, is flowing in an external gravitational field set by the dark matter. Under suitable conditions the baryonic matter condensates into stars within the dark matter field making the first generation of galaxies. Hierarchal merging progressively builds up larger and larger objects, such as more massive galaxies, clusters of galaxies or super-clusters of galaxies. However, these physical processes are waiting for a detailed explanation; some processes may even still be missing in this picture.

In the early days of observational cosmology, galaxies were often seen just as signposts of the total mass distribution. The uncertainty in how they trace the dark matter was simply coined *galaxy bias*, and was initially more of a nuisance than anything else; the main interest was to unravel the statistical properties of the total matter distribution, and galaxies were the only means by which this could be achieved. This is changing, since we now have other means to study the mass distribution directly. Weak gravitational lensing allows us to probe the large-scale dark matter distribution without the need for any luminous tracer. The gravitational field of the large-scale matter distribution deflects light that is traversing space so that images of distant galaxies become distorted. Coherent distortions of the shapes of distant galaxies –so-called *cosmic shear*– are used to measure the distribution of the total matter content in the Universe. The distortions of galaxy images imprinted by the gravitational lensing effect are, except in rare cases, small and can only be revealed statistically by averaging over many galaxies.

Everything contributes to the light deflection, whether it is directly visible or not. Weak gravitational lensing therefore provides a unique method to study the dark matter distribution independently from the galaxy distribution, and to compare the two in order to measure the galaxy bias. By looking at galaxy bias we can learn about the formation and evolution of galaxies: differences in the distribution of dark matter and galaxies, or special types of galaxies, hint at the conditions that have to be fulfilled to form galaxies.
The following gives a broad overview of the thesis:

- Chapter 1 sets the framework for describing cosmic structure formation. In particular, it introduces statistical quantities that are commonly employed to quantify clustering and galaxy bias. Another aim of the chapter is to outline the definitions of the key quantities in weak gravitational lensing.

- Chapter 2 derives a phenomenological model for the evolution of galaxy bias on large scales. The important bottom line of this model is that the evolution of galaxy bias is sensitive to the details of the physical process that locally adds galaxies to, or removes galaxies from, a population of galaxies.

- The aperture statistics incorporating weak gravitational lensing, that can be used to measure the galaxy bias from contemporary wide-field galaxy surveys, are explained and discussed in Chapter 3. The main effort is to draw a comparison between two practical estimators of the aperture statistics on the basis of simulated weak lensing surveys. Under realistic circumstances both estimators yield clearly different results. Only the most reliable estimator is used in the remainder of the thesis.

- In Chapter 4, the aperture statistics are applied to the Garching-Bonn Deep Survey (GaBoDS). Using these data the dark matter-galaxy bias is measured for a range of scales and three typical redshifts. The galaxy samples are found to be differently clustered with respect to the dark matter. Various practical aspects of the technique are discussed here. The survey does not allow, however, to select galaxies from a narrow redshift range or to distinguish between different types of galaxies because only the apparent brightnesses of galaxies in one filter band are available. Such a selection would be required to investigate galaxy bias as a function of redshift and galaxy type.

- The data of COMBO-17 do not have these limits, but is, however, limited by the relatively small survey area. It is analysed with focus on galaxy bias in Chapter 5. The aperture statistics is used there to measure the dark matter-galaxy bias for early-type and late-type, broadly selected by colour, galaxies belonging to four distinct narrow redshift bins. Moreover, the aperture statistics is extended so that it can also be employed to measure the relative bias between the two galaxy populations. By applying this extension it is shown that the spatial distributions of both populations are significantly different. An evolution of galaxy bias with redshift larger than the statistical uncertainties of the measurement is not found.

- Leaving the topic of galaxy bias, Chapter 6 studies how constraints on the redshifts of source galaxies improve the confidence on cosmological parameters derived from second-order cosmic shear correlations. A new method is introduced, based on the recipe for Monte Carlo simulation in Chapter 3, to estimate the covariances of the statistical errors in measured cosmic shear correlations.

This thesis concludes with an outlook and a final summary.

CHAPTER 1

Scientific framework

1.1. Structure formation in the universe

Gravity is the dominating force on large scales in the Universe. It made cosmic structures such as galaxy (super)clusters, galaxies, stars, planets, *etc.* from small inhomogeneities that emerged from a very early phase in cosmic history. Moreover, gravity dictates the global expansion or contraction of the Universe as a whole.

The standard model of cosmology rests on two pillars: *Einstein's General Relativity* (GR), and the *Cosmological Principle* that states that at every epoch the Universe presents the same aspect from every point, except for local irregularities. In other words, the Universe is homogeneous and isotropic on large scales. This assumption derives largely from two fundamental observations: most galaxies appear to be receding from us and the distribution of distant objects on the sky is isotropic. Based on these pillars, structure –local irregularities– grows under the influence of self-gravity on top of a homogeneous and isotropic large-scale background cosmology.

1.1.1. The standard model of cosmology

In GR, gravity is a geometrical property of a $(3+1)$-dimensional metric space-time in which particle trajectories are geodesics of stationary Eigenzeit (cf. Weinberg 1972). The workplace of GR is a Riemannian manifold whose metric $g_{\mu\nu}$ defines the infinitesimal line element by

$$\mathrm{d}s^2 = g_{\mu\nu}\,\mathrm{d}x^\mu\,\mathrm{d}x^\nu\ . \tag{1.1}$$

The infinitesimal $\mathrm{d}s$ indicates the change of Eigenzeit obtained from an infinitesimal displacement $\mathrm{d}x^\mu$ in the space-time coordinate frame x^μ.

Friedmann equations

It is an important conclusion of the theory of relativity that measurements of lengths and time differences depend on the reference frame of the observer. For a universe in which the Cosmological Principle applies, events are witnessed by a set of *fundamental observers*. The fundamental observers see local isotropy and measure time as *cosmic time.* They are said to be *comoving* with the Hubble flow. The spatial coordinate system in which the fundamental observers are at rest is the Hubble frame. Coordinates defining the position within the Hubble frame are so-called *comoving coordinates.* In 1935 and 1936, Robertson and Walker showed independently of each other that in a perfectly homogeneous and isotropic universe the space-time metric has to be maximally-symmetric,

$$\mathrm{d}s^2 = c^2\mathrm{d}t^2 - a^2(t)\left[\mathrm{d}w^2 + f_\mathrm{K}^2(w)\left(\mathrm{d}\theta^2 + \sin^2\theta\mathrm{d}\phi^2\right)\right] \ , \tag{1.2}$$

where w is the comoving radial distance, c is the vaccum speed of light and θ, ϕ are angular coordinates; they together form spherical coordinates relative to a fixed but arbitrary origin. The variable a is the *scale factor*, and t is the cosmic time. The expression $f_\mathrm{K}(w)$ is the *comoving angular diameter distance*

$$f_\mathrm{K}(w) = \int_0^w \frac{\mathrm{d}w'}{\sqrt{1-Kw'^2}} = \begin{cases} K^{-1/2}\sin(K^{1/2}w) & (K>0) \\ w & (K=0) \\ (-K)^{-1/2}\sinh[(-K)^{1/2}w] & (K<0) \end{cases} \ , \tag{1.3}$$

where K is the *curvature.* The curvature discriminates between three different geometries of the three-dimensional spacelike hypersurfaces defined by $t=$ const: $K=0$ for Euclidean surfaces, $K>0$ for a spherical geometry and $K<0$ for a hyperbolic geometry. The metric is therefore parametrised by only two parameters: the curvature and the scale factor.

The tensor field equations of GR connect the space-time metric to the energy-momentum tensor $T_{\mu\nu}$

$$R_{\mu\nu} - \frac{1}{2}g_{\mu\nu}R + g_{\mu\nu}\Lambda = \frac{8\pi G}{c^4}T_{\mu\nu} \ , \tag{1.4}$$

where $R_{\mu\nu} = R^\alpha_{\mu\nu\alpha}$ and $R = g^{\mu\alpha}R_{\alpha\mu}$ are the Ricci tensor and Ricci scalar, G is Newton's constant of gravitation. The tensor $R^\alpha_{\mu\nu\gamma}$ is the Riemann tensor describing the differential curvature of space-time; it is essentially a function of the metric $g_{\mu\nu}$ and its partial derivatives (first and second order). The expression Λ is the *cosmological constant.* Einstein introduced the cosmological constant to admit a static universe, thus a universe that is neither expanding nor contracting, *i.e.* $a=$ const. Later, as it was discovered that the Universe is actually dynamic and expanding, Einstein regretted Λ as his "biggest blunder".

Likewise, as for the metric, the highly idealised assumption of the Friedmann cosmology allows only an energy-momentum tensor that is independent of position and orientation. In 1932, Weyl suggested that for cosmological applications the most suitable form for $T_{\mu\nu}$ is that of a perfect fluid, that fills space, obeying

$$T_{\nu\mu} = [p(t)/c^2 + \rho(t)]U_\mu U_\nu - p(t)g_{\mu\nu} \ , \tag{1.5}$$

where p is the pressure, ρ the comoving density and U_μ the fluid 4-velocity. In general we have $\vec{U} = \gamma\,(c, \vec{v})$ where $\gamma = (1-|\vec{v}|^2/c^2)^{-1/2}$ and $\vec{v}$ the bulk velocity of the fluid. As the fluid is here considered at rest in the Hubble frame, $\vec{v} = \vec{0}$, we have simply $U_\mu = c\,\delta_{\mu 0}$. Both energy density and pressure may evolve with cosmic time but do not change with comoving position. The Friedmann equations are obtained by applying the field equations (1.4) of GR to the idealised space-time metric and energy-momentum tensor:

$$\left(\frac{\dot{a}}{a}\right)^2 = \frac{8\pi G}{3}\rho - \frac{\mathrm{K}c^2}{a^2} + \frac{\Lambda}{3}, \tag{1.6}$$

$$\frac{\ddot{a}}{a} = -\frac{4\pi G}{3}\left(\rho + \frac{3p}{c^2}\right) + \frac{\Lambda}{3} \tag{1.7}$$

The dot in, for example, $\dot{a}$ is an abbreviation for the derivative with respect to the cosmic time. Differentiating Eq. (1.6) and inserting it into Eq. (1.7) results in a conservation law for the energy density

$$\mathrm{d}(\rho a^3)c^2 = -p\,\mathrm{d}(a^3)\ . \tag{1.8}$$

This last equation together with (1.6) and an equation of state $p(\rho)$ completely determines the evolution of the scale factor a.

Redshift

In 1929, Slipher and Hubble observed that the emission and absorption lines of distant galaxies are at longer wavelengths than found in the laboratory, they are said to be redshifted. The conclusion was that the redshift ("recession velocity") increases linearly with the distance of the galaxies.

The standard model of cosmology attributes this observation to a scale factor that changes with cosmic time. Light travelling large distances in the universe is affected by a varying $a(t)$: the electromagnetic spectrum is shifted in wavelength by the factor $a(t)/a(t')$ where t' is the cosmic time of the light emission and t the cosmic time of the observation. For $a(t) > a(t')$ the spectrum is shifted towards longer wavelengths by the factor $1 + z = a(t)/a(t')$, where z is the *redshift*.

Energy density

In a cosmological context, we have for the fluid filling space an equation of state of the form $p = \alpha\,\rho c^2$, with α being constant. The complete cosmic fluid is a mixture of different components having different α. For a single component with such an equation of state, (1.8) directly implies

$$\rho \propto a^{-3(\alpha+1)}\ . \tag{1.9}$$

This covers all components of importance. It is adequate for particles or objects with a low velocity dispersion ("dust"), $\alpha = 0$, and radiation or relativistic particles, $\alpha = 1/3$.

Terms in the Friedmann equations involving the cosmological constant, Λ, can formally also be attributed to a hypothetical fluid with negative pressure $\alpha = -1$ and density $\rho_\Lambda = \Lambda/(8\pi G)$. In cosmological measurements (see below), one finds a clear contribution to the cosmic expansion from Λ or some something with an equation of state close or equal to $\alpha = -1$ but its nature remains completely unclear ("Dark energy" or "Phantom energy"). Particle physicists noted that the vacuum energy may behave as ρ_Λ (*cf.* Caroll *et al.* 1993). Moreover, inflationary theories which have become an important part of the modern paradigm of cosmology predict fields with similar properties. However, so far cosmology is far from providing a convincing explanation for the observed Λ-component in the cosmic fluid.

The total energy density ρc^2 is in general a mixture of several components each with a different equation of state:

$$\rho = \rho_\mathrm{m} + \rho_\mathrm{r} + \rho_\Lambda\ . \tag{1.10}$$

We use ρ_m, ρ_r and ρ_Λ for dust-like matter, radiation and dark energy, respectively. Note that in the following we consider solely dark energy with exactly $\alpha = -1$. For a different dark energy equation of state the equations are easily modified using Eq. (1.9).

Density parameters

It is common in cosmology to rewrite the Friedmann Eq. (1.6) with the above specified ρ in a different form:

$$\begin{aligned} H(t) &= H_0 \sqrt{\Omega_\Lambda + (1-\Omega_0)\, a^{-2} + \Omega_\mathrm{m}\, a^{-3} + \Omega_\mathrm{r}\, a^{-4}} && (1.11) \\ \Omega_0 &\equiv \Omega_\mathrm{r} + \Omega_\mathrm{m} + \Omega_\Lambda \,, && (1.12) \end{aligned}$$

where $H(t) \equiv \dot{a}/a$ is the *Hubble function* expressing the cosmic expansion rate at cosmic time t. As initial conditions for this first-order differential equation one uses $a(t_0) = 1$ and $H_0 \equiv H(t_0)$ for the present scale factor and the Hubble parameter. The parameters Ω_i are the *density parameters* at present times which for $i \in \{\Lambda, \mathrm{r}, \mathrm{m}\}$ are generally defined by $\Omega_i(t) \equiv \rho_i(t)/\rho_\mathrm{crit}(t)$ where

$$\rho_\mathrm{crit}(t) \equiv \frac{3H^2(t)}{8\pi G} \tag{1.13}$$

is the *critical density.* A universe with an average density above this threshold will be spatially closed, while a lower-density universe will be spatially open.

Cosmic horizons

The size of causally connected regions in the Universe is called the *particle horizon* size. It determines the maximum, in this form comoving, distance of two points that can have communicated with each other by the exchange of light signals emitted at cosmic time t_0:

$$w_\mathrm{ph}(t) = c \int_{t_0}^{t} \frac{\mathrm{d}t'}{a(t')} \,. \tag{1.14}$$

Another horizon scale of importance in cosmology is the comoving *Hubble radius* that is defined as the (comoving) distance at which fundamental observers see other fundamental observers recede at the speed of light

$$w_\mathrm{h} = \frac{c}{a(t)H(t)} \,. \tag{1.15}$$

It defines the size of the visible universe at a given time.

Hot big bang

Lately different methods for determining the cosmological density parameters have reached a concordance constraining the density parameters (Seljak *et al.* 2004b; Tegmark *et al.* 2004a; Spergel *et al.* 2003). The consensus reached so far is that we have *today* a flat, *i.e.* $\Omega_\Lambda + \Omega_\mathrm{m} = 1$, or almost flat Λ-cosmology with $H_0 = 100\,h\ \mathrm{km\,s^{-1}\,Mpc^{-1}}$ where $h \sim 0.7$, $\Omega_\Lambda \sim 0.7$ and $\Omega_\mathrm{m} \sim 0.3$. The relativistic density parameter including photons and neutrinos is roughly $\Omega_\mathrm{r} h^2 \sim 4.2 \times 10^{-5}$ (*cf.* Peacock 2001) and therefore at present times of no importance.

With these density parameters the Friedmann equations demand that the scale factor was $a = 0$ about 14 Gyrs ago; this is taken to be the age of the Universe. Moreover, this implies that the Universe had a hot and compact beginning since the energy densities scale with a^{-3} and a^{-4} for matter and radiation, respectively. This scenario was coined the *hot big bang* (Kolb & Turner 1990). In this scenario, the Universe, filled with radiation and elementary

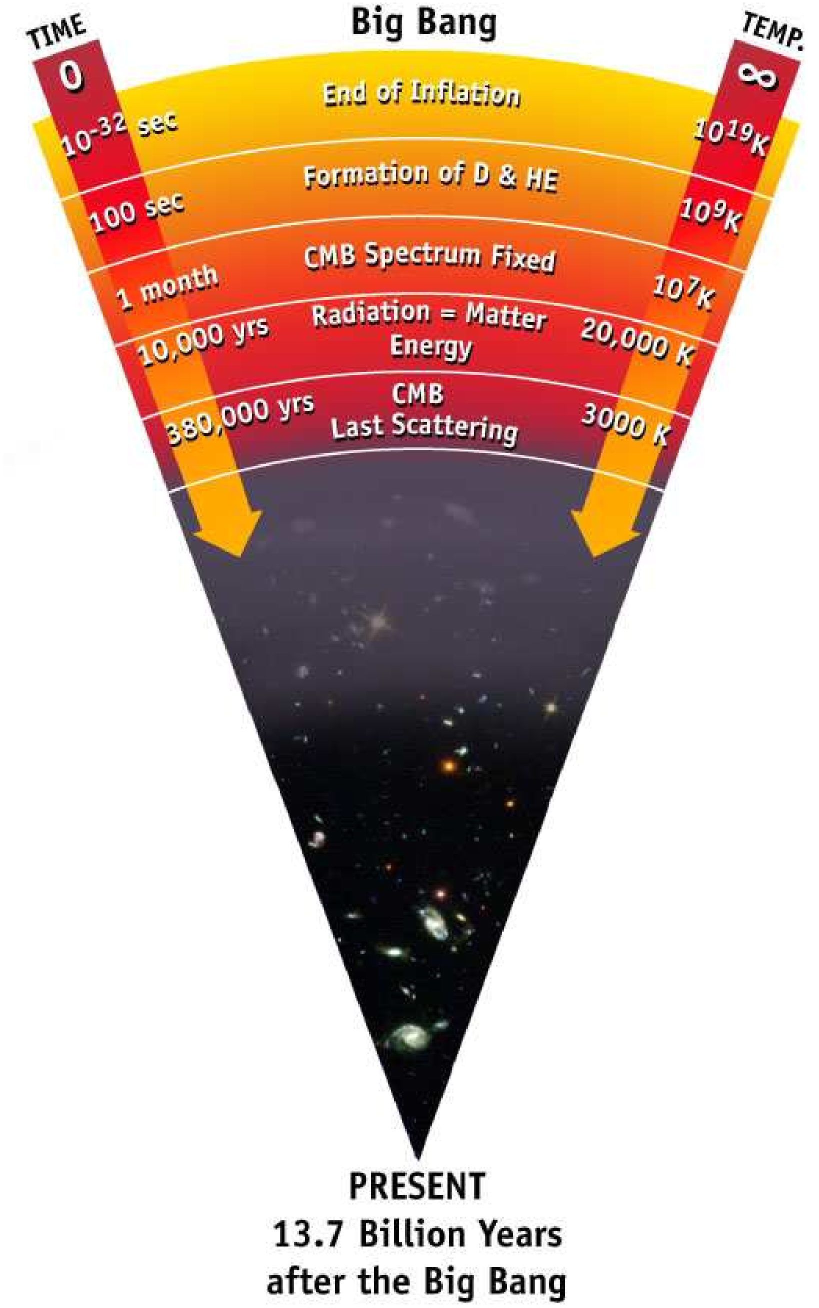

Figure 1.1.: *Sketch of the thermal history in the hot big bang scenario. The figure is from the WMAP mission webpage* `http://map.gsfc.nasa.gov`.

particles, evolved through a sequence of states of thermal equilibrium which finally has resulted in the state that we observe today. The phases in the thermal history were characterised by the masses, interaction cross-sections between the particles and/or radiation, and the cosmic expansion rate. In the proceeding of cosmic expansion, the Universe continuously cooled and particles decoupled from the thermal equilibrium with other particles once their interaction rates fell below the cosmic expansion rate. After decoupling the particles cooled adiabatically isolated from the rest. A sketch of the timeline of phases is shown in Fig. 1.1.

Primordial nucleosynthesis

Gamow proposed in 1946 that about 100 seconds after the big bang at a temperature of about $T \sim 10^9\,K$ the first light nuclei were formed. Shortly before this point, at $T \sim 10^{10}$K, neutrinos that kept protons and neutrons in equilibrium by weak interactions had decoupled. This effectively froze the neutron to proton ratio in to $[n/n+p] \sim 0.16$. Coincidently, this temperature is right about at a level at which a bound state between one proton and one neutron, namely deuterium, can form, so that many proton-neutron pairs could be converted into deuterium before all neutrons β-decayed away into protons. Since deuterium is a good neutron absorber, the primordial deuterium allowed the first simple chemical reactions by which it was mainly processed into ^{4}He and other light elements. Considering the chemical reactions the predicted mass fraction of helium is about 24% which is roughly observed, such as in the interstellar medium, stellar atmospheres and in the gas between galaxies. The conversion from hydrogen to helium via deuterium is not perfect, leaving some tiny fractions of other light elements behind. The precise predictions for the primordial abundances of deuterium and other light elements can be obtained by numerical modelling of the coupled chemical reactions taking into account the general cooling due to the cosmic expansion. This was first achieved by Wagoner *et al.* (1967). One finds that the fractions

$$\frac{^4\mathrm{He}}{\mathrm{H}},\ \frac{\mathrm{D}+{}^3\mathrm{He}}{\mathrm{H}},\ \frac{^3\mathrm{He}}{\mathrm{H}}\ \text{and}\ \frac{^7\mathrm{Li}}{\mathrm{H}} \tag{1.16}$$

all depend in a *different* way on $\Omega_\mathrm{b}h^2$, on the density parameter of the baryons. By measuring these ratios we can infer the baryon content in the Universe; each light-element abundance yields an estimate for $\Omega_\mathrm{b}h^2$ individually. Recent measurements found close agreement between the estimates for Ω_b and conclude that $0.015 \lesssim \Omega_\mathrm{b}h^2 \lesssim 0.023$ (Olive *et al.* 2000).

The Cosmic Microwave Background

The decoupling of the photons happened about 380.000 yrs after the big bang at the epoch of *recombination* where the Universe was cool enough, $T \sim 3000\,K$, to allow electrons and nuclei to combine into atoms. From that time onwards the Universe has become transparent for photons. Gamow postulated in 1949 that the decoupled photons should still be observable today as microwave background radiation with a Planck spectrum. Penzias & Wilson accidently discovered in 1965 this radiation, the *cosmic microwave background* (CMB), and made one of the most important discoveries in cosmology of the 20th century. The space-based experiment COBE made the first full-sky map of the CMB that is almost perfectly fit by a Planck function with characteristic temperature $T = 2.728 \pm 0.004\,K$ (Fixen *et al.* 1996).

Moreover, by transforming the measurements into a reference system of a fundamental observer and by subtracting the galactic foreground the CMB is almost isotropic. This suggests

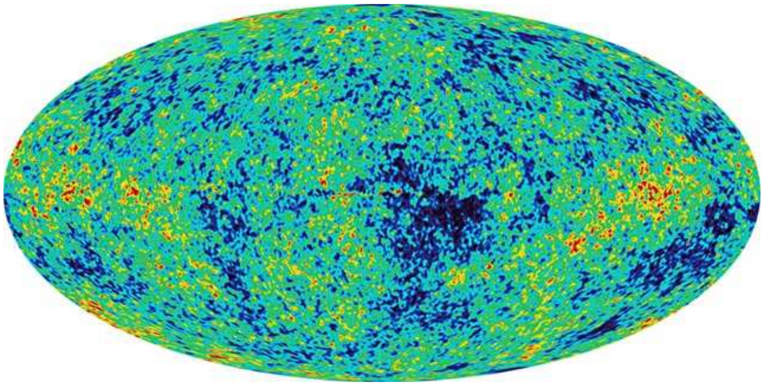

Figure 1.2.: *The microwave sky image from the WMAP Mission. Red colours indicate regions warmer than average, blue colours regions cooler than average. The temperature fluctuations are on a level of* $\delta T/T \sim 10^{-5}$. *The figure is from the WMAP mission webpage* `http://map.gsfc.nasa.gov`.

an extragalactic origin of the radiation. A full-sky picture of the corrected CMB is shown in Fig. 1.2. Apparently, it is not completely isotropic: one does not observe exactly the same black body temperature along every direction. The remaining temperature fluctuations, however, are tiny, namely on a level of $\delta T/T \sim 10^{-5}$. They reflect the fluctuations in the baryonic density field at the time of recombination. Despite of their smallness they are though to be the precursors of the structures we observe today. The change of temperature fluctuations with scale depends sensitively on cosmological parameters. The so far most accurate constraints on cosmological parameters were obtained from the CMB measurements of the Wilkinson Microwave Anisotropy Probe (WMAP, Spergel *et al.* 2003). In particular, the WMAP measurements yield $\Omega_{\rm b}h^2 = 0.0224(9)$ in agreement with estimates obtained from the abundances of light elements, which is a completely different kind of observation and which originates from a different epoch in cosmic thermal history.

Dark matter

Zwicky discovered in 1933 that galaxies in the Coma cluster are moving faster than one would expect if the gravitational field that is holding the cluster together was solely due to the luminous mass in galaxies. He attributed the missing mass to the probable existence of a non-luminous matter component, which has become known as *dark matter*. A similar effect was noticed in the density profiles of hot X-ray gas filling rich galaxy clusters. On galactic scales, it was found that the rotation speed of spiral galaxies as a function of distance from the rotation centre –the rotation curve– does not decline as expected from the starlight distribution of the galaxy. Instead, the rotation curve often remains flat out to large radii implying some sort of spherical dark matter halo in the outer parts of spiral galaxies. Another evidence for a dark matter component comes from the already mentioned CMB measurements and the abundance of light elements which imply a matter density parameter of $\Omega_{\rm m} \sim 0.3$ in contrast to a baryonic density parameter of $\Omega_{\rm b} \sim 0.04$. According to these findings, stars and gas can make up only about 10% of the mass necessary to explain the dynamics of stars, galaxies or the anisotropies in the CMB. Moreover, the dark matter component cannot be ordinary, baryonic matter made out of electrons, protons and neutrons.

1.1.2. Growth of structure in a Friedmann background

In the modern paradigm of structure formation, the galaxies and their distribution on large scales are a result of primordial inhomogeneities that collapsed by the influence of gravitation in a globally expanding universe. Mainly responsible for the collapse is the pressureless dark matter component in the cosmic fluid. This section is dedicated to the question how we can describe the growth of perturbations in the matter density.

Classical approximation

The true universe is obviously not perfectly homogeneous and isotropic in the sense of the Friedmann models. The Friedmann models are still valid, however, if the universe complies with the cosmological principle on large scales. This means that the global expansion (or collapse) according to $H\,(a)$ is observable by *averaging* over many objects; the energy density and pressure in the Eqs. (1.6), (1.7) are the average density and pressure in the universe. Local inhomogeneities are modelled as fluctuations about the average density with velocities measured relative to the Hubble flow frame (*peculiar velocities*). Although set in a cosmological context, for scales less than the cosmic horizon scale the physics of structure formation is well modelled by classical, non-relativistic Newtonian physics. Newtonian physics still holds on these scales because inhomogeneities in the gravitation field, $\delta\phi$, and the peculiar bulk velocities, δv, are small, $\delta\phi/c^2 \ll 1$ and $\delta v/c \ll 1$. The background cosmology is included into the Newtonian picture by expressing spatial coordinates, $\vec{r}$, as comoving coordinates $\vec{x}$

$$\vec{r} = a\,\vec{x}\ , \tag{1.17}$$

and velocities, $\dot{\vec{r}}$, as deviations, $\vec{v} = a\,\dot{\vec{x}}$ (proper), from the Hubble flow, $H(a)\vec{r}$, namely

$$\dot{\vec{r}} = \vec{v} + a\,H(a)\vec{x}\ . \tag{1.18}$$

The scale factor a in the resulting equations is evolved according to Eq. (1.11).

N-body simulations of structure formation

The “dark matter gas” is a many particle system. In classical statistical mechanics, a system with N particles is described by the BBGKY hierarchy. It is a set of N coupled equations that relates the phase-space probability distribution of $n \leq N$ particles to the distribution of $n-1$ particles in terms of integral equations. Theoretically, in order to model the phase-space distribution of the dark matter, the BBGKY hierarchy has to be put into the cosmological context (*cf.* Peebles 1980).

The most successful approach so far for getting approximate solutions is the N-body approach (*cf.* Jenkins *et al.* 1998). Here, the dark matter gas is represented by superparticles whose trajectories are followed numerically in phase-space on a computer. Due to hardware limitations, the number of superparticles is relatively small and the simulation volume is finite.[1] Therefore, the N-body simulations can only make reliable predictions on a limited range of scales. Nevertheless they have shown, among many quantitative predictions, that our paradigm of structure formation can explain the filamentary structure –the cosmic web– that is observed in the distribution of galaxies (see Fig. 1.3 and Fig. 1.4).

---

[1] The current record is 1024^3 particles in the Millennium-run simulations with a simulation volume of $500 \times 500 \times 500\,h^{-3}\mathrm{Mpc}^3$.

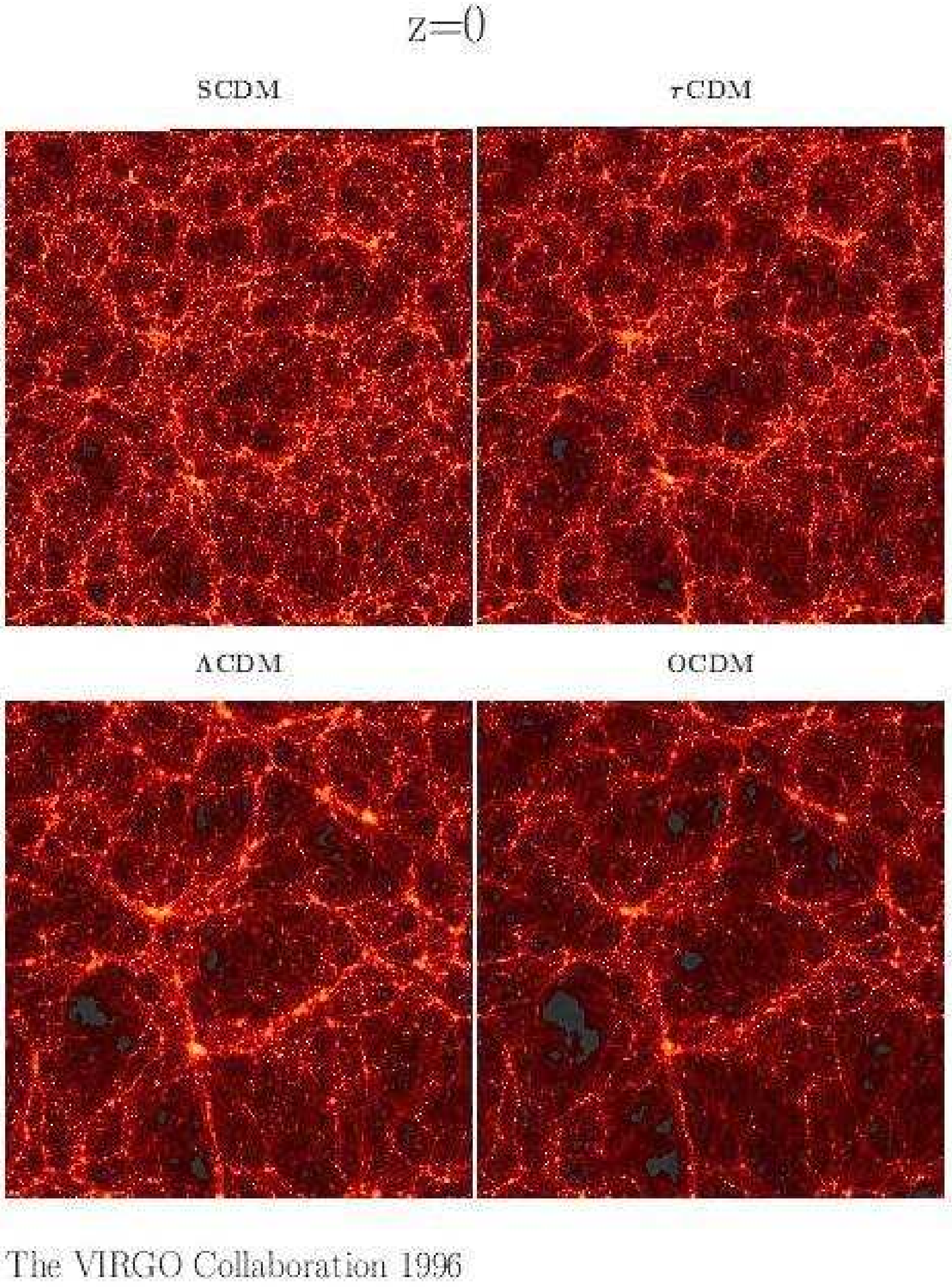

Figure 1.3.: *The simulated density distribution of dark matter in a box of* $240 \times 240 \times 240$ Mpc^3 *at redshift* $z = 0$ *for four different cold dark matter models:* ΛCDM $(\Omega_\mathrm{m} = 0.3, \Omega_\Lambda = 0.7, \Gamma = 0.21, \sigma_8 = 0.9, h = 0.7)$*, SCDM*$(1.0, 0.0, 0.5, 0.51, 0.5)$*, OCDM*$(0.3, 0.0, 0.21, 0.85, 0.7)$ *and* τCDM $(1.0, 0.0, 0.21, 0.51, 0.5)$ *(Jenkins* et al. *1998).*

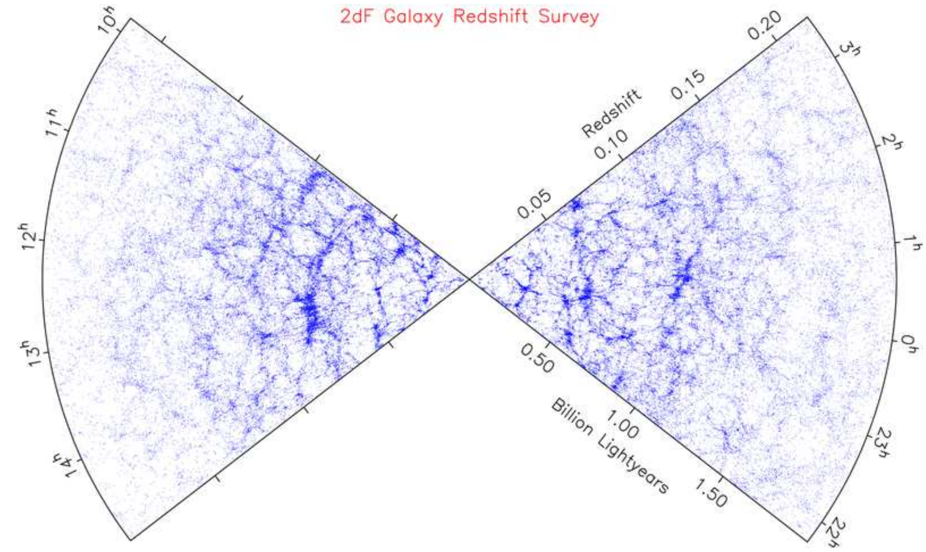

Figure 1.4.: *Clustering of galaxies in two thin strips,* 75° × 4° *(galactic north: left) and* 75° × 4° *(galactic south: right), of the local universe (median redshift* $\langle z \rangle = 0.11$*) as observed in the 2dFGRS (Peacock* et al. *2001). The figure shown contains about* 63.000 *galaxies which is only a fraction of the total survey. The galaxies presumable roughly trace the structure of the total matter field which is mainly made up by the invisible dark matter. Note that this is the distribution in redshift space which depends on both the distance and the peculiar velocities of the galaxies.*

Eulerian fluid approximation

As an alternative to the numerical approach, one may seek analytic solutions to the structure formation problem. Due to its intractability, this inevitable means breaking down the BBGKY hierarchy in some way. One way is to neglect the graininess of the dark matter gas and to approximate it by collisionless fluid. This results in the collisionless Boltzmann or Vaslov equation. Another *Ansatz*, the *hierarchal Ansatz*, is motivated by the observed spatial correlation of galaxies. All higher-order correlation functions are expressed in terms of products of two-point correlations (*cf.* Balian & Schaeffer 1989).

In this thesis, we will make analytical predictions for the structure formation on large scales with emphasis on the time after recombination. As many other authors we will use the fluid dynamical approach and focus only on the local density, $\rho_{\rm m}$, and (comoving) bulk velocity, $\vec{v}$, of the dark matter. We do not attempt to model the full phase-space distribution of dark matter. As long as no shell-crossing occurs, *i.e.* no crossing of the trajectories that belong to different particles, we can employ the Euler equation of hydrodynamics and the continuity equation for that purpose. It is customary to express the system in terms of the *density contrast* $\delta_{\rm m}$

$$\rho_{\rm m} \equiv \langle \rho_{\rm m} \rangle \left(1 + \delta_{\rm m}\right) \; . \tag{1.19}$$

In comoving coordinates cosmological hydrodynamics is (Peebles 1980):

$$\begin{aligned} \frac{\partial \vec{v}}{\partial t} + H(a)\vec{v} + \frac{1}{a}(\vec{v}\nabla)\vec{v} + \frac{1}{a}\frac{\nabla \delta p}{\langle \rho_{\rm m} \rangle} + \frac{1}{a}\nabla\delta\phi &= 0 \; , & (1.20) \\ \frac{\partial \delta_{\rm m}}{\partial t} + \frac{1}{a}\nabla\vec{v} + \frac{1}{a}\nabla\left(\delta_{\rm m}\vec{v}\right) &= 0 \; , & (1.21) \end{aligned}$$

$$\nabla^2 \delta\phi - \frac{3}{2} a^2 H^2\left(a\right) \Omega_{\rm m}(a) \delta_{\rm m} \quad = \quad 0 \; . \tag{1.22}$$

Note that the pressure term can be set to zero, $\delta p = 0$, for a dark matter component with negligible velocity dispersion (random motions), *i.e.* for "cold" dark matter. Eq. (1.22), is the classical Poisson equation for the perturbations $\delta\phi$ in the gravitational field produced by the density fluctuations $\delta_{\rm m}$. Eqs. (1.20) and (1.21) are the Euler equation and continuity equation, respectively.

Linear Eulerian fluid equations

Solutions to cosmological hydrodynamics (1.20)-(1.22) can be found by expanding $\delta_{\rm m}$ and $\vec{v}$ as perturbation series in terms of powers of the initial conditions, which are small in amplitude, or in powers of the growing mode of the linearised equations of hydrodynamics (*cf.* Fry 1984; Goroff *et al.* 1986; Bernardeau 1994). The linearised equations are obtained by neglecting the rotational part of the velocity field, $\nabla \times \vec{v} \equiv \vec{0}$, all terms containing products of $\delta_{\rm m}$ with $\vec{v}$ and products of $\vec{v}$:

$$\begin{aligned}
\frac{\partial^2 \delta_{\rm m}}{\partial t^2} + 2H(a)\frac{\partial \delta_{\rm m}}{\partial t} &= \frac{1}{a^2 \left\langle \rho_{\rm m} \right\rangle} \nabla^2 \delta p + \frac{3}{2} a^2 H^2(a) \Omega_{\rm m}(a)\, \delta_{\rm m} & (1.23)\\
\frac{\partial \delta_{\rm m}}{\partial t} + \frac{1}{a} \nabla \vec{v} &= 0 & (1.24)\\
\left\langle \rho_{\rm m} \right\rangle &= \frac{3H^2(a)}{8\pi G} \Omega_{\rm m}(a)\; . & (1.25)
\end{aligned}$$

The growing mode solution of $\delta_{\rm m}$ in the linearised equations is (*cf.* Carol *et al.* 1992):

$$\begin{aligned}
\delta_{\rm m}(\vec{r}, a) &= \frac{D_+\left(a\right)}{D_+\left(a_{\rm init}\right)}\, \delta_{\rm m}(\vec{r}, a_{\rm init})\; , & (1.26)\\
D_+\left(a\right) &\equiv H\left(a\right) \int_0^a {\rm d}a' \, \frac{1}{\left[a' H\left(a'\right)\right]^3}\; , & (1.27)
\end{aligned}$$

where $\delta_{\rm m}(\vec{r}, a_{\rm init})$ are the initial density fluctuations. The scaling of $D_+(a)$ preserves the structure of the density perturbations since only the perturbation amplitude is affected, independent of the position in the field. See Fig. 1.5 for the time-dependence of the linear growth factor $D_+(a)$.

Fluctuations are small on large scales, $|\delta_{\rm m}| \ll 1$ and $|\vec{v}| \ll 1$. Therefore, the linear solution is a good description for the growth of the density contrast on large smoothing scales. As a rule-of-thumb, by large scales we mean scales larger than about $8h^{-1}$Mpc which corresponds to the typical size of rich galaxy clusters.

Dark matter flavours

The way structures form in this paradigm depends on the velocity dispersion of the dark matter; it is determined by the mass of the dark matter particles and whether they were relativistic or non-relativistic at the time of decoupling. There are two extremes: in *cold dark matter* scenarios (CDM), the velocity dispersions are non-relativistic, $\delta p = 0$. Here, structure forms first on small scales, larger structures form later on by merging of smaller

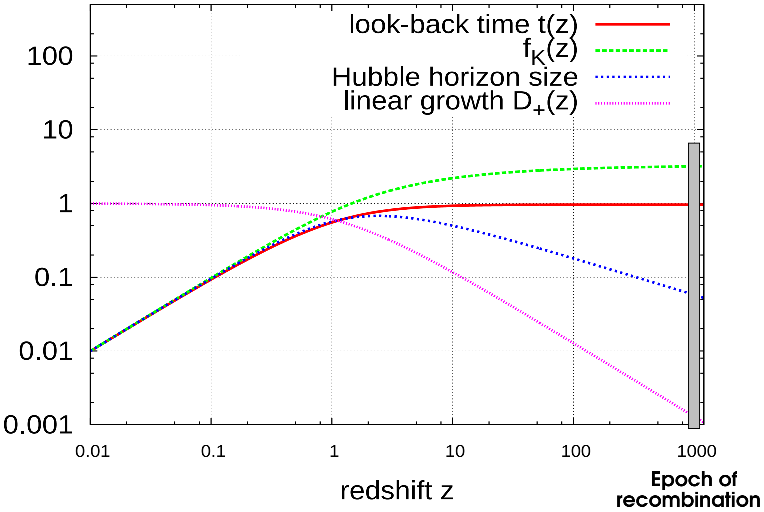

Figure 1.5.: *Evolution of some global parameters assuming the concordance* ΛCDM *(Spergel* et al. *2003). $t(z)$ is the look-back time in units of $1/H_0 \approx 14$ Gyrs. "$f_{\rm K}(w)$" is the comoving angular diameter distance as function of the comoving radial distance w (in units of $c/H_0 \approx 4.2$ Gpc). The Hubble horizon defines the comoving size of the visible universe (in units of $c/H_0 \approx 4.2$ Gpc). $D_+(z)$ denotes the linear growth factor relative to the growth factor at $z = 0$. On linear scales, fluctuations have grown by a factor of about 10^3 since recombination.*

objects (*hierarchical clustering* or bottom-up structure formation). This is in contrast to *hot dark matter* scenarios (HDM) where the velocities of the dark matter particles are relativistic at decoupling; a candidate for hot dark matter particles are neutrinos. Small-scale fluctuations are wiped out due to diffusion ("free-streaming mixing") of the "fast" particles. Structures form therefore first on larger scales by gravitational collapse that at later times fragment into smaller objects (top-down). CDM and HDM scenarios are extreme cases. Also hybrid scenarios are discussed in cosmology, such as the warm dark matter model (WDM).

Strong constraints from observations, in particular the CMB observations, (*e.g.* Tegmark *et al.* 2004a; Seljak *et al.* 2004b) favour the CDM scenario, although there are concerns about its detailed predictions. For example, the predicted number of small, compact dark matter on sub-galactic scales appears to be too high compared to observations. On the other hand, maybe the numerical simulations making the CDM predictions are flawed in that respect, or the interpretation of the observations, that never directly observe dark matter clumps, is wrong. Another issue is that the rotation curves of dwarf galaxies imply density profiles that seem to be at odds with the universal, cuspy, density profiles of the CDM picture.

1.2. Quantifying structure with correlation functions

Cosmology cannot explain the detailed appearance of the Universe. For example, it does not say why the Andromeda galaxy M31 is at the position where it is currently observed, neither why it has its measured mass or age. Instead, cosmology makes statistical statements, *e.g.* about the mass distribution of galaxies, the probability to obtain a galaxy within a certain distance of another galaxy, the angular correlation of the CMB temperature anisotropies, *etc.*

In the statistical approach of cosmology, we consider the observed universe as realisation of a random field (see Appendix A.3), as a *cosmic random field.* Owing to the Cosmological Principle, statistical quantities of cosmic fields have certain symmetries which are going to be listed in the following.

The presence of structure generates correlations between values, $\delta(\vec{x})$, at different positions in the cosmic field. Studying cosmic structure can therefore be achieved by looking at the correlators

$$\xi^{(n)}\left(\vec{x}_1,\vec{x}_2,\dots,\vec{x}_n\right)\equiv\left\langle\delta\left(\vec{x}_1\right)\,\delta\left(\vec{x}_2\right)\,\dots\,\delta\left(\vec{x}_n\right)\right\rangle\;, \tag{1.28}$$

where $\delta(\vec{x}_i)$ are values of the random field at the positions $\vec{x}_i$.[2] The operator $\langle\dots\rangle$ denotes the average over all possible field configurations, the ensemble average. Alternatives aimed at quantifying the structure are the genus statistics or, more generally, Minkowski functionals (Mecke, Buchert & Wagner 1994; Hamilton, Gott & Weinberg 1986; Gott, Melott & Dickinson 1986); they quantify the topology of iso-density surfaces in the random fields.

1.2.1. Symmetries of cosmic fields

The Cosmological Principle implies fundamental symmetries for the n-point correlation functions $\xi^{(n)}$ of random fields in cosmology:

1. Cosmic fields are *statistically homogeneous*,

   $$\xi^{(n)}\left(\vec{x}_1+\vec{c},\dots,\vec{x}_n+\vec{c}\right)=\xi^{(n)}\left(\vec{x}_1,\dots,\vec{x}_n\right)\;, \tag{1.29}$$

   where $\vec{c}$ is an arbitrary constant translation vector in space.

2. Cosmic fields are *statistically isotropic*,

   $$\xi^{(n)}\left(\mathbf{A}\vec{x}_1,\dots,\mathbf{A}\vec{x}_n\right)=\xi^{(n)}\left(\vec{x}_1,\dots,\vec{x}_n\right)\;, \tag{1.30}$$

   where $\mathbf{A}$ is an arbitrary spatial rotation.

3. Cosmic fields obey the *fair-sample hypothesis*, meaning that averaging over a large enough volume of one field realisation is, in principle, equivalent to performing an ensemble average.[3]

Items 1 and 2 have as consequence that the values of n-point correlators only depend on the relative distances of the points $\vec{x}_i$ with respect to each other. They therefore depend neither on the absolute position nor on the orientation of the polygon defined by $\vec{x}_i$. Item 3 allows us to estimate $\xi^{(n)}$, in fact all statistical quantities, from one single realisation alone by averaging over all possible polygon orientations and positions. Therefore, we can interpret the ensemble average $\langle\dots\rangle$ as average over all possible rotations $\mathbf{A}$ and translations $\vec{c}$ in one single random field realisation if the realisation area is sufficiently large enough.

---

[2] In general, the values $\delta(\vec{x}_i)$ could be from different or partly from different random fields. As this case does, mathematically, not make much difference we consider here only one random field. However, later on we will encounter cross-correlations, such as by looking at correlations between spatial distributions of different galaxy populations.

[3] This item is not completely independent from the statements 1 and 2.

1.2.2. Polyspectra of cosmic fields

Equivalent to the correlators $\xi^{(n)}$ we can study the correlations of the Fourier transforms of the (here: three dimensional) random fields

$$\tilde{\delta}(\vec{k}\,) = \int \mathrm{d}^3x\, \delta(\vec{x}\,)\, e^{+\mathrm{i}\vec{k}\cdot\vec{x}} \quad , \quad \delta(\vec{x}\,) = \int \frac{\mathrm{d}^3k}{(2\pi)^3}\, \tilde{\delta}(\vec{k}\,)\, e^{-\mathrm{i}\vec{k}\cdot\vec{x}} \tag{1.31}$$

by means of the Fourier space correlator

$$\lambda^{(n)}(\vec{k}_1, \vec{k}_2, \ldots, \vec{k}_n) \equiv \left\langle \tilde{\delta}(\vec{k}_1)\tilde{\delta}(\vec{k}_2)\ldots\tilde{\delta}(\vec{k}_n) \right\rangle \; . \tag{1.32}$$

This definition is fairly general. If we consider Fourier space correlations in cosmology we can make use of the statistical homogeneity which makes almost all values for $\lambda^{(n)}$ zero, namely

$$\lambda^{(n)}(\vec{k}_1, \vec{k}_2, \ldots, \vec{k}_n) \;=\; (2\pi)^3\, \delta_{\mathrm{D}}^{(3)} \left(\sum_{i=1}^{n} \vec{k}_i \right) P^{(n)}(\vec{k}_1, \vec{k}_2, \ldots, \vec{k}_n) \; , \tag{1.33}$$

where $\delta_{\mathrm{D}}^{(3)}$ is the Dirac delta function. Thus, statistical homogeneity dramatically reduces the number of non-zero entries in $\lambda^{(n)}$. They can possibly only be non-zero if their corresponding wave-vectors $\vec{k}_i$ form a closed polygon, *i.e.* $\sum_i \vec{k}_i = \vec{0}$. The newly introduced $P^{(n)}$ are called the *polyspectra* of the cosmic fields.[4]

The isotropy argument also has an impact on the symmetry of the polyspectra. It makes them independent of the orientation of $\vec{k}_i$-polygon. The polyspectra are only functions of the internal angles $\sphericalangle \vec{k}_i, \vec{k}_j$ and side lengths of the polygon; this further reduces the degrees of freedom of the polyspectra.

Power spectrum and bispectrum

It is a convention to define the *power spectrum*, $P(k)$,

$$P^{(2)}(\vec{k}, -\vec{k}\,) = P(|\vec{k}\,|) \equiv P(k) \; , \tag{1.34}$$

and the *bispectrum*, $B(k_1, k_2, \phi)$,

$$P^{(3)}(\vec{k}_1, \vec{k}_2, -\vec{k}_1 - \vec{k}_2) = B(|\vec{k}_1|, |\vec{k}_2|, \sphericalangle \vec{k}_1, \vec{k}_2) \equiv B(k_1, k_2, \phi) \; , \tag{1.35}$$

where $\phi \in [0, 2\pi[$ is the angle between the two k-vectors $\vec{k}_1$ and $\vec{k}_2$.

In this thesis, we give sometimes polyspectra or random fields an additional index that is used to parametrise their time-dependence, for example as in $P\,(k, w)$ or $\delta(\vec{x}, w)$. The comoving distance, w, is used in this context to specify the time $t(w)$ in the past at which a photon had to be emitted at distance w to arrived at $w = 0$ today.

---

[4] Due to the constraint of closed polygons imposed by statistical homogeneity, $P^{(n)}$ depends actually only on $n-1$ $\vec{k}$-vectors since, $\vec{k}_n = -\sum_{i=1}^{n-1} \vec{k}_i$.

1.2.3. Polyspectra of projected cosmic fields

The cosmic fields are observed as two-dimensional projections $\hat{\delta}(\vec{\theta}\,)$ on the sky, where the vector $\vec{\theta}$ defines the direction in which we are looking. An example may be the angular distribution of galaxies on the sky. Now consider a three-dimensional random field $\delta(\vec{x}, w)$ for which the coordinate system is chosen such that w is a comoving distance along some fixed reference line-of-sight and $\vec{x}$ a 2D-vector perpendicular to the reference line-of-sight. Let $\hat{\delta}(\vec{\theta}\,)$ be a general projection of field δ seen through a radial selection filter $q(w)$:

$$\hat{\delta}(\vec{\theta}\,) = \int_0^\infty \mathrm{d}w \; q(w)\, \delta(f_\mathrm{K}\,(w)\,\vec{\theta}\,, w) \;, \tag{1.36}$$

where $f_\mathrm{K}(w)$ is the comoving angular diameter distance.

Since $\delta(\vec{x}, w)$ is a random cosmic field also $\hat{\delta}(\vec{\theta}\,)$ will be a statistically homogeneous and isotropic random field, but living on the unit-sphere. In this thesis, we assume that we always observe only small patches of this sphere; small enough to approximate the topology of the patch by a tangential, Cartesian plane (*flat-sky approximation*). How do the polyspectra of the projected fields in the flat sky approximation look? The answer to that question is given by the general form of *Limber's equation* in Fourier space (Kaiser 1998). It states how one can transform the time-dependent 3D-polyspectra $P^{(n)}_\mathrm{3D}(k_1, \dots, k_n, w)$ (in comoving coordinates) into the 2D-polyspectra $P^{(n)}(\ell_1, \dots, \ell_n)$:

$$P^{(n)}(\ell_1, \dots, \ell_n) = \int_0^{w_\mathrm{h}} \mathrm{d}w \; \frac{\prod_{i=1}^n q_i(w)}{[f_\mathrm{K}(w)]^{2(n-1)}} \;\; P^{(n)}_\mathrm{3D}\left(\frac{\ell_1}{f_\mathrm{K}(w)}, \dots, \frac{\ell_n}{f_\mathrm{K}(w)}, w\right) \;, \tag{1.37}$$

where $q_i\,(w)$ are the (possibly different) selection filters for the n projected random fields. Note that the $P^{(n)}$ can also be cross-correlation polyspectra. The quantity w_h is the comoving Hubble radius, thus the farthest distance in space we can possibly look at. The arguments ℓ_i are angular wave modes; they are the Fourier space counterparts of angular distances θ_i in the tangential plane.

Throughout this thesis, we use this equation only for projecting power spectra:

$$P(\ell) = \int_0^{w_\mathrm{h}} \mathrm{d}w \; \frac{q_1(w) q_2(w)}{f_\mathrm{K}^2(w)} P_\mathrm{3D}\left(\frac{\ell}{f_\mathrm{K}(w)}, w\right) \;. \tag{1.38}$$

1.3. The dark matter power spectrum

The gravitational collapse of the dark matter is the main reason for the formation of structure in the Universe. The dark matter structure can be quantified by the mode correlations – the polyspectra– of the over- and underdensities in the density field. What does the power spectrum –the simplest of all polyspectra– of the dark matter density perturbations look and how does it evolve with time?

1.3.1. The linear power spectrum

Eqs. (1.20)-(1.22) provide a model for the evolution of the dark matter density contrast on large scales. As the polyspectra of the density perturbations, and in particular the power spectrum, are functions of δ_m, this model also predicts their time evolution, starting from a given initial condition. The initial condition is given by the *primordial power spectrum*.

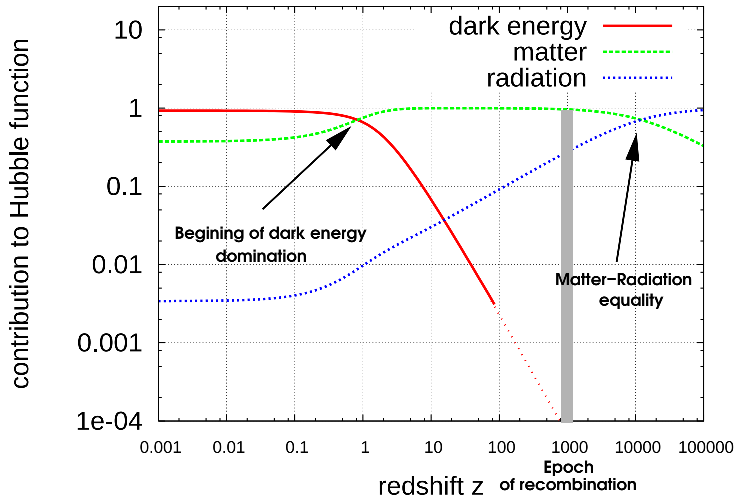

Figure 1.6.: *Depending on the cosmic scale factor, a, the cosmic expansion is dominated by different components of the cosmic fluid which has an impact on how structure grows. To illustrate this effect this figure plots the contribution of* Ω_i *to the total Hubble function* $H(a)$ *evaluated by* $H_i(a)/H(a)$ *with* $H_i(a) = \sqrt{\Omega_i\, a^n}$, $\Omega_i = \Omega_\mathrm{r}, \Omega_\Lambda, \Omega_\mathrm{m}$ *and* $n = -4, 0, -3$ *for radiation, dark energy and dark matter, respectively. As values for the density parameters the results from Spergel* et al. *(2003) are taken. In the redshift range plotted are three typical epochs of the cosmic expansion: the dark energy dominated era* $(z < 1)$, *the dark matter dominated era* $1 < z < 1.2\times10^4$ *and the radiation dominated era* $z < 1.2\times10^4$.

Primordial power spectrum

The shape of the primordial power spectrum is not *a priori* clear. As educated guess one assumes a featureless power law without any preferred scale (Kolb & Turner 1990)

$$P_\mathrm{prim}(k) \propto k^n \ , \tag{1.39}$$

where n is the *primordial spectral index*. This index is, besides a possible tilt, predicted by inflationary models. In these models, the origin of the primordial fluctuations are quantum fluctuations that had been blown up to macroscopic scales during a phase of exponential expansion in the very early universe shortly after the Planck time, $t_\mathrm{p} \sim 10^{-42}$ s, (Fig. 1.1) ignited by a phase-transition that released latent heat (Guth 1981). Inflationary cosmology was originally developed as a clever way to solve some problems in the classical standard big bang model, and has now become an important part in the modern cosmological paradigm furnishing us with an elegant picture of the early Universe. For a review we refer the reader to Liddle & Lyth (1993).

Growth of perturbations

Until the epoch of recombination, $z_\mathrm{re} \backsimeq 1000$, the fluctuations were small enough to apply the linearised theory of structure formation. In the linearised model, the different modes of the fluctuation field grow independently from each other, $\tilde{\delta}_\mathrm{m}(\vec{k}, a) \propto D_+(a)$. Yet the physics is not straightforward since one has in a general model a) to distinguish between different epochs of cosmic expansion (Fig. 1.6), b) between possible different components like hot/warm/cold dark matter, radiation and baryonic matter and c) between different possible modes of perturbations referring to the relation between the perturbation in the matter and radiation field (adiabatic, isothermal, iso-curvature perturbations). The following discussion briefly outlines some of the relevant physics that took place.

During the *radiation dominated era*, modes of all components with a wavelength $\lambda = 2\pi/k$ greater than the Hubble radius $w_{\rm h}$ grow roughly with $D_+(a) \propto a^2$. Once $\tilde{\delta}_{\rm m}(\vec{k})$ enters the Hubble horizon, $\lambda < w_{\rm h}$, the growth becomes stagnated by the Mészarós effect (Mészarós 1974) since the cosmic expansion time scale exceeds the free-fall time-scale; the modes are said to be "frozen in". In addition, for baryonic components that fall below the Jeans length scale during this era,

$$w_{\rm h} > \lambda_{\rm J} \equiv c\sqrt{\frac{\pi}{3G\rho_{\rm b}}}\,, \tag{1.40}$$

the modes also start to oscillate: due to their own gravitation field, $\rho_{\rm b}$ is the baryon density, they try to collapse further, but the radiation pressure of the photon field forces them back. As the photons are diffusing during the process of oscillation, there is Silk damping that dissipates energy and on average reduces the amplitude of the oscillating modes (Silk 1968). Damping can also occur for relativistic particles due to the random motions of fast particles. This diffusion process is called free-streaming damping.

By the time $t_{\rm eq}$ at which the radiation domination ends, the Mészarós effect has thus imprinted a characteristic peak at $k \sim 2\pi/d_{\rm h}(t_{\rm eq})$ on the primordial power spectrum of the dark matter. In the following time, the universe is then *matter dominated.* Now, modes inside the Hubble horizon can grow since the cosmic expansion has slowed down. Dark matter modes both inside and outside the Hubble horizon grow with roughly $D_+(a) \propto a$. Baryonic modes, on the other hand, are only allowed to continue growing if $\lambda > \lambda_{\rm J}$, otherwise they carry on oscillating and dissipating because they are still coupled to the radiation pressure by Thomson scattering. After the recombination, during which the nuclei and free electrons form neutral atoms, the coupling between the baryonic component and the photons stops. From then onwards, the baryonic component only feels its own gas pressure which dramatically lowers the Jeans length scale. Now the baryonic modes can grow on almost all scales giving birth to the first generation of stars. As a further complication, at all times components are coupled with each other by the gravitational field they generate.

Transfer function

This interplay of constituents and effects shaped the original post-inflation primordial dark matter fluctuations to a new fluctuation spectrum $P_{\rm lin}$ after the recombination; see *e.g.* Peacock (2001) for a detailed description. The shape of the (linear) power spectrum $P_{\rm lin}$ can be simulated by elaborated numerical codes like CMBFAST (Zaldarriaga & Seljak 2000). The outcomes of such simulations have been fitted for particular component models by analytic formulae, the *transfer function* $T(k)$:

$$P_{\rm lin}(k) \propto P_{\rm prim}(k)\, T^2(k)\ . \tag{1.41}$$

In this thesis, we extensively use the adiabatic CDM transfer function from Bardeen *et al.* (1986) to model $P_{\rm lin}$:

$$T(k) = \frac{\ln(1+2.34q)}{2.34q}\left[1+3.89q+(16.1q)^2+(5.46q)^3+(6.71q)^4\right]\ , \tag{1.42}$$

where $q \equiv \frac{k\,h{\rm Mpc}^{-1}}{\Gamma}$ with Γ being the so-called *shape parameter.* The value of Γ is roughly $\Omega_{\rm m}h \sim 0.21$, provided the baryonic component $\Omega_{\rm b}$ is very small compared to $\Omega_{\rm m}$ (Efstathiou *et al.* 1992). Also the Bardeen at al. transfer function assumes a negligible fraction of baryonic matter. The acoustic oscillations imprinted by baryonic component before the recombination are therefore not included in this power spectrum model. For a more accurate prescription of $T(k)$ including the baryonic effect see Eisenstein & Hu (1999).

Power spectrum normalisation

Nothing has been said about the normalisation of the power spectrum so far. This parameter has to be obtained from observations, usually by measuring the variance σ_8^2 of the galaxy number inside spheres of $8h^{-1}$Mpc –the typical size of large galaxy-clusters– in the local universe (*cf.* White, Efstathiou & Frenk 1993), or by measuring the amplitude of the temperature fluctuations in the CMB on a particular scale. Either way, both methods observe (indirectly) the fluctuations of $\delta_{\rm m}$ through a smoothing window $W(r)$:

$$\left\langle\delta_{\rm m}^2\right\rangle = \left\langle\left[\int {\rm d}^3r\,\frac{1}{R^3}W\left(\frac{|\vec{r}|}{R}\right)\ \delta_{\rm m}(\vec{r})\right]^2\right\rangle = \frac{1}{2\pi^2}\int {\rm d}k\,k^2\,|\tilde{W}(Rk)|^2P_{\rm m}(k)\ , \tag{1.43}$$

where $\tilde{W}(x)$ denotes the Fourier transform of the window function and is R its characteristic size. By definition, for σ_8 a top-hat window with size $R = 8\,h^{-1}$Mpc has to be used:

$$W(x) = \begin{cases} \frac{3}{4\pi} & \text{for } x<1 \\ 0 & \text{otherwise}\end{cases}\ , \tag{1.44}$$

$$\tilde{W}(x) = \frac{3}{x^3}\left(\sin x - x\cos x\right)\ . \tag{1.45}$$

The window size for σ_8 is large enough to take essentially only modes into account for which linear theory roughly still applies; it has a value of about $\sigma_8 \sim 0.9$. Therefore, σ_8 can be used to fix the amplitude of the linear power spectrum linearly evolved to the present day, $P_{\rm lin}(k, a=1)$. In conclusion, the transfer function, the primordial power spectrum and the normalisation completely defines the linear dark matter power spectrum.

1.3.2. The non-linear power spectrum

The effect of the physics in the early universe on the spectral shape of the primordial power spectrum is encoded in the transfer function. How does the dark matter power spectrum evolve afterwards up to the present time? A first guess is to apply, as before, the linear theory of structure formation. The theory predicts that the amplitude of the power spectrum scales with $P_{\rm lin}(k,a) \propto D_+^2(a)P_{\rm lin}(k,1)$. However, this is a good approximation only on large scales where $\left\langle\delta_{\rm m}^2\right\rangle \ll 1$.

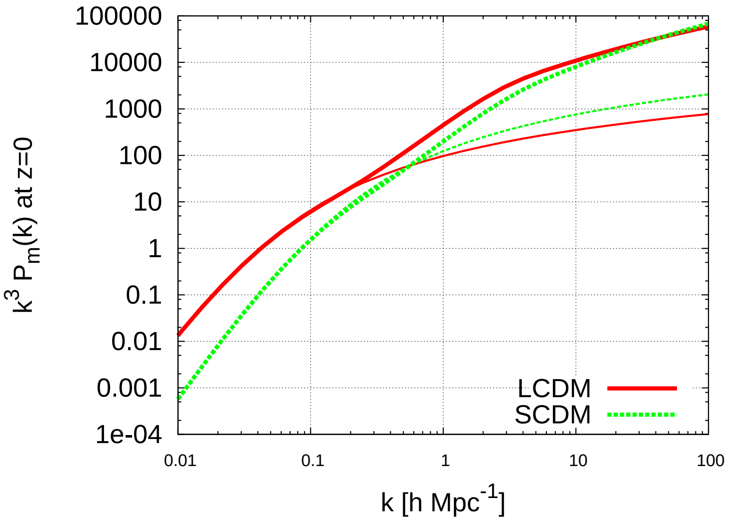

Figure 1.7.: *The dark matter power spectrum for two different models: LCDM* ($\Omega_{\rm m} = 0.3, \Omega_\Lambda = 0.7, \Gamma = 0.21, \sigma_8 = 0.9$)*, SCDM* $(1.0, 0.0, 0.70, 0.6)$ *and* $h = 0.7$ *for both models. The thinner lines are the linear power spectra while the thicker lines indicate the non-linear power spectra as predicted by Peacock & Dodds (1996).*

Can we also work out the dark matter power spectrum on non-linear scales? To make predictions on non-linear scales one has to solve the full problem of structure formation which until today can only be achieved using N-body simulations. An interesting semi-analytical prescription for the evolution of the dark matter power spectrum seen in such simulations has been proposed by Peacock & Dodds (1996, PD96). Their prescription is based on the “HKLM procedure” (Hamilton *et al.* 1991) which suggests a way to model the transition between the linear regime –large distances r– and the highly non-linear regime –small distances r– in the 2-point correlation $\xi^{(2)}(r)$ of the dark matter clustering. As for the linear regime, the highly non-linear regime can also be understood analytically. PD96 used the HKLM prescription, modified for the power spectrum, and supplemented it by generic functions fitted to the N-body results. The practical result is an algorithm that maps the linear power spectrum, $P_{\rm lin}$, to the non-linear power spectrum. The accuracy achieved by PD96 is about 10 percent, which for the purpose of this thesis is accurate enough. A more accurate prescription has been recently proposed by Smith *et al.* (2003). In Fig. 1.7, we plotted two examples for the linear and corresponding non-linear dark matter power spectrum at $z = 0$. As can be seen in the plot, the linear and non-linear power spectra agree on large scales but disagree clearly on small scales where the linear theory underestimates the fluctuations.

1.4. Galaxies and their relation to the dark matter

In comparison to the total mass in the universe, galaxies take, considering their mass, only a minor part in the big picture of structure formation. They formed from the perturbations in the baryonic component whose total mean density is very much lower than that of dark matter. Not even all of the baryonic matter has been converted into galaxies. Most of it is residing as

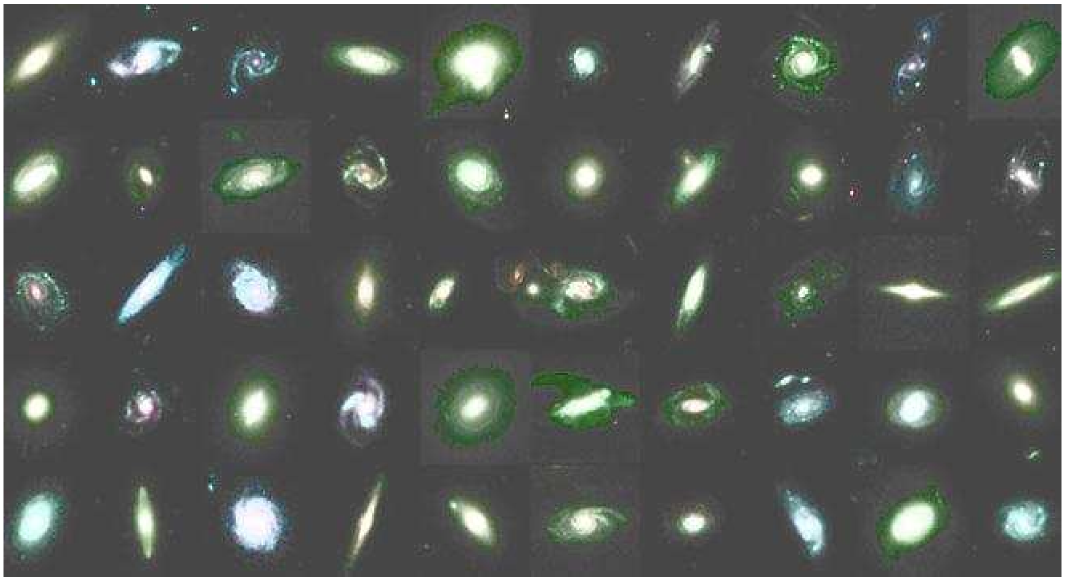

Figure 1.8.: *A collection of galaxy morphologies as observed in the GEMS survey (* cf. *Rix* et al. *2004). The survey consists of one* $28' \times 28'$ *field patched with* 120 *HST images; it is centred on the Chandra Deep Field South providing structural parameters and morphologies of about* 10.000 *galaxies. Already in the optical we observe a large diversity in galaxy morphologies.*

hot gas between galaxies. Due to their relatively easy observability, it would be very convenient if galaxies were perfect tracers –*unbiased tracers*– of the total mass distribution; all statistical properties of the mass structure could then be derived from galaxy catalogues (Fig. 1.4).

Indeed, it is rather unlikely that galaxies are unbiased tracers, because the laws determining the galaxy distribution are very complex and highly non-linear. The primordial gas from which they form requires special conditions to be able to cool and fragment into galaxies (White & Frenk 1991; White & Rees 1978). Due to shock heating of the baryons and energy feedback between galaxies and baryons, the properties of the gas feeding galaxy formation have been gradually changing with time. Furthermore, galaxies interact with each other or with the baryonic intergalactic medium, merge or get accreted into other more massive galaxies (Cole *et al.* 2000). These mechanisms probably produced the large diversity in galaxy masses, colours, morphologies (Fig. 1.8) and chemistry we observe today. The processes are subject of current research but the details remain as yet unknown. Based on our current knowledge it would be very surprising if this complexity would eventually result in a simple, linear, one-to-one relationship between the galaxy density and total matter density, making galaxies unbiased tracers.

But this should not be seen as a disadvantage, because by studying this dark matter-galaxy relationship we can learn more about galaxies. Observing the relation between the invisible dark matter field and the galaxies is a particularly tough problem. However, with gravitational lensing at hand and upcoming wide-field galaxy surveys, we now have a technique to directly unravel this relationship. This thesis will focus on the lensing technique.

From the point of view of statistics, quantifying galaxy bias leads to the question how one can parametrise differences in the statistical properties –not the obvious differences between two particular realisations– of two random fields; both the distribution of galaxies and the distribution of dark matter are thought to be realisations of statistcially homogeneous and isotropic random fields. Naturally, since random fields are being described by correlation functions, or equivalently powerspectra or aperture moments (see Appendix A.3), bias parameters are expressed in terms –in fact as ratios– of these basic quantities. In the following, two concepts are going to be introduced: the linear stochastic bias, which takes into account only the two-point statistics of randoms fields and is blind with respect to hight-order correlations, and the non-linear stochastic bias.

1.4.1. Classification of galaxies

Galaxies can, at the crudest level, be divided into two basic types: *spiral galaxies* and *elliptical galaxies* (Fig. 1.8). Their morphological appearance is mainly due to a central bulge, which is close to spherically symmetric, and a disk component. The motion of stars in the bulge component is anisotropic, while disk stars move in circular orbits about the galaxy centre. Depending on how pronounced the components are in an individual galaxy the whole range from spirals, with dominating disks, to ellipticals, with dominating bulges, is covered. For historical reasons (Hubble 1936), spirals are also called late-type galaxies, whereas ellipticals are called early-type galaxies.

Elliptical galaxies are usually red in colour, harbour little dust and interstellar gas and show no sign of active star formation. Their spectrum has no or only weak emission lines in the optical. Stars are formed in the disk components of spiral galaxies usually giving them a blue appearance and, depending on the rate of star formation, strong emission lines.

The ratio in numbers of spiral and elliptical galaxies strongly depends on the local galaxy density (Dressler 1980; Dressler *et al.* 1997). Spiral galaxies tend to be depleted in clusters relative to ellipticals, while few elliptical galaxies are found in low density regions. Outside of galaxy clusters about 3/4 of galaxies are spirals and 1/4 are ellipticals.

The distribution of masses of ellipticals is broad, extending from 10^5 to 10^{12} $\mathrm{M}_\odot$ including the mass of globular star clusters, where $\mathrm{M}_\odot \sim 2 \times 10^{30}$ kg is the mass of the sun. Spiral galaxies have a smaller spread in masses, with a typical mass of 10^{11} $\mathrm{M}_\odot$. Elliptical galaxies tend to be more massive than spiral galaxies.

The differential distribution of galaxy luminosities, L, is well described by the functional form (Schechter 1976)

$$\phi(L)\frac{\mathrm{d}L}{L_*} = \phi_0 \left(\frac{L}{L_*}\right)^{-\nu} \exp\left(-\frac{L}{L_*}\right)\frac{\mathrm{d}L}{L_*} \;, \tag{1.46}$$

with the parameters (*e.g.* Efstathiou *et al.* 1988; Marzke *et al.* 1994a; Marzke *et al.* 1994b)

$$\nu \approx 1.1, \quad L_* \approx 1.1 \times 10^{10} L_\odot, \quad \phi_0 \approx 1.5 \times 10^{-2} h^3 \mathrm{Mpc}^{-3} \;, \tag{1.47}$$

where $L_\odot \sim 4 \times 10^{26}$ W is the solar luminosity. Due to the sharp cutoff in $\phi(L)$ only few galaxies with luminosities beyond $\sim L_*$ are found.

1.4.2. Explaining galaxy bias

Simple models for galaxy biasing

A plausible simplification of this complicated physics justifying biased galaxies is the *natural bias* introduced by White *et al.* (1987). It relies on the idea that galaxies form inside dark matter halos. In regions of large-scale overdensities, halos form earlier by gravitational collapse than halos of the same mass in large-scale underdensities. Therefore, galaxies form first in overdense regions and are thus similarly clustered as the large-scale peaks of the dark matter density field. However, this can explain biasing only for some limited period of time, since sooner or later dark matter halos will have collapsed even in the large-scale low-density regions. A very simple version of this model is the *high-peak bias*. It assumes that galaxies can form only in dark matter density regions above a certain density threshold. This automatically relates the clustering of galaxies to the clustering of high-density regions the dark matter field (Coles 1993; Bardeen *et al.* 1986; Kaiser 1984). However, justifying this threshold on physical grounds is difficult (for discussion see Peacock 2001, page 578).

Numerical models for the galaxy bias

A more sophisticated approach is to include baryonic matter in N-body simulations along with the dark matter; galaxies are "formed" in these simulations according to phenomenological local conditions that have to be fulfilled by the baryonic matter in order to condense into stars (Weinberg *et al.* 2004; Yoshikawa *et al.* 2001; Pearce *et al.* 2001; Cen & Ostriker 2000; Blanton *et al.* 2000; Katz, Hernquist & Weinberg 1999). However, gas cooling, shocks and feedback with galaxies (metal enrichment, winds) are difficult issues in these simulations and not easily accounted for. Furthermore, the spatial resolution of the simulations is yet not good enough to properly resolve single galaxies nor to model interactions between galaxies.

Another numerical model approach for predicting galaxy clustering is also based on N-body codes. However, no baryonic matter is included. Galaxy mock catalogues are generated by identifying virialised dark matter halos in the simulations and by populating them with galaxies according to a prescription taken directly from semi-analytic models of galaxy formation (Somerville *et al.* 2001; Benson *et al.* 2001; Benson *et al.* 2000b; Kauffmann *et al.* 1999a,b).[5] See Fig. 1.9 for an example. The parameters for populating the halos with galaxies depend solely on the halo mass. If the mass of the halo is too large, then, according to the model, due to shock heating the primordial baryonic matter will be too hot to collapse into stars. On the other hand, in halos that are too small gas gets easily reheated by feedback processes which prohibits further galaxy formation. Between these two extremes halos of mass $\sim 10^{12}\,M_\odot$ are most efficient in producing galaxies (Benson *et al.* 2000). Another variant of the numerical approach is to run high-resolution N-body simulations with dark matter particles only and to identify small sub-halos with galaxies (Colin *et al.* 1999; Kravtsov & Klypin 1999).

All computational models are quite successful in reproducing many aspects of the observed galaxy population and relating them to fundamental physical quantities. In particular, they predict a galaxy biasing that evolves with time and depends on the type of galaxies. But the models have many parameters, not all of them have been measured in observations. A lot more observational input is needed to constrain and test the model assumptions. Such input are parameters –bias parameters– quantifying the difference in dark matter and galaxy clustering as a function of scale, galaxy type and redshift, or clustering differences between galaxies populations.

---

[5] The *halo model* is an analytical prescription that was motivated by this type of simulations (Cooray & Sheth 2002 and references therein).

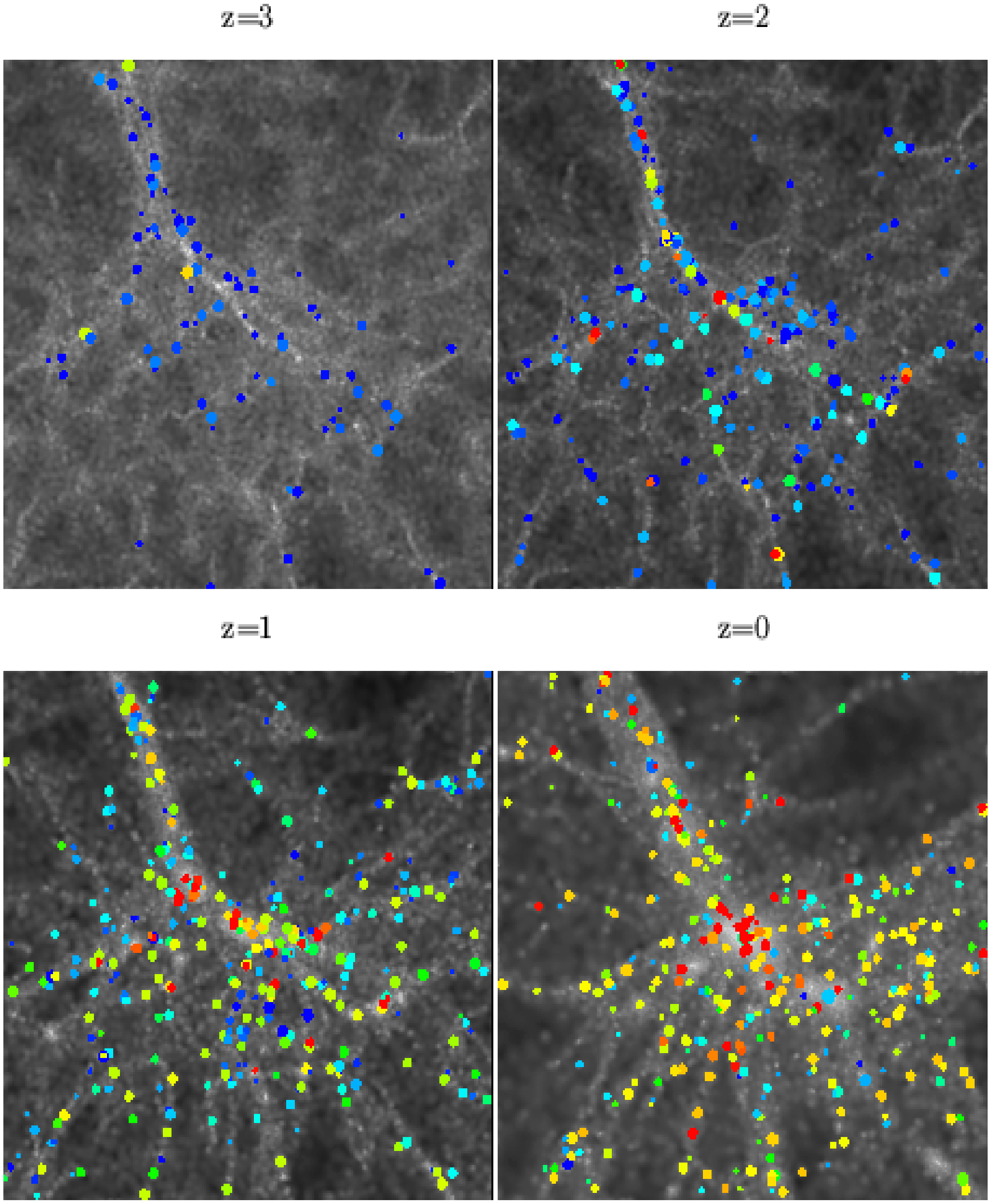

Figure 1.9.: *Simulated position of galaxies (differently coloured dots) that have formed in the dark matter density field (blurry grey colours) according to a semi-analytical recipe for galaxy formation (Kauffmann* et al. *1999a,b). The galaxies tend to form at the highest density regions of the dark matter. Each panel corresponds to a simulated volume of* 42 × 42 × 16 Mpc^3. *This picture was created by A. Diaferio and J. Colberg.*

1.4.3. Quantifying galaxy bias

To measure galaxy bias we have to know how to quantify it properly. It is worthwhile to have look at the scientific development in the field of biasing. The first bias description was introduced by Kaiser (1984, 1987) as a single parameter that rescales the two-point correlation function (2PCF) of the galaxy density field to yield the expected 2PCF for dark matter clustering. In the case of galaxy clustering, the 2PCF is a measure for the probability to find a galaxy within a certain distance of another galaxy. One way to justify such a rescaling is if the fluctuation field, or density contrast $\delta_{\rm m} \equiv \rho_{\rm m}/\bar{\rho}_{\rm m} - 1$, of the matter density field is a linear function of the galaxy density contrast, $\delta_{\rm g} \equiv n_{\rm g}/\bar{n}_{\rm g} - 1$, thus

$$\delta_{\rm b} = b\delta_{\rm m} \ . \tag{1.48}$$

The parameter b is called *deterministic linear bias* or sometimes simply "the bias factor". The densities $\rho_{\rm m}$ and $n_{\rm g}$ are the matter and galaxy number density fields, respectively. The bar denotes the mean density.

Along this line of arguing, motivated by the idea that the galaxy number density may be described as a simple local function of the dark matter density field, other more general descriptions were sought. Fry & Gaztańaga (1993) proposed the field of $\delta_{\rm g}$ to be an arbitrary, not just linear, analytic local function of $\delta_{\rm m}$ (local *Eulerian biasing*) opening the door to, in principle, arbitrarily many bias parameters which can be measured only if higher-order statistics are invoked. Moreover, these parameters can be different if different smoothing scales of the density fields are considered (*scale-dependence of bias*). An alternative picture to the Eulerian bias model is to assume that the galaxy distribution or a part of it (like recently formed galaxies), is only a local function of the dark matter field at one particular time (*Lagrangian bias*: *e.g.* Catelan *et al.* 2000).

In order to look at general features of the statistics of transformed random fields, Coles (1993) derived constraints for the clustering of galaxies that follow from a local mapping of a Gaussian random field. It was found that on large scales, where clustering is small, the shape of the 2PCF of the matter and the galaxies is then identical, so that here a simple linear bias scheme may still be used here (see also Narayanan, Berlind & Weinberg 2000 and Mann, Peacock & Heavens 1998). This is even true for non-Gaussian fields $\delta_{\rm m}$ (Coles, Melott & Munshi 1999) provided the n-point correlations of $\delta_{\rm m}$ behave like products of 2PCFs (clustering hierarchy). The most general attempt to study the correlations of a number density field of galaxies obtained as a local or non-local mapping of a dark matter density field has been undertaken by Matsubara (1995).

Another degree of freedom had to be inserted into the biasing schemes once it was realised that a deterministic mapping between the matter and galaxy distribution does not suffice: The relation between the matter and the galaxy density field is very likely a stochastic one (Weinberg *et al.* 2004; Somerville *et al.* 2001; Blanton 2000; Benson et al. 2000; Tegmark & Bromley 1999; Dekel & Lahav 1999; Matsubara 1999; Scherrer & Weinberg 1998; Cen & Ostriker 1992) due to "hidden parameters" of galaxy formation/evolution that cannot be incorporated into a simple picture that involves only the densities.

One therefore employs a statistical approach to relate $\delta_{\rm m}$ and $\delta_{\rm g}$.[6] The pair of values of the density contrasts $\delta_{\rm m}$ and $\delta_{\rm g}$ found at one point in space is thought to be a realisation

---

[6] In the following various definitions of bias parameters, we will discuss $\delta_{\rm m}$ and $\delta_{\rm g}$ as being the density contrast of the dark matter and galaxies. But, naturally, these definitions do not depend on these

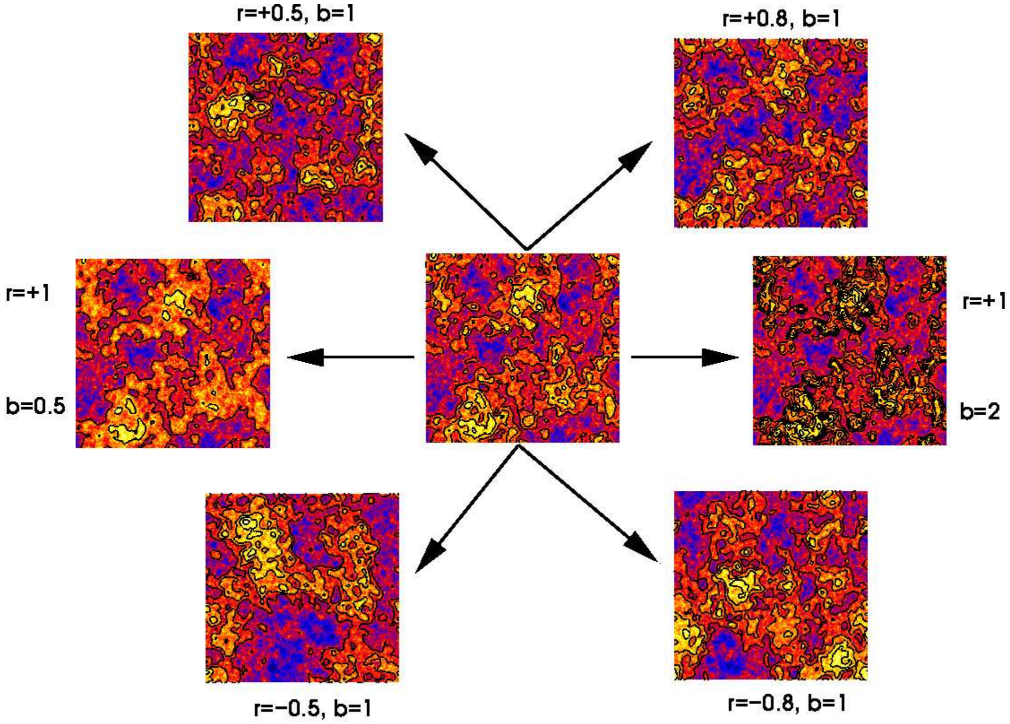

Figure 1.10.: *Example illustrating the linear stochastic bias (scale-independent). The (Gaussian) random field in the centre is statistically related to the other (Gaussian) random fields according to six different combinations of bias factors, b, and correlation coefficients, r, Eqs. (1.54). The fields could be models for the large-scale density contrast of galaxies or dark matter. The contours encircle regions with positive values for the density contrast (overdensity regions). The contour levels are the same for all fields.*

of an underlying probability distribution function $P(\delta_{\rm m},\delta_{\rm g})$ (PDF); the density contrasts are statistically homogeneous and isotropic random fields (Sect. 1.2). Studying the stochastic biasing between $\delta_{\rm g}$ and $\delta_{\rm m}$ thus means quantifying their joint PDF. The density contrasts are *smoothed to a certain scale* before looking at the PDF; by varying the smoothing scale we can scan through the different scales.

Linear stochastic bias

Characterising the stochastic biasing, using two-point statistics only, boils down to two bias parameters, which define a *linear stochastic bias*:

$$b(R)=\sqrt{\frac{\langle\delta_{\rm g}^2\rangle}{\langle\delta_{\rm m}^2\rangle}}\;\;;\;\;r(R)=\frac{\langle\delta_{\rm m}\delta_{\rm g}\rangle}{\sqrt{\langle\delta_{\rm m}^2\rangle\,\langle\delta_{\rm g}^2\rangle}}\,. \tag{1.49}$$

These parameters differ from unity in the case of two biased fields. They depend in general on scale, since the joint PDF is a function of the smoothing applied to the density contrasts of

specific fields; they may be the density contrasts of any random field, such as of two different galaxy populations as in Chapter 5 for the relative galaxy bias.

the fields. This is expressed by the variable R which denotes the typical smoothing scale. The values for the biasing parameters obviously depend on the details of the applied smoothing window. Often in the literature, as in the Kaiser (1984) for b, we find b and r in terms of the 2PCFs $\xi_{\rm m}(R) = \langle\delta_{\rm m}(x+R)\delta_{\rm m}(x)\rangle$, $\xi_{\rm gm}(R) = \langle\delta_{\rm g}(x+R)\delta_{\rm m}(x)\rangle$ and $\xi_{\rm m}(R) = \langle\delta_{\rm g}(x+R)\delta_{\rm g}(x)\rangle$,

$$b(R) = \sqrt{\frac{\xi_{\rm g}(R)}{\xi_{\rm m}(R)}} \quad ; \quad r(R) = \frac{\xi_{\rm gm}(R)}{\sqrt{\xi_{\rm g}(R)\,\xi_{\rm m}(R)}}\;, \tag{1.50}$$

instead of the smoothed, second-order moments $\langle\delta_{\rm m}^2\rangle$, $\langle\delta_{\rm m}\delta_{\rm g}\rangle$ and $\langle\delta_{\rm g}^2\rangle$, respectively. Although this alternative definition of linear bias is equivalent to the foregoing definition –one can be transformed into the other– it gives in general different values for the same scale R (Dekel & Lahav 1999). Moreover, an important difference is that $r(R)$ as defined in (1.50) can assume values larger than 1, whereas $r(R)$ as in (1.49), which is based on rms-fluctuations in the density fields, must always lie in the range $[-1,1]$.

Another equivalent definition of linear stochastic bias is to express the bias parameters in terms of power spectra:

$$\left\langle\tilde\delta_{\rm m}(\vec k)\tilde\delta^*_{\rm m}(\vec k')\right\rangle = (2\pi)^3\delta_{\rm D}(\vec k-\vec k')P_{\rm m}(|\vec k|), \tag{1.51}$$

$$\left\langle\tilde\delta_{\rm m}(\vec k)\tilde\delta^*_{\rm g}(\vec k')\right\rangle = (2\pi)^3\delta_{\rm D}(\vec k-\vec k')P_{\rm gm}(|\vec k|), \tag{1.52}$$

$$\left\langle\tilde\delta_{\rm g}(\vec k)\tilde\delta^*_{\rm g}(\vec k')\right\rangle = (2\pi)^3\delta_{\rm D}(\vec k-\vec k')P_{\rm g}(|\vec k|)\;. \tag{1.53}$$

The quantities $\tilde\delta_{\rm m}(\vec k)$ and $\tilde\delta_{\rm g}(\vec k)$ are the Fourier mode representation of the density contrasts $\delta_{\rm m}$ and $\delta_{\rm g}$, respectively, at the spatial frequency $\vec k$. The expression $\delta_{\rm D}$ is the Dirac delta function, c^* is the complex conjugate of c. $P_{\rm m}$, $P_{\rm g}$ and $P_{\rm gm}$ are the power spectra of the fluctuations in the dark matter density, galaxy number density and their cross-power, respectively. The linear stochastic bias in Fourier space is defined as follows

$$b\,(k) \equiv \sqrt{\frac{P_{\rm g}\,(k)}{P_{\rm m}\,(k)}} \quad ; \quad r\,(k) \equiv \frac{P_{\rm gm}\,(k)}{\sqrt{P_{\rm m}\,(k)\,P_{\rm g}\,(k)}}\;. \tag{1.54}$$

If both $\delta_{\rm m}$ and $\delta_{\rm g}$ are Gaussian random fields, then $P(\delta_{\rm m},\delta_{\rm g})$ is a bivariate Gaussian and is hence completely determined by its second-order moments. This is approximately the case for large smoothing scales where the fluctuations are small, thus for $\langle\delta^2_{\rm g,m}\rangle \ll 1$. Therefore, the linear stochastic bias is a good candidate for describing biasing on large scales. Examples for scale-independent linear stochastic bias between Gaussian random fields is given in Fig. 1.10.

Non-linear stochastic bias

The linear stochastic bias picture is incomplete if the relation between $\delta_{\rm m}$ and $\delta_{\rm g}$ differs from a bivariate Gaussian. Due to the constraint $\delta_{\rm g,m} \geq -1$ this is necessarily the case where $|\delta_{\rm g,m}| \ll 1$ no longer holds. In particular, bias and correlation factor mix non-linear and stochastic effects: The correlation factor is no longer a unique measure for stochasticity because it can become $|r| \neq 1$ even in a completely deterministic case, $\delta_{\rm g} = f(\delta_{\rm m})$, since in general

$$r = \frac{\langle\delta_{\rm m} f(\delta_{\rm m})\rangle}{\sqrt{\langle\delta^2_{\rm m}\rangle\,\langle[f(\delta_{\rm m})]^2\rangle}} \neq 1\;. \tag{1.55}$$

As example, take the purely non-linear mapping $\delta_{\rm g} = f(\delta_{\rm m}) = \delta_{\rm m}^3$ and a normal Gaussian PDF $P[\delta_{\rm m}]$. In this (made up) case we have $r \approx 0.77$ although the relation between $\delta_{\rm m}$ and $\delta_{\rm g}$ is strictly deterministic! In addition, we have $b = \sqrt{\langle [f(\delta_{\rm m})]^2 \rangle \,/\, \langle \delta_{\rm m}^2 \rangle} \approx 3.87$ which means that the "linear" bias factor is also sensitive to non-linear terms.

In order to clearly separate stochasticity from a non-linear but deterministic biasing relation, Dekel & Lahav (1999) introduced the *non-linear stochastic bias*. In this scheme, one defines a typical value for $\delta_{\rm g}$ that is found at positions in the field where the dark matter density contrast has a particular value $\delta_{\rm m}$. The characteristic value is defined to be the conditional mean

$$\langle \delta_{\rm g} | \delta_{\rm m} \rangle \equiv \int {\rm d}\delta_{\rm g}\, \delta_{\rm g}\, P(\delta_{\rm g} | \delta_{\rm m}) \;, \tag{1.56}$$

where $P(\delta_{\rm g}|\delta_{\rm m})$ denotes the conditional PDF, thus the probability to obtain a particular value $\delta_{\rm g}$ for a given $\delta_{\rm m}$. In the case of deterministic biasing, we will find always the same value $\delta_{\rm g}$ for a given value $\delta_{\rm m}$, namely exactly $\langle \delta_{\rm g}|\delta_{\rm m}\rangle$. For stochastic biasing, this relationship only exists on average with a residual scatter of

$$\epsilon^2(\delta_{\rm m}) = \left\langle (\delta_{\rm g}|\delta_{\rm m} - \langle \delta_{\rm g}|\delta_{\rm m}\rangle)^2 \right\rangle = \int {\rm d}\delta_{\rm g}\, (\delta_{\rm g} - \langle \delta_{\rm g}|\delta_{\rm m}\rangle)^2\, P(\delta_{\rm g}|\delta_{\rm m}) \;. \tag{1.57}$$

Using these quantities, one can define bias parameters that distinguish between stochasticity and non-linearity: non-linearity is given if the conditional mean is a non-linear function, $\langle \delta_{\rm g}|\delta_{\rm m}\rangle \neq b\,\delta_{\rm m}$ with b constant, or if equivalently

$$b(\delta_{\rm m}) \equiv \frac{\langle \delta_{\rm g}|\delta_{\rm m}\rangle}{\delta_{\rm m}} \tag{1.58}$$

is not a constant. $b(\delta_{\rm m})$ has been coined the biasing function. It is the local slope in the relation between $\langle \delta_{\rm g}|\delta_{\rm m}\rangle$ and $\delta_{\rm m}$. Thus, the biasing function generalises the local mapping function considered in the deterministic biasing schemes. Stochasticity is given if the scatter $\epsilon^2(\delta_{\rm m})$ about the biasing function is non-vanishing. The non-linear stochastic bias expresses this concept in terms of three numbers $\hat{b}$, $\tilde{b}$ and σ_b:[7]

$$\hat{b} \equiv \frac{\langle b(\delta_{\rm m})\delta_{\rm m}^2\rangle}{\langle \delta_{\rm m}^2\rangle} \quad ; \quad \tilde{b}^2 \equiv \frac{\langle b^2(\delta_{\rm m})\delta_{\rm m}^2\rangle}{\langle \delta_{\rm m}^2\rangle} \quad ; \quad \sigma_b^2 \equiv \frac{\langle \epsilon^2(\delta_{\rm m})\rangle}{\langle \delta_{\rm m}^2\rangle} \;. \tag{1.59}$$

These numbers globally average the non-linearity and stochasticity over all possible values $\delta_{\rm m}$. As before, the bias parameters are in general a function of the typical scale of the smoothing kernel applied to $\delta_{\rm m}$ and $\delta_{\rm g}$. The operator "$\langle \ldots \rangle$" should here be understood as ensemble average over the one-dimensional PDF of $\delta_{\rm m}$, $P(\delta_{\rm m})$. For stochastic biasing, we have $\sigma_b^2 \neq 0$. A non-linear biasing relation is given if the ratio $\tilde{b}/\hat{b}$ differs from unity.

The linear stochastic bias parameters of the foregoing section are functions of the three non-linear bias parameters:

$$b = \hat{b} \left(\frac{\tilde{b}^2}{\hat{b}^2} + \frac{\sigma_b^2}{\hat{b}^2} \right)^{1/2} \quad ; \quad r = \left(\frac{\tilde{b}^2}{\hat{b}^2} + \frac{\sigma_b^2}{\hat{b}^2} \right)^{-1/2} \;. \tag{1.60}$$

---

[7] The parameter $\hat{b}$ is the slope of the regression line $\hat{b}\delta_{\rm m}$, least-square fitted to $\langle \delta_{\rm g}|\delta_{\rm m}\rangle$; this can be seen by the Eq. (A.14). The parameter $\tilde{b}$, used to quantify the non-linearity, is obtained by fitting a straight line $\tilde{b}^2\delta_{\rm m}$ to $\langle \delta_{\rm g}|\delta_{\rm m}\rangle^2/\delta_{\rm m}$ which only for a strict linear relation between $\langle \delta_{\rm g}|\delta_{\rm m}\rangle$ and $\delta_{\rm m}$ results in $\hat{b}^2$.

This again shows that the correlation coefficient r, Eqs. (1.49), mixes non-linear and stochastic effects. But also the linear bias coefficient b, picking up differences in the rms-fluctuations, of the fields obviously is affected by non-linearity and stochasticity and does therefore not measure the statistical average $\bar{b}$ in "$\delta_{\rm g} = \bar{b}\delta_{\rm m}$"; in fact, it is always larger than or equal that value since $b = \hat{b}/r$.

For $\tilde{b} = \hat{b}$, the formalism of Dekel & Lahav naturally reduces to the linear stochastic bias with $\hat{b} = b\,r$ and $\sigma_{\rm b} = b(1-r^2)^{1/2}$. For deterministic biasing, $\sigma_b = 0$, we find $\tilde{b} = b$ and as usual $\hat{b} = b\,r$. For linear and deterministic biasing, $\sigma_b = 0$ and $\tilde{b}/\hat{b} = 1$, we recover the linear deterministic bias factor $b = \hat{b}$. See Appendix A.4 for a general relation between the joint PDF $P(\delta_{\rm g}, \delta_{\rm m})$ and the non-linear stochastic bias.

1.4.4. Galaxy bias in observations and simulations

Observationally, the bias can be measured by redshift space-distortions (Sigad, Branchini & Dekel 2000; Pen 1998; Kaiser 1987), weak gravitational lensing (Sheldon *et al.* 2004; Seljak *et al.* 2004a; Pen *et al.* 2003; Hoekstra *et al.* 2002; Wilson *et al.* 2001; van Waerbeke 1998; Schneider 1998) and counts-in-cells statistics (Conway *et al.* 2004; Tegmark & Bromley 1999; Efstathiou *et al.* 1990). The count-in-cells statistics can only be applied to measure the bias between galaxy populations, though. Additionally, the large-scale flow of galaxies can be used to make a POTENT reconstruction of the total mass field on large scales which can be compared to the galaxy distribution (*e.g.* Sigad *et al.* 1998; Dekel *et al.* 1993).

The current status of the observational results is summarised in the following. Note that the given conclusions to some extend depend on the assumed cosmological model. We quote only the conclusions given by the listed authors for the concordance ΛCDM model.

In the local universe, $L_\star$ galaxies are almost unbiased tracers on linear scales of about $8h^{-1}$Mpc and larger (Seljak *et al.* 2004a; Verde *et al.* 2002; Lahav *et al.* 2002; Loveday *et al.* 1996). However, this is probably not true on smaller scales. A comparison of the theoretical dark matter clustering –which is constrained by the cosmic microwave background anisotropies, gravitational lensing and the Lyman-α forest (*cf.* Tegmark *et al.* 2004a)– and the observable galaxy clustering suggests that on smaller scales $r \sim 1h^{-1}$Mpc galaxies are less clustered than the dark matter ("anti-biased") becoming positively biased, $b > 1$, on even smaller scales below $r \sim 0.1h^{-1}$Mpc. This is because the observed galaxy spatial 2PCF is approximately a power law over a scale range of $0.02h^{-1}{\rm Mpc} \lesssim r \lesssim 20h^{-1}$Mpc (Zehavi et al. 2002) while the theoretical dark matter 2PCF clearly deviates from a power law due to the non-linear evolution of the clustering on small scales (see Fig. 1.11, left panel). If this is true, then we should expect a "dip" in the bias factor on intermediate scales.

In their work on the VIRMOS-DESCART (van Waerbeke *et al.* 2001b) survey and RCS (Gladders & Yee 2001), Hoekstra *et al.* (2001,2002) use weak gravitational lensing to measure the linear stochastic bias for galaxies with a median redshift of $\langle z\rangle = 0.35$ covering a range from $0.1h^{-1}$Mpc to $6.3h^{-1}$Mpc. They claim to have observed such a dip in the linear bias factor, Eq. (1.54), with a minimum of $b = 0.71$ as well as a dip in the correlation factor $r = 0.57$, both minima at about $0.7h^{-1}{\rm Mpc} \lesssim r \lesssim 1.4h^{-1}$Mpc. As mentioned earlier, a value of r less than unity is an indication for either a non-linear bias or a stochastic bias or both. Moreover, Hoekstra *et al.* conclude that their data is consistent with no biasing on scales of about $8h^{-1}$Mpc. However, due to the technique applied (see Sect. 3.2.3) the statistical uncertainties are largest on this scale; a linear bias factor between $0.7 \lesssim b \lesssim 1.3$ is still possible within 1σ

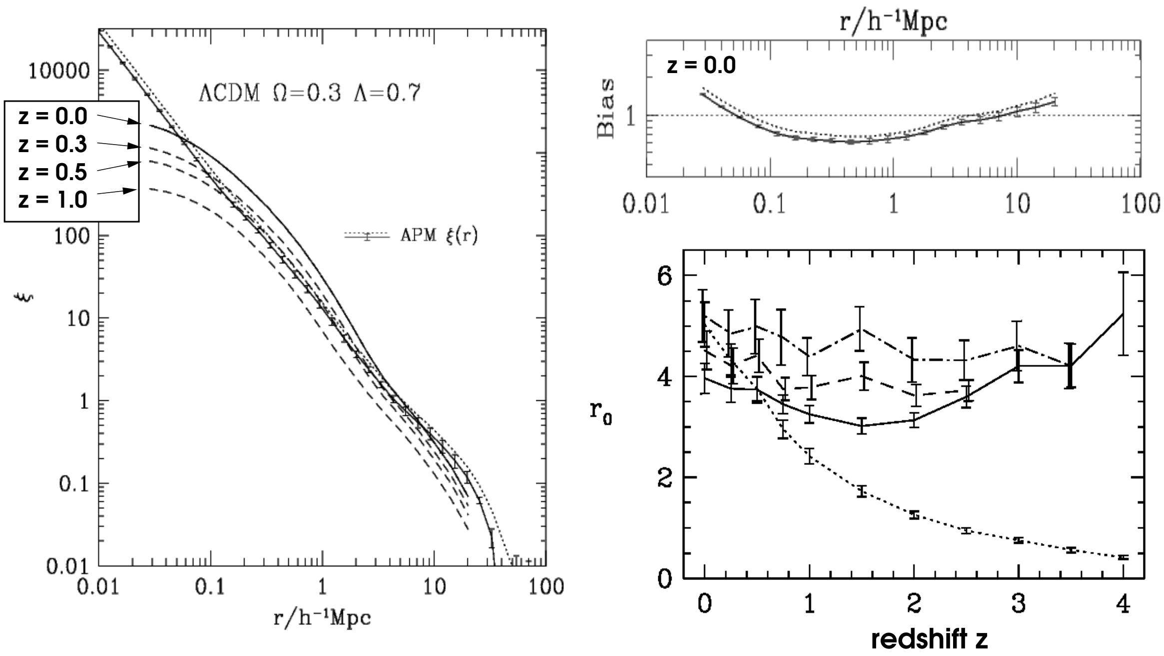

Figure 1.11.: ***Left and upper right panel**: Theoretical evolution of the dark matter correlation function, $\xi_{\rm m}(r) = \langle\delta_{\rm m}(x)\delta_{\rm m}(x+r)\rangle$, with redshift compared to the observed galaxy clustering, $\xi_{\rm g}(r)$, in the APM survey. The difference in shape of the galaxy and dark matter correlation function results in a scale-dependence of the bias factor $b(r) = [\xi_{\rm g}(r)/\xi_{\rm m}(r)]^{1/2}$ (upper right panel). Both figures are from Jenkins* et al. *(1998). **Bottom right panel**: Evolution of the galaxy clustering amplitude r_0 with redshift in comoving h^{-1}Mpc for a power law $\xi_{\rm g}(r) = (r/r_0)^\gamma$ fitted to the 2PCF of the simulated galaxy catalogue; γ does not change much with redshift (not shown). The solid line is for all galaxies, the dashed line for the* 500 *most massive galaxies and the dashed-dotted line for the* 200 *most massive galaxies. The dotted line is the dark matter clustering amplitude. The figure is from Weinberg* et al. *(2004).*

confidence. Also based on gravitational lensing there is evidence that the ratio b/r stays close at unity from submegaparsec scales up to $\sim 8h^{-1}$Mpc (Sheldon *et al.* 2004; Hoekstra *et al.* 2002; Guzik & Seljak 2001; Fisher *et al.* 2000), thus from non-linear to linear scales.

The analysis of the bispectrum of the galaxy clustering in the 2dFGRS (Colless *et al.* 2001) lead Verde *et al.* (2002) to the conclusion that on scales between $5h^{-1}$Mpc and $30h^{-1}$Mpc the biasing relation between dark matter and galaxies is linear (see also: Lahav *et al.* 2002). The same conclusion was drawn several years earlier by Gaztañaga & Frieman (1994) based on the APM survey (Maddox *et al.* 1990). However, recently the work of Kayo *et al.* (2004) has questioned a strict linear relation on scales $\lesssim 10h^{-1}$Mpc by studying the three-point correlation of galaxy clustering as a function of morphology, colour and luminosity, this time in SDSS (York *et al.* 2000).

A complex biasing relation is definitely found by subdividing the galaxy catalogues into various subsets. It has long been known that the clustering of galaxies depends on the properties of the galaxies, namely on *galaxy morphology* (*e.g.* Hubble 1936; Zwicky et al. 1968; Davis & Geller 1976; Dressler 1980; Postmann & Geller 1984; Lahav & Saslaw 1992; Santiago & Strauss 1992; Iovino *et al.* 1993; Hermit *et al.* 1996; Guzzo *et al.* 1997; Willmer *et* *al.* 1998; Zehavi *et al.* 2002; Goto *et al.* 2003), *colour* (e.g Le Févre *et al.* 1996; Tucker *et al.* 1997; Willmer *et al.* 1998; Brown *et al.* 2000; Norberg *et al.* 2001; McKay *et al.* 2001; Zehavi *et al.* 2002; Wild *et al.* 2004; Sheldon *et al.* 2004), *spectral type* (*e.g.* Loveday *et al.* 1999; Shepherd *et al.* 2001; Norberg et al. 2002; Budavari *et al.* 2003; Madgwick *et al.* 2003), *selection passband* (*e.g.* Lahav *et al.* 1990; Peacock 1997; Baker *et al.* 1998; Hoyle *et al.* 1999) and *luminosity* (Davis *et al.* 1988; Hamilton 1988; White *et al.* 1988; Park *et al.* 1994; Loveday *et al.* 1995; Benoist *et al.* 1996; Guzzo *et al.* 1997; Small *et al.* 1999; Norberg *et al.* 2001; Zehavi *et al.* 2002; Firth et al. 2002; Kayo *et al.* 2004;). The more luminous galaxies are, the stronger is their spatial clustering (Norberg *et al.* 2001):

$$\frac{b(L)}{b(L_*)} = 0.85 + 0.15\frac{L}{L_*} \ , \tag{1.61}$$

where b is the linear bias factor for low-redshift galaxies on intermediate non-linear scales and L the luminosity of the galaxies. A similar result has been found by Tegmark *et al.* (2004b), while the work of Benoist *et al.* (1996) on the Southern Sky Redshift Survey 2 (da Costa *et al.* 1988) concluded a somewhat steeper slope in this empirical relation. Note that there has been a long debate on this issue because no dependence on luminosity was found by some authors (*e.g.* Hawkins *et al.* 2001; Szapudi *et al.* 2000; Loveday *et al.* 1995; Hasegawa & Umemura 1993; Philips & Shanks 1987) based on older surveys with relatively small galaxy numbers and limited volumes. Nowadays with the upcome of large galaxy surveys such as SDSS and 2dFGRS this dispute seems to be settled.

Late-type, blue, spiral or star forming galaxies are less clustered than early-type, elliptical or red galaxies (*e.g.* Wild *et al.* 2004; Connay *et al.* 2004; Zehavi *et al.* 2002; Norberg *et al.* 2002). On large scales, the biasing between red and blue galaxies does not seem to be well described by a linear bias model which, according to Wild *et al.* (2004, see also Conway *et al.* 2004), is ruled out with high significance using counts-in-cells statistics in redshift space. Their statement is that a bivariate lognormal model for the joint PDF $P(\delta_{\rm red}, \delta_{\rm blue})$ describes best the measured non-linear stochastic biasing between red, $\delta_{\rm red}$, and blue, $\delta_{\rm blue}$, galaxies (scales $7h^{-1}{\rm Mpc} \leq L \leq 31h^{-1}{\rm Mpc}$). In the same work, Wild *et al.* observe a scale-dependent non-linear bias between red and blue galaxies with stochasticity $\sigma_{\rm b}/\hat{b} = 0.44 \pm 0.02, 0.27 \pm 0.05$ and non-linearity $\tilde{b}/\hat{b} = 1.054, 1.003$ (no errors given in paper) for typical physical scales of $7h^{-1}$Mpc and $31h^{-1}$Mpc, respectively. Observational evidence that the relation between red and blue galaxies is non-deterministic was already given some years ago by the work of Tegmark & Bromley (1999), which was based on the Las Campas Redshift Survey (Shectman *et al.* 1996), and by Blanton (2000).

Observations also suggest that on large scales the bias factor b increases with redshift up to a value of about $b \sim 4$ at $z \sim 3$ (Hildebrandt *et al.* 2005; Magliocchetti *et al.* 2000; Adelberger et al. 1998; Steidel *et al.* 1998; Wechsler *et al.* 1998; Matarrese et al. 1997). Thus, at redshifts of $z \sim 3$ galaxies are more clustered than the dark matter by a factor of about $b^2 \sim 16$. Intriguingly, the galaxy clustering –expressed by the spatial galaxy 2PCF as function of comoving separation– evolves only little. See Fig. 1.11, bottom right panel, for a simulated evolution of the galaxy clustering that is supported by observations (see references in Weinberg *et al.* 2004). Even at high redshifts $z \sim 3$ the Lyman-break galaxies are as much clustered as the galaxies today. It is the clustering of the dark matter that grows with time reducing the bias factor of the galaxies (Fig. 1.12). However, interpretations of biasing in the high-redshift universe are difficult since the surveys get increasingly affected by selection effects.

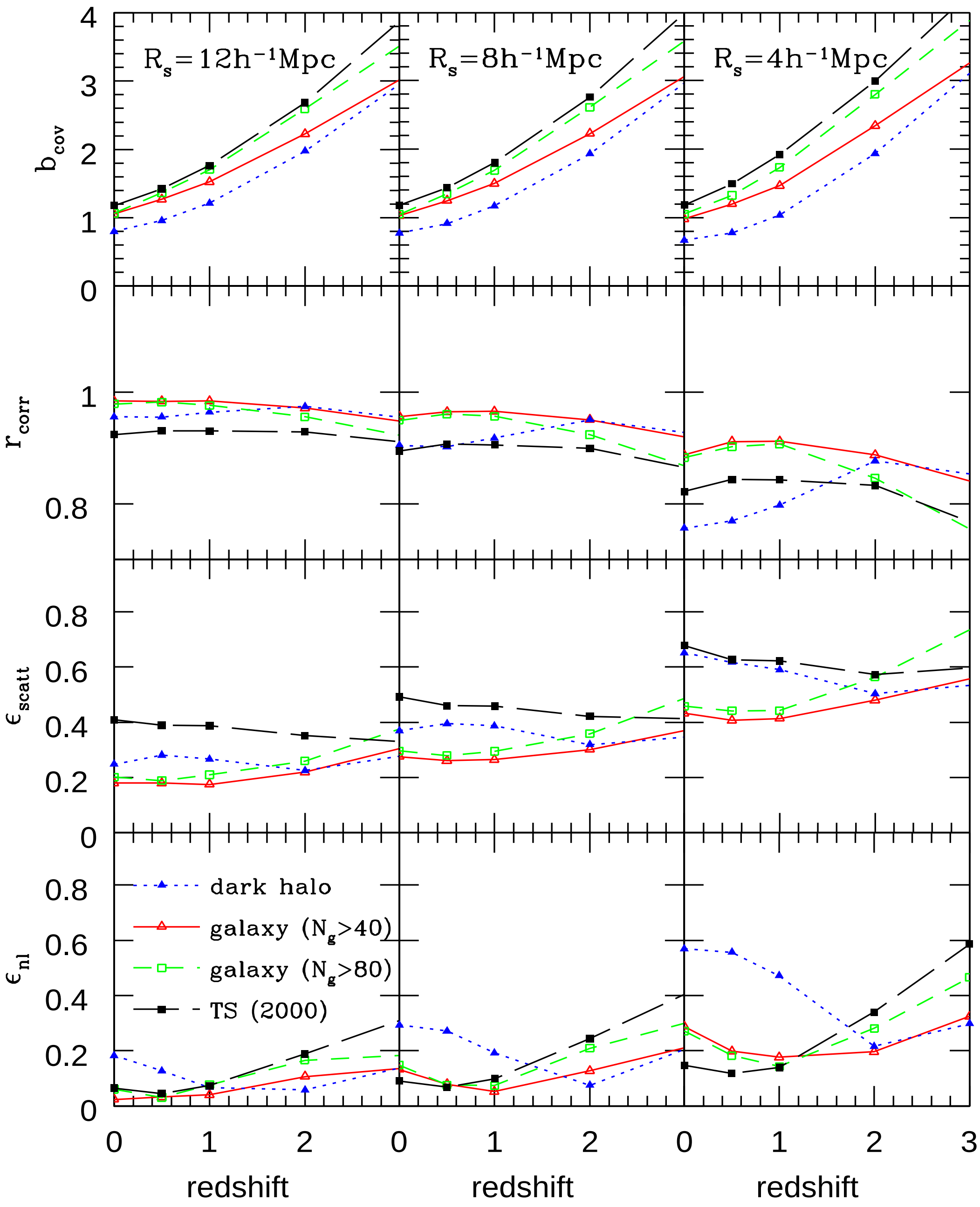

Figure 1.12.: *Evolution of the non-linear stochastic bias, Eqs. (1.59), of galaxies (solid lines) and dark halos (dotted lines) for three different smoothing scales (columns) as predicted by the simulations of Yoshikawa* et al. *(2001).* b_{cov} *is the non-linear bias factor* $\hat{b}$ *and* $r_{\mathrm{corr}} = (1+\epsilon^2_{\mathrm{scatt}}+\epsilon^2_{\mathrm{nl}})^{-1/2}$ *the linear correlation factor (Eqs. 1.54); Yoshikawa et al. use the definitions* $\epsilon^2_{\mathrm{scatt}} = \sigma^2_b/\hat{b}^2$ *and* $\epsilon^2_{\mathrm{nl}} = \tilde{b}^2/\hat{b}^2 - 1$ *for the stochasticity and non-linearity parameter, respectively.* N_{g} *is a simulation parameter having an influence on the gas mass threshold for galaxies to form; they are not of importance in here. The bias factor displays a clear evolution with redshift but only with a weak dependence on scale. On large scales, stochasticity,* $\epsilon_{\mathrm{scatt}}$*, and non-linearity,* ϵ_{nl}*, are small, stochasticity effects are always larger than non-linearity.*

For instance, due to the limiting magnitude of a survey, one is systematically only looking at galaxies brighter than the magnitude limit. Therefore, the median rest-frame luminosity of the detected galaxies increases at higher redshifts. As biasing is a function of the galaxy luminosity, this affects the observed galaxy bias by overestimating its value (Magliocchetti *et al.* 2000).

In conclusion, biasing of galaxies is a function of scale, redshift and galaxy type (age, luminosity, colour and metallicity). At the end of the day, the measurements of observables like the linear or non-linear stochastic bias have to be interpreted in terms of physical quantities and/or to be compared with numerical models for galaxy formation and evolution (*cf.* Weinberg *et al.* 2004; Somerville *et al.* 2001; Yoshikawa *et al.* 2001, Blanton *et al.* 2000, see Fig. 1.12) in order to gain insight in the physics of galaxies. The most promising quantity in that respect seems to be the halo occupation distribution of galaxies (Blanton *et al.* 2004; Seljak *et al.* 2004a; Berlind *et al.* 2003; Berlind & Weinberg 2002).

1.5. Gravitational lensing

As outlined in the foregoing sections, we cannot rely on galaxies being perfect tracers of the total matter distribution. Moreover, the dark matter which accounts for most of the matter is *really* dark: it neither emits nor absorbs light. So, how can we then study the matter distribution?

1.5.1. Light propagation in the universe

The propagation of light through the universe is affected by inhomogeneities in the matter field: light rays are pulled towards matter overdensities and pushed away from underdensity regions. The cumulative result of all light-ray deflections is that the images of distant galaxies become distorted as through an optical lens; large-scale matter inhomogeneities are imprinted in the images of galaxies. Therefore, one can investigate the matter distribution indirectly by analysing the shapes of galaxy images. In order to quantify the lensing effect on the images of galaxies, which are essentially bundles of very close light rays, we consider in the following the propagation of close single light rays.

Consider two photons emitted at the observer's position, one into direction $\vec{\theta}_0 \equiv \vec{0}$ and the other one into a slightly ($|\vec{\theta}| \ll 1$) different direction $\vec{\theta}_0 + \vec{\theta}$. The vector $\vec{\theta}$ is a two-dimensional vector in the plane perpendicular to $\vec{\theta}_0$. The photon initially travelling into direction $\vec{\theta}_0$ is a fiducial photon defining the reference direction for a bundle of light rays travelling into approximately the same direction. In a perfectly homogeneous universe (Sect. 1.1.1), after travelling a comoving distance w the two photons have a comoving separation of $\vec{x}(\vec{\theta}, w) = f_{\rm K}(w)\,\vec{\theta}$ where $f_{\rm K}(w)$ is the angular diameter distance (Eq. 1.3); for a flat universe we recover the well-known Euclidean case $f_{\rm K}(w) = w$. The relation for the comoving separation of the photons can also be expressed as a solution of the following differential equation that propagates $\vec{x}$ to a certain comoving distance w:

$$\frac{{\rm d}^2\vec{x}}{{\rm d}w^2} + K\vec{x} = 0\;, \tag{1.62}$$

where K is the curvature of the universe; for the initial condition at $w = 0$, we have $\vec{x} = \vec{0}$ and $\frac{{\rm d}\vec{x}}{{\rm d}w} = \vec{\theta}$.

In a slightly perturbed universe[8], equation (1.62) can no longer be true because the inhomogeneities deflect the photons. It can be shown (cf. van Waerbeke & Mellier 2003) that for slight perturbations in the gravitational field, $\delta\phi$, Eq. (1.62) becomes modified to

$$\frac{\mathrm{d}^2\vec{x}}{\mathrm{d}w^2} + K\vec{x} = -\frac{2}{c^2}\left[\nabla_\perp\delta\phi^{(1)}(w) - \nabla_\perp\delta\phi^{(0)}(w)\right] , \tag{1.64}$$

where $\nabla_\perp^{(i)}\delta\phi$ denotes the 2D gradient of the potential perturbations perpendicular to either path of the photons, $\nabla_\perp\delta\phi^{(1)}$ for photon "1" and $\nabla_\perp\delta\phi^{(0)}$ for the fiducial photon "0". The solution to Eq. (1.64) is the integral (cf. Schneider *et al.* 1998)

$$\vec{x}(\vec{\theta},w) = f_\mathrm{K}(w)\vec{\theta} - \frac{2}{c^2}\int_0^w \mathrm{d}w' f_\mathrm{K}(w-w')[\nabla_\perp\delta\phi(\vec{x}(\vec{\theta},w'),w') - \nabla_\perp\delta\phi^{(0)}(w')] , \tag{1.65}$$

where $\delta\phi(\vec{x}(\vec{\theta},w'),w')$ is the perturbation potential at comoving distance w' and comoving separation $\vec{x}(\vec{\theta},w')$ perpendicular to the fiducial line-of-sight.

Eq. (1.65) states that a light source with "true" position at $\vec{\beta}$ on the sky is in general observed at a different position $\vec{\theta}$ if the perturbations, $\delta\phi$, are "switched on". This is because light deflections due to $\delta\phi$ lead to a different physical separation, $\vec{x}(\vec{\theta},w) \neq f_\mathrm{K}(w)\vec{\beta}$, at comoving distance w. In this sense, $\delta\phi$ defines a mapping between the unperturbed, $\vec{\beta}$, and perturbed, $\vec{\theta}$, coordinate frame:

$$\vec{\beta} = \frac{\vec{x}(\vec{\theta},w)}{f_\mathrm{K}(w)} . \tag{1.66}$$

This equation is called the *lens equation.* For $\delta\phi = 0$, we obtain trivially $\vec{\beta} = \vec{\theta}$ since in that case we have $\vec{x}(\vec{\theta},w) = f_\mathrm{K}(w)\vec{\theta}$. In general, the solution for $\vec{\theta}$ does not have to be unique. Photons from the same source, $\vec{\beta}$, could arrive from different directions giving rise to multiple images. This, however, is never the case in the regime relevant for this thesis where the light deflections are assumingly small.

We will only be interested in local properties of the mapping. Locally about the direction $\vec{\theta}$ this mapping is described by the Jacobian matrix

$$A_{ij}(\vec{\theta},w) \equiv \frac{\partial\beta_i}{\partial\theta_j} . \tag{1.67}$$

By means of Eq. (1.65) one obtains[9]

$$A_{ij}(\vec{\theta},w) = \delta_{ij} - \frac{2}{c^2}\int_0^w \mathrm{d}w'\,\frac{f_\mathrm{K}(w-w')f_\mathrm{K}(w')}{f_\mathrm{K}(w)}\sum_{k=1}^{2}\delta\phi_{,ik}(\vec{x}(\vec{\theta},w'),w')A_{kj}(\vec{\theta},w') , \tag{1.68}$$

---

[8] By a "slightly perturbed" universe we mean specifically a universe with metric

$$\mathrm{d}s^2 = c^2\left(1+\frac{2\delta\phi}{c^2}\right)\mathrm{d}t^2 - a^2(t)\left(1-\frac{2\delta\phi}{c^2}\right)\left[\mathrm{d}w^2 + f_\mathrm{K}^2(w)(\mathrm{d}\theta^2 + \sin^2\theta\,\mathrm{d}\phi^2)\right] , \tag{1.63}$$

and $\delta\phi/c^2 \ll 1$. For $\delta\phi \rightarrow 0$ the metric approaches asymptotically the Robertson-Walker metric (1.2).

[9] Note that the term $f_\mathrm{K}(w')A_{kj}(\vec{\theta},w') = \frac{\partial x_k(\vec{\theta},w')}{\partial\theta_j}$ (from Eqs. 1.66 and 1.67) on the RHS of this equation appears according to the chain rule that is applied to $\frac{\partial\nabla_\perp\delta\phi(\vec{x}(\vec{\theta},w'),w')}{\partial\theta_j}$.

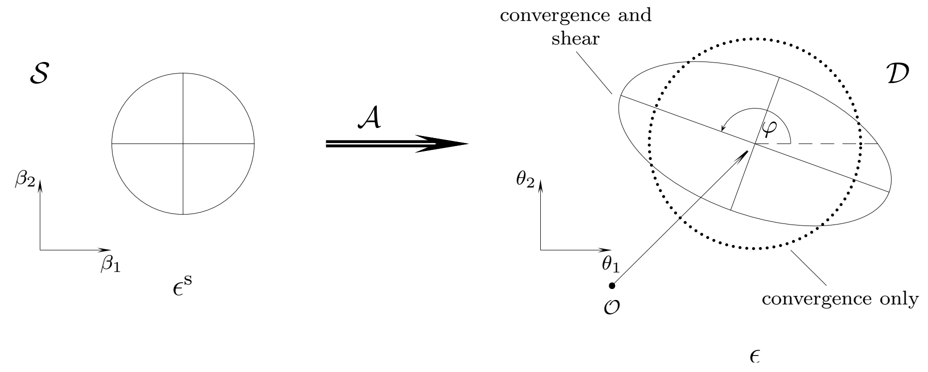

Figure 1.13.: *Transformation of a circular source (left) under the influence of a linear transformation* **A**. *The convergence of* **A** *changes the size of the image, while the shear stretches the image along a particular direction* ϕ *(from Bradač 2004).*

where $\delta\phi_{,ik}$ is the Hessian matrix of $\delta\phi$ using spatial partial derivatives perpendicular to the fiducial light ray. This equation is not easily solved, since in order to work out $A_{ij}(\vec{\theta},w)$ we need to know $A_{ij}(\vec{\theta},w')$ and $\vec{x}(\vec{\theta},w)$ for $w'<w$.

Numerically, for a given $\delta\phi$ or $\delta_{\rm m}$ (Eq. 1.22), it is possible to find solutions of A_{ij} using the lens-plane approach (Jain, Seljak & White 2000). This approach approximates the continuous field of $\delta\phi_{,ij}$ by a discrete set of N flat planes and successively works out over some area in the sky, the distortion A_{ij} after every following lens plane starting from the plane closest to the observer.

Analytically, we can approximate the solution of A_{ij} to lowest-order by setting $A_{ij}(\vec{\theta},w')=\delta_{ij}$ and $\vec{x}=f_{\rm K}(w)\vec{\theta}$ in the RHS of Eq. (1.68):

$$A_{ij}(\vec{\theta},w)\approx\delta_{ij}-\frac{2}{c^2}\int_0^w {\rm d}w'\,\frac{f_{\rm K}(w-w')f_{\rm K}(w')}{f_{\rm K}(w)}\,\delta\phi_{,ij}(f_{\rm K}(w')\vec{\theta},w')\;. \tag{1.69}$$

This approximation is called the *lowest-order Born approximation* of A_{ij}.

1.5.2. Weak gravitational lensing

In a regime where the light deflections are small, the distortion matrix A_{ij} is invertible, $\det\mathbf{A}\neq0$, and the lens equation possesses only one solution $\vec{\beta}$ for a given $\vec{\theta}$. We call this regime the *weak lensing regime.*

Convergence and shear of the gravitational tidal field

Weak gravitational lensing (Schneider 2004; van Waerbeke & Mellier 2003; Bartelmann & Schneider 2001) uses the shapes of distant galaxies, the *source galaxies*, to infer the distribution of the total matter. This is based on the fact, as explained in the last section, that light is deflected by mass overdensities so that the gravitational tidal field of the matter density inhomogeneities along the line-of-side towards a galaxy changes the shape of its image. This distortion effect of the tidal gravitational field is, for small $\delta\phi$, well described by a two-dimensional linear mapping *over the whole apparent size of one galaxy*, hence by the matrix **A** in Eq. (1.68).

A linear mapping does not have many ways to change the shape of a galaxy. The relevant[10] components of the linear transformation $\mathbf{A}$ are the *convergence* κ, which magnifies or demagnifies the size of a galaxy, and the *shear*, $\gamma \equiv \gamma_1 + \mathrm{i}\gamma_2$, which stretches the image of a galaxy along some direction:

$$\mathbf{A}(\vec{\theta}, w) = \left(\begin{array}{cc} 1-\kappa-\gamma_1 & -\gamma_2 \\ -\gamma_2 & 1-\kappa+\gamma_1 \end{array} \right) = (1-\kappa) \left(\begin{array}{cc} 1-g_1 & -g_2 \\ -g_2 & 1+g_1 \end{array} \right) , \tag{1.70}$$

where $g \equiv \gamma/(1-\kappa)$ is the *reduced shear.* See Fig. 1.13 for an illustration of the action of such a linear transformation. The linear transformation, and also convergence and (reduced) shear, is a function of the direction $\vec{\theta}$ and the distance w of the source galaxy. If the exact radial distance w of a source galaxy is not known, we have to consider the expected distortion $\mathbf{A}$ for a (normalised) distribution $p_g(w)$ of galaxies:

$$\mathbf{A}(\vec{\theta}) = \int_0^{w_\mathrm{h}} \mathrm{d}w \, p_g(w) \, \mathbf{A}(\vec{\theta}, w) \; . \tag{1.71}$$

This is the case in most of the contemporary weak lensing galaxy surveys, and the following formulae also assume this case. We can, however, always recover the corresponding expressions for an exactly known source galaxy distance, simply by setting $p_g(w) = \delta_\mathrm{D}(w - w')$ where w' is the comoving distance of the galaxy.

With the approximation (1.69) at hand, we can relate convergence and shear in the direction of $\vec{\theta}$ to the three-dimensional matter density contrast $\delta_\mathrm{m}(\vec{r}, w)$. The vector $\vec{r}$ is a 2D-vector perpendicular to the fiducial light ray. Employing the Born approximation and the Poisson equation, Eq. (1.22), yields for convergence and shear

$$\begin{aligned} \kappa(\vec{\theta}) &\equiv \frac{1}{2}(1 - A_{11} - A_{22}) & (1.72) \\ &= \frac{3}{2}\frac{H_0^2}{c^2}\Omega_\mathrm{m} \int \mathrm{d}w \, \frac{\bar{W}(w) \, f_\mathrm{K}(w)}{a(w)} \, \delta_\mathrm{m}(f_\mathrm{K}(w)\,\vec{\theta}, w) & \\ \bar{W}(w) &\equiv \int \mathrm{d}w' \, p_g(w') \, \frac{f_\mathrm{K}(w'-w)}{f_\mathrm{K}(w')} & (1.73) \\ \gamma(\vec{\theta}) &\equiv \frac{1}{2}\left[A_{22} - A_{11} - \mathrm{i}(A_{12} + A_{21})\right] & (1.74) \\ &= \frac{1}{\pi} \int \mathrm{d}^2\vec{\theta}' \, \kappa(\vec{\theta} - \vec{\theta}') \frac{\theta_2'^2 - \theta_1'^2 - 2\mathrm{i}\theta_1'\theta_2'}{|\vec{\theta}'|^4} \; , & \end{aligned}$$

where $a(w)$ corresponds to the scale factor at comoving radial distance w.

These equations say that the convergence of the mapping in some direction $\vec{\theta}$ on the sky is proportional to the weighted matter density contrast towards that direction, and that the shear is a convolution of the convergence; the weight solely depends on the large-scale geometry of the universe and the distribution of the source galaxies in distance. As convergence and shear are projections of δ_m, Eq. (1.36), the polyspectra of δ_m and the convergence/shear polyspectra are related according to the Limber's equation, Eq. (1.37).

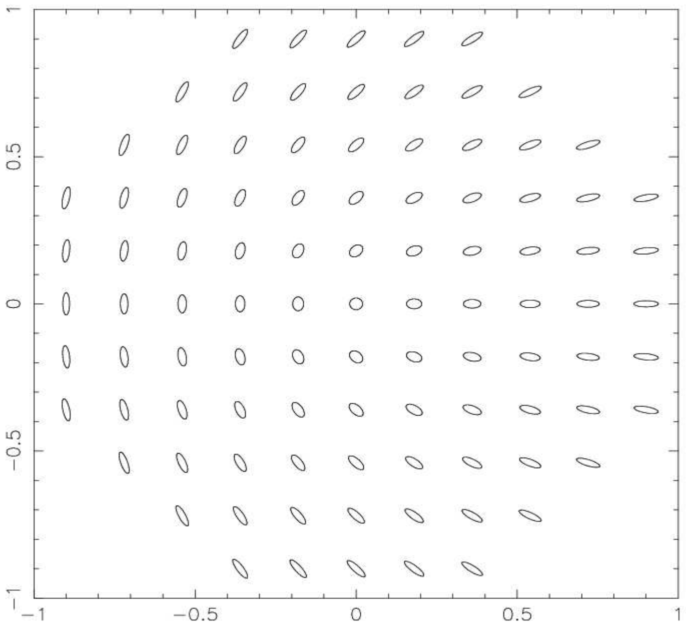

Figure 1.14.: *The shape of image ellipses for a circular source, in dependence of the ellipticity components χ_1 and χ_2; a corresponding plot for ϵ_1 and ϵ_2 would look similar (source: D. Clowe, see also Schneider 2004).*

Connection to the real world

We now define a quantity for the shape of a galaxy. A single galaxy ellipticity ϵ is defined as a complex number in terms of the (central) *quadrupole moment* Q_{ij} of the light profile $I(\vec{\theta}\,)$ of the observed image with $\vec{\theta} = \vec{0}$ sitting at the centre,

$$\vec{\theta}_{\rm cen} = \int \mathrm{d}^2\theta \; I(\vec{\theta})W(\vec{\theta}\,)\,\vec{\theta}\;, \tag{1.75}$$

of the galaxy image:

$$Q_{ij} = \frac{\int \mathrm{d}^2\theta \; I(\vec{\theta})W(\vec{\theta}\,)\,\theta_i\,\theta_j}{\int \mathrm{d}^2\theta \; I(\vec{\theta})W(\vec{\theta}\,)} \;\;;\; \epsilon \equiv \frac{Q_{11} - Q_{22} + 2\mathrm{i}Q_{12}}{Q_{11} + Q_{22} + 2\sqrt{Q_{11}Q_{22} - Q_{12}^2}}\;. \tag{1.76}$$

The function $W(\vec{\theta}\,)$ denotes an appropriate aperture mask within which the quadrupole moment is measured. For circular isophotes, one has $Q_{11} = Q_{22}$ and $Q_{12} = 0$ and therefore $\epsilon = 0$; the trace of $\mathbf{Q}$ defines the size or area of the isophotes. Another common definition for the ellipticity in gravitational lensing is

$$\chi \equiv \frac{Q_{11} - Q_{22} + 2\mathrm{i}Q_{12}}{Q_{11} + Q_{22}}\;, \tag{1.77}$$

---

[10] We only consider the symmetric part of the Jacobian $\mathbf{A}$, *i.e.* $\frac{1}{2}(A_{ij} + A_{ji})$, because the asymmetric, rotational part, *i.e.* $\frac{1}{2}(A_{ij} - A_{ji})$, of the transformation is irrelevant for gravitational lensing.

which has the same phase as ϵ but a different modulus. The orientation and ellipticity of the isophotes for various complex ellipticities is plotted in Fig. 1.14. Note that complex ellipticities, χ and ϵ, are polar quantities and hence do not transform like vectors under rotation: They transform according to $\epsilon' = \mathrm{e}^{-2\mathrm{i}\psi}\,\epsilon$ where ψ is the rotation angle.

Seitz & Schneider (1997) showed that under the action of a linear transformation **A** the *intrinsic ellipticity*, *i.e.* unlensed galaxy ellipticity, ϵ_s of a source galaxy image is transformed into ϵ_i according to

$$\epsilon_\mathrm{i} = \frac{\epsilon_\mathrm{s} + g}{1 + g^*\,\epsilon_\mathrm{s}}\ , \tag{1.78}$$

if the reduced shear of the linear transformation is $|g| \leq 1$, or into $1/\epsilon_\mathrm{i}^*$ otherwise. In the weak lensing regime, the projected δ_m is small: $|\gamma| \ll 1$, $\kappa \ll 1$, thus $|g| \ll 1$ and $1 + g^*\,\epsilon_\mathrm{s} \approx 1$. Therefore, we can make a further approximation:

$$\epsilon_\mathrm{i} \approx \epsilon_\mathrm{s} + g \approx \epsilon_\mathrm{s} + \gamma\ . \tag{1.79}$$

Furthermore, we make the fundamental assumption that the unlensed ellipticities ϵ_s of galaxies that are not physically close are randomly oriented with no preferred direction in the sky, i.e. $\langle\epsilon_\mathrm{s}\rangle = 0$, yielding

$$\langle\epsilon_\mathrm{i}\rangle \approx \gamma(\vec{\theta}\,) \tag{1.80}$$

for an average over the ellipticities of source galaxies lying in the same line-of-sight direction $\vec{\theta}$. Therefore, we come to the conclusion that the ellipticities ϵ_i of the source galaxies themselves are unbiased estimators of the shear.

Of course, galaxies are in general not intrinsically round objects, $\epsilon_s \neq 0$. In fact, the ellipticities of galaxies have typically $|\epsilon_s| \approx 0.3$. This makes them very noisy estimators of the shear considering that the shear signal induced by (weak) gravitational lensing is typically about one percent of this value. Therefore, an average over many galaxy ellipticities in weak lensing applications is required.

The shear is a function of the convergence, and the convergence is related to the projected δ_m. Consequently, is should be possible to make, to some extent, a reconstruction of the total matter distribution based on the observed ellipticities of source galaxies. With such a reconstruction a direct comparison with the galaxy distribution for investigations of the galaxy bias is possible, as will be shown in Chapter 3.

CHAPTER 2

A model for the evolution of galaxy bias on linear scales

2.1. Introduction

As mentioned in the Sect. 1.4 the relative clustering of galaxies compared to the dark matter seems to be a function of redshift. Apparently, galaxies were biased in the past but are little biased today. Moreover, biasing of galaxies depends on the galaxy type. A natural question to ask is whether the bias evolution, if observed for different galaxy types, can reveal something on the nature of the evolution and formation of a particular class of galaxies. Lead by this question, we develop in this chapter a time evolution model for the linear stochastic bias, Eq. (1.54), of galaxies on linear (large) scales. This model demonstrates that bias evolution can depend on the details how galaxies are formed from, or transformed into, another class of objects.

Analytical models for the bias evolution fall into two categories: test particle models and halo models. Test particle models (Basilakos & Plionis 2001; Matsubara 1999; Taruya & Soda 1999; Taruya *et al.* 1999; Tegmark & Peebles 1998, hereafter TP98; Fry 1996, hereafter F96; Nusser & Davis 1994) assume that galaxies passively follow the bulk flow of the dark matter field. A common characteristic of these models is that they use perturbation theory for modelling structure formation and are, therefore, at most applicable to weakly non-linear scales like in Taruya *et al.* (1999). Halo models (Berlind & Weinberg 2002; Taruya & Suto 2000; Seljak 2000; Peacock & Smith 2000; Kauffmann *et al.* 1999a,b; Sheth & Lemson 1999; Bagla 1998; Catelan *et al.* 1998; Matarrese *et al.* 1997; Mo & White 1996), on the other hand, picture the dark matter density field to be made up out of typical haloes that host galaxies, so that the clustering of galaxies is related to the clustering of their hosts and typical halo properties (dark matter density profiles and clustering of the halo centres as function of halo mass; these parameters are taken from N-body simulations). They also make predictions on non-linear scales, but, certainly, at the cost of several assumptions. Overall the halo model together with the galaxy halo occupation statistics seems to be a fairly good description (*cf.* Seljak, Makarov & Mandelbaum 2004). Both model concepts –halo-model and test particle models– agree on a debiasing of the galaxy field with time, but there are differences in the details (Magliocchetti *et al.* 2000).

We extend the test particle model of TP98 for the linear stochastic parameter evolution and include several galaxy populations that are allowed to interact with each other. By "interaction" we mean the local change of the number of galaxies. The rate of galaxy interaction is assumed to be a function of all density fields. Treated is also the evolution of the relative bias of the populations with respect to each other, not only the bias relative to the dark matter field.

The structure of this chapter is the following. The second section develops a model based on the bulk flow hypothesis including a general sink/source term for galaxy destruction/creation. We derive differential equations for the auto- and cross-correlation power spectra (galaxy-galaxy, galaxy-dark matter), valid on scales where the fields are Gaussian, thus on linear scales (Sect. 2.2.3). The equations are then transformed to obtain differential equations for the linear stochastic bias parameters (Sect. 2.2.4). In Sect. 2.3, scenarios conserving galaxy-number are briefly visited. In Sect. 2.4, we focus on linear and quadratic interaction rates and work out the relevant terms needed for the bias model equations based on this interaction (Table 2.1). Furthermore, we demonstrate in Sect. for a few toy models the effect on the evolution of the large-scale bias in the presence of these specific galaxy interactions. This chapter is concluded with a discussion.

2.2. Derivation of the bias model

Here we derive differential equations for the density contrasts of a set of galaxy populations based on the central assumption that the velocity fields of the galaxies are identical to that of the dark matter. This *bulk flow hypothesis* is shared by other similar models (*cf.* TP98; F96).

2.2.1. Evolution of density contrasts

The dark matter peculiar bulk velocity $\vec{v}$ is on large scales described by the Eqs. (1.20)-(1.22) and (1.11). Solutions to these differential equations have been extensively studied in the literature, especially using the perturbation approach (*e.g.* Bernardeau *et al.* 2001 for a review; Goroff *et al.* 1986) and therefore will not be discussed here. We simply assume in the following that the solutions for $\delta_{\rm m}$ and $\vec{v}$ are (approximately) known.

As well as the perturbations in the dark matter density we express the inhomogeneities in the distribution of galaxies as density contrast δ_i of a galaxy number density field n_i:

$$n_i = \bar{n}_i(1+\delta_i) \; . \tag{2.1}$$

The index i is used to distinguish between different galaxy populations. Generally, every galaxy population has its own bulk velocity field $\vec{v}_{\rm g}$ and set of Euler equations for their evolution. The fundamental assumption on the galaxy bulk flow, however, reduces the treatment for the galaxy number density evolution solely to the number conservation equation, which for a *conserved number of galaxies* looks as Eq. (1.21) (TP98):

$$\frac{\partial \delta_i}{\partial t} + \frac{1}{a}\nabla\vec{v} + \frac{1}{a}\nabla\left(\delta_i\vec{v}\right) = 0 \; , \tag{2.2}$$

since we set the galaxy bulk flow equal to the dark matter bulk flow, $\vec{v}_{\rm g} = \vec{v}$. The term $\frac{1}{a}\nabla\vec{v}$ can be removed by subtracting Eq. (1.21), arriving at an equation that clearly shows how the galaxies are coupled to the dark matter field

$$\frac{\partial \delta_i}{\partial t} = \frac{\partial \delta_{\rm m}}{\partial t} + \frac{1}{a}\nabla\left(\vec{v}\left[\delta_{\rm m} - \delta_i\right]\right) \ . \tag{2.3}$$

fOur main modification in this continuity equation consists of dropping the constraint that the mean number of galaxies –expressed by $\bar{n}_i$– is conserved. We allow for a sink/source term Φ_i in the conservation equation for the galaxy population n_i that incorporates galaxy-galaxy and galaxy-dark matter interactions, and is thought to be a function of all the density fields. Note that in this formalism interaction is equivalent to a change in galaxy number density.

In order to include Φ_i in Eq. (2.2) and to eventually obtain a modified formula (2.3), we have to start with the number conservation equation for the galaxies plus the new interaction rate Φ_i:[1]

$$\frac{\partial n_i}{\partial t} + \frac{1}{a}\nabla\left(\vec{v} n_i\right) = \Phi_i \ . \tag{2.4}$$

The term Φ_i locally creates or destroys galaxies belonging to the population n_i. Later on, we will relate this term to the number densities of other galaxy populations and the dark matter density. Setting $\Phi_i = 0$ would result again in Eq. (2.3). Substitution of n_i by the definition in (2.1) yields:

$$\frac{\partial \delta_i}{\partial t} + \frac{1}{a}\nabla\vec{v} + \frac{1}{a}\nabla\left(\vec{v}\,\delta_i\right) = \frac{1}{\bar{n}_i}\left[\Phi_i - \left(1+\delta_i\right)\frac{\partial \bar{n}_i}{\partial t}\right] \ . \tag{2.5}$$

For the last step we had to take into account that the mean galaxy density $\bar{n}_i$ is a function of time. Compared to Eq. (2.2), we obviously have a new term on the right hand side (RHS) that has to be accounted for. Again, subtracting Eq. (1.21) from the last equation gives the time evolution equation for the density contrasts of the galaxies but this time accounting for the impact of a varying mean galaxy density due to Φ_i

$$\frac{\partial \delta_i}{\partial t} = \frac{\partial \delta_{\rm m}}{\partial t} + \frac{1}{a}\nabla\left(\vec{v}\left[\delta_{\rm m} - \delta_i\right]\right) + \frac{1}{\bar{n}_i}\left[\Phi_i - \delta_i\frac{\partial \bar{n}_i}{\partial t}\right] - \frac{1}{\bar{n}_i}\frac{\partial \bar{n}_i}{\partial t} \ . \tag{2.6}$$

2.2.2. Evolution of mean densities

In order to get the time-dependence of the (comoving) mean galaxy density $\bar{n}_i$, we take the ensemble average[2] $\langle ... \rangle$ of Eq. (2.6):

$$\frac{\partial \bar{n}_i}{\partial t} = \langle \Phi_i \rangle \ , \tag{2.7}$$

where we used $\langle \delta_i \rangle = \langle \delta_{\rm m} \rangle = \langle \nabla\left(\vec{v}\,\delta_i\right) \rangle = \nabla\left\langle \vec{v}\,\delta_i \right\rangle = 0$.

The terms $\nabla\left\langle \vec{v}\,\delta_{\rm m}\right\rangle$ and $\nabla\left\langle \vec{v}\,\delta_i\right\rangle$ vanish, because the net flux

$$\langle n\vec{v} \rangle = \bar{n}\left\langle \vec{v}\,\delta\right\rangle + \bar{n}\left\langle \vec{v}\right\rangle = 0 \tag{2.8}$$

of any population n over the whole volume has to be zero, since we work in the rest frame of the Hubble expansion. In particular, Eq. (2.7) has general validity and is not restricted to Gaussian fields only.

---

[1] We use comoving number densities, *i.e.* $n_i' = a^{-3}\, n_i$ where n_i' is the proper galaxy density. The source term Φ_i also prescribes the change in number of galaxies per comoving volume, *i.e.* $\Phi_i(n_j) = a^3\, \Phi_i'(a^{-3}\, n_j)$ where Φ_i' is per proper volume.

[2] Due to the ergodicity of the random fields involved, volume and ensemble average are identical.

2.2.3. Linear scale evolution of correlation power spectra

We will primarily be interested in the evolution of the linear stochastic bias which may be expressed in terms of the cross- and auto-correlation power spectra. Therefore, the next logical step is to work out the time dependence of these power spectra. For that reason, we decompose the density perturbation into Fourier modes,

$$\tilde{\delta}(\vec{k}) = \int \mathrm{d}^3 r \; \delta(\vec{r})\, \mathrm{e}^{+\mathrm{i}\vec{k}\vec{r}} \;, \tag{2.9}$$

to obtain the corresponding equation for the Fourier coefficients

$$\frac{\partial \tilde{\delta}_i}{\partial t} = \frac{\partial \tilde{\delta}_\mathrm{m}}{\partial t} + \frac{1}{\bar{n}_i}\left[\tilde{\Phi}_i - \tilde{\delta}_i \frac{\partial \bar{n}_i}{\partial t}\right] + \frac{\mathrm{i}\,\vec{k}}{a}\left(\tilde{\vec{v}} * \left[\tilde{\delta}_\mathrm{m} - \tilde{\delta}_i\right]\right) \;, \tag{2.10}$$

where the irrelevant terms at $\vec{k} = 0$ have been neglected. For convenience, we omit the arguments in the brackets of the Fourier coefficients. By the asterisk "$*$" we denote the convolution of two fields in Fourier space

$$(\tilde{f} * \tilde{g})(\vec{k}) \equiv \int \mathrm{d}^3 k' \tilde{f}(\vec{k}')\tilde{g}(\vec{k} - \vec{k}') \tag{2.11}$$

that enter when products of fields are Fourier transformed. A tilde "$\tilde{}$" always denotes the Fourier transform of a random field or function beneath the tilde.

We restrict ourselves to the case of *strictly Gaussian fields*, which is a reasonable assumption on linear scales (see *e.g.* Bernardeau *et al.* 2002). As a consequence, all connected higher-order correlation terms like bispectra vanish, which makes the following equations a lot simpler. Further, in the cosmological context the density fields are statistically *isotropic and homogeneous* random fields.

The correlation power spectrum $P(k)$ between two real homogeneous random fields with the Fourier coefficients $\tilde{\delta}_1(\vec{k})$ and $\tilde{\delta}_2(\vec{k})$ is defined by

$$(2\pi)^3\, \delta_D(\vec{k} - \vec{k}')P(|\vec{k}|) = \left\langle \tilde{\delta}_1(\vec{k})\tilde{\delta}_2^*(\vec{k}')\right\rangle \;. \tag{2.12}$$

This relation also states that the power spectrum $P(k)$ is related to the correlator, RHS, in the following way

$$P(|\vec{k}|) = \int \frac{\mathrm{d}^3 k'}{(2\pi)^3}\left\langle \tilde{\delta}_1(\vec{k})\tilde{\delta}_2^*(\vec{k}')\right\rangle \;. \tag{2.13}$$

Due to this relation, we are going to use a slightly different definition $\langle ... \rangle'$ of the ensemble average:

$$\left\langle \tilde{\delta}_1(\vec{k})\tilde{\delta}_2^*(\vec{k}')\right\rangle' \equiv \int \frac{\mathrm{d}^3 k'}{(2\pi)^3}\left\langle \tilde{\delta}_1(\vec{k})\tilde{\delta}_2^*(\vec{k}')\right\rangle \;, \tag{2.14}$$

which in the following is useful to derive the differential equations for the correlation power spectra. We also introduce the convention to omit the $\vec{k}$-arguments for the correlators and the power spectra. Instead, we use the following notation: Power spectra have as well as the first field in the two-point correlator (in the above definition $\tilde{\delta}_1$) as argument always $\vec{k}$, whereas the second field in the correlator has the argument $\vec{k}'$. For example, according to this convention the following two lines are identical:

$$\begin{aligned} P(k) &= \left\langle \tilde{\delta}_1(\vec{k})\tilde{\delta}_2^*(\vec{k}')\right\rangle' \\ P &= \left\langle \tilde{\delta}_1\tilde{\delta}_2^*\right\rangle' . \end{aligned} \tag{2.15}$$

After explaining the notation, we now accordingly define the correlation power spectra between the model random fields by

$$P_{ij} = P_{ji} \equiv \left\langle \tilde{\delta}_i\tilde{\delta}_j^*\right\rangle' \quad P_i \equiv \left\langle \tilde{\delta}_i\tilde{\delta}_{\mathrm{m}}^*\right\rangle' \quad P_{\mathrm{m}} \equiv \left\langle \tilde{\delta}_{\mathrm{m}}\tilde{\delta}_{\mathrm{m}}^*\right\rangle' , \tag{2.16}$$

where P_{ij} is the correlation power spectrum between galaxy population n_i and n_j, thus for $i = j$ the auto-correlation of population n_i. P_i denotes the cross-correlation between the population n_i and the dark matter field ρ_{m}. P_{m} is the dark matter auto-correlation.

To work out their evolution, we first multiply both sides of Eq. (2.10) by $\tilde{\delta}_{\mathrm{m}}^*(\vec{k}')$, take the (modified) ensemble average $\langle ... \rangle'$ and use the definition of the power spectra to get

$$\left\langle \frac{\partial\tilde{\delta}_i}{\partial t}\tilde{\delta}_{\mathrm{m}}^*\right\rangle' = \left\langle \frac{\partial\tilde{\delta}_{\mathrm{m}}}{\partial t}\tilde{\delta}_{\mathrm{m}}^*\right\rangle' + \frac{1}{\bar{n}_i}\left[\left\langle \tilde{\Phi}_i\tilde{\delta}_{\mathrm{m}}^*\right\rangle' - P_i\frac{\partial\bar{n}_i}{\partial t}\right] . \tag{2.17}$$

Note that all terms containing bispectra (three-point correlations) have been neglected. They turn up when the correlation of two convolved fields with a third field is calculated (see Appendix B.1) as for the velocity term in Eq. (2.10).

The equation simplifies further, if we use the following two relations, obtained by taking the time derivative of the power spectra definitions (2.16)

$$\frac{\partial P_{\mathrm{m}}}{\partial t} = \left\langle \frac{\partial\tilde{\delta}_{\mathrm{m}}}{\partial t}\tilde{\delta}_{\mathrm{m}}^*\right\rangle' + \left\langle \tilde{\delta}_{\mathrm{m}}\frac{\partial\tilde{\delta}_{\mathrm{m}}^*}{\partial t}\right\rangle' = 2\left\langle \frac{\partial\tilde{\delta}_{\mathrm{m}}}{\partial t}\tilde{\delta}_{\mathrm{m}}^*\right\rangle' \tag{2.18}$$

$$\left\langle \frac{\partial\tilde{\delta}_i}{\partial t}\tilde{\delta}_{\mathrm{m}}^*\right\rangle' = \frac{\partial P_i}{\partial t} - \left\langle \frac{\partial\tilde{\delta}_{\mathrm{m}}^*}{\partial t}\tilde{\delta}_i\right\rangle' . \tag{2.19}$$

Eq. (2.18) utilises the fact that the power spectra are real number functions, thus identical to its complex conjugate. Eq. (2.17) can according to Eq. (2.18) and (2.19) be written as

$$\frac{\partial P_i}{\partial t} = \frac{1}{2}\frac{\partial P_{\mathrm{m}}}{\partial t} + \frac{1}{\bar{n}_i}\left[\left\langle \tilde{\Phi}_i\tilde{\delta}_{\mathrm{m}}^*\right\rangle' - P_i\frac{\partial\bar{n}_i}{\partial t}\right] + \left\langle \frac{\partial\tilde{\delta}_{\mathrm{m}}^*}{\partial t}\tilde{\delta}_i\right\rangle' \tag{2.20}$$

leaving us with an equation for the dark matter-galaxy power spectrum.

As a second step, we try to do something similar for the galaxy-galaxy power spectra P_{ij}. Multiplying both sides of (2.10) by $\tilde{\delta}_j^*(\vec{k}')$ and taking the ensemble average yields:

$$\left\langle \frac{\partial\tilde{\delta}_i}{\partial t}\tilde{\delta}_j^*\right\rangle' = \left\langle \frac{\partial\tilde{\delta}_{\mathrm{m}}}{\partial t}\tilde{\delta}_j^*\right\rangle' + \frac{1}{\bar{n}_i}\left[\left\langle \tilde{\Phi}_i\tilde{\delta}_j^*\right\rangle' - P_{ij}\frac{\partial\bar{n}_i}{\partial t}\right] . \tag{2.21}$$

This is already the first term out of two we need for the time evolution of P_{ij}:

$$\frac{\partial P_{ij}}{\partial t} = \left\langle \frac{\partial\tilde{\delta}_i^*}{\partial t}\tilde{\delta}_j\right\rangle' + \left\langle \frac{\partial\tilde{\delta}_j}{\partial t}\tilde{\delta}_i^*\right\rangle' . \tag{2.22}$$

The second is obtained by swapping the indices i and j and taking the complex conjugate of Eqs. (2.21). Combining these eventually gives

$$\begin{aligned}\frac{\partial P_{ij}}{\partial t} &= \left\langle \frac{\partial \tilde{\delta}_{\rm m}}{\partial t}\tilde{\delta}_j^*\right\rangle' + \frac{1}{\bar{n}_i}\left[\left\langle \tilde{\Phi}_i\tilde{\delta}_j^*\right\rangle' - P_{ij}\frac{\partial \bar{n}_i}{\partial t}\right] \\ &+ \left\langle \frac{\partial \tilde{\delta}_{\rm m}^*}{\partial t}\tilde{\delta}_i\right\rangle' + \frac{1}{\bar{n}_j}\left[\left\langle \tilde{\Phi}_j^*\tilde{\delta}_i\right\rangle' - P_{ij}\frac{\partial \bar{n}_j}{\partial t}\right] .\end{aligned} \tag{2.23}$$

For the next step, we would like to approximate in Eqs. (2.20) and (2.23) the time derivative $\frac{\partial \tilde{\delta}_{\rm m}}{\partial t}$ using perturbation theory. For our purposes, the lowest-order approximation of $\tilde{\delta}_{\rm m}$ is sufficient, because we have restricted the model to large (linear) scales. Considering only the growing mode, we have according to Eqs. (1.26)

$$\begin{aligned}\tilde{\delta}_{\rm m} &= D_+\;\tilde{\delta}_{\rm m}|_{t_i} \\ \Longrightarrow \frac{\partial \tilde{\delta}_{\rm m}}{\partial t} &= \frac{\partial D_+}{\partial t}\;\tilde{\delta}_{\rm m}|_{t_i} = \frac{1}{D_+}\frac{\partial D_+}{\partial t}\;\tilde{\delta}_{\rm m} = \frac{\partial \ln D_+}{\partial t}\;\tilde{\delta}_{\rm m} ,\end{aligned} \tag{2.24}$$

where $\tilde{\delta_{\rm m}}|_{t_i}$ denotes the density perturbation mode at some initial time and $D_+ \equiv \frac{D_+(t)}{D_+(t_i)}$ the linear growth factor (see Eq. 1.27). Employing the lowest-order approximation of $\tilde{\delta}_{\rm m}$ yields for the terms in question

$$\begin{aligned}\left\langle \frac{\partial \tilde{\delta}_{\rm m}^*}{\partial t}\tilde{\delta}_i\right\rangle' &= \left\langle \frac{\partial \ln D_+}{\partial t}\tilde{\delta}_{\rm m}^*\tilde{\delta}_i\right\rangle' = \frac{\partial \ln D_+}{\partial t}\;P_i \equiv \frac{R\,(t)}{2}\;P_i \\ \frac{\partial P_{\rm m}}{\partial t} &= \left\langle \frac{\partial \ln D_+}{\partial t}\tilde{\delta}_{\rm m}^*\tilde{\delta}_{\rm m}\right\rangle' + \left\langle \tilde{\delta}_{\rm m}^*\frac{\partial \ln D_+}{\partial t}\tilde{\delta}_{\rm m}\right\rangle' \\ &= 2\frac{\partial \ln D_+}{\partial t}\;P_{\rm m} \equiv R\,(t)\;\;P_{\rm m} .\end{aligned} \tag{2.25}$$

The newly introduced function

$$R\,(t) \equiv \frac{1}{P_{\rm m}}\frac{\partial P_{\rm m}}{\partial t} = 2\frac{\partial \ln D_+}{\partial t} \tag{2.26}$$

is the rate at which the power spectrum of the dark matter is growing on linear scales.

Plugging this expression into Eqs. (2.20) and (2.23) enables us to write the differential equations for the correlation power spectra in a closed form

$$\frac{\partial P_i}{\partial t} - R\,(t)\,\frac{P_{\rm m}+P_i}{2} = \frac{\left\langle \tilde{\Phi}_i\tilde{\delta}_{\rm m}^*\right\rangle'}{\bar{n}_i} - P_i\frac{\langle\Phi_i\rangle}{\bar{n}_i} \tag{2.27}$$

$$\frac{\partial P_{ij}}{\partial t} - R\,(t)\,\frac{P_j+P_i}{2} = \frac{\left\langle \tilde{\Phi}_i\tilde{\delta}_j^*\right\rangle'}{\bar{n}_i} + \frac{\left\langle \tilde{\Phi}_j^*\tilde{\delta}_i\right\rangle'}{\bar{n}_j} - P_{ij}\left[\frac{\langle\Phi_i\rangle}{\bar{n}_i} + \frac{\langle\Phi_j\rangle}{\bar{n}_j}\right] . \tag{2.28}$$

The terms on the left hand side (LHS) containing $R\,(t)$ are responsible for driving a biased galaxy distribution towards the dark matter distribution. Setting these terms to zero, switches off the coupling to the dark matter field due to the bulk flow assumption. The expressions on the RHS encode the impact on the power spectra due to the creation or destruction of galaxies.

2.2.4. Linear scale evolution of linear stochastic bias

We define the bias parameters with one index, thus r_i and b_i, to be the bias of the i-th galaxy population with respect to the dark matter, whereas two indices, b_{ij} and r_{ij}, denote the relative bias between the i-th and j-th galaxy population:

$$\begin{aligned} b_i &\equiv \sqrt{\frac{P_{ii}}{P_\mathrm{m}}} \qquad r_i \equiv \frac{P_i}{\sqrt{P_{ii}P_\mathrm{m}}} \\ b_{ij} &\equiv \sqrt{\frac{P_{ii}}{P_{jj}}} \qquad r_{ij} \equiv \frac{P_{ij}}{\sqrt{P_{ii}P_{jj}}} \ . \end{aligned} \tag{2.29}$$

Using these definitions, we can write down differential equations for $(b_i, r_i, b_{ij}, r_{ij})$ based on Eqs. (2.27) and (2.28). Appendix B.2 shows how this is done in detail. The main result there is the following set of equations (the equation for the mean density $\bar{n}_i$ has been added for the sake of completeness) showing the evolution of the bias parameters for any kind of interaction term Φ_i:

$$\frac{\partial b_i}{\partial t} = R\,(t)\,\frac{r_i - b_i}{2} + I_i^1 \tag{2.30}$$

$$\frac{\partial b_{ij}}{\partial t} = R\,(t)\,\frac{r_i b_j - r_j b_i}{2 b_i b_j} b_{ij} + b_{ij}\left[\frac{I_i^1}{b_i} - \frac{I_j^1}{b_j}\right] \tag{2.31}$$

$$\frac{\partial r_i}{\partial t} = R\,(t)\,\frac{1 - r_i^2}{2 b_i} + I_i^2 \tag{2.32}$$

$$\frac{\partial r_{ij}}{\partial t} = R\,(t)\left[\frac{r_i - r_{ij} r_j}{2 b_j} + \frac{r_j - r_{ij} r_i}{2 b_i}\right] + I_{ij}^3 + \left[I_{ji}^3\right]^* \tag{2.33}$$

$$\frac{\partial \bar{n}_i}{\partial t} = \langle \Phi_i \rangle = \langle \tilde{\Phi}_i \rangle \Big|_{k=0} \ , \tag{2.34}$$

where we used the following definitions for interaction terms arising if the number of galaxies is not conserved

$$\begin{aligned} I_i^0 &\equiv \frac{1}{\bar{n}_i} \frac{\left\langle \tilde{\Phi}_i \tilde{\delta}_i^* \right\rangle'}{P_\mathrm{m}} \frac{1}{b_i} \\ I_i^1 &\equiv I_i^0 - \frac{b_i}{\bar{n}_i} \langle \Phi_i \rangle = I_i^0 - \frac{b_i}{\bar{n}_i} \langle \tilde{\Phi}_i \rangle \Big|_{k=0} \\ I_i^2 &\equiv \frac{1}{\bar{n}_i} \left[\frac{\left\langle \tilde{\Phi}_i \tilde{\delta}_m^* \right\rangle'}{P_\mathrm{m}} \frac{1}{b_i} - \frac{\left\langle \tilde{\Phi}_i \tilde{\delta}_i^* \right\rangle'}{P_\mathrm{m}} \frac{r_i}{b_i^2} \right] \\ I_{ij}^3 &\equiv \frac{1}{\bar{n}_i} \left[\frac{\left\langle \tilde{\Phi}_i \tilde{\delta}_j^* \right\rangle'}{P_\mathrm{m}} \frac{1}{b_i b_j} - \frac{\left\langle \tilde{\Phi}_i \tilde{\delta}_i^* \right\rangle'}{P_\mathrm{m}} \frac{r_{ij}}{b_i^2} \right] \ . \end{aligned} \tag{2.35}$$

The interaction terms I_i^1, I_i^2 and I_{ij}^3 vanish for $\Phi_i = 0$; they are responsible for deviations from the interaction-free evolution of the linear bias parameters. In Eq. (2.34), we equivalently expressed the interaction rate in terms of the Fourier representation of Φ_i. Depending on the definition of Φ_i this representation can be mathematically of advantage, especially when derivatives or integrals are involved.

2.2.5. Constraints on correlation factors

As initial condition, one can set the bias parameters b_i freely in the Eqs. (2.30)-(2.33). The relative bias b_{ij} between the different galaxy populations is thereby also fixed, namely $b_{ij} = b_i/b_j$.

The choice of the initial conditions of the correlation coefficients (r_i, r_{ij}) is not free, however. For example, we cannot demand population A, say, to be 100 percent correlated to both population B and population C, but, at the same time, population B to be not correlated to C. To be more general, we arrange the density contrasts of the dark matter and N galaxy fields in terms of one single vector

$$\vec{x}\,(\vec{k}\,) = \left(\tilde{\delta}_{\rm m}(\vec{k}\,)\ \ \tilde{\delta}_1(\vec{k}\,)\ \ ...\ \ \tilde{\delta}_{\rm N}(\vec{k}\,)\right)^{\rm t}\ , \tag{2.36}$$

with $\vec{x}^{\,\rm t}$ being the transpose of $\vec{x}$. Concerning the bias parameters, we are restricted by the fact that the covariance matrix $\mathbf{C}(\vec{k}\,) = \left\langle \vec{x}\,(\vec{k}\,)[\vec{x}\,(\vec{k}^{\prime})]^{\rm t}\right\rangle^{\prime}$ has to be positive semidefinite, thus the determinant of

$$\mathbf{C}(\vec{k}\,) = P_{\rm m}(|\vec{k}\,|)\begin{pmatrix} 1 & r_1b_1 & r_2b_2 & ... & r_Nb_N \\ r_1b_1 & b_1^2 & b_1b_2r_{12} & ... & b_1b_Nr_{1N} \\ ... & ... & ... & ... & ... \\ r_Nb_N & b_1b_Nr_{1N} & ... & ... & b_N^2 \end{pmatrix}$$

has to be greater than or equal to zero (as before, we have left out the $\vec{k}$-dependence of the bias parameter in the notation).

For three random fields (or two galaxy populations plus the dark matter field), this statement is equivalent to

$$2r_1r_2r_{12} \geq r_1^2 + r_2^2 + r_{12}^2 - 1\ , \tag{2.37}$$

if the definitions of $\mathbf{C}$, r_1, r_2, r_{12} are used (calculation not shown here). It holds for all scales and the large-scale parameter considered in particular. Going back to the example above, it follows immediately from this equation that if we fix two of the three correlation coefficients with one, say $r_1 = r_2 = 1$, the third automatically is also forced to be one. Even more general, if only one of the correlations is set to one, say r_1, then the other two have to be equal, since we are told by the above constraint that

$$(r_2 - r_{12})^2 \leq 0\ . \tag{2.38}$$

Already for four random fields (or three galaxy populations plus the dark matter field) this condition of positive semi-definiteness becomes rather lengthy:

$$\begin{aligned} & r_1^2r_{23}^2 + r_2^2r_{13}^2 + r_3^2r_{12}^2 + \\ & 2[r_1r_2r_{12} + r_1r_3r_{13} + r_2r_3r_{23} + r_{12}r_{13}r_{23} - \\ & r_1r_2r_{13}r_{23} - r_1r_3r_{12}r_{23} - r_2r_3r_{12}r_{13}] \\ & \geq r_1^2 + r_2^2 + r_3^2 + r_{12}^2 + r_{13}^2 + r_{23}^2 - 1\ . \end{aligned} \tag{2.39}$$

By setting all correlations with the third population to zero ($r_3 = r_{13} = r_{23} = 0$), one can see that this reduces to the forgoing inequality (2.37). Thus, the constraint for three galaxy populations is a more general expression that simplifies to the condition for two populations if one of the three galaxy populations is not all correlated to the two others and the dark matter; it is in a statistical sense disconnected from the others.

2.3. Galaxy-number conserving bias evolution

With no interaction present, $\Phi_i = 0$, the number of galaxies is conserved. Such models are treated in the second section of TP98. Fig. 2.1 shows a diagram similar to the one in their paper: it can be seen that an initially biased galaxy distribution is more and more relaxing towards the dark matter distribution, asymptotically closing in to $r = 1$ and $b = 1$ ("debiasing"). That this is indeed a stationary state, *i.e.* $\frac{\partial b_i}{\partial t} = \frac{\partial r_i}{\partial t} = 0$, can be seen from Eqs. (2.30) and (2.32) for which the only stationary solutions are $b_i = r_i = \pm 1$ (without interaction, hence $I_i^1 = I_i^2 = 0$).

The second solution with $b_i = r_i = -1$ has to be excluded, because the bias factor is by definition always positive. The only possible way to be attracted by this stationary point is that we have $r_i = -1$ at all time. For all other values $r_i > -1$, the correlation parameter is an increasing function with time, inevitably approaching the other stationary solution. This peculiarity is therefore avoided if we exclude $r_i = -1$ as initial condition.

The bias *between* two galaxy populations also has a stationary solution at $b_{ij} = b_i/b_j = r_{ij} = 1$. This follows from Eqs. (2.31) and (2.33) ($I_i^2 = I_{ij}^3 = 0$). Fig. 2.2 shows as an illustration the evolution of the relative bias between two galaxy populations while they are getting debiased with respect to the dark matter.

2.4. Toy models not conserving galaxy number

In this section, we present a few examples to illustrate the impact on the evolution of the linear bias parameters of interactions that destroy or produce galaxies. These include the bias of each galaxy population with respect to both the dark matter and all other populations. For predicting the bias evolution on large scales, we incorporate the model Eqs. (2.30) to (2.34).

2.4.1. Modelling galaxy interactions

Linear and quadratic interaction terms

To be specific about the interaction term in Eq. (2.4), we make the following *Ansatz* for Φ_i, namely a series expansion in n_i and $\rho_{\rm m}$ up to second order:

$$\Phi_i = A_i + B_i^r n_r + \hat{C}_i \rho_{\rm m} + D_i^{rs} n_r n_s + \hat{E}_i \rho_{\rm m}^2 + \hat{F}_i^r \rho_{\rm m} n_r \; . \tag{2.40}$$

A_i, B_i^r, $\hat{C}_i$, D_i^{rs}, $\hat{E}_i$ and $\hat{F}_i^r$ are phenomenological coupling constants. Note that we are using the Einstein summing convention that abbreviates *e.g.* the expression $\sum_{rs} D_i^{rs} n_r n_s$ through $D_i^{rs} n_r n_s$. As before, we skip the position arguments of the density fields.

This particular Φ_i is motivated by the idea that locally the galaxy density may be changed –apart from converging or diverging bulk flows– by galaxy collisions or mergers with interaction

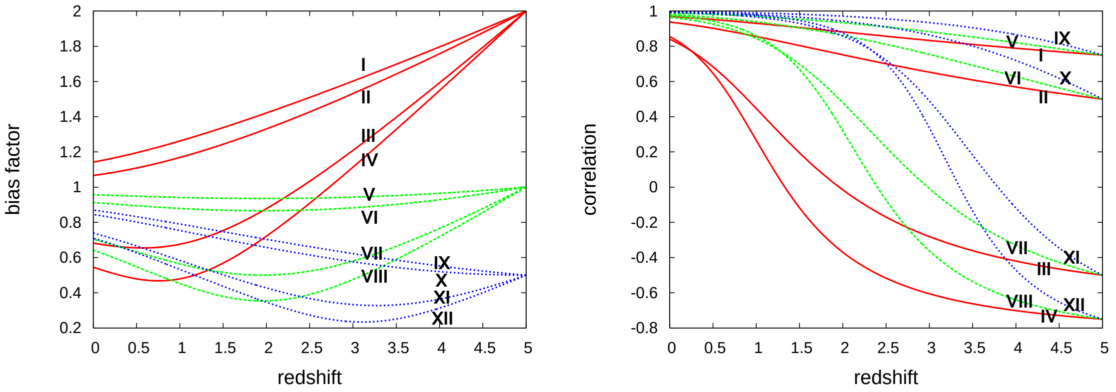

Figure 2.1.: *Evolution of the linear bias with no coupling between the galaxy species or to the dark matter present; the number of galaxies is hence conserved. One curve from the right and one curve from the left panel always belong together for one plotted model, twelve models are presented (roman numbers). The left panel shows the bias* b *evolving for three quadruples of models from the initial values* $b = 2, 1, 0.5$ *at redshift* $z = 5$ *to* $z = 0$*; the curves of each quadruple belong to initially (from upper to lower):* $r = 0.75, 0.5, -0.5, -0.75$*. In the right panel we depict the corresponding correlation parameter.*

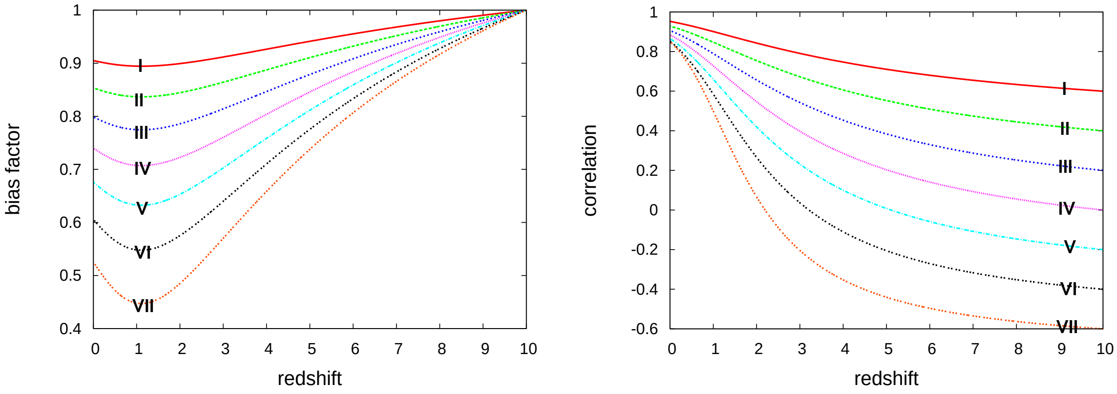

Figure 2.2.: *Evolution of the relative linear bias between two galaxy species, both starting off at* $z = 10$ *with* $b_1 = b_2 = 4$*. The correlation of one species to the dark matter is always* $r_1 = 1$*, whereas the second species has* $r_2 = 0.6, 0.4, 0.2, 0.0, -0.2, -0.4, -0.6$ *for the curves in the left panel (upper to lower). The initial correlations* between *the galaxies where chosen to be* $r_{12} = 0.6, 0.4, 0.2, 0.0, -0.2, -0.4, -0.6$*. The left panel plots the evolution of* b_{12}*, the right panel* r_{12}*, same roman numbers correspond to one model. No coupling is present, hence the galaxy number is conserved.*

rates proportional to the product of the density fields involved (D_i^{rs}, $\hat{E}_i$ and $\hat{F}_i^r$). In addition, we also include all lower-order terms, like, for instance, a constant rate of galaxy production A_i or a rate that is linear with some density field (B_i^r and $\hat{C}_i$). As the non-linear, quadratic couplings linear couplings may also have a physical interpretation in this context: a galaxy of one population is with a constant probability –independent of its environment– transformed into a member of another population (passive evolution).

Interaction correlators

Actually needed inside Eqs. (2.30) to (2.34) are, however, not the Φ_i but the interaction terms in Eqs. (2.35). Those are mainly functions of the *interaction correlators* $\langle\tilde{\Phi}_i\tilde{\delta}_j^*\rangle'$ and $\langle\tilde{\Phi}_i\tilde{\delta}_{\rm m}^*\rangle'$ whose evaluation can be found in Appendix B.3.

Number density evolution

We have to evaluate the interaction rate per unit volume in Eq. (2.34), too:

$$\begin{aligned}\langle\Phi_i\rangle &= A_i + C_i + E_i + \left(B_i^r + F_i^r\right)\bar{n}_r + D_i^{rs}\bar{n}_r\bar{n}_s \\ &+ D_i^{rs}\bar{n}_r\bar{n}_s\left\langle\delta_r\delta_s\right\rangle + E_i\left\langle\delta_{\rm m}^2\right\rangle + F_i^r\bar{n}_r\left\langle\delta_{\rm m}\delta_r\right\rangle\ ,\end{aligned} \tag{2.41}$$

where the mean dark matter density $\bar{\rho}_{\rm m}$ has been absorbed inside the coupling constants (Appendix B.3). Note that the density contrasts here are in real space. For linear couplings only, $D_i^{rs} = E_i = F_i^r = 0$, the evolution of the mean volume density of galaxies is apparently independent from the way the galaxies are clustered, because then Eq. (2.34) only depends on $\bar{n}_i$. Quadratic couplings, however, introduce terms like $\langle\delta_i\delta_j\rangle$, so that the mean density evolution gets linked to the correlations between δ_i and $\delta_{\rm m}$, and the fluctuations of these fields. The meaning of this is, that under quadratic couplings the mean density of highly clustered galaxies evolves in a different way than a completely homogeneous galaxy field.

To develop the last equation a bit further, we now would like to express the (real space) fluctuations/correlations $\langle\delta_i\delta_j\rangle$ and $\langle\delta_{\rm m}\delta_j\rangle$ in terms of linear bias parameters and the dark matter density fluctuations $\left\langle\delta_{\rm m}^2\right\rangle$ only. Expanding the correlator $\langle\delta_i\delta_j\rangle$ in Fourier space employing Eqs. (1.54) gives

$$\langle\delta_i\delta_j\rangle = \frac{1}{2\pi^2}\int {\rm d}k\ k^2\left|\tilde{W}\left(k\right)\right|^2 b_i\left(k\right)b_j\left(k\right)r_{ij}\left(k\right)P_{\rm m}\left(k\right) = \widehat{b_ib_jr_{ij}}\ \left\langle\delta_{\rm m}^2\right\rangle\ , \tag{2.42}$$

with

$$\left\langle\delta_{\rm m}^2\right\rangle = \frac{1}{2\pi^2}\int {\rm d}k\ w\left(k\right)\ , \tag{2.43}$$

and using the definitions

$$\widehat{b_ib_jr_{ij}} \equiv \frac{\int {\rm d}k\ w\left(k\right)b_i\left(k\right)b_j\left(k\right)r_{ij}\left(k\right)}{\int {\rm d}k\ w\left(k\right)}\ , \tag{2.44}$$

$$w\left(k\right) \equiv k^2\left|\tilde{W}\left(k\right)\right|^2 P_{\rm m}\left(k\right)\ . \tag{2.45}$$

We have introduced a *window function* $\tilde{W}\left(k\right)$ to account for the fact that the density fields δ_i and $\delta_{\rm m}$ entering the interaction rate Φ_i as quadratic coupling terms in general may be

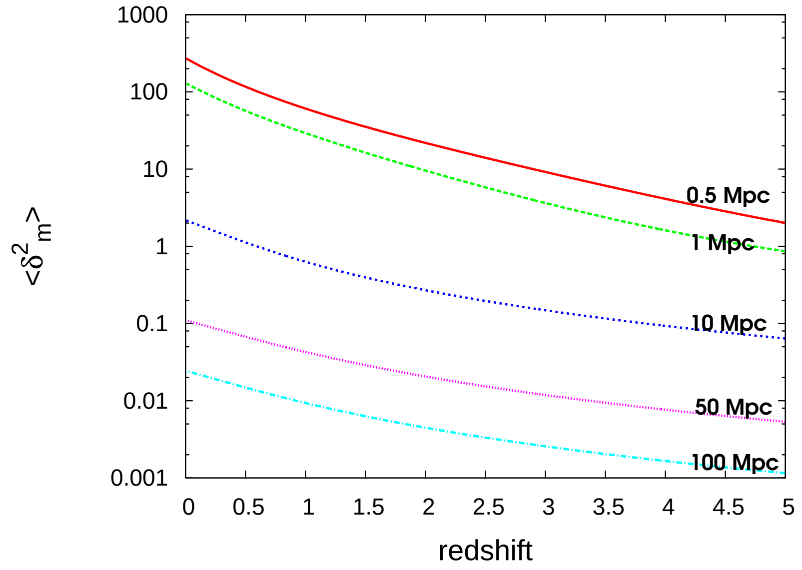

Figure 2.3.: *Estimated fluctuations $\langle\delta^2_m\rangle$, Eq. (2.43), of the dark matter density field seen through differently sized windows (comoving) using the PD96 prescription for the non-linear clustering regime; see Sect. 2.4 for cosmological parameters.*

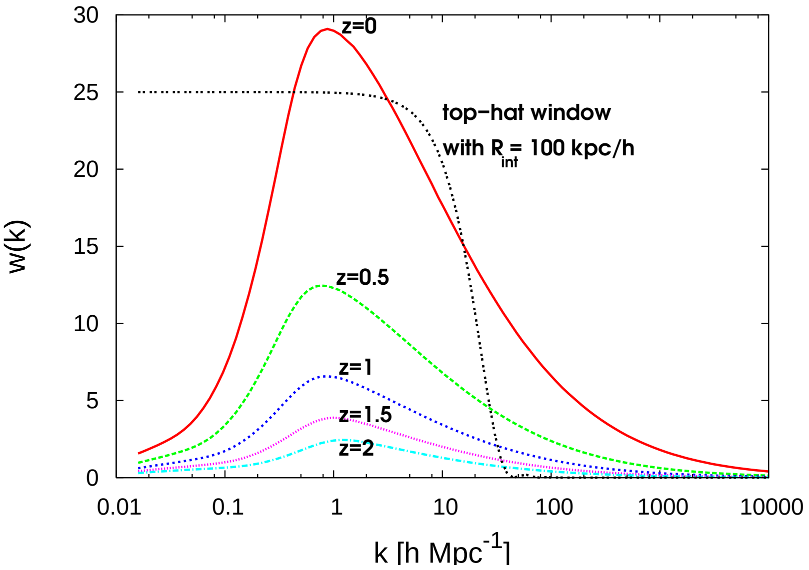

Figure 2.4.: *Weighting factors $w(k)$ (in arbitrary units, see Eq. 2.45) for different redshifts, the window $\tilde{W}(k)$ was set to one. The weight maximum stays roughly at the same scale in the plotted redshift interval; the peak is quite broad however. Also plotted here is the window function $|\tilde{W}(k)|^2$ (not normalised) of a top-hat $W(r)$ with $R_{\rm int} = 100\,h^{-1}{\rm kpc}$ which would cut-off the weights beyond $k_{\rm int}/2\pi = 10\,h{\rm Mpc}^{-1}$. See Sect. 2.4 for cosmological parameters; the PD96 prescription was used for non-linear regime.*

smoothed with some kernel $W(r)$. It is, for instance, plausible that fluctuations of the fields much smaller than the typical size of a galaxy are not relevant for galaxy interactions, although mathematically the density fields may have an infinite resolution. In that particular case, $W(r)$ could be modelled as a top hat of some typical width $R_{\rm int}$ with the following $\tilde{W}(k)$

$$\tilde{W}(y) = \frac{3}{y^3}(\sin y - y\cos y) \ , \tag{2.46}$$

where $y \equiv kR_{\rm int}$ (*e.g.* Peacock 2001, page 500).

The expression $\widehat{b_i b_j r_{ij}}$ is the weighted mean of $b_i(k)\, b_j(k)\, r_{ij}(k)$ over all scales. Fig. 2.4 shows for $\tilde{W}(k) = 1$ the weights $w(k)$ for some redshifts and one particular cosmological model. In the plotted redshift range, the weight peaks at about $1\, h^{-1}$Mpc, but has a considerable width though. In an analogue manner, we obtain

$$\langle \delta_i \delta_{\rm m} \rangle = \widehat{b_i r_i}\ \langle \delta_{\rm m}^2 \rangle\,;\ \ \widehat{b_i r_i} \equiv \frac{\int {\rm d}k\ w(k)\, b_i(k)\, r_i(k)}{\int {\rm d}k\ w(k)} \ . \tag{2.47}$$

Eq. (2.41) hence can be written as

$$\begin{aligned} \langle \Phi_i \rangle &= A_i + C_i + E_i + B_i^r \bar{n}_r \\ &+ D_i^{rs}\left[1 + \widehat{b_r b_s r_{rs}}\,\langle \delta_{\rm m}^2 \rangle\right]\bar{n}_r \bar{n}_s \\ &+ F_i^s\left[1 + \widehat{b_s r_s}\,\langle \delta_{\rm m}^2 \rangle\right]\bar{n}_s + E_i\,\langle \delta_{\rm m}^2 \rangle \ . \end{aligned} \tag{2.48}$$

Interaction terms for bias evolution

Table 2.1 summarises the final result for I_i^0, I_i^2, I_{ij}^3 and $\langle \Phi_i \rangle$ as list of contributions stemming from the various linear and quadratic interaction terms in (2.40). As both the interaction terms and the mean galaxy interaction rate are linear in Φ_i, all different coupling contributions of interest are simply added in order to obtain the final terms.

To give an example, assume that the change of number of galaxies n_1 and n_2 depends linearly on both n_1 and n_2. These are interactions of the B_i^j-type. In our notation, (b_1, r_1), (b_2, r_2) and (b_{12}, r_{12}) are the linear bias parameters of population n_1 with respect to the dark matter, of population n_2 with respect to the dark matter and of population n_1 with respect to population n_2 respectively. According to Table 2.1, the interaction terms are explicitly (after some algebra using $r_{11} = r_{22} = 1$ and $r_{12} = r_{21}$):

$$\begin{aligned} I_1^0 &= B_1^1\ b_1 + \frac{\bar{n}_2}{\bar{n}_1} B_1^2\ r_{12} b_2; & I_2^0 &= B_2^2\ b_2 + \frac{\bar{n}_1}{\bar{n}_2} B_2^1\ r_{12} b_1 \\ I_1^2 &= B_1^2\ \frac{\bar{n}_2 b_2}{\bar{n}_1 b_1}(r_2 - r_1 r_{12})\,; & I_2^2 &= B_2^1\ \frac{\bar{n}_1 b_1}{\bar{n}_2 b_2}(r_1 - r_2 r_{12}) \\ I_{12}^3 &= B_1^2\ \frac{\bar{n}_2 b_2}{\bar{n}_1 b_1}\left(1 - r_{12}^2\right); & I_{21}^3 &= B_2^1\ \frac{\bar{n}_1 b_1}{\bar{n}_2 b_2}\left(1 - r_{12}^2\right) \\ I_{11}^3 &= 0; & I_{22}^3 &= 0 \\ \langle \Phi_1 \rangle &= B_1^1 \bar{n}_1 + B_1^2 \bar{n}_2; & \langle \Phi_2 \rangle &= B_2^2 \bar{n}_2 + B_2^1 \bar{n}_1\ . \end{aligned}$$

Table 2.1.: *Three tables listing the contributions of the different couplings in Sect. 2.4.1 to the interaction terms* I_i^0, I_i^2, I_{ij}^3 *and the mean interaction rate* $\langle\Phi_i\rangle$ *sorted by the coupling constants; they are required by Eqs. (2.30) to (2.34).* A_i *corresponds to a constant galaxy production/destruction,* B_i^l *couples galaxy field* n_l *to* n_i *(linear),* C_i n_i *to the dark matter field* $\rho_{\rm m}$ *(linear),* D_i^{ls} *couples* n_l *and* n_s *to* n_i *(quadratic),* E_i *couples* $\rho_{\rm m}^2$ *to* n_i *(quadratic), and* F_i^l *couples* n_l *to* n_i *and the dark matter field* $\rho_{\rm m}$ *(quadratic). The whole expression contributing is the product between the coupling constant, first column, and the expression in the second column or third column. Different contributions from different couplings are just added; we are using Einstein's summation convention for the variables* l *and* s*. Note that we have the special case* $r_{ii} \equiv 1$ *by definition of the correlation parameter. The bias parameters* $\widehat{b_i r_i}$ *and* $\widehat{b_j b_j r_{ij}}$*, and* $\langle\delta_{\rm m}^2\rangle$ *are explained in Sect. 2.4.1. They are only needed for modelling the mean galaxy density in the presence of quadratic couplings.*

term	$\mathbf{I_i^0}$	$\langle\mathbf{\Phi_i}\rangle$
$\mathbf{A_i}$	0	1
$\mathbf{B_i^l}$	$\frac{\bar{n}_l}{\bar{n}_i} r_{il} b_l$	$\bar{n}_l$
$\mathbf{C_i}$	$\frac{1}{\bar{n}_i} r_i$	1
$\mathbf{D_i^{ls}}$	$\frac{\bar{n}_l \bar{n}_s}{\bar{n}_i} \times$ $(r_{li} b_l + r_{si} b_s)$	$\bar{n}_l \bar{n}_s \times$ $\left(1 + \widehat{b_l b_s r_{ls}} \left\langle\delta_{\rm m}^2\right\rangle\right)$
$\mathbf{E_i}$	$\frac{2}{\bar{n}_i} r_i$	$1 + \left\langle\delta_m^2\right\rangle$
$\mathbf{F_i^l}$	$\frac{\bar{n}_l}{\bar{n}_i} (r_i + r_{li} b_l)$	$\bar{n}_l \left(1 + \widehat{b_l r_l} \left\langle\delta_{\rm m}^2\right\rangle\right)$

term	$\mathbf{I_i^2}$
$\mathbf{A_i}$	0
$\mathbf{B_i^l}$	$\frac{\bar{n}_l}{\bar{n}_i} \frac{b_l}{b_i} (r_l - r_i r_{li})$
$\mathbf{C_i}$	$\frac{1}{\bar{n}_i} \frac{1}{b_i} \left(1 - r_i^2\right)$
$\mathbf{D_i^{ls}}$	$\frac{\bar{n}_l \bar{n}_s}{\bar{n}_i} \frac{1}{b_i} \times$ $([r_l - r_{li} r_i]\, b_r + [r_s - r_{si} r_i]\, b_s)$
$\mathbf{E_i}$	$\frac{2}{\bar{n}_i} \frac{1}{b_i} \left(1 - r_i^2\right)$
$\mathbf{F_i^l}$	$\frac{\bar{n}_l}{\bar{n}_i} \frac{1}{b_i} (1 - r_i + [r_l - r_{li}]\, b_l)$

term	$\mathbf{I_{ij}^3}$
$\mathbf{A_i}$	0
$\mathbf{B_i^l}$	$\frac{\bar{n}_l}{\bar{n}_i} \frac{b_l}{b_i} (r_{lj} - r_{li} r_{ij})$
$\mathbf{C_i}$	$\frac{1}{\bar{n}_i} \frac{1}{b_i} (r_j - r_i r_{ij})$
$\mathbf{D_i^{ls}}$	$\frac{\bar{n}_l \bar{n}_s}{\bar{n}_i} \frac{1}{b_i} \times$ $([r_{lj} - r_{ij} r_{li}]\, b_l + [r_{sj} - r_{ij} r_{si}]\, b_s)$
$\mathbf{E_i}$	$\frac{2}{\bar{n}_i} \frac{1}{b_i} (r_j - r_i r_{ij})$
$\mathbf{F_i^l}$	$\frac{\bar{n}_l}{\bar{n}_i} \frac{1}{b_i} ([r_{lj} - r_{li} r_{ij}]\, b_l + r_j - r_i r_{ij})$

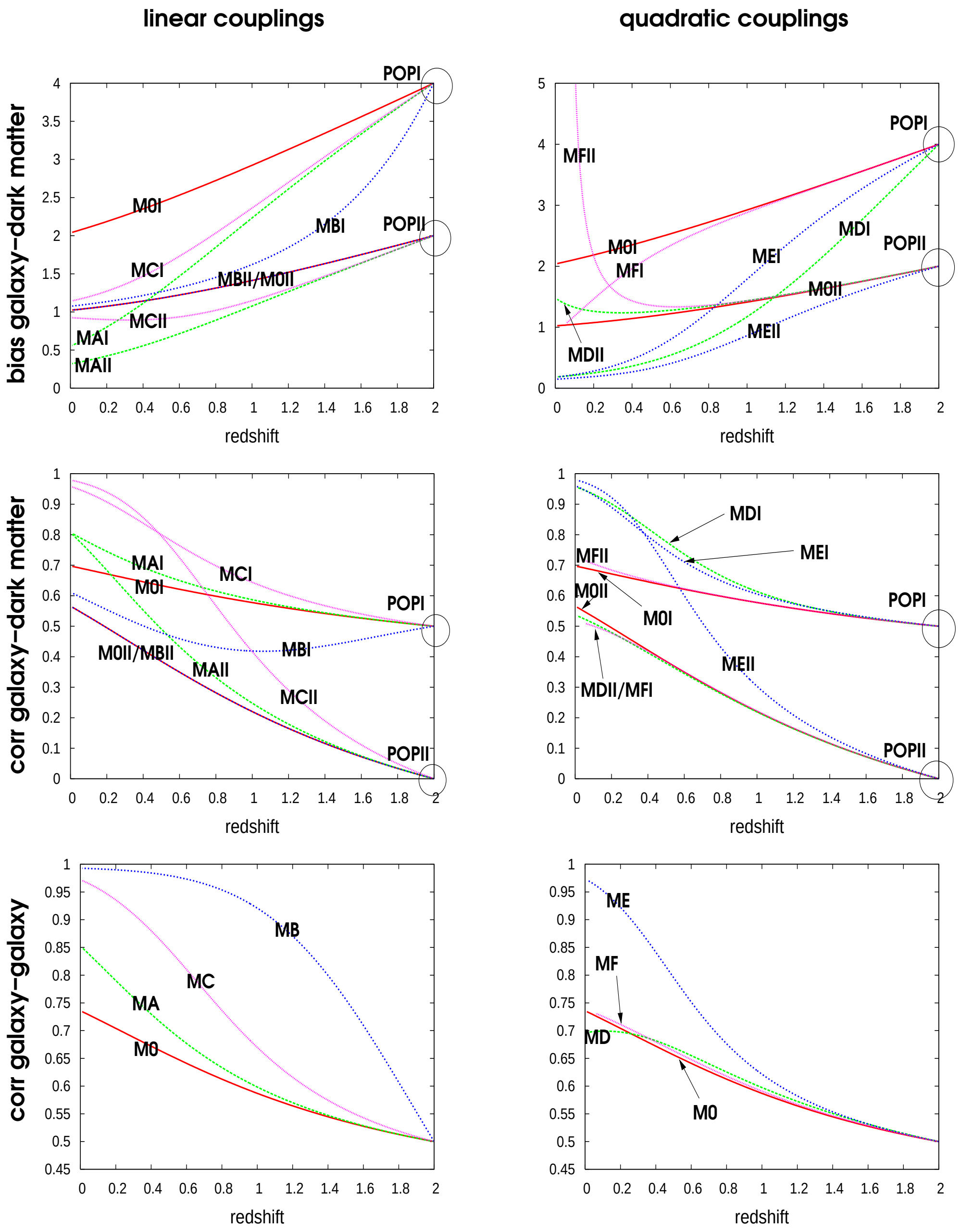

Figure 2.5.: *Example evolutionary tracks of two galaxy populations POPI and POPII subject to different interactions. All scenarios share same initial conditions at* $z = 2$ *(POPI:* $b_I = 4$*,* $r_I = 0.5$*; POPII:* $b_{II} = 2$*,* $r_{II} = 0$*;* $r_{I/II} = 0.5$*). Depicted are as a function of redshift (upper to lower row): bias factors* b_I *and* b_{II} *with respect to dark matter, correlations* r_I *and* r_{II} *to the dark matter field, and correlation* $r_{I/II}$ *between the two galaxy fields (see Sect. 2.4.2 for details)*

left column (linear couplings): *(arbitrary units)* ***M0****: interaction free case;* ***MA****: constant creation of galaxies with* $A_I = A_{II} = 10$*;* ***MB****: POPII galaxies being transformed to POPI galaxies with* $B_I^{II} = -B_{II}^{II} = 10$*;* ***MC****: linear coupling of both POPI and POPII to dark matter field with* $C_I = C_{II} = 10$

right column (quadratic couplings): *(arbitrary units)* ***M0****: interaction free evolution;* ***MD****: "colliding" POPII galaxies are transfered to POPI with* $D_I^{II\ II} = -D_{II}^{II\ II} = 10^{-4}$*;* ***ME****: both populations are coupled to* ρ_m^2 *with* $E_I = E_{II} = 1$*;* ***MF****: POPI galaxies are produced by* $\Phi_I \propto \mathrm{n}_{II}\rho_m$ *as much as POPII galaxies are destroyed,* $F_I^{II} = -F_{II}^{II} = 0.1$*.*

2.4.2. Models with linear and quadratic couplings

Owing to the large number of free parameters and ways to combine them, there are many models to look at in Eq. (2.40). To explore some of them, we focus on two galaxy populations and "switch on" only one parameter out of $A_i - F_i^j$ while setting the others to zero. This allows us to look at the effect of the coupling parameters separately. For the discussion of these toy models see Sect. 2.5.

The evolution is plotted in redshift. Therefore, we have to transform derivatives which are with respect to cosmic time t:

$$\frac{\partial}{\partial t} = \frac{\partial a}{\partial t}\frac{\partial}{\partial a} = aH(a)\frac{\partial}{\partial a} = \frac{\partial a}{\partial t}\frac{\partial z}{\partial a}\frac{\partial}{\partial z} = \left.\frac{H\left(a\right)}{a}\right|_{a=(1+z)^{-1}}\frac{\partial}{\partial z}\,. \tag{2.49}$$

The dark matter growth rate defined in Eq. (2.26) is accordingly as function of redshift

$$R\left(z\right) = R\left(t\right)|_{t=t(z)} = 2\left.\left[aH\left(a\right)\frac{\partial \ln D_+}{\partial a}\right]\right|_{a=(1+z)^{-1}} \tag{2.50}$$

which then may be evaluated using Eqs. (1.27); the Hubble parameter, $H\left(a\right)$, is defined in Eq. (1.11).[3]

It may be useful to have these expressions for a simple cosmology, like for the Einstein-de Sitter Universe for which $D_+ = a$ and $H\left(a\right) = H_0 a^{-3/2}$ ($a \equiv 1$ at $z = 0$):

$$\left.\begin{array}{rcl} R\left(z\right) & = & +2H_0\left(1+z\right)^{3/2} \\ \frac{\partial}{\partial t} & = & -H_0\left(1+z\right)^{5/2}\frac{\partial}{\partial z} \end{array}\right\}\text{Einstein} - \text{de Sitter}\,. \tag{2.51}$$

Our cosmology in the examples stated here is a ΛCDM model with $\Omega_{\rm m} = 0.3$, $\Omega_\Lambda = 0.7$, $\mathrm{H}_0 = 70\ \mathrm{km\,s^{-1}Mpc^{-1}}$. Furthermore, a scale-invariant, $n = 1$, Harrison-Zel'dovich spectrum for the primordial fluctuations is assumed. For the 3D power spectrum of the matter fluctuations we use the fitting formula of Bardeen *et al.* (1986) for the transfer function, and the Peacock & Dodds (1996), hereafter PD96, prescription for the evolution in the non-linear regime. The power spectrum normalisation is parameterised with $\sigma_8 = 0.9$ and the shape parameter is assumed to be $\Gamma = 0.21$ (the 3D matter fluctuations spectrum is needed for the quadratic coupling models only).

Linear couplings

We first focus on the linear couplings by the A_i, B_i^j and C_i interaction terms. For these three scenarios (MA, MB and MC respectively), we plot in Fig. 2.5 the evolutionary tracks of the linear bias of two different galaxy populations.

The first population, hereafter POPI, has initially at redshift $z = 2$ a bias factor $b_I = 4$ and correlation $r_I = 0.5$ with respect to the dark matter. The second population, hereafter POPII, has $b_{II} = 2$ and $r_{II} = 0$ at $z = 2$; it is thus initially not correlated to the dark matter. The relative correlation between POPI and POPII we set to $r_{I/II} = 0.5$, well below the maximum

---

[3] An excellent approximation is $R(t) = 2H(a)\frac{\partial \ln D_+}{\partial \ln a} \approx 2H(a)f(\Omega_{\rm m},\Omega_\Lambda)$ with $f(\Omega_{\rm m},\Omega_\Lambda) = \Omega_{\rm m}^{0.6} + \frac{\Omega_\Lambda}{20}(1+\frac{\Omega_{\rm m}}{2})$ (Peebles 1980).

possible value of $r_{I/II} = 0.87$ (according to Eq. 2.37). The number density (not plotted) of galaxies is not constant due to the interaction.

For the scenario MB, we assume that POPI is coupled to POPII such that galaxies are transfered from POPII to POPI, $B_{II}^{II} < 0$ and $B_{I}^{II} > 0$, keeping the overall galaxy number unchanged, thus $B_{I}^{II} = -B_{II}^{II}$. Moreover, for that particular scenario we set the initial number of POPII galaxies so that $\bar{n}_{II} = 10\bar{n}_{I}$. In all other scenarios we used $\bar{n}_{I} = \bar{n}_{II}$. Everywhere we use $\bar{\mathrm{n}}_I = 1$ in arbitrary units.

Quadratic couplings

For the toy models in this section, we assume that the bias parameters are scale-independent, so that $\widehat{b_i b_j r_{ij}} = b_i b_j r_{ij}$ and $\widehat{b_j r_{ij}} = b_j r_{ij}$, where $(b_i, b_{ij}, r_i, r_{ij})$ are the large-scale bias parameter as described in Sect. 2.2.4. Furthermore, we model the window $\tilde{W}(k)$ (see Sect. 2.4.1) as a constant function with a cutoff beyond a typical interaction scale $k_{\rm int} = 2\pi/R_{\rm int}$, here chosen to be $R_{\rm int} = 1$ Mpc. We use the PD96 approximation for the non-linear evolution of the dark matter power spectrum to estimate

$$\left\langle \delta_m^2 \right\rangle = \frac{1}{2\pi^2} \int_0^{k_{\rm int}} \mathrm{d}k\, k^2\, P_{\rm m}(k) \ . \tag{2.52}$$

Fig. 2.3 shows the estimates for different scales.

Fig. 2.5 shows examples of non-linear (quadratic) couplings as conveyed by the interaction terms D_i^{rs}, E_i and F_i^r. These interactions lead to the scenarios MD, ME and MF respectively. Again, as in the foregoing section, we have two galaxy populations POPI and POPII with the aforementioned initial conditions for biasing. For the mean galaxy density we set $\bar{n}_{II} = 100\,\bar{\mathrm{n}}_I$, except for ME where we assumed the same initial density for both populations.

As before, we do not plot the evolution of the number densities. MD couples POPI to POPII such that galaxies are added to POPI by "collisions" of POPII galaxies, while the same amount of galaxies is taken from POPII ($D_I^{II\,II} = -D_{II}^{II\,II}$, all others are zero). MF transfers galaxies from POPII to POPI by a quadratic coupling of the dark matter and POPII density field, hence creating new POPI galaxies everywhere where the density of both the dark matter and POPII galaxies is high. Here, we also adjust the coupling constants F_i^j such that the overall galaxy density remains constant ($F_I^{II} = -F_{II}^{II}$).

2.5. Discussion and conclusions

Taking the hypothesis for granted that the bulk flow of galaxies is identical to the bulk flow of the dark matter field, we derive a set of differential equations that describe on linear scales the evolution of the two-point correlations between different galaxy populations and the dark matter density field in terms of correlation power spectra (Eqs. 2.27, 2.28 and 2.7). Incorporated into this model is an "interaction" Φ_i that allows for the destruction or creation of galaxies; the term interaction is used equivalently to a local change of the galaxy number density. It may have explicit time dependence.

The model is valid only on scales where three-point correlations of all cosmological fields (density and velocity fields) are negligible. This is fulfilled on large scales where the fields are Gaussian due to the initial conditions of structure formation at high redshifts (as seen in the

CMB) and due to the fact that the field evolution is essentially linear on large scales. On small scales, this assumption is definitely wrong, because gravitational instability has been destroying Gaussianity proceeding gradually from smallest to larger scales. The present stage of structure formation in the local Universe is such that this transition form linear to non-linear scales occurs at about $10h^{-1}$Mpc; at earlier times, this scale was smaller. A linear model based on the bulk-flow hypothesis is a good approximation, even on mildly non-linear scales, as has been pointed at by Blanton *et al.* (2000) for the galaxy-number conserved case.

We closely study an interaction rate Φ_i that is a local function of the (smoothed) dark matter density field and the galaxy number density fields up to second order; within the model, the choice of the interaction is completely free though. With this interaction, we introduce the coupling constants A_i, B_i^r, C_i, D_i^{rs}, E_i and F_i^r (see Eq. 2.40). Generally, this interaction term may be pictured as the series expansion of some complicated interaction $\Phi_i\left(\mathrm{n}_j,\rho_\mathrm{m}\right)$ up to second order. Nevertheless, some of the terms associated with the coupling constants taken alone bear a simple interpretation. D_i^{rs} may be used to describe interaction rates of galaxy-galaxy collisions or mergers. Merging is an important process in the currently favoured ΛCDM Universe (*e.g.* Lacey & Cole 1993). Linear couplings between the galaxy fields, B_i^r, have a physical analogue as well: they describe processes that transfer a certain fraction of one galaxy population to another population per volume and time, making the local creation/destruction rate of galaxies proportional to the local density of the other population (passive evolution). A constant production/destruction rate of galaxies, A_i, is just a special case as it acts like a linear coupling to a completely homogeneous field of galaxies.

The second-order couplings between dark matter and galaxy fields, E_i and F_i^r, and the linear coupling between dark matter and galaxies, C_i, may be used, for instance, to describe formation processes that directly require the presence of dark matter overdensities, albeit the interpretation of these terms alone is less clear. At least, one can say that linear couplings to the dark matter field produce galaxies that are not biased with respect to the dark matter, while a quadratic coupling makes relatively more galaxies in overdensity regions.

General descriptions of a local stochastic bias like the one from Dekel & Lahav (1999) are based on the joint PDF of the (smoothed) density contrasts of the considered fields. Therefore – whatever the defined bias parameters may look like– they have to be functions of the cumulants $\langle\delta_{i_1}^{n_1}\ldots\delta_{i_N}^{n_N}\rangle_c$ of this PDF, so that these are the basic quantities that should be examined. Due to the Gaussianity of the fields on linear scales only the second-order cumulants are non-vanishing and hence only the linear stochastic bias parameters in (1.54) are relevant; the first-order cumulants vanish according to the definition of the density contrasts. Their evolution is described by means of Eqs. (2.30) to (2.34); Table 2.1 lists the interaction terms based on the interaction correlators for the second-order power series expansion of Φ_i. Our model distinguishes between the linear bias (b_i, r_i) of a galaxy population with respect to the dark matter field and the linear bias (b_{ij}, r_{ij}) between two galaxy populations. The bias factor "b" can be pictured as the ratio of the clustering strengths of the two fields, whereas the correlation parameter "r" measures how strongly the peaks and valleys of the density fields coincide. Note, however, that also a possible non-linearity in the relation between δ_i and δ_j affects the bias parameters (Dekel & Lahav 1999). On the large smoothing scales considered in this chapter this is negligible though.

For all fields perfectly correlated to the dark matter field, thus $r_i = r_{ij} = 1$, the interaction terms I_i^2 and I_{ij}^3 always vanish and therefore all correlations (r_i, r_{ij}) are "frozen in" according to Eqs. (2.32) and (2.33). In that case, the model reduces basically to Eq. (2.30) and (2.34)

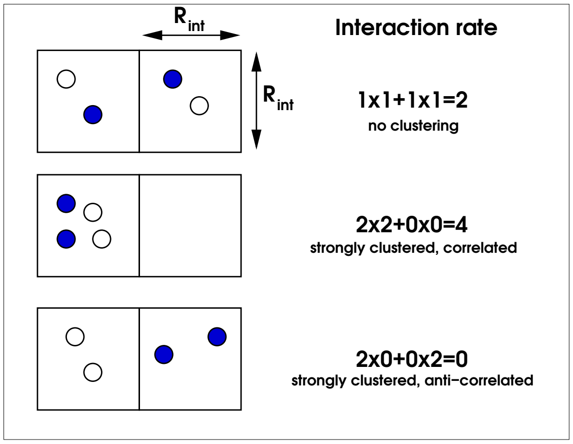

Figure 2.6.: *Sketch illustrating the effect of clustering and correlation on the mean interaction rate* $\langle\Phi\rangle$*, thus mean density evolution for quadratic couplings ("collisions")* $\Phi_{12} \propto n_1 n_2$ *between bright and dark particles. The space is divided into two cells only whose size corresponds to some typical interaction distance* $R_{\rm int}$*; interactions take place between particles within the same cell. From top to bottom: homogeneous distribution, strong clustering and high correlation between particles, strong clustering and high anti-correlation between particles. Strong clustering and high correlation obviously results in the highest interaction rate and hence influences the mean density evolution the most.*

with all correlations set to one ($b_{ij} = b_i/b_j$):

$$\frac{\partial b_i}{\partial t} = R\,(t)\,\frac{1-b_i}{2} + I^1_i\big|_{r_i=r_{ij}=1} \ . \tag{2.53}$$

The bias b_i is then called *deterministic*, since there is no randomness in the relationship of the local density contrasts. For highly correlated fields, this can be a good approximation.

With no interaction present (Sect. 2.3), we obtain as TP98 and others a debiasing of an initially biased galaxy field; this makes the galaxy distribution looking more and more like the distribution of the underlying dark matter distribution (Fig. 2.1). The bias factor $b_i > 1$ of a galaxy population that is less correlated to the dark matter field declines faster than a more correlated population (Fig. 2.2). The figure also demonstrates that differently correlated galaxy populations can temporarily evolve a relative bias factor $b_{ij} \neq 1$ with respect to each other even though they may have had $b_{ij} = 1$ at some time and they are not interacting. Moreover, characteristic for an only slightly correlated population, $r_i < 1$, is an "overshoot" that makes the population anti-biased, *i.e.* $b_i < 1$, after some time. Later on, the bias factor increases again thereby producing a relative minimum in b_i. This minimum is clearly seen in Fig. 2.2; according to Eq. (2.30) it has to occur at the time where $r_i = b_i$, because $\frac{\partial b_i}{\partial t}$ vanishes there. On the other hand, this means that a possible local minimum of b_i always has to be smaller than one since $r_i \leq 1$. In the absence of any interaction, the relative correlation is a monotonic, always increasing function; this is due to the RHS of Eq. (2.32) which always has a positive sign as long as $R\,(t) > 0$.

A few examples for linear couplings are plotted in Fig. 2.5. A linear coupling of a field "II" to a field "I" via $\Phi_I \propto n_{II}$ has the effect that the field of *newly formed or recently destroyed galaxies* type "I", $\mathrm{d}n_I = \Phi_I \mathrm{d}t$, has the same bias than the field of the galaxies "II". In case of the formation of galaxies "I" (positive sign in Φ_I), this enriches the population "I" with new galaxies having the same correlations as the galaxies in field “II”. Therefore, the bias factor between “I” and “II” is being reduced while their correlation is being increased. A positive linear coupling to the dark matter field hence debiases a galaxy field quicker than without interaction (like the populations POPI and POPII in scenario MC). The linear coupling of POPII to POPI literally “drags” the population POPI towards POPII as can be seen in MBI, while POPII (MBII), even though loosing galaxies, shows the same behaviour as without interaction in M0II; this is because it is linearly coupled to itself. The interaction A_i creates or destroys galaxies (depending on the sign) with the same rate everywhere; this can be pictured as a linear coupling to an absolutely homogeneous, fluctuation free field, having $b = 0$ with respect to any other field. I_i^0 for B_i^j in Table 2.1 indeed reduces up to a everywhere constant to the I_i^0 for A_i, if we set $b_j = 0$. It is therefore not surprising that a constant production of galaxies pulls the bias towards zero (see MAI and MAII), more and more suppressing the density fluctuations.

In conclusion, a linear coupling of a field “II” to field “I” only influences the bias evolution of “I” if “II” is biased with regard to “I”. In particular, a new population “I” being created solely from a linear coupling to some other population “II” can never become biased with respect to “II”. Early-type galaxies that may be formed from spiral galaxies can therefore not be produced by a linear coupling to the spiral galaxy field if they are biased with respect to spirals as observations imply (Norberg *et al.* 2002). The fact that values for $\beta = \Omega_{\rm m}^{0.6}/b$ derived from the IRAS (preferentially spiral galaxies) and the ORS (optically selected galaxies) are consistent if a relative bias of $b_{\rm ORS}/b_{\rm IRAS} = 1.4$ is assumed (Baker *et al.* 1998), also implies a bias between spirals and ellipticals on large scales. If this is the case then following the above arguments, ellipticals cannot simply be passively evolved spirals.

Quadratic interactions, physically interpreted as collisions or mergers, could do the job however. The reason is that the field of newly formed or recently destroyed galaxies of type “I”, coupled quadratically to “II” is proportional to n_{II}^2. These galaxies have therefore the bias factor of n_{II}^2, which in general is different from the bias factor of “II”; in fact, the density contrast $\delta_{\rm new}$ of the *newly formed galaxies type “I”* is then

$$\delta_{\rm new} = \frac{n_{II}^2}{\left\langle n_{II}^2 \right\rangle} - 1 = \frac{2\delta_{II} + \delta_{II}^2 - \left\langle \delta_{II}^2 \right\rangle}{1 + \left\langle \delta_{II}^2 \right\rangle} \; . \tag{2.54}$$

Smoothing $\delta_{\rm new}$ out to sufficiently large scales gives

$$\delta_{\rm new} \approx \frac{2\delta_{II}}{1 + \left\langle \delta_{II}^2 \right\rangle} \; , \tag{2.55}$$

because δ_{II}^2 smoothed on large scales is approximately $\left\langle \delta_{II}^2 \right\rangle$ due to the ergodicity of the random field. Small fluctuations $\left\langle \delta_{II}^2 \right\rangle \ll 1$ make the newly formed galaxies biased with a bias factor of about $b_{\rm new} \approx 2$ since $1 + \left\langle \delta_{\rm II}^2 \right\rangle \approx 1$ and $\delta_{\rm new} \approx 2\delta_{\rm II}$. Intriguingly, this is roughly the relative bias factor between early- and late-type galaxies found (see references in Sect. 5.4.5). For non-negligible fluctuations, on the other hand, this bias is roughly $b_{\rm new} = 2/\left(1 + \left\langle \delta_{\rm II}^2 \right\rangle\right)$, thus taking a value between 0 and 2. This particular example, as a side remark, demonstrates nicely that interactions on very small scales can have an impact on the large-scale bias. As an example, see Fig. 2.7. Here we have a hypothetical population of galaxies (POPI) unbiased with respect to another population (POPII). Collisions of POPII galaxies add galaxies to POPI which then become biased or anti-biased depending on whether $\left\langle \delta_{\rm II}^2 \right\rangle \ll 1$ (scenario MX) or $\left\langle \delta_{\rm II}^2 \right\rangle \gg 1$ (scenario MY).

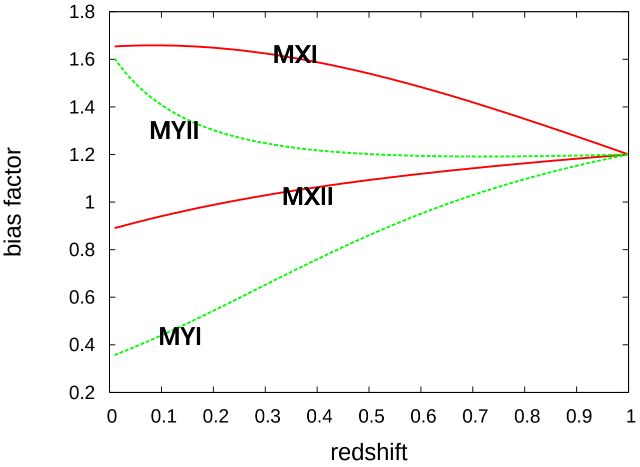

Figure 2.7.: *Evolutionary tracks of the bias factor with respect to the dark matter of two galaxy populations POPI and POPII for two scenarios MX and MY (initially at* $z = 1$*: deterministic bias* $b_I = b_{II} = 1.2$*,* $\bar{n}_I = 1$ *and* $\bar{n}_{II} = 10^{-1}$*). Both scenarios assume that collisions of POPII galaxies create POPI with* $D_I^{II\ II} = -D_{II}^{II\ II} \equiv D$*; colliding galaxies are removed.* ***MX****: sets* $\left\langle \delta_{\rm m}^2 \right\rangle = 0$ *or equivalently* $\widehat{b_I b_{II} r_{I/II}} = 0$ *and* $D = 0.1$*;* ***MY****: sets* $\left\langle \delta_{\rm m}^2 \right\rangle$ *according to Fig. 2.3 with* $\mathrm{R}_{\rm int} = 1$*Mpc and* $D = 0.01$ *in order to have roughly the same evolution of* $\bar{n}_I$ *and* $\bar{n}_{II}$ *as MX.*

Quadratic interactions present a challenging problem to the model since one has to know the fluctuations of the density fields on small scales, or equivalently (see Eq. 2.42) the dispersion of the dark matter $\left\langle \delta_{\rm m}^2 \right\rangle$, the linear bias parameters $\hat{b} \equiv (\widehat{b_i b_j r_{ij}}, \widehat{b_i r_j})$ and a window function $W(r)$; the linear bias parameters $\hat{b}$ are the weighted means of the bias parameters over all scales k, or the (real space) bias parameter on a typical scale defined by $W(r)$ (like in Eq. 1.49). The window function actually *defines* what is meant by fluctuations on small scales by introducing a smoothing scale $R_{\rm int}$ of the (real space) fields entering Φ_i, like for instance n_i and n_j in $\Phi_i \propto n_i n_j$. This scale is determined by the physical process underlying the interaction and therefore lies presumably deep in the non-linear regime. Why are these additional parameters needed for quadratic couplings? This can be seen by the following argument. One could think of the whole model volume being subdivided into small cubic cells with side length $R_{\rm int}$; a cell contains $N_i = n_i R_{\rm int}^3$ "particles" of the i-th population. Roughly speaking, the model predicts the evolution of the correlations between the particle numbers N_i of cells which are far apart (large scale) and the mean number of particles $\langle N_i \rangle$ inside the cells taking into account the gravitational field of the dark matter, its increasing clustering and the background cosmology. The interaction term Φ_i changes the number of galaxies N_i inside a particular cell depending on the number of galaxies and/or dark matter mass present in the same cell by $\mathrm{d}N_i = R_{\rm int}^3 \Phi_i \mathrm{d}t$. For linear couplings $\Phi_i \propto n_j$, the size of these cells does not have an impact on $\langle \dot{N}_i \rangle$ and thus $\langle \dot{n}_i \rangle$ since $\langle \Phi_i \rangle$ depends only on the total number of particles inside all cells; hence $R_{\rm int}$ does not turn up in the model Eq. (2.34). For non-linear couplings, however, the mean interaction rate indeed depends on how the particles are distributed among the cells which is expressed by $\hat{b}$.

To be able to explore a toy model including quadratic couplings, we made the assumption that the small-scale bias parameters are identical to the bias parameters on large scales; we hence assumed no scale-dependence for the linear bias. In fact, this is not what is expected for some galaxy populations: on large scales early and late type galaxies share approximately the same distribution (more galaxies inside super-clusters, less in the voids outside), while on smaller, cluster-scales the distribution of early- and late-types decorrelate as seen in the density-morphology relation (Dressler *et al.* 1997).

The terms containing elements of $\hat{b}$ only have an impact if $\mathrm{R}_{\mathrm{int}}$ is small enough making $\left\langle\delta_{\mathrm{m}}^2\right\rangle \gtrsim 1$ (see Eq. 2.43) *and* if the correlations $\left|\widehat{b_i b_j r_{ij}}\right|$ and $\left|\widehat{b_i r_j}\right|$ are significantly different from zero. The strength of these terms can change the evolution of the linear bias completely, as can be seen in Fig. 2.7. There, galaxies of a population I (POPI) are created by the collision/merger of galaxies of another population II (POPII). The difference between the models MX and MY is that the former switches off the $\left\langle\delta_{\mathrm{m}}^2\right\rangle$ terms while the other takes them into account. Both scenarios predict the emergence of a bias of POPI relative to POPII at $z = 0$. However, in MX we finally have $b_I > b_{II}$ at $z = 0$ while in MY we have $b_I < b_{II}$. This demonstrates that for second-order interactions, the evolution of the mean densities depends strongly on the homogeneity of the "soup" of the interacting populations. The mean density of a completely homogeneous mixture of galaxies evolves slower than for a mixture of galaxies with some substructure/clustering, if the interacting populations are highly correlated (Fig. 2.6 for an illustration). Therefore, to predict the bias evolution in the context of quadratic interactions the knowledge of both $\left\langle\delta_{\mathrm{m}}^2\right\rangle$ and the small-scale bias may be crucial.

Fitting the model presented in this chapter to observed large-scale bias parameters with the intention to look for quadratic couplings states therefore a practical problem: the weighted bias $\hat{b}$ and $\left\langle\delta_{\mathrm{m}}^2\right\rangle$ are required. The weighted bias parameters $\hat{b}$, however, are beyond the scope of the model of this chapter, since the model is valid only on large scales. However, the knowledge of $\hat{b}$ is only needed for the mean density evolution (see Eq. 2.34). In practice, both the bias parameter and the galaxy number densities are, at least principally, observables. Therefore, this problem may be disarmed by directly estimating $\bar{n}_i$ and $\langle\Phi_i\rangle = \frac{\partial\bar{n}_i}{\partial t}$ through, for instance, fitting generic functions to the observed mean galaxy number density (polynomials, for example). An estimate of the number density[4], however, requires the knowledge of the galaxy luminosity function at different redshifts for every preferred galaxy population which is a formidable task –but not impossible (Bell *et al.* 2004). Measuring the scale-dependence of the bias parameters (*e.g.* Hoekstra *et al.* 2002, H02) is another option here. The bias at and about the scale of maximum weight $w(k)$ (see Eq. 2.45) could be used as an estimate for $\hat{b}$ which then is inserted as a constraint into the fitting procedure for the *large-scale bias*; $\left\langle\delta_{\mathrm{m}}^2\right\rangle$ may be predicted using the PD96 prescription along with assumptions on R_{int}.

Compared to TP98, we did not include a random component for the galaxy formation (their Sect. 2.4.1); the production/destruction of galaxies is always a deterministic function of the density fields. However, such an random element could by included by a coupling to an additional field that is only weakly or not all correlated to the dark matter field. The effect of this is that a galaxy population gets more and more polluted by newly formed galaxies that are not or only weakly correlated to the dark matter (Blanton *et al.* 2000, 1999). Thereby the relaxation to the dark matter field gets retarded or even reverted. This scenario has a physical analogy if one imagines the newly formed galaxies as a condensate from a baryonic matter

---

[4] We would like to remind the reader here that the mean densities are comoving mean densities which for number conserved populations is constant for all time.

field at places of high density but low temperature in order to meet the Jeans criterion for self-collapse (White & Frenk 1991; White & Rees 1978). At early time, these places were inside dark matter haloes; massive enough to attract the appropriate amount of baryonic matter and to let it cool efficiently, thus at positions highly correlated to the peaks of the dark matter density field. Later on, however, the intergalactic medium probably got too hot inside the haloes to form more galaxies, so that the formation of galaxies may have been shifted outside the highest density peaks. Consequently, the formation sites of later formed galaxies may have not been as much correlated to the dark matter field as the sites of the galaxies made earlier on (Blanton et al. 1999). The construction of Appendix B.4 may be used to mimic the behaviour of this baryonic field.

The practical application of this or similar models may be to work out the relation between galaxy populations in terms of fundamental coupling constants attached to the galaxies based on observations of the bias evolution. These parameters may help to disentangle the zoo of galaxy types and to reconstruct evolutionary paths. Such observations could be extracted, for instance, from weak gravitational lensing surveys (H02) or from the redshift space distortion in galaxy redshift surveys (Pen 1998). In order to recover the redshift evolution of the bias, it is however necessary to subdivide the data set into redshift bins and even further into galaxy population bins. Considering that recent works (H02) focus on the bias of the galaxies on the whole at one average redshift, it is clear that this cannot be done with currently available data.

CHAPTER 3

Studying two estimators for the linear stochastic bias

3.1. Introduction

Different techniques were used in the past to measure the galaxy bias (Sect. 1.4). A relatively new approach using weak gravitational lensing was proposed by Schneider (1998) and van Waerbeke (1998). The method exploits the fact that the biasing is reflected by the way the projected galaxy number density is related to the cosmic shear field. Particularly useful in this context is the aperture statistics that examines the galaxy number density fluctuations and the fluctuations in the cosmic shear field inside a circular aperture. With the right choice of an aperture filter, that weights the number density and shear depending on the aperture centre distance, the bias can be observed on a very narrow range of scales. By varying the aperture radius one can scan through different scales. Moreover, this method is somewhat special compared to other techniques, because a scale-dependence of bias can be inferred without knowing the fiducial cosmology (van Waerbeke 1998).

Hoekstra *et al.* (2001) applied the technique for the first time analysing the Red-Sequence Cluster Survey (RSCS) taken with the Canada-France-Hawaii Telescope. The authors used practical estimators for the aperture statistics that had been introduced by Schneider (1998). The estimates are obtained from single circular apertures placed into the data field, taking into account the positions of "foreground" galaxies and the ellipticities and positions of "background" galaxies inside the aperture; estimates from different apertures are combined to get the final estimate. In a subsequent work, Hoekstra *et al.* (2002) applied aperture statistics to the RSCS combined with the VIRMOS-DESCART survey in order to measure the linear stochastic bias of galaxies. The practical estimators of the aperture statistics they used this time, however, were different. They were transformations of two-point correlation functions of the foreground galaxy clustering, galaxy-galaxy lensing and cosmic shear. In this chapter, both estimator approaches are introduced in detail and compared with each other by applying them to Monte Carlo samples of simulated weak lensing surveys. The focus is on the questions a) how well the estimators recover the statistics in the data, b) how sensitive they are to gaps in the data field, and c) which estimator outcomes have less statistical noise. Furthermore, the simulated data is a crucial test for the computer codes that implement the estimators. The implementations are employed in the following chapters of this thesis to make measurements on real data.

For the purpose of this chapter, a generic algorithm is proposed that quickly generates mock catalogues of galaxy positions and their ellipticities based on arbitrary correlation power spectra for cosmic shear, galaxy clustering and galaxy-galaxy lensing. There is no physics in this algorithm; the physics enters with the power spectra for the cosmic shear and galaxy clustering that are fed into the algorithm. The emphasis of the mock data is on two-point statistics only.

The outline of this chapter is as follows. We start in Sect. 3.2.1 with a definition of the aperture statistics and explain in Sect. 3.2.3 how the local second-order aperture moments are related to the linear stochastic bias. In Sect. 3.2.4, two practical estimators for the second-order moments are defined and scrutinised using simulated weak lensing surveys, Sect. 3.4. The details on the Monte Carlo sampler generating the simulated data are given in Sect. 3.3.

3.2. Aperture statistics as a means of measuring galaxy bias

It was discussed in Sect. 1.5 that due to gravitational lensing inhomogeneities in the matter distribution shear the images of galaxies. Based on this effect lensing can be used to obtain information on the total matter distribution between us and a population of source galaxies, provided we are able to measure the shapes of the galaxies accurately enough. The bias in the distribution between galaxies and matter, which is mainly dark matter, can therefore be measured. For this purpose, we introduce the aperture statistics.

3.2.1. Aperture mass

In weak gravitational lensing, the convergence is a measure for the line-of-sight matter density. In order to probe the bias of galaxies as a function of smoothing scale we do not need to know the convergence field itself but the convergence field $\kappa(\vec{\theta})$ smoothed to some typical scale. The appropriate quantity for this purpose is the *aperture mass* (Schneider *et al.* 1998) defined as

$$M_{\rm ap}(\vec{\theta},\theta_{\rm ap}) \equiv \int {\rm d}^2\theta'\; U_{\theta_{\rm ap}}(|\vec{\theta}-\vec{\theta}'|)\;\kappa(\vec{\theta}')\,, \tag{3.1}$$

$$= \frac{1}{\theta_{\rm ap}^2}\int {\rm d}^2\theta'\; u\left(\frac{|\vec{\theta}'-\vec{\theta}|}{\theta_{\rm ap}}\right)\kappa(\vec{\theta}')\,, \tag{3.2}$$

where we assumed for the smoothing kernel, *i.e.* for the filter $U_{\theta_{\rm ap}}$, the following scaling behaviour

$$U_{\theta_{\rm ap}}(\phi) = \frac{1}{\theta_{\rm ap}^2}\,u\left(\frac{\phi}{\theta_{\rm ap}}\right)\,. \tag{3.3}$$

Such a functional form applies for virtually all filters considered in the literature, such as the polynomial filters of Schneider (1998) or the exponential filter of van Waerbeke (1998). The quantity $\theta_{\rm ap}$ is the aperture radius defining the filter scale. The value of the aperture mass depends on the direction $\vec{\theta}$ of the line-of-sight. It has been shown that if the filter $u(x)$ is *compensated*, $\int {\rm d}x\; x\; u(x)=0$, then the aperture mass can be determined from the shear field itself (Schneider 1996):

$$M_{\rm ap}(\vec{\theta},\theta_{\rm ap}) = \frac{1}{\theta_{\rm ap}^2}\int {\rm d}^2\theta'\; q\left(\frac{|\vec{\theta}-\vec{\theta}'|}{\theta_{\rm ap}}\right)\gamma_{\rm t}(\vec{\theta}') \tag{3.4}$$

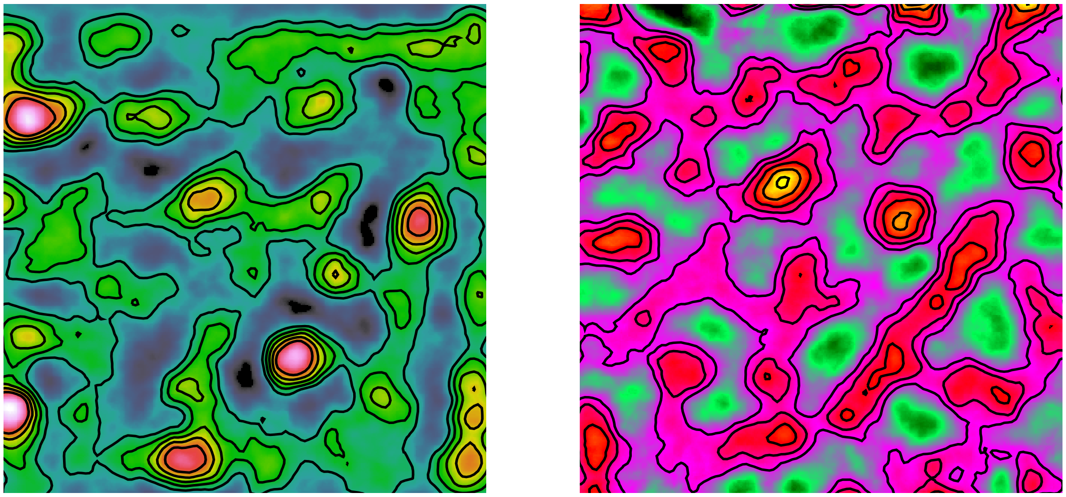

Figure 3.1.: *Aperture number count (left panel) and aperture mass map (right panel) of the A901 field in the COMBO-17 survey. Near the centre is the location of the Abell A901/A902 supercluster,* $z = 0.16$*, which is visible as a density peak in* $M_{\rm ap}$*. The angular size of the maps is* $22' \times 21'$*. The intensity levels span an interval of* $N \in [-0.3, +0.7]$ *(left) and* $M_{\rm ap} \in [-0.04, 0.04]$ *(right), the contour levels are* $\{0, 0.1, 0.2, 0.3, 0.4\}$ *(left) and* $\{0, 0.01, 0.02, 0.03, 0.04\}$ *(right). All foreground galaxies with photometric redshifts between* $0.4 \le z \le 0.6$ *(left) and background galaxies with R-band magnitude* $21.5 \le R \le 24.5$ *were chosen. The aperture filter is a polynomial filter, Eq. (3.86), the aperture radius* 3.8 *arcmin. Note that both maps are noisy.*

$$q\,(x) \;\equiv\; \frac{2}{x^2}\int_0^x {\rm d}s\, s\, u\,(s) - u\,(x)\;. \tag{3.5}$$

We use the following definitions for the tangential, $\nu_{\rm t}$, and cross component, $\nu_\times$, of a complex quantity $\nu = \nu_1 + {\rm i}\nu_2$ with respect to a centre $\vec{\theta} \equiv \theta_1 + {\rm i}\theta_2$:

$$\nu_{\rm t}(\vec{\theta}\,) \;\equiv\; -{\rm Re}\,\left(\nu\,{\rm e}^{-2{\rm i}\arg\theta}\right) = -\frac{1}{2}\left(\nu\,\frac{\vec{\theta}^{\,*}}{\vec{\theta}} + \nu^*\,\frac{\vec{\theta}}{\vec{\theta}^{\,*}}\right) \tag{3.6}$$

$$\nu_\times(\vec{\theta}\,) \;\equiv\; -{\rm Im}\,\left(\nu\,{\rm e}^{-2{\rm i}\arg\theta}\right) = -\frac{1}{2}\left(\nu\,\frac{\vec{\theta}^{\,*}}{\vec{\theta}} - \nu^*\,\frac{\vec{\theta}}{\vec{\theta}^{\,*}}\right)\;, \tag{3.7}$$

where “$\arg\theta$” is the argument of the complex number $\theta_1 + {\rm i}\theta_2$. Accordingly, $\gamma_{\rm t}(\vec{\theta}\,)$ and $\gamma_\times(\vec{\theta}\,)$ are the tangential and cross component, respectively, of the shear γ relative to the aperture centre $\vec{\theta}$.

Since the ellipticity of a galaxy in the direction $\vec{\theta}$ is, in the weak lensing regime, an unbiased estimator of the shear $\gamma(\vec{\theta}\,)$, we naturally also have an estimator $\hat{M}_{\rm ap}$ for the aperture mass that can be calculated directly from a galaxy catalogue:

$$\hat{M}_{\rm ap}(\vec{\theta},\theta_{\rm ap}) = \frac{\pi}{\sum_{i=1}^{N_{\rm b}} w_i}\sum_{i=1}^{N_{\rm b}} q\left(\frac{|\vec{\theta}_i - \vec{\theta}\,|}{\theta_{\rm ap}}\right) w_i\,\epsilon_{{\rm t},i}\;. \tag{3.8}$$

$N_{\rm b}$ is the number of source galaxies to be considered for the aperture, $\vec{\theta}_i$ the position of the i-th galaxy and $\epsilon_{{\rm t},i}$ its tangential ellipticity with respect to the aperture centre $\vec{\theta}$. The w_i

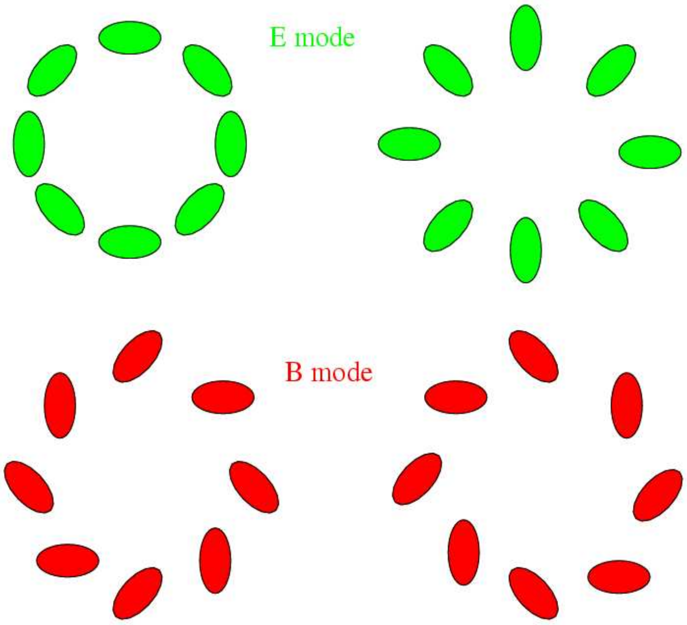

Figure 3.2.: ***top***: *Local shear patterns allowed by gravitational lensing around a matter overdensity (left) and underdensity (right).* ***bottom***: *B-mode shear patterns that are not produced by means of lensing. The figure is from van Waerbeke & Mellier (2003).*

are statistical weights of the individual galaxies which are used to account for the fact that the values of the image ellipticities, ϵ_i, of the galaxies do not have all the same confidence. Ellipticities of fainter and smaller galaxies are determined with a lower confidence than for larger and brighter galaxies. The value of $\hat{M}_{\rm ap}$ for different positions $\vec{\theta}$ can be used to make aperture mass maps, see Fig. 3.1 for an example. Such maps have been used to search for galaxy clusters or to constrain the density profiles of galaxy clusters.

E-modes and B-modes

The cosmic shear γ is related to the convergence κ by the convolution (1.74). As the shear originates from a single scalar field κ the two shear components are related to each other (*cf.* Schneider *et al.* 2002a). Therefore not all conceivable shear field configurations are allowed in gravitational lensing. The allowed configurations of γ are called E-modes, while the other independent configurations are called B-modes. For an illustration of E-mode and B-mode configurations see Fig. 3.2.[1] If we substitute the tangential component of ellipticity or shear in the foregoing and following equations by the cross components, $\epsilon_{\rm t} \leftrightarrow \epsilon_\times$ or $\gamma_{\rm t} \leftrightarrow \gamma_\times$, then we will obtain the signal originating from the B-mode component of the shear field instead of the E-mode signal, such as a B-mode aperture mass in Eq. (3.8). Ideally, in gravitational lensing applications the B-mode should vanish since lensing is only capable of producing E-modes.

---

[1] The E-mode configurations in this figure are obtained from Eq. (1.74) by assuming a convergence field that is non-zero only in one single point, $\kappa(\vec{\theta}) = \pm\delta_{\rm D}(\vec{\theta})$, where the positive and negative sign are for an overdensity and underdensity, respectively.

For that reason, a signature of B-modes can be used as a measure for the signal noise level and as an indicator for systematics in the data reduction, especially the point-spread function (PSF) correction, which has to be performed to compensate the instrumental and atmospheric influence on the galaxy image (*cf.* Kaiser *et al.* 1995). Note however, that on small scales a non-zero B-mode can be produced by intrinsic alignments of the source galaxies[2] (Heavens et al. 2000; Crittenden *et al.* 2001; Croft & Metzler 2000; Catelan *et al.* 2000) or spatial clustering of the source galaxies (Schneider *et al.* 2002a). The B-mode contamination due to the intrinsic alignments of the source galaxies is uncertain, whereas the contamination due to the source clustering is expected to become significant on scales below about $1'$.

3.2.2. Aperture number count

In a similar fashion to the aperture mass, we can define (*cf.* Schneider 1998; van Waerbeke 1998) the *aperture number count* $N(\vec{\theta},\theta_{\rm ap})$ which measures the fluctuations of the *galaxy number density* with the same filter $u(x)$ as $M_{\rm ap}$ for the convergence field,[3]

$$\begin{aligned} N(\vec{\theta},\theta_{\rm ap}) &\equiv \frac{1}{\theta_{\rm ap}^2}\int {\rm d}^2\theta'\, u\left(\frac{|\vec{\theta}-\vec{\theta}'|}{\theta_{\rm ap}}\right)\delta n(\vec{\theta}') & (3.9)\\ &= \frac{1}{\theta_{\rm ap}^2}\int {\rm d}^2\theta'\, u\left(\frac{|\vec{\theta}-\vec{\theta}'|}{\theta_{\rm ap}}\right)\frac{n_{\rm f}(\vec{\theta}')}{\bar{n}_{\rm f}}\,, & (3.10)\end{aligned}$$

where $n_{\rm f}(\vec{\theta})$ and $\bar{n}_{\rm f}$ denote the (projected) number density of galaxies in some direction $\vec{\theta}$ and the mean number density of galaxies, respectively. The quantity $\delta n = n_{\rm f}/\bar{n}_{\rm f} - 1$ is the projected number density *contrast* of the galaxies. As the number of galaxies inside an angular area is an estimate for $n_{\rm f}$ we can write down an unbiased estimator of the aperture number count based on galaxy positions (Schneider 1998):

$$\hat{N}(\vec{\theta},\theta_{\rm ap}) = \frac{\pi}{\bar{N}_{\rm f}}\sum_{i=1}^{N_{\rm f}} u\left(\frac{|\vec{\theta}_i-\vec{\theta}|}{\theta_{\rm ap}}\right)\,, \tag{3.11}$$

where $\vec{\theta}_i$ are the positions of the galaxies having to be considered for the aperture number counts map.[4] The number $\bar{N}_f = \pi\theta_{\rm ap}^2\bar{n}_{\rm f}$ is the average number of galaxies inside the aperture. See Fig. 3.1 for an example of an aperture number count map.

[2] By intrinsic alignments one means non-vanishing correlations between the intrinsic ellipticities, $\epsilon_{\rm s}$, of different source galaxies, thus $\langle\epsilon_{\rm s}^{(1)}\epsilon_{\rm s}^{(2)}\rangle \neq 0$. Intrinsic alignments are expected for physically close galaxies, hence for galaxies that have essentially identical redshifts.

[3] We have used $\int {\rm d}^2\theta'\, u(|\vec{\theta}'|) = 2\pi\int {\rm d}\theta'\,\theta'\,u(\theta') = 0$ since $u(x)$ is compensated.

[4] It is also possible to define an aperture number count estimator that weighs galaxies as the estimator for the aperture mass (3.8) does:

$$\hat{N}(\vec{\theta},\theta_{\rm ap}) = \frac{\pi}{\sum_{i=1}^{N_{\rm f}} w_i}\sum_{i=1}^{N_{\rm f}} u\left(\frac{|\vec{\theta}_i-\vec{\theta}|}{\theta_{\rm ap}}\right) w_i\,, \tag{3.12}$$

where w_i are the statistical weights for the galaxy positions $\vec{\theta}_i$. A nice application of this is to choose for w_i the luminosities of the individual galaxies. Thereby $\hat{N}$ can be used to map the luminosity distribution of a galaxy sample. However, note that the estimator (3.12) is different from (3.11)

Usually, the galaxies probed with $N(\vec{\theta}, \theta_{\rm ap})$ and those galaxies used to construct $M_{\rm ap}(\vec{\theta}, \theta_{\rm ap})$ maps are different; the $M_{\rm ap}$-galaxies tend to be more in the background as their purpose is to probe the matter field the N-galaxies are located in. For that reason, we call the N-galaxies *foreground galaxies* and the $M_{\rm ap}$-galaxies *background galaxies*.

3.2.3. Linear stochastic bias using aperture statistics

To summarise, the aperture mass $M_{\rm ap}$, Eq. (3.4), is proportional to the (weighted) projected total matter density contrast $\delta_{\rm m}$, whereas N, Eq. (3.9), is proportional to the number density contrast of the galaxy distribution δn. Both aperture measures are defined on some scale by the filter function $u\,(x)$ and the aperture size $\theta_{\rm ap}$. This is exactly what we need to study the biasing of the galaxy distribution with respect to the matter distribution, as has been pointed out by Schneider (1998) and van Waerbeke (1998). Therefore we can define biasing parameters in analogy to Eqs. (1.49) (Hoekstra *et al.* 2002)

$$
\begin{aligned}
b\,(\theta_{\rm ap}) &= f_1\,(\theta_{\rm ap})\sqrt{\frac{\langle N^2\,(\theta_{\rm ap})\rangle}{\langle M^2_{\rm ap}\,(\theta_{\rm ap})\rangle}} \qquad (3.13)\\
r\,(\theta_{\rm ap}) &= f_2\,(\theta_{\rm ap})\frac{\langle N\,(\theta_{\rm ap})\,M_{\rm ap}\,(\theta_{\rm ap})\rangle}{\sqrt{\langle N^2\,(\theta_{\rm ap})\rangle\,\langle M^2_{\rm ap}\,(\theta_{\rm ap})\rangle}}\ .
\end{aligned}
$$

In practice, the ensemble average $\langle ... \rangle$ has to be understood as the average of all aperture positions $\vec{\theta}$ (fair sample hypothesis). The factors f_1 and f_2 are needed for calibration because the three-dimensional number density that N is sensitive to covers in general not the same volume that is probed by $M_{\rm ap}$. The calibration is discussed in more detail in Sect. 4.3.2 where we apply these statistics to real data.

3.2.4. Practical estimators for the second-order aperture statistics

To determine the linear stochastic bias parameters in practice, we require estimators for the second-order moments $\langle N^n\,(\theta_{\rm ap})\,M^m\,(\theta_{\rm ap})\rangle$ with $n+m=2$. From the statistical point of view, the moments are fluctuations, for $m,n=2$, and correlation, for $n=m=1$, of smoothed random fields. They are therefore auto- and cross-correlation power spectra seen through a filter $[I\,(x)]^2$ (Hoekstra *et al.* 2002)

$$
\begin{aligned}
\langle M^2_{\rm ap}\,(\theta_{\rm ap})\rangle &= 2\pi\int_0^\infty {\rm d}s\,s\,P_\kappa\,(s)\,[I\,(s\theta_{\rm ap})]^2 \qquad (3.14)\\
\langle N\,(\theta_{\rm ap})\,M_{\rm ap}\,(\theta_{\rm ap})\rangle &= 2\pi\int_0^\infty {\rm d}s\,s\,P_{{\rm n}\kappa}\,(s)\,[I\,(s\theta_{\rm ap})]^2\\
\langle N^2\,(\theta_{\rm ap})\rangle &= 2\pi\int_0^\infty {\rm d}s\;s\;P_{\rm n}\,(s)\,[I\,(s\theta_{\rm ap})]^2\\
I\,(x) &\equiv \int_0^\infty {\rm d}y\,y\,u\,(y)\,J_0\,(y\,x)\ ,
\end{aligned}
$$

which implicitly weighs all galaxies with $w_i=1$. The subtle difference between the estimators is that (3.12) estimates $\bar{N}_{\rm f}$ by the actual number of galaxies inside the aperture, $N_{\rm f}$, which only on average is identical with $\bar{N}_{\rm f}=\langle N_{\rm f}\rangle$. This can be seen by setting $w_i=1$ in (3.12).

where P_κ, $P_{\kappa\mathrm{n}}$ and P_n are the convergence auto-correlation, convergence/galaxy number density contrast cross-correlation and the galaxy number contrast auto-correlation power spectrum, respectively. Analytical expressions for these power spectra are given in Sect. 3.3.3. The function $J_n(x)$ denotes the n-th order Bessel function of the first kind.

There are two principle ways to estimate the second-order moments: either by placing apertures at different positions into the field (Hoekstra *et al.* 2001), or indirectly by estimating and transforming the two-point correlation function of the galaxy number density, cosmic shear and their cross-correlation (Hoekstra *et al.* 2002). We are going to present both approaches in the following.

Placing apertures into the field

In the first approach, apertures at all positions $\vec{\theta}$ in the field-of-view of a survey are estimates of the moments of the local joint PDF of N and M_ap. As estimators of the second-order moments one can use the following:[5]

$$\widehat{M^2_\mathrm{ap}}(\vec{\theta},\theta_\mathrm{ap}) = \frac{\pi^2}{N_\mathrm{b}\,(N_\mathrm{b}-1)}\sum_{j\neq i}^{N_\mathrm{b}} q_i q_j\,\epsilon_{\mathrm{t},i}\,\epsilon_{\mathrm{t},j} \tag{3.15}$$

$$\widehat{NM}_\mathrm{ap}(\vec{\theta},\theta_\mathrm{ap}) = \frac{\pi^2}{N_\mathrm{b}\bar{N}_\mathrm{f}}\sum_{i}^{N_\mathrm{b}}\sum_{j}^{N_\mathrm{f}} q_i u_j\,\epsilon_{\mathrm{t},i} \tag{3.16}$$

$$\widehat{N}^2(\vec{\theta},\theta_\mathrm{ap}) = \frac{\pi^2}{\bar{N}^2_\mathrm{f}}\sum_{i\neq j}^{N_\mathrm{f}} u_i u_j\ , \tag{3.17}$$

where $\widehat{M^2_\mathrm{ap}}$ is discussed in Schneider *et al.* (1998), whereas the two other estimators are defined in analogy to $\widehat{M^2_\mathrm{ap}}$ (Hoekstra *et al.* 2001). The expression $\epsilon_{\mathrm{t},i}$ denotes the tangential ellipticities of the background galaxies relative to the aperture centre $\vec{\theta}$. The variables q_i and u_i are the values of the filters $u(x)$ and $q(x)$ at the galaxy positions $\vec{\theta}_i$:

$$q_i = q(|\vec{\theta}-\vec{\theta}_i|/\theta_\mathrm{ap}) \tag{3.18}$$

$$u_i = u(|\vec{\theta}-\vec{\theta}_i|/\theta_\mathrm{ap}) \tag{3.19}$$

with respect to the aperture centre $\vec{\theta}$.[6]

Each aperture placed into the field yields one moment estimate. All estimates gathered from different positions $\vec{\theta}$ are averaged to obtain the combined final result. The final result can be optimised if the average is weighted with the number of galaxies inside the apertures (Schneider *et al.* 1998).

[5] These estimators give all galaxies the same statistical weight. As they are only going to be applied to simulated data a weighting scheme is not necessary.

[6] The "size" of an aperture is defined by the smallest distance from the aperture centre at which the filters $u(x)$ and $q(x)$ either vanish or where they become sufficiently small. The polynomial filters proposed by Schneider (1996) all vanish at $x \geq 1$, so that the size of the aperture is θ_ap.

Using two-point correlators

An alternative approach described in Hoekstra *et al.* (2002) relates the second-order moments in $\left\langle N^n M_{\rm ap}^m \right\rangle$ to *two-point correlators*. These correlators are a) the spatial clustering of the foreground galaxies, $\omega\left(\theta\right)$, b) the galaxy-galaxy lensing between the foreground galaxies and the source galaxies, $\left\langle\gamma_{\rm t}\right\rangle\left(\theta\right)$, and c) the shear-shear correlations $\xi_{\pm}\left(\theta\right)$ as determined from the ellipticities of the background galaxies:

$$\begin{aligned}
\omega\left(\theta\right) &= \left\langle \delta n\left(\theta+x\right)\delta n\left(x\right)\right\rangle = \int_0^\infty \frac{{\rm d}s\; s}{2\pi} P_{\rm n}\left(s\right) J_0\left(s\theta\right), \qquad (3.20)\\
\left\langle\gamma_{\rm t}\right\rangle\left(\theta\right) &= \left\langle \delta n\left(\theta+x\right)\gamma_{\rm t}\left(\theta\right)\right\rangle = \int_0^\infty \frac{{\rm d}s\; s}{2\pi} P_{\kappa{\rm n}}\left(s\right) J_2\left(s\theta\right),\\
\xi_{\pm}\left(\theta\right) &= \left\langle \gamma_{\rm t}\left(\theta+x\right)\gamma_{\rm t}\left(\theta\right)\right\rangle \pm \left\langle \gamma_{\times}\left(\theta+x\right)\gamma_{\times}\left(\theta\right)\right\rangle = \int_0^\infty \frac{{\rm d}s\; s}{2\pi} P_{\kappa}\left(s\right) J_{0,4}\left(s\theta\right)\ .
\end{aligned}$$

The correlator $\omega(\theta)$ is a measure for the probability of finding a galaxy in a distance θ from another galaxy. The galaxy-galaxy lensing, $\langle\gamma_{\rm t}\rangle$, is the mean tangential shear around a foreground galaxy at a distance θ, and the two-point shear-shear correlations, $\xi_{\pm}$, quantify the correlations of the cross- and tangential shear components relative to the line connecting two background galaxies with a angular distance θ.

The relations between the correlators and the power spectra (3.20) can be inverted with respect to the power spectra due to the closure relation of the Bessel functions J_n:

$$\int_0^\infty {\rm d}x\, x\, J_n(ux)\, J_n(vx) = \frac{1}{u}\delta_{\rm D}(u-v)\ , \qquad (3.21)$$

which holds for $n > -1/2$. The resulting expressions for the power spectra inserted into the Eqs. (3.14) yield the second-order aperture moments in terms of the two-point correlators:

$$\begin{aligned}
\left\langle M_{\rm ap}^2\left(\theta_{\rm ap}\right)\right\rangle &= \frac{1}{2}\int_0^\infty {\rm d}x\ x\ \left[\xi_+\left(x\theta_{\rm ap}\right)T_+\left(x\right) + \xi_-\left(x\theta_{\rm ap}\right)T_-\left(x\right)\right], \qquad (3.22)\\
\left\langle N\left(\theta_{\rm ap}\right)M_{\rm ap}\left(\theta_{\rm ap}\right)\right\rangle &= \int_0^\infty {\rm d}x\ x\ \left\langle\gamma_{\rm t}\right\rangle\left(x\theta_{\rm ap}\right)F\left(x\right), \qquad (3.23)\\
\left\langle N^2\left(\theta_{\rm ap}\right)\right\rangle &= \int_0^\infty {\rm d}x\ x\ \omega\left(x\theta_{\rm ap}\right)T_+\left(x\right), \qquad (3.24)
\end{aligned}$$

where we introduced the auxiliary functions

$$\begin{aligned}
T_{\pm}\left(x\right) &\equiv \left(2\pi\right)^2\int_0^\infty {\rm d}s\ s\ \left[{\rm I}\left({\rm s}\right)\right]^2 J_{0,4}\left(sx\right), \qquad (3.25)\\
F\left(x\right) &\equiv \left(2\pi\right)^2\int_0^\infty {\rm d}s\ s\ \left[{\rm I}\left({\rm s}\right)\right]^2 J_2\left(sx\right), \qquad (3.26)\\
{\rm I}\left(x\right) &\equiv \int_0^\infty {\rm d}s\, s\, u\left(s\right) J_0\left(sx\right)\ . \qquad (3.27)
\end{aligned}$$

In practice, the correlators are estimated by using

$$\hat\omega\left(\theta\right) = \frac{DD}{RR} - 2\frac{DR}{RR} + 1, \qquad (3.28)$$

$$\widehat{\langle\gamma_{\rm t}\rangle}\left(\theta\right) = \frac{\sum_{i,j}^{N_{\rm f},N_{\rm b}} \epsilon_{{\rm t},i} w_i \Delta_{ij}\left(\theta\right)}{\sum_{i,j}^{N_{\rm f},N_{\rm b}} w_i \Delta_{ij}\left(\theta\right)}, \tag{3.29}$$

$$\widehat{\xi_\pm}\left(\theta\right) = \frac{\sum_{i,j}^{N_{\rm b}} w_i w_i \Delta_{ij}\left(\theta\right)\left(\epsilon_{{\rm t},i}\epsilon_{{\rm t},j} \pm \epsilon_{\times,i}\epsilon_{\times,j}\right)}{\sum_{i,j}^{N_{\rm b}} w_i w_j \Delta_{ij}\left(\theta\right)}, \tag{3.30}$$

$$\Delta_{ij}\left(\theta\right) \equiv \left\{\begin{array}{ll} 1 & \theta \leq |\theta_i - \theta_j| < \theta + \delta\theta \\ 0 & \text{otherwise} \end{array}\right. . \tag{3.31}$$

The estimator of the spatial correlation $\hat{\omega}\left(\theta\right)$ has been introduced by Landy & Szalay (1993). It requires to count the number of galaxy pairs with a distance between θ and $\theta + \delta\theta$, namely the number of pairs in the data (foreground galaxies), denoted by DD, the number of pairs in a random mock catalogue, RR, and the number of pairs that can be formed with one data galaxy and one mock data galaxy, DR. The random mock catalogue is computed by randomly moving around the data galaxies taking into account the geometry of the data field, *i.e.* by avoiding outmasked regions. In this thesis, we make 25 random galaxy catalogues and average the pair counts obtained for DR and RR.

Concerning the estimator for mean tangential shear, $\widehat{\langle\gamma_{\rm t}\rangle}\left(\theta\right)$, all pairs between foreground and background galaxies within a distance of θ and $\theta + \delta\theta$ have to be considered; $\epsilon_{{\rm t},i}$ is the tangential ellipticity component of the background galaxy with respect to the line connecting the foreground and background galaxy. Similarly, for $\widehat{\xi_\pm}\left(\theta\right)$ all pairs of background galaxies within some distance interval are considered (*cf.* Schneider *et al.* 2002b); $\epsilon_{{\rm t},i/j}$ and $\epsilon_{\times,i/j}$ are the tangential and cross ellipticity components relative to the line connecting the pair, respectively.

3.3. Monte Carlo simulations of weak lensing surveys

After shortly reviewing in the following section how single Gaussian random fields can be simulated, we introduce in Sect. 3.3.2 a general algorithm that can be used to make realisations of a set of correlated Gaussian random fields. This algorithm is employed in Sect. 3.4 to make simulated number density and shear fields of various galaxy sets; number density and shear fields are distinct random fields. The auto- and cross-correlation power spectra of these fields needed as necessary input parameters of the algorithm are calculated in Sect. 3.3.3.

3.3.1. Realisation of a single Gaussian random field

Consider a statistically homogeneous and isotropic random Gaussian field $\delta(\mathbf{r})$. The vector $\mathbf{r}$ has n dimensions. Let us further assume that the random field is finite with "volume" V; for $n = 2$ we have a two-dimensional random field and V denotes the area of the random field. Since the field is Gaussian and homogeneous, the Fourier coefficients,

$$c(\mathbf{k}) = \int_V {\rm d}^n\mathbf{r}\;\delta\left(\mathbf{r}\right)\exp\left({\rm i}\mathbf{k}\cdot\mathbf{r}\right), \tag{3.32}$$

are only correlated as pairs (see Sect. 1.2.2)

$$\langle c(\mathbf{k})c(-\mathbf{k}')\rangle = \frac{1}{V}\delta_{\mathbf{k}\mathbf{k}'}P(\mathbf{k}), \tag{3.33}$$

where $\delta_{\mathbf{k}\mathbf{k}'}$ is the Kronecker delta and $P(\mathbf{k})$ is the *power spectrum* of the random field. All higher-order moments can be traced back to second-order correlations, or, equivalently, all connected moments vanish (Appendix A.3). In addition, the Fourier coefficients, real and imaginary part separately, are Gaussian random variables because they are linear combinations of the field variables $\delta(\mathbf{r})$. As we will see soon, this simplicity makes the realisation of a Gaussian random field relatively easy if it is done in Fourier space, *i.e.* for the coefficients $c(\mathbf{k})$. We only have to take care of the fact that the real and imaginary parts of just two Fourier coefficients are statistically correlated to each other. How does this correlation look like?

It follows for $\mathbf{k} \neq 0$ from Eq. (3.33) that $\langle c(\mathbf{k})c(\mathbf{k})\rangle = 0$, or if we split the equation into real and imaginary part

$$\langle [\mathrm{Re}\; c(\mathbf{k})]^2 \rangle = \langle [\mathrm{Im}\; c(\mathbf{k})]^2 \rangle \qquad \langle \mathrm{Re}\; c(\mathbf{k})\, \mathrm{Im}\; c(\mathbf{k}) \rangle = 0 \,. \tag{3.34}$$

This means that in a homogeneous random field, real and imaginary part of $c(\mathbf{k})$ are not correlated and both, individually, must have the same variance. Furthermore, we can deduce quite generally that for $\mathbf{k} \neq 0$

$$\begin{aligned} \langle c(\mathbf{k})c(-\mathbf{k})\rangle = \frac{P(\mathbf{k})}{V} & \qquad \Longrightarrow & \qquad (3.35)\\ \langle \mathrm{Re}\; c(\mathbf{k})\, \mathrm{Re}\; c(-\mathbf{k})\rangle = -\langle \mathrm{Im}\; c(\mathbf{k})\, \mathrm{Im}\; c(-\mathbf{k})\rangle & \quad = \quad \frac{\mathrm{Re}\;[P(\mathbf{k})]}{2V} & \qquad (3.36)\\ \langle \mathrm{Re}\; c(\mathbf{k})\, \mathrm{Im}\; c(-\mathbf{k})\rangle = +\langle \mathrm{Im}\; c(\mathbf{k})\, \mathrm{Re}\; c(-\mathbf{k})\rangle & \quad = \quad \frac{\mathrm{Im}\;[P(\mathbf{k})]}{2V}\,. & \qquad (3.37) \end{aligned}$$

This confines the correlations between all combinations of real and imaginary parts of the coefficient pair $c(\mathbf{k})$ and $c(-\mathbf{k})$. As we consider only cases in which the power spectrum is purely real, Re $P(\mathbf{k}) = P(\mathbf{k})$ and Im $P(\mathbf{k}) = 0$, the imaginary and real parts of $c(\mathbf{k})$ and $c(-\mathbf{k})$ in Eq. (3.37) are not correlated. Generally, if $\delta(\mathbf{r})$ is a complex field with unrelated real and imaginary parts this has not necessarily to be case.

The strategy for a Gaussian field realisation would be to make a random number generator that yields as output four numbers, namely the real and imaginary parts of $c(\mathbf{k})$ and $c(-\mathbf{k})$, that have as joint PDF a multivariate Gaussian with the covariance (3.34), (3.36) and (3.37). This generator would then used to obtain values –independently for different positive modes $\mathbf{k}$– for all $c(\mathbf{k})$ and $c(-\mathbf{k})$ included in the random field.

We consider a more specialised case by restricting ourselves to *real Gaussian fields* with $\delta\,(\mathbf{r}) = \delta^*\,(\mathbf{r})$. This introduces an additional condition that follows from the definition (3.32) of the $c(\mathbf{k})$:

$$c(\mathbf{k}) = c^*(-\mathbf{k}) \quad \Longleftrightarrow \quad \left\{ \begin{array}{ll} \mathrm{Re}\; c(\mathbf{k}) & = +\mathrm{Re}\; c(-\mathbf{k}) \\ \mathrm{Im}\; c(\mathbf{k}) & = -\mathrm{Im}\; c(-\mathbf{k}) \end{array} \right. \,. \tag{3.38}$$

This further simplifies the task of making a field realisation. We will only need a random number generator that makes a realisation of one single number based on a Gaussian PDF. The conditions (3.33) and (3.38) are easily accounted for if, say, only the $c(\mathbf{k})$ for half of the spatial frequencies $\mathbf{k}$ are worked out and the $c(-\mathbf{k})$ frequencies are set accordingly. Hence, for our choice, whenever we talk about $c(\mathbf{k})$ we actually mean only Fourier coefficients in the right half-plane. Furthermore, the real and imaginary parts of $c(\mathbf{k})$ are uncorrelated, and both follow the same Gaussian PDF. This PDF has zero mean[7] and a variance

$$\sigma_{\mathbf{k}}^2 = \frac{1}{2V} P(\mathbf{k}) \; , \tag{3.39}$$

according to Eq. (3.36).

The procedure for making *one* Gaussian field realisation thus requires two steps: 1. drawing numbers for the real and imaginary parts for every $c(\mathbf{k})$ with a Gaussian random number generator, and 2. transformation of this Fourier space representation to real space in order to obtain the field realisation. For the second step we used an FFT algorithm from Press *et al.* (1992).

3.3.2. Realisation of correlated Gaussian fields

The procedure of making one Gaussian random field realisation also holds when realisations of more than one, but *uncorrelated* Gaussian fields are desired. "Uncorrelated" means that if we denote the Fourier coefficients of, say, N Gaussian random fields by $c_{\mathbf{k}}^{(i)}$ with $i \in [1, N]$ then for those fields the relation

$$\left\langle c_{\mathbf{k}}^{(i)} \left[c_{\mathbf{k}'}^{(j)} \right]^* \right\rangle = \frac{1}{V} P^{(ii)}(\mathbf{k}) \delta_{ij} \delta_{\mathbf{k}\mathbf{k}'} \tag{3.40}$$

holds, where δ_{ij} is also a Kronecker symbol, this time for the Gaussian field indices. The expression $P_{\mathbf{k}}^{(ii)}$ is the previously introduced power spectrum, or *auto-correlation* power spectrum, of the i-th random field. Thus, correlations between $c(\mathbf{k})$ of different random fields vanish.

For the purposes of this work, however, we need to be able to allow for cross-correlations between different random fields $i \neq j$ in a defined manner, like

$$\left\langle c_{\mathbf{k}}^{(i)} \left[c_{\mathbf{k}'}^{(j)} \right]^* \right\rangle = \frac{1}{V} P^{(ij)}(\mathbf{k}) \delta_{\mathbf{k}\mathbf{k}'} \; . \tag{3.41}$$

The function $P^{(ij)}(\mathbf{k})$ is, for $i \neq j$, the *cross-correlation* power spectrum. Like for the auto-correlations, only certain pairs of Fourier coefficients of different Gaussian fields are correlated. This follows from the assumption that the cross-correlations are also statistically homogeneous. Note that $P^{(ij)}(\mathbf{k}) = P^{(ji)}(\mathbf{k})$.

In order to find a recipe for making realisations of that kind, we make the *Ansatz* that the N Fourier coefficients $c_{\mathbf{k}}^{(i)}$ are a *linear transformation* $\mathbf{A}_{\mathbf{k}}$ of N different uncorrelated coefficients $d_{\mathbf{k}}^{(i)}$ with an equal Gaussian PDF for the real and imaginary parts, zero mean and a $1/\sqrt{2}$ dispersion

$$\left\langle d_{\mathbf{k}}^{(i)} \left[d_{\mathbf{k}'}^{(j)} \right]^* \right\rangle = \delta_{ij} \delta_{\mathbf{k}\mathbf{k}'} \; ; \; c_{\mathbf{k}}^{(i)} = \sum_q \left[\mathbf{A}_{\mathbf{k}} \right]^i_{\;q} \; d_{\mathbf{k}}^{(q)} \; . \tag{3.42}$$

The matrix $\mathbf{A}_{\mathbf{k}}$ is a $N \times N$ linear transformation matrix. The linearity of this transformation guarantees that the resulting set of coefficients $c_{\mathbf{k}}^{(i)}$ still obeys a Gaussian statistics, because linear combinations of Gaussian random variables are also Gaussian.

Since for real Gaussian fields real and imaginary parts of the Fourier coefficients are not correlated, and by our *Ansatz* neither are the real and imaginary parts of $d_{\mathbf{k}}^{(i)}$, only real

---

[7] In the case that $\delta(\mathbf{r})$ has a non zero mean, $\langle c(\mathbf{k}) \rangle$ for $\mathbf{k} = 0$ becomes different from zero.

numbers for the components $[\mathbf{A_k}]^i{}_q$ are allowed; an additional imaginary part of $\mathbf{A_k}$ would mix real and imaginary parts of $d_{\mathbf{k}}^{(i)}$, thereby possibly introducing correlations between real and imaginary parts in $c_{\mathbf{k}}$. A matrix $\mathbf{A_k}$ that is purely imaginary would be an alternative choice, though.

Eqs. (3.42) can now be combined to give

$$\begin{aligned}
\left\langle c_{\mathbf{k}}^{(i)} \left[c_{\mathbf{k}}^{(j)}\right]^* \right\rangle &= \sum_{q,r} \left\langle [\mathbf{A_k}]^i{}_q \, d_{\mathbf{k}}^{(q)} \, [\mathbf{A_k}]^j{}_r \left[d_{\mathbf{k}}^{(r)}\right]^* \right\rangle \\
&= \sum_{q,r} [\mathbf{A_k}]^i{}_q \, [\mathbf{A_k}]^j{}_r \left\langle d_{\mathbf{k}}^{(q)} \left[d_{\mathbf{k}}^{(r)}\right]^* \right\rangle \\
&= \sum_{q,r} [\mathbf{A_k}]^i{}_q \, [\mathbf{A_k}]^j{}_r \, \delta_{qr} \\
&= \sum_{q} [\mathbf{A_k}]^i{}_q \, [\mathbf{A}^{\mathrm{t}}_{\mathbf{k}}]^q{}_j \ , \qquad (3.43)
\end{aligned}$$

where $\mathbf{A}^{\mathrm{t}}_{\mathbf{k}}$ denotes the transpose of $\mathbf{A_k}$. Hence, together with equation (3.41) this puts another constraint on the matrix $\mathbf{A_k}$, namely

$$\frac{1}{V} P^{(ij)}(\mathbf{k}) = \sum_q [\mathbf{A_k}]^i{}_q \, [\mathbf{A}^{\mathrm{t}}_{\mathbf{k}}]^q{}_j \ . \qquad (3.44)$$

For convenience we introduce the *power matrix* defined as $[\mathbf{P_k}]^i{}_j \equiv \frac{1}{V} P^{(ij)}(\mathbf{k})$ to abbreviate this equation:

$$\mathbf{P_k} = \mathbf{A_k} \mathbf{A}^{\mathrm{t}}_{\mathbf{k}} \ . \qquad (3.45)$$

The power matrix is the covariance matrix between the Fourier coefficients of a set of Gaussian fields for a certain $\mathbf{k}$.

This shorthand of N^2 equations does not uniquely determine the matrix $\mathbf{A_k}$, because it contains only $N(N+1)/2$ linearly independent equations, since both the matrix on the LHS and the matrix product on the RHS are symmetric. As there are no further constraints on $\mathbf{A_k}$, we are allowed to set the remaining $N^2 - N(N+1)/2 = N(N-1)/2$ constraints of $\mathbf{A_k}$ as we like. We do this by assuming that $\mathbf{A_k}$ is symmetric, so that we finally obtain

$$\mathbf{P_k} = \mathbf{A}^2_{\mathbf{k}} \quad \Rightarrow \quad \mathbf{A_k} = \sqrt{\mathbf{P_k}} \ . \qquad (3.46)$$

In general the square root is not unique (see *e.g.* Higham 1997). However, we are already satisfied with one particular solution to this problem. In order to determine such a solution, note that $\mathbf{P_k}$ is a symmetric positive (semi)definite matrix, which is ensured by the properties of the power spectra the power matrix consists of:

$$\begin{aligned}
P^{(ij)}(\mathbf{k}) &= P^{(ji)}(\mathbf{k}) \ , \qquad (3.47) \\
\left[P^{(ij)}(\mathbf{k})\right]^2 &\leq P^{(ii)}(\mathbf{k}) P^{(jj)}(\mathbf{k}) \ . \qquad (3.48)
\end{aligned}$$

Therefore, this matrix can uniquely be decomposed into

$$\mathbf{P_k} = \mathbf{R}^{\mathrm{t}}_{\mathbf{k}} \, \mathbf{D_k} \, \mathbf{R_k} \ , \qquad (3.49)$$

where $\mathbf{R_k}$ is an orthogonal matrix whose column vectors are the eigenvectors of $\mathbf{P_k}$, while their corresponding, real and non-negative, eigenvalues λ_i are the elements of the diagonal matrix $\mathbf{D_k} = \mathrm{diag}\left(\lambda_1, \lambda_2, ..., \lambda_\mathrm{N}\right)$. As one particular square root we pick out

$$\begin{aligned} \mathbf{A_k} &= \mathbf{R}^\mathrm{t}_\mathbf{k}\,\sqrt{\mathbf{D_k}}\,\mathbf{R_k} \\ \sqrt{\mathbf{D_k}} &\equiv \mathrm{diag}\left(\sqrt{\lambda_1}, \sqrt{\lambda_2}, ..., \sqrt{\lambda_N}\right) \end{aligned} \tag{3.50}$$

which is a solution due to $\sqrt{\mathbf{D_k}}\sqrt{\mathbf{D_k}} = \mathbf{D_k}$.

To sum up, for every $\mathbf{k}$ mode considered, the process for the realisation of correlated Gaussian random fields requires one to find the square root $\mathbf{A_k}$ of the power matrix $\mathbf{P_k}$. This defines a linear transformation for a vector of uncorrelated random complex numbers (real and imaginary part of the same coefficient are also uncorrelated) with zero mean, real and imaginary parts obeying a Gaussian PDF with variance $1/\sqrt{2}$. Applying $\mathbf{A_k}$ yields a vector of Fourier coefficients belonging to the realisations of the correlated Gaussian random fields. Due to (3.38) this is performed only for one half of the spatial frequencies considered. The other half is set accordingly to fulfil this condition.

3.3.3. Power spectra

The algorithm of the forgoing section is the backbone of the Monte Carlo method for weak lensing surveys presented in the following. In order to put this algorithm into a cosmological context, we have to specify and compute all relevant correlation power spectra which include the auto-correlation of all participating fields and the cross-correlations between them. We distinguish between two kinds of random fields: 1. the convergence (shear) fields, and 2. the galaxy number density fields. The fields will be realised on a two-dimensional grid representing the field-of-view of the survey. Different sets of galaxies are allowed. Every set of galaxies is associated with its own shear and number density field that depend on the redshift distribution of the galaxy set and their bias with respect to the dark matter and the other galaxy sets.

Galaxy - dark matter bias

The dark matter power spectrum P_dm, Sect. 1.3, is the central quantity for the Monte Carlo sampler. Any power spectrum involving galaxy number density fields is referred to P_dm in terms of the stochastic linear bias r_i, r_{ij} and b_i (Eq. 1.54):

$$P^{(i)}_\mathrm{dm,n}\left(k,w\right) = r_i\left(k,w\right)b_i\left(k,w\right)\;P_\mathrm{dm}\left(k,w\right) \tag{3.51}$$

$$P^{(ij)}_\mathrm{n}\left(k,w\right) = r_{ij}\left(k,w\right)b_i\left(k,w\right)b_j\left(k,w\right)\;P_\mathrm{dm}\left(k,w\right)\;, \tag{3.52}$$

where $P^{(i)}_\mathrm{dm,n}$ is a cross-correlation power spectrum between the galaxy number density contrast

$$\delta n_i\left(\vec{x},w\right) \equiv \frac{n_i\left(\vec{x},w\right)}{\langle n_i\rangle} - 1 \tag{3.53}$$

and the dark matter density contrast, and $P^{(ij)}_\mathrm{n}$ the correlation between the density contrasts of two galaxy number density fields.

Note that the power spectra are for three-dimensional (comoving coordinates) random fields that may have a time-dependence. The parameter w denotes the lookback time t_back in terms of the comoving distance light can travel over a time span $t_{\rm back}$. Therefore, $w=0$ is the present time.

The functions r_i and r_{ij} are correlation parameters which have values in $[-1,1]$; r_{ij} denotes the correlation between two galaxy sets, i and j, and r_i denotes the correlation between the i-th galaxy set and the dark matter field; we have $r_{ii}=1$ by definition. The bias factor b_i may assume any value greater than 0. For $r_i=b_i=1$, we call the i-th galaxy set unbiased with respect to the dark matter field.

For convenience and to save space, we will omit in the following the arguments k and w in the bias functions. By definition we demand that they have the same argument as the adjacent power spectrum. For example,

$$b_j\;P_{\rm dm}\left(\frac{\ell}{f_{\rm K}\left(w\right)},w\right)\equiv b_j\left(\frac{\ell}{f_{\rm K}\left(w\right)},w\right)\;P_{\rm dm}\left(\frac{\ell}{f_{\rm K}\left(w\right)},w\right)\;. \tag{3.54}$$

We have thus defined the three-dimensional power spectra of the galaxy and dark matter density fields. In order to simulate the angular distribution of galaxies and the weak gravitational lensing effect on the images of the galaxies –the shear– as realisations of random fields we have to project the power spectra onto the sky. This is done in the following.

Galaxy power spectra

Consider a very small volume $\Delta x\times\Delta y\times\Delta w$ of comoving space that is located at a comoving distance of w; Δw is the extent of the the volume in radial direction. If $n_i(w)$ is the comoving number density of galaxies at the position of the cube, then we observe $N=n_i(w)\Delta x\Delta y\Delta w$ galaxies inside the cube. The area of the cube seen as projection on the sky is $A=\Delta x/f_{\rm K}(w)\times\Delta y/f_{\rm K}(w)$. Therefore, the observed projected number density of galaxies inside the volume element equals approximately $\hat{n}_i(\vec{\theta})=N/A=n_i(w)[f_{\rm K}(w)]^2\Delta w$. Summing up the contributions from all cubes along the line-of-sight in direction $\vec{\theta}$ gives in the limit $\Delta w\rightarrow{\rm d}w$ a total galaxy number density of

$$\hat{n}_i(\vec{\theta})=\int_0^{w_h}{\rm d}w\,[f_{\rm K}(w)]^2\,S_i(w)\,n_i(f_{\rm K}(w)\vec{\theta},w)\;. \tag{3.55}$$

We introduced a selection function, $S_i(w)\le 1$, to account for the fact that we may not see all galaxies $n_i(w)$ from $w\in[0,w_{\rm h}]$ (incompleteness), or/and for the fact that we may select only galaxies from a certain redshift range.

The angular number density can be transformed to obtain the *density contrast*, $\delta\hat{n}_i=\hat{n}_i/\left\langle\hat{n}_i\right\rangle-1$, of the galaxy number density *on the sky* in terms of the three-dimensional, time-dependent density contrast δn_i (Eq. 3.53):

$$\delta\hat{n}_i(\vec{\theta})=\int_0^{w_h}{\rm d}w\,p_g^{(i)}(w)\,\delta n_i(f_{\rm K}(w)\vec{\theta},w)\;, \tag{3.56}$$

where we included the combined effect of the selection $S_i(w)$, the mean number of galaxies per comoving volume $\left\langle n_i\right\rangle(w)$ and the geometrical (selection) factor $[f_{\rm K}(w)]^2$ in

$$p_g^{(i)}(w)\equiv\frac{[f_{\rm K}(w)]^2\,S_i(w)\,\left\langle n_i\right\rangle(w)}{\int_0^{w_h}{\rm d}w\,[f_{\rm K}(w)]^2\,S_i(w)\,\left\langle n_i\right\rangle(w)}\;. \tag{3.57}$$

We use the function $p_g^{(i)}(w)$ for the distribution of the i-th galaxy set in comoving distance; this distribution is by definition normalised, $\int_0^{w_h} \mathrm{d}w\, p_g^{(i)}(w) = 1$, and $p_g^{(i)}(w)\mathrm{d}w$ is the probability of finding a galaxy within comoving distance w and $w + \mathrm{d}w$. The PDF $p_g^{(i)}(w)$ will be given to the algorithm as parameter.

According to Eq. (3.56) the density contrast of the galaxy number density on the sky is a projection of the three-dimensional density contrast, thus it is equivalent to Eq. (1.36) with the radial filter set to $q(w) = p_g^{(i)}(w)$. We can therefore apply Limber's equation (1.38) to obtain the auto-correlation power spectrum of the projected galaxy number density

$$\begin{aligned} P_{\mathrm{n}}^{(ii)}(\ell) &= \int \mathrm{d}w\, \frac{[p_g^{(i)}(w)]^2}{f_{\mathrm{K}}^2(w)} P_{\mathrm{n}}^{(ii)}\left(\frac{\ell}{f_{\mathrm{K}}(w)}, w\right) \\ &= \int \mathrm{d}w\, \frac{[p_g^{(i)}(w)]^2}{f_{\mathrm{K}}^2(w)}\, b_i^2\, P_{\mathrm{dm}}\left(\frac{\ell}{f_{\mathrm{K}}(w)}, w\right) . \end{aligned} \tag{3.58}$$

Likewise, also using the Limber equation, we can write the cross-correlation between the i-th and j-th galaxy set taking into account that they have different radial filters:

$$P_{\mathrm{n}}^{(ij)}(\ell) = \int \mathrm{d}w\, \frac{p_g^{(i)}(w)\, p_g^{(j)}(w)}{f_{\mathrm{K}}^2(w)}\, r_{ij} b_i b_j\, P_{\mathrm{dm}}\left(\frac{\ell}{f_{\mathrm{K}}(w)}, w\right) , \tag{3.59}$$

where the three-dimensional cross-correlation power spectrum (3.52) has been inserted. Clearly, Eq. (3.58) is a special case of Eq. (3.59) since $r_{ij} = 1$ for $i = j$.

Cosmic shear power spectra

The fluctuations in the dark matter density field imprint by means of gravitational lensing different shape distortions on the various galaxy sets. Thus, the galaxies "see" in general different convergence and shear fields, $\kappa_i(\vec{\theta})$ and $\gamma_i(\vec{\theta})$, respectively. The index i denotes the galaxy set.

The convergence and shear of the gravitational lensing are according to Eq. (1.74) related to each other by a convolution. In Fourier space, the convolution is equivalent to the multiplication with the Fourier transform of the convolution kernel:

$$\tilde{\gamma}_i(\vec{\ell}) = \frac{\ell_1^2 - \ell_2^2 + 2\mathrm{i}\ell_1\ell_2}{\ell_1^2 + \ell_2^2}\, \tilde{\kappa}_i(\vec{\ell}) \qquad \vec{\ell} \equiv \begin{pmatrix} \ell_1 \\ \ell_2 \end{pmatrix} , \tag{3.60}$$

where $\vec{\ell}$ is the Fourier mode associated with the direction $\vec{\theta}$. The functions $\tilde{\kappa}_i$ and $\tilde{\gamma}_i$ are the Fourier coefficients of the convergence and shear, respectively. As we are working in the flat-sky approximation, the vectors $\vec{\theta}$ and $\vec{\ell}$ are Cartesian vectors.

For $\vec{\ell} = \vec{0}$, the convolution kernel is not defined so that we have an additional degree of freedom between convergence and shear, called the mass-sheet degeneracy. As we exclude any external shear, our choice is $\tilde{\gamma}_i = 0$ for $\vec{\ell} = \vec{0}$. Note that the Fourier transform of the convolution kernel is a simple phase factor with modulus unity. This implies that the power spectra of the convergence and shear are identical.

In our Monte Carlo recipe, we are going to make realisations of the convergence on a grid, one field for each galaxy set, that is transformed later on to obtain the complex shear fields.

As in Eq. (1.72), the convergence exerted on the i-th galaxy population is, for a given dark matter density contrast $\delta_{\rm dm}(\vec{x}, w)$,

$$\kappa_i(\vec{\theta}) = \frac{3}{2}\frac{H_0^2}{c^2}\Omega_{\rm m}\int {\rm d}w\,\frac{\bar{W}^{(i)}(w)f_{\rm K}(w)}{a(w)}\;\delta_{\rm dm}\left(f_{\rm K}(w)\,\vec{\theta}, w\right)\;, \tag{3.61}$$
$$\bar{W}^{(i)}(w) \equiv \int {\rm d}w'\;p_g^{(i)}(w')\frac{f_{\rm K}(w'-w)}{f_{\rm K}(w')}\;.$$

In words, the convergence κ_i is the dark matter density contrast seen trough the radial filter $q(w) = \frac{3H_0^2}{2c^2}\Omega_{\rm m}\frac{\bar{W}^{(i)}(w)f_{\rm K}(w)}{a(w)}$. This, again, is a projection in the sense of Eq. (1.36) so that Limber's equation (1.38) can be employed to write down the auto-correlation of the convergence field:

$$P_\kappa^{(ii)}(\ell) = \frac{9}{4}\frac{H_0^4}{c^4}\Omega_{\rm m}^2\int {\rm d}w\;\frac{\left[\bar{W}^{(i)}(w)\right]^2}{a^2(w)}P_{\rm dm}\left(\frac{\ell}{f_{\rm K}(w)}, w\right)\;. \tag{3.62}$$

Note that even though the i-th galaxy set may be biased with respect to the dark matter density field it has no impact on the measured convergence or cosmic shear. Equivalently, we have for the cross-correlation between the different convergence fields:

$$P_\kappa^{(ij)}(\ell) = \frac{9}{4}\frac{H_0^4}{c^4}\Omega_{\rm m}^2\int {\rm d}w\;\frac{\bar{W}^{(i)}(w)\,\bar{W}^{(j)}(w)}{a^2(w)}P_{\rm dm}\left(\frac{\ell}{f_{\rm K}(w)}, w\right)\;. \tag{3.63}$$

Cosmic shear-Galaxy cross correlation

Applying for a last time the Limber equation, we also can write down the cross-correlation between the various galaxy number densities, Eq. (3.55), and the convergence, Eq. (3.61); they are projections of δn_i and $\delta_{\rm dm}$ with the radial filters $q(w) = p_g^{(i)}(w)$ and $q(w) = \frac{3H_0^2}{2c^2}\Omega_{\rm m}\frac{\bar{W}^{(i)}(w)f_{\rm K}(w)}{a(w)}$, respectively. We thereby obtain:

$$\begin{aligned} P_{{\rm n}\kappa}^{(ij)}(\ell) &= \frac{3}{2}\frac{H_0^2}{c^2}\Omega_{\rm m}\int {\rm d}w\;\frac{p_g^{(i)}(w)\bar{W}^{(j)}(w)}{a(w)f_{\rm K}(w)}\;P_{\rm dm,n}^{(i)}\left(\frac{\ell}{f_{\rm K}(w)}, w\right) \\ &= \frac{3}{2}\frac{H_0^2}{c^2}\Omega_{\rm m}\int {\rm d}w\;\frac{p_g^{(i)}(w)\bar{W}^{(j)}(w)}{a(w)f_{\rm K}(w)}\;b_i r_i\;P_{\rm dm}\left(\frac{\ell}{f_{\rm K}(w)}, w\right)\;. \end{aligned} \tag{3.64}$$

Note that this power spectrum is not symmetric in i and j. This correlation between galaxy positions (number density) and cosmic shear is called "galaxy-galaxy lensing". A non-zero $P_{{\rm n}\kappa}^{(ij)}$ requires that at least some galaxies in $p_g^{(i)}(w)$ are in front of some galaxies contained in the distribution $p_g^{(j)}(w)$, otherwise $p_g^{(i)}(w)\bar{W}^{(j)}(w) = 0$.

3.3.4. Monte Carlo sampler

We now explain in detail how the power spectra (3.59), (3.63), (3.64) and the algorithm in Sect. 3.3.2 are combined to make a mock weak lensing survey with $i \in [1, N_{\rm sets}]$ distinct sets of galaxies distributed in comoving radial distance according to $p_g^{(i)}(w)$. As additional parameters, one has to define for every galaxy set the linear stochastic bias relative to the dark matter, b_i and r_i, and the correlation r_{ij} relative to any other j-th set of galaxies. The latter only, however, if the distributions $p_g^{(i)}(w)$ and $p_g^{(j)}(w)$ overlap, otherwise their cross-correlation $P_{\rm nn}^{(ij)}$ is zero. An example of the various power spectra that need to be taken into account for two galaxy sets is plotted in Fig. 3.3.

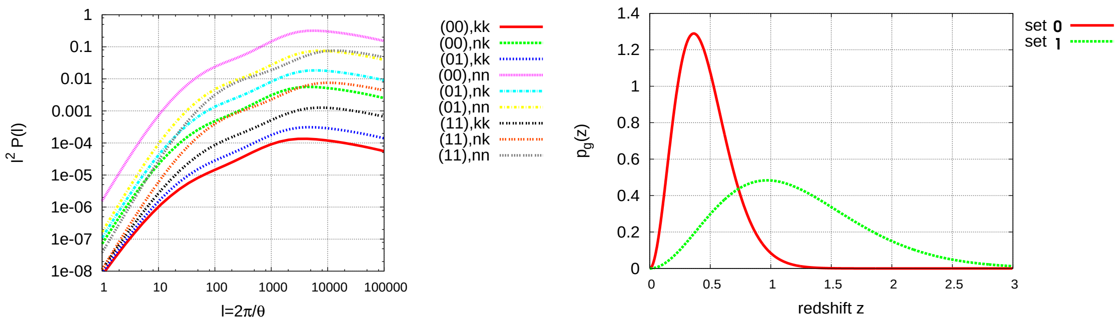

Figure 3.3.: ***left panel**: Correlation power spectra between the cosmic shear, denoted as "k" and galaxy number density fields, denoted as "n", of two galaxy sets having different distributions in redshift. "(00), kk" means $P_{\kappa\kappa}^{(00)}$, "(01), nk" means $P_{\rm nk}^{(01)}$ and so on. **right panel**: Distribution in redshift of the two galaxy sets. Both galaxy sets are assumed to be unbiased with respect to the dark matter.*

Convergence and galaxy number density contrast

A full Monte Carlo realisation requires $2 \times N_{\rm sets}$ random fields: $N_{\rm sets}$ galaxy number density contrast fields, $\delta n_i(\vec{\theta})$, plus the same number of convergence fields $\kappa_i(\vec{\theta})$. The fields are realised on a regular grid; they are two-dimensional matrices whose sizes are determined by the number of grid points $\vec{\theta}_i$. Usually, the grids have square geometry with, say, width L. Realistic parameters for the grid are 1024×1024 grid points and $L \sim 60'$.

We arrange the grid values as a $2N_{\rm sets}$-dimensional vector

$$\mathbf{R}(\vec{\theta}_i) = \Big(\kappa_1(\vec{\theta}_i), \kappa_2(\vec{\theta}_i), \dots, \kappa_{N_{\rm sets}}(\vec{\theta}_i), \delta n_1(\vec{\theta}_i), \delta n_2(\vec{\theta}_i), \dots, \delta n_{N_{\rm sets}}(\vec{\theta}_i)\Big)^{\rm t} , \tag{3.65}$$

where δn_i and κ_i are the number density contrast and convergence of the i-th galaxy set, respectively. We define the Fourier transform of $\mathbf{R}(\vec{\theta}_i)$ by

$$\tilde{\mathbf{R}}(\vec{\ell}_i) \equiv \Big(\tilde{\kappa}_1(\vec{\ell}_i), \tilde{\kappa}_2(\vec{\ell}_i), \dots, \tilde{\kappa}_{N_{\rm sets}}(\vec{\ell}_i), \delta\tilde{n}_1(\vec{\ell}_i), \delta\tilde{n}_2(\vec{\ell}_i), \dots, \delta\tilde{n}_{N_{\rm sets}}(\vec{\ell}_i)\Big)^{\rm t} , \tag{3.66}$$

meaning the vector of the separately Fourier transformed components of $\mathbf{R}(\vec{\theta}_i)$.

Now, the procedure is to browse through half of all grid points $\vec{\ell}_i$ in Fourier space and to make realisations of the vector $\tilde{\mathbf{R}}(\vec{\ell}_i)$. For this task the power matrix $\mathbf{P}(|\vec{\ell}_i|)$ is required, which is the covariance of the $\tilde{\mathbf{R}}(\vec{\ell}_i)$:

$$\mathbf{P}\left(\ell\right) = \left\langle \tilde{\mathbf{R}}^{\rm t}\left(\ell\right)\tilde{\mathbf{R}}^{*}\left(\ell\right)\right\rangle = \begin{pmatrix} \mathbf{A}_{\kappa\kappa}\left(\ell\right) & \mathbf{A}_{{\rm n}\kappa}\left(\ell\right) \\ \mathbf{A}_{{\rm n}\kappa}^{\rm t}\left(\ell\right) & \mathbf{A}_{\rm nn}\left(\ell\right) \end{pmatrix} , \tag{3.67}$$

where we used the following definitions for the sub-matrices:

$$\mathbf{A}_{\kappa\kappa}\left(\ell\right) \equiv \begin{pmatrix} P_{\kappa}^{(11)}\left(\ell\right) & \dots & P_{\kappa}^{(1N_{\rm sets})}\left(\ell\right) \\ \dots & \dots & \dots \\ P_{\kappa}^{(N_{\rm sets}1)}\left(\ell\right) & \dots & P_{\kappa}^{(N_{\rm sets}N_{\rm sets})}\left(\ell\right) \end{pmatrix} \tag{3.68}$$

$$\mathbf{A}_{\mathrm{n}\kappa}(\ell) \equiv \left(\begin{array}{ccc} P_{\mathrm{n}\kappa}^{(11)}(\ell) & \dots & P_{\mathrm{n}\kappa}^{(1N_{\mathrm{sets}})}(\ell) \\ \dots & \dots & \dots \\ P_{\mathrm{n}\kappa}^{(N_{\mathrm{sets}}1)}(\ell) & \dots & P_{\mathrm{n}\kappa}^{(N_{\mathrm{sets}}N_{\mathrm{sets}})}(\ell) \end{array}\right) \tag{3.69}$$

$$\mathbf{A}_{\mathrm{nn}}(\ell) \equiv \left(\begin{array}{ccc} P_{\mathrm{n}}^{(11)}(\ell) & \dots & P_{\mathrm{n}}^{(1N_{\mathrm{sets}})}(\ell) \\ \dots & \dots & \dots \\ P_{\mathrm{n}}^{(N_{\mathrm{sets}}1)}(\ell) & \dots & P_{\mathrm{n}}^{(N_{\mathrm{sets}}N_{\mathrm{sets}})}(\ell) \end{array}\right) . \tag{3.70}$$

They are the correlations between the different convergence fields, convergence and galaxy fields, and galaxy fields, respectively. The matrices $\mathbf{A}_{\kappa\kappa}$ and $\mathbf{A}_{\mathrm{nn}}$ are symmetric, while the matrix $\mathbf{A}_{\mathrm{n}\kappa}$ is not due to $P_{\mathrm{n}\kappa}^{(mn)}(\ell) \neq P_{\mathrm{n}\kappa}^{(nm)}(\ell)$. By $\mathbf{A}_{\mathrm{n}\kappa}^{\mathrm{t}}$ we denote the transpose of $\mathbf{A}_{\mathrm{n}\kappa}$. According to the Sect. 3.3.2 a realisation of $\tilde{\mathbf{R}}(\ell)$ can then be found by means of

$$\tilde{\mathbf{R}}(\ell) = \frac{1}{\sqrt{2L^2}} \sqrt{\mathbf{P}(\ell)}\, \vec{U} \;, \tag{3.71}$$

where $\vec{U}$ is a $2 \times N$ sized vector of uncorrelated complex random variables with real and imaginary parts independently drawn from a Gaussian PDF with mean zero and unity variance.

After the full Fourier representation of all involved fields $\tilde{\kappa}_i$ and $\delta\tilde{n}_i$ for all $\vec{\ell}_i$ has been calculated, we transform the convergence realisations to the shear realisations $\tilde{\gamma}_i$ according to Eq. (3.60). Finally, the fields are transformed from Fourier to real space.

Depending on the number of grid points and galaxy sets the memory demand can be high. We handled this problem by storing the realisations of the individual Fourier coefficients $\tilde{\mathbf{R}}(\vec{\ell}_i)$ to disk immediately after they have been calculated. After all coefficients have been computed, the fields can be processed separately, restoring only one field at one time from the disk.

Improving the statistics for the galaxy clustering

The number density fields of the galaxy sets on the sky emerging from the foregoing section are, as the convergence fields, Gaussian random fields. For high-amplitude fluctuations ($\delta \approx 1$) in the galaxy number density, however, the Gaussian model is a bad description. Since density contrasts always have to be $\delta \leq -1$, in reality the one-dimensional density contrast PDF of fields with large fluctuations necessarily becomes skewed –a feature that is not contained in a Gaussian distribution. Instead, a Gaussian description allows values for $\delta < -1$ (negative densities) which make realisations of mock galaxy catalogues including discrete galaxy positions (next section) impossible. In particular, this insufficient description poses a problem for the highly clustered galaxy distributions at low redshift. Hence, the above algorithm has to be modified for the δn_i.

Our modification consists in realising the galaxy fields as *lognormal random fields*. Lognormal fields have two important properties: first, their field values δ_{ln} are always greater than some minimum value and, second, they can be obtained by locally transforming an *underlying Gaussian field* δ_{g}. One special case from the whole class of lognormal fields is:

$$\delta_{\mathrm{ln}} = \exp\left(\delta_{\mathrm{g}} - \frac{1}{2}\left\langle \delta_{\mathrm{g}}^2 \right\rangle\right) - 1 \, . \tag{3.72}$$

It is always $\delta_{\mathrm{ln}} \leq -1$ and has a variance $\langle \delta_{\mathrm{ln}}^2 \rangle$ that asymptotically approaches $\left\langle \delta_{\mathrm{g}}^2 \right\rangle$ for $|\delta_{\mathrm{g}}| \ll 1$. This type of statistics is attractive because it is a good approximation to the real galaxy fields (Coles & Jones 1991; Colombi 1994). See Fig. 3.4 for illustration.

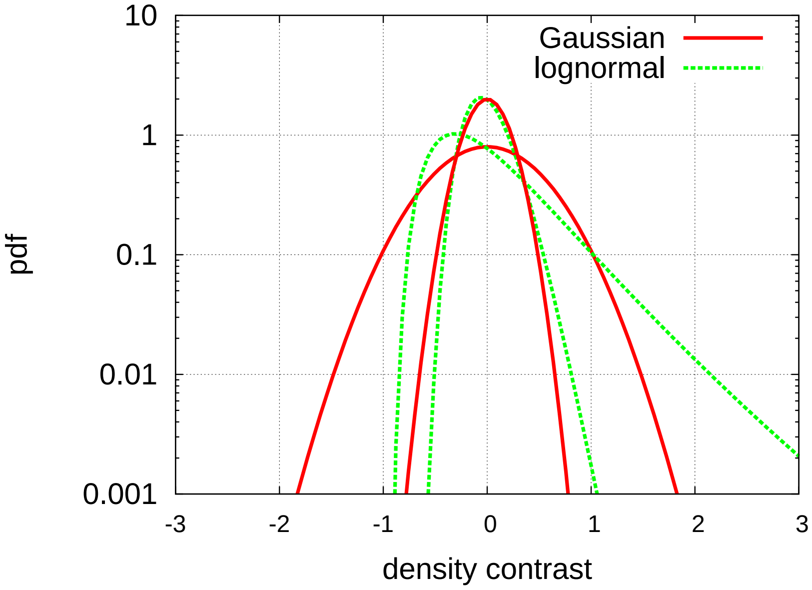

Figure 3.4.: *A lognormal probability distribution in comparison to a Gaussian distribution for two different variances* $\sigma = 0.5$ *(wide) and* $\sigma = 0.2$ *(narrow). For* σ *getting smaller the lognormal and Gaussian profile approach each other. The lognormal PDF is always zero for values smaller than* -1.

Moreover, most conveniently, lognormal fields require only a slight extension of the algorithm presented in the foregoing section which, originally, is only suitable for Gaussian fields: We are using last section's recipe to make the realisations of the convergence fields and the Gaussian fields of the galaxy distributions' *underlying* the lognormal realisations. After applying the algorithm, we perform the local transformation (3.72) to obtain the final galaxy field density contrasts. Therefore, all we have to change, apart from adding the final transformation, is to work out the correlation power spectra of the Gaussian fields underlying the lognormal galaxy fields. How do those power spectra look like?

First of all, we have three kinds of power spectra to distinguish: 1. correlations between Gaussian fields, $P_\kappa^{(ij)}$, 2. correlations between lognormal fields, $P_{\rm n}^{(ij)}$, and 3. correlations between lognormal and Gaussian fields, $P_{{\rm n}\kappa}^{(ij)}$. The $P_\kappa^{(ij)}$ spectra remain unaffected since we do not change the statistics of the convergence fields; they are considered Gaussian fields[8].

Let us turn first of all to $P_{\rm n}^{(ij)}$. Imagine we have two statistically homogeneous and isotropic random Gaussian fields living in the same space with coordinates $\vec{\theta}$. The average of the values in both fields is assumed to be zero, like for the convergence and galaxy number density. We pick one field value δ_1 at $\vec{\theta}_1$ from one random field and another value δ_2 at $\vec{\theta}_2$ from the other field. The correlation $\xi = \langle\delta_1\delta_2\rangle$ of the two field values depends only on the distance $\theta = |\vec{\theta}_1 - \vec{\theta}_2|$ since the fields are statistically homogeneous and isotropic; this is the spatial

[8] A lognormal statistics may even be a better approximation for the statistics of convergence fields (Taruya *et al.* 2002). If so, it can easily be included in the algorithm outlined in this chapter, simply by treating the convergence fields the same way as the galaxy number density fields. As in this case all fields have lognormal statistics, all power spectra will have to be transformed by the procedure described below.

two-point correlation between the fields at the distance θ. Moreover, the joint PDF $P(\delta_1,\delta_2)$ of both points has to be a bivariate Gaussian since both fields are Gaussian random fields:

$$P(\delta_1,\delta_2)=\frac{1}{2\pi\sigma_1\sigma_2\sqrt{1-\psi(\xi)^2}}\exp\left(-\frac{\delta_1^2\,\sigma_2^2+\delta_2^2\,\sigma_1^2-2\xi\,\delta_1\,\delta_2}{2\sigma_1^2\sigma_2^2(1-\psi(\xi)^2)}\right)\,, \tag{3.73}$$

where we are using the definitions $\sigma_1^2\equiv\left\langle\delta_1^2\right\rangle$, $\sigma_2^2\equiv\left\langle\delta_2^2\right\rangle$ and $\psi(\xi)\equiv\xi/(\sigma_1\sigma_2)$. Now we apply the local transformation (3.72), symbolically denoted by $f[\delta_1]$ and $f[\delta_2]$, in order to convert both Gaussian fields to lognormal fields $\Delta_1=f[\delta_1]$ and $\Delta_2=f[\delta_2]$. How are the values Δ_1 and Δ_2 between the lognormal fields correlated? The answer to this question is the following integral (see Peacock 2001):[9]

$$\begin{aligned}\xi_{\log} &= \langle\Delta_1\Delta_2\rangle=\langle f[\delta_1]f[\delta_2]\rangle \qquad (3.75)\\ &= \left\langle\exp\left(\delta_1+\delta_2-\frac{1}{2}[\sigma_1^2+\sigma_2^2]\right)\right\rangle-\left\langle\exp\left(\delta_1-\frac{1}{2}\sigma_1^2\right)\right\rangle-\left\langle\exp\left(\delta_2-\frac{1}{2}\sigma_2^2\right)\right\rangle+1\\ &= \exp\left(\psi(\xi)\sigma_1\sigma_2\right)-1-1+1=\mathrm{e}^{\xi}-1\,,\end{aligned}$$

where the ensemble average of an arbitrary $g(\delta_1,\delta_2)$ is defined as

$$\langle g(\delta_1,\delta_2)\rangle\equiv\int\mathrm{d}\delta_1\mathrm{d}\delta_2\,P(\delta_1,\delta_2)\,g(\delta_1,\delta_2)\,. \tag{3.76}$$

As the transformation to the lognormal fields has not changed the distance θ of the field values, $\xi_{\log}$ is the two-point correlation at distance θ between the lognormal fields. This result, therefore, states that the two-point correlation function between the lognormal fields and the two-point correlation function between the Gaussian fields underlying the lognormals are related by

$$\xi=\ln\left(\xi_{\log}+1\right)\,. \tag{3.77}$$

Using the relation between the two-point correlation $\xi\left(\theta\right)$ and the power spectrum $P\left(\ell\right)$ (a 2D-Fourier transform assuming isotropy), see (A.46):

$$\xi\left(\theta\right) = \frac{1}{2\pi}\int_0^\infty\mathrm{d}\ell\,\ell\,P\left(\ell\right)J_0\left(\ell\theta\right) \tag{3.78}$$

$$P\left(\ell\right) = 2\pi\int_0^\infty\mathrm{d}\theta\,\theta\,\xi\left(\theta\right)J_0\left(\ell\theta\right)\,, \tag{3.79}$$

we can translate this result into the language of power spectra which are the important quantities in the Monte Carlo recipe to make the random fields. The required steps for transforming $P_{\rm n}^{(ij)}$ are:

1. calculating $\xi_{\log}$ from $P_{\rm n}^{(ij)}$, Eq. (3.59), via Eq. (3.78),

---

[9] We extensively make use of:

$$\langle\exp\left(\alpha\,\delta_1+\beta\,\delta_2+\gamma\right)\rangle=\exp\left(\frac{1}{2}\alpha^2\,\sigma_1^2+\frac{1}{2}\beta^2\,\sigma_2^2+\psi(\xi)\sigma_1\sigma_2\alpha\beta+\gamma\right)\,, \tag{3.74}$$

where α, β and γ are constant.

2. application of Eq. (3.77) for obtaining ξ which is the two-point correlation between the underlying Gaussian fields, and
3. performing the integral (3.79) to get the power spectrum of the underlying Gaussians for the Monte Carlo sampler.

How do we have to modify the cross-correlation power spectra $P_{\mathrm{n}\kappa}^{(ij)}$ between lognormal and Gaussian fields? Surprisingly, they can be left unchanged as can be shown by the following argument. As before, we pick two values δ_1 and δ_2 with distance θ from two Gaussian random fields; their correlation is $\xi = \langle \delta_1 \delta_2 \rangle$. If one of the field values, δ_2 say, is transformed according to Eq. (3.72) by $\Delta_2 = f[\delta_2]$ their correlation becomes

$$\begin{aligned} \xi' &= \langle \delta_1 \Delta_2 \rangle = \langle \delta_1 f[\delta_2] \rangle \\ &= \left\langle \exp\left(\delta_2 - \frac{1}{2}\sigma_2^2\right)\delta_1 \right\rangle - \langle \delta_1 \rangle = \frac{\mathrm{d}}{\mathrm{d}\alpha} \left\langle \exp\left(\alpha\delta_1 + \delta_2 - \frac{1}{2}\sigma_2^2\right) \right\rangle \Big|_{\alpha=0} - 0 \\ &= \left[\left(\alpha\sigma_1^2 + \psi(\xi)\sigma_1\sigma_2\right) \mathrm{e}^{\alpha^2/2\,\sigma_1^2 + \alpha\psi(\xi)\sigma_1\sigma_2} \right] \Big|_{\alpha=0} = \xi \; . \end{aligned} \tag{3.80}$$

This means that the two-point correlation between a Gaussian and a lognormal field is actually identical to the correlation of the same Gaussian field and the Gaussian field underlying the lognormal field!

One last comment on the integrals (3.78) and (3.79). They have to be handled with care because the Bessel function kernel J_0 is oscillating. The *fast Hankel transforms* (Hamilton 2000), briefly presented in Appendix A.1, are well suited for this task, especially because in our case the integral transformation has to be performed over many orders of magnitude in both directions.[10]

Galaxy mock catalogue

The next step is to convert the density contrasts δn_i to a catalogue of galaxy positions sampling the realised number density field; observed are galaxy positions and not number density fields of galaxies. The number density is related to the density contrast by

$$n_i(\vec{\theta}) = \langle \hat{n}_i \rangle \left[1 + \delta n_i(\vec{\theta})\right] \; , \tag{3.81}$$

the absolute number of galaxies in a particular field-of-view is $N_i = \langle \hat{n}_i \rangle \times L^2$ where L^2 is the area of the square field-of-view.

The positions of the N_i galaxies belonging to the i-th set are random, with a PDF that is dictated by the density contrast realisation. In order to obtain a random position of a galaxy based on the number density field we incorporate a *rejection method*: a particular realisation of $1 + \delta n_i$ is normalised to the maximum value $n_i^{\max} = \max\left(1 + \delta n_i\right)$ of the field, so that all values of $[1 + \delta n_i]/n_i^{\max}$ lie between 0 and 1. In the next step, we chose from a uniform random number generator a candidate position $\vec{\theta}'$ in the field. This candidate is accepted as the final galaxy position if another random variable drawn from a uniform PDF with values between 0 and 1 is less or equal $[\delta n_i(\vec{\theta'}) + 1]/n_i^{\max}$. Otherwise, the last step is repeated. The whole

---

[10] In detail, we performed an unbiased Hankel transform, $q = 0$, with $\xi\left(r\right) = \frac{1}{2\pi}\frac{a(r)}{r}$ and $P\left(k\right) = \frac{\tilde{a}(k)}{k}$ in the notation of Hamilton (2000), Appendix therein.

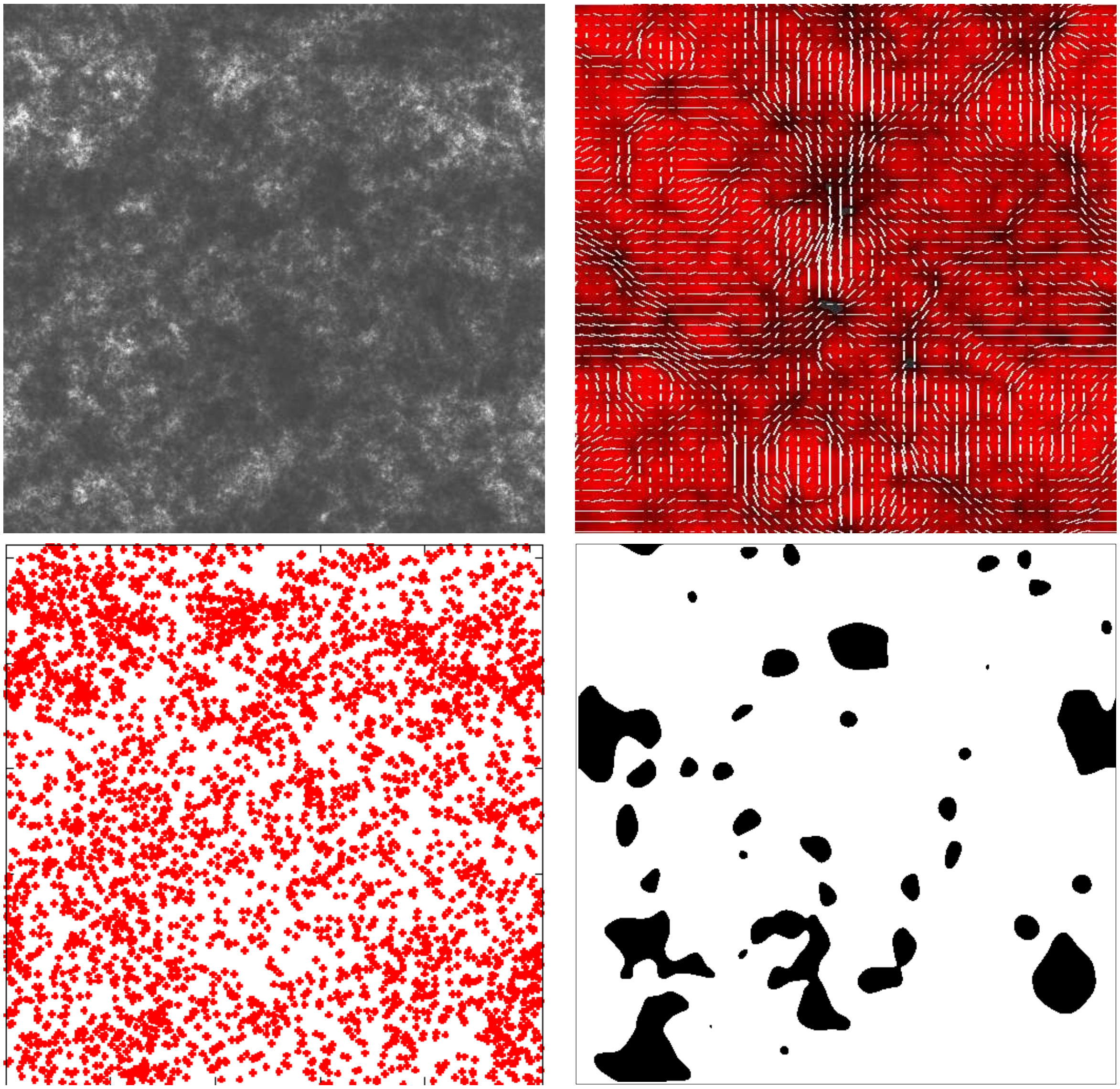

Figure 3.5.: *Example output of one simulation run. The upper left panel shows the density contrast (lognormal) of one galaxy set with redshifts between* 0 *and* 0.5 *unbiased with respect to the dark matter; the field-of-view has a size of* $30' \times 30'$*. In the upper right, we have displayed the cosmic shear (white sticks) and smoothed convergence (grey colour) imprinted in the image shapes of this galaxy set. The lower left is a scatter plot of the galaxy positions produced using the rejection method applied to the density contrast in the panel above. The lower right panel is a obscuration mask calculated from a real survey that is used here to include masking.*

procedure is repeated N_i times for every set of galaxies. The result is a catalogue of galaxy positions sampling the number density field of the corresponding galaxy set. As in practice, this catalogue allows at best the reconstruction of the original galaxy density field only up to the *shot noise* uncertainty.

Fig. 3.5 shows an example for a simulated galaxy density contrast field and a scatter plot of the computed galaxy positions and cosmic shear field.

Assembling the galaxy shape

The final step is to assemble the shape information –the ellipticity– of the galaxies whose angular positions $\vec{\theta}$ are now known from the last section. The ellipticity of a galaxy is computed from the cosmic shear signal $\gamma = \gamma_i(\vec{\theta})$ at the position of the galaxy in the shear field belonging to the corresponding galaxy set , and the intrinsic ellipticity, $\epsilon_{\rm s}$, of the galaxy. In the weak lensing regime, both can be combined to obtain the final galaxy ellipticity ϵ by (follows from Eq. 1.79)

$$\epsilon = \epsilon_{\rm s} + \gamma \; . \tag{3.82}$$

For the intrinsic ellipticity $\epsilon_{\rm s}$ we draw for both imaginary and real part a random number x from a Gaussian PDF, $P[x]$, truncated beyond 1 and below -1, with variance σ_ϵ:

$$P[x] = \frac{\exp\left(-x^2/\sigma_\epsilon^2\right)}{\pi\sigma_\epsilon\left[1-\exp\left(-1/\sigma_\epsilon^2\right)\right]} \; . \tag{3.83}$$

An implementation of a Gaussian random number generator could be the Box-Müller Method (Press *et al.* 1992).

Sometimes it is desired to simulate a survey whose galaxy ellipticities “look” like in a particular real survey. In that case, the galaxy ellipticities of the real survey could serve as a bootstrap sample; simulated $\epsilon_{\rm s}$ are randomly drawn from the scrambled real data set (and put back into the bootstrap sample). The cosmic shear correlations in the real data set are destroyed due to the shuffling of the galaxy positions.

Masking

Foreground stars, large galaxies, galaxy clusters or gaps in the CCD coverage obscure in practice parts of the fields. This effect is easily included by putting a defined obscuration mask on top of the simulated fields, taking away all galaxies lying inside gap regions. Such an obscuration mask is displayed in Fig. 3.5 in the lower right. It was obtained from real data (AXAF in GaBoDS, see Chapter 4).

3.4. Comparing two estimators for aperture statistics

The Monte Carlo mock data, whose generation has been outlined in the foregoing section, is used here to compare two different estimator approaches for the second-order aperture statistics (Sect. 3.2.4). In particular, we would like to compare the effectiveness of both approaches in the presence of gaps in the data field.

3.4.1. Parameters of the simulated data

Geometry and galaxy parameter

Overall, we made 4×500 different statistically independent Monte Carlo realisations of a square field, 30×30 arcmin in size, as described in Sect. 3.3: one set of 500 fields with the field mask in Fig. 3.5 (gap area about 15 percent of total area), another set without any gaps, and both sets without and with intrinsically circular source galaxies ($\sigma_\epsilon=0.3$). The field size is typical for the current wide field surveys. In order to include also spatial modes greater than $\sqrt{2}\times30$ arcmin, this field is chopped out of a 60×60 arcmin field realised on a 2048×2048 pixel grid. For the redshift distribution of the galaxies, we assumed an empirical distribution (Smail *et al.* 1995; Baugh & Efstathiou 1993) which is appropriate for a flux-limited survey:[11]

$$p_g\left(z\right)\mathrm{d}z=\frac{1}{z_0^3}\frac{z^2}{\Gamma\left(3/\beta\right)\beta}\exp\left[-\left(\frac{z}{z_0}\right)^\beta\right]\mathrm{d}z\;. \tag{3.85}$$

We chose $\beta=1.5$ and $z_0=0.602$ as in the COMBO-17 survey (Brown *et al.* 2003); this corresponds to a mean redshift of $\langle z\rangle=0.85$. We consider two galaxy sets with non-overlapping redshift distributions, namely $z\in[0.2,0.6]$ and $z\in[0.6,2.0]$ for the foreground and background, respectively; within the redshift bins galaxies are distributed according to (3.85). In the mock data, the galaxies perfectly trace the dark matter distribution, thus we have $r_{ij}=r_i=b_i=1$ for all scales. Using the estimators, we correlate the aperture mass map of the background galaxies with the aperture number count map of the foreground galaxies, and we measure the variance of both maps on different scales.

The overall galaxy density, which is the sum of background and foreground, was set to $\bar{n}=30$ galaxies arcmin^{-2}. Typically, this figure gives about 7500 foreground galaxies, mean redshift $\langle z\rangle=0.44$, and 19300 galaxies in the background, mean redshift $\langle z\rangle=1.0$.

Fiducial cosmology

Our cosmology throughout is a ΛCDM model with $\Omega_{\rm m}=0.3$, $\Omega_\Lambda=0.7$. A scale-invariant ($n=1$, Harrison-Zel'dovich) spectrum of primordial dark matter fluctuations is assumed. Predicting the shear correlation functions requires a model for the redshift evolution of the 3-D dark matter power spectrum. We use the fitting formula of Bardeen *et al.* (1986) for the transfer function (adiabatic CDM), and the Peacock & Dodds (1996) prescription for evolution in the non-linear regime. For the power spectrum normalisation we have $\sigma_8=0.9$, and as shape parameter $\Gamma=0.21$.

3.4.2. Aperture filter and related functions

For the aperture statistics, a polynomial filter is used (Schneider *et al.* 1998)

$$u\left(x\right)\;=\;\frac{9}{\pi}\left(1-x^2\right)\left(\frac{1}{3}-x^2\right)H(1-x)\;, \tag{3.86}$$

---

[11] The transformation between a PDF in redshift, $p_z(z)$, and a PDF in comoving distance, $p_w(w)$, is as follows:

$$p_w(w)=p_z(z)\,\frac{\mathrm{d}z}{\mathrm{d}w}=p_z(z)\,\frac{H(z)}{c}\;, \tag{3.84}$$

where the differential transformations $c\,\mathrm{d}t=a\,\mathrm{d}w=-\frac{c}{H(a)a}\,\mathrm{d}a=\frac{c}{H(z)(1+z)}\,\mathrm{d}z$ are used.

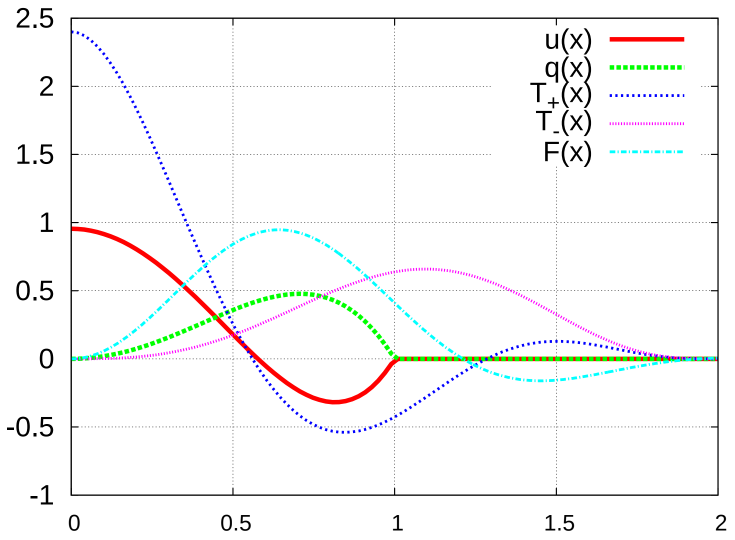

Figure 3.6.: *Polynomial filter used and the auxiliary functions $T_\pm(x)$ and $F(x)$ derived from the aperture filter. The filter $u(x)$ and $q(x)$ vanish beyond $x \geq 1$, whereas the auxiliary functions, needed for transforming the two-point correlators to $\left\langle N^n M_{\rm ap}^m \right\rangle$, $n+m=2$, are zero beyond $x \geq 2$.*

$$q\left(x\right) \;=\; \frac{6}{\pi}x^2\left(1-x^2\right)H(1-x)\;,$$

where $H(x)$ denotes Heaviside Step Function. Adopting these aperture filters results in the following auxiliary functions required for transforming the two-point correlators to the second-order aperture statistics (Hoekstra *et al.* 2002, see Sect. 3.2.4 for definitions)

$$\begin{aligned}
I\left(x\right) &= \frac{12}{\pi}\frac{1}{x^2}J_4\left(x\right)\;, &&(3.87)\\
T_+\left(x\right) &= \frac{6\left(2-15x^2\right)}{5}\left[1-\frac{2}{\pi}\arcsin\left(x/2\right)\right]H(2-x)+\\
&\quad\frac{x\sqrt{4-x^2}}{100\pi}\times\left(120+2320x^2-754x^4+132x^6-9x^8\right)H(2-x)\;,\\
T_-\left(x\right) &= \frac{192}{35\pi}x^3\left(1-\frac{x^2}{4}\right)^{7/2}H(2-x)\;,\\
F\left(x\right) &= 576\int_0^\infty\frac{ds}{s^3}J_2\left(sx\right)\left[J_4\left(s\right)\right]^2\;.
\end{aligned}$$

The auxiliary function $F(x)$ has to be worked out numerically, as no analytic solution to this integral is known. All auxiliary functions vanish outside the interval $x \in [0,2]$ due to the finite support of $u(x)$ and $q(x)$. See Fig. 3.6 for a plot of all functions.

The aperture filter choice for $u(x)$ makes the integral kernel $[I(x)]^2$ in the analytical expressions of $\left\langle N^2\right\rangle$, $\left\langle NM_{\rm ap}\right\rangle$ and $\left\langle M_{\rm ap}^2\right\rangle$, Eqs. (3.14), oscillating. A convenient way to work out these equations numerically are the fast Hankel transforms (Appendix A.1).

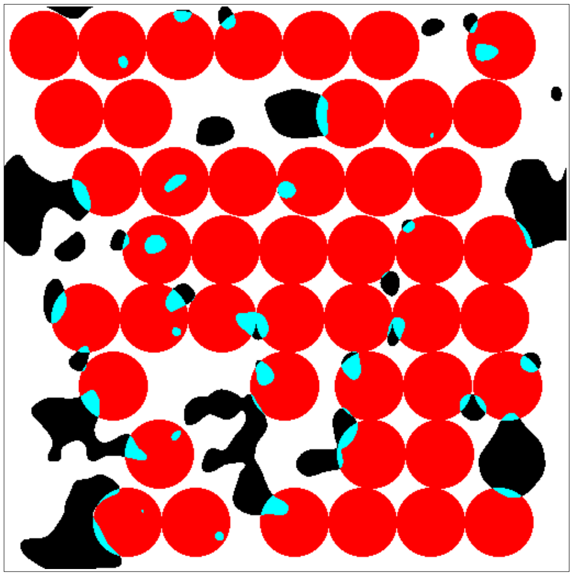

Figure 3.7.: *Examples illustrating the tolerance scheme for placing apertures. Displayed are allowed aperture positions (dark grey disks) in the field area if at maximum an overlap (light grey) with the gaps (black) of* 10% *is tolerated. Note that the regions outside the square field also count as gap.*

3.4.3. Technical aspects of the estimators

As estimators of $\left\langle N^2\right\rangle$, $\langle N M_{\rm ap}\rangle$ and $\left\langle M_{\rm ap}^2\right\rangle$ we applied the two methods described in Sect. 3.2.4, which either estimate two-point correlation functions being transformed to the aperture statistics afterwards, or which place circular apertures into the field and obtain estimates from every individual aperture being combined for a final estimate. All galaxies in the synthetic data have equal weight, $w_i = 1$. In the following section, we denote the estimator methods by "I" and "II", respectively. If possible, estimates were taken for 40 equally spaced angular bins ranging between 0 and 20 arcmin. The program code implementing the estimators invokes data structures based on the tree-code data structure (Pen & Zhang 2003; Moore *et al.* 2001) to reduce the computation time, which is mostly due to finding pairs of galaxies at a certain distance ("I") or to finding galaxies inside the apertures ("II").

Estimator "I"

The two-point correlators for the angular galaxy clustering, Eq. (3.28), galaxy-galaxy lensing, Eq. (3.29), and shear-shear correlations, Eq. (3.30), are estimated from the data of each field realisation inside 600 logarithmic θ-bins ranging between $1''.74$ and $42'.19$. For the transformation of the two-point correlators to the corresponding apertures statistics, we approximate the transformation integrals (3.22)-(3.24) by a sum.

Estimator "II" with tolerance scheme

For the estimators placing apertures into the field, Eq. (3.15)-(3.17), we introduce a *tolerance scheme*. An additional parameter defines a tolerance threshold that determines how much maximum overlap between a circular aperture and the gap mask is allowed. Values for the tolerance parameter range between 100% and 0% corresponding to total ignorance with respect to gaps and no allowed gap overlap, respectively. Apertures exceeding the tolerance limit are rejected fore the final average. As an example, see Fig. 3.7 with some allowed aperture positions for a tolerance level of 10%. Below we assume a tolerance level of 20% but also, for comparison, evaluate the estimates with a tolerance of 100% (all apertures are accepted). For the aperture centres, we take the grid points of a 128 × 128 grid (maximum 16384 apertures) which is laid on top of the field of view.

3.4.4. Results and discussion

In every Monte Carlo sample, we measure the second-order aperture statistics $\langle N^n M_{\rm ap}^m \rangle$, $n+m=2$, for a range of aperture radii using the estimators "I" and "II". The averages of all measurements are summarised by the Figs. 3.8 and 3.9. The samples without gaps are a test for the Monte Carlo code and the codes implementing the estimators. Here, both estimators should on average reproduce the theoretical values (3.14) of the power spectra P_κ, $P_{{\rm n}\kappa}$ and $P_{\rm n}$ having been put into the simulated data. As the deviations from theory are too small to be clearly visible in the left column of Fig. 3.8, we made the plot in Fig. 3.9 (top row) which displays the relative deviations of the estimates. These plots have error bars which indicate the remaining statistical uncertainty expected from 500 Monte Carlo samples; similar errors bars for Fig. 3.8 would be barely visible and are therefore not plotted. First of all, we conclude from Fig. 3.9 that the ensemble averages of the estimators "I" and "II" are broadly consistent considering the statistical errors. Second, both estimators fairly well agree with theory for $\langle N^2 \rangle$ (upper left panel). However, the estimates are clearly offset by about $2\% - 4\%$ in the case of $\langle M_{\rm ap}^2 \rangle$ and maybe offset by $< 2\%$ for $\langle N M_{\rm ap} \rangle$. As both estimators are consistent with each other and are the results of independent computer codes and different algorithms, we suspect that this small offset originates from the Monte Carlo samples. To check this suspicion we looked at the average power spectra $P_{\rm n}$, $P_{{\rm n}\kappa}$ and P_κ of all field realisations. We find that they differ from the desired power spectra, Eqs. (3.14), by about 1%, $1\% - 3\%$ and $3\% - 4\%$, respectively, with a slight dependence on scale. Therefore, the apparent inaccuracy of the estimators can indeed be attributed to the Monte Carlo samples and is probably not a real estimator effect. By scrutinising the Monte Carlo sampler code we traced the cause of the inaccuracy back to the power matrix, Eq. (3.67), which is employed for the sample realisation process. It turned out that a small inaccuracy in the numerical calculation of the power spectra makes the power matrix slightly negative-definite so that, in principle, a real square root of the power matrix cannot be found. The computer code copes with this problem by assuming that all negative Eigenvalues of the power matrix are actually very close to zero and sets them to zero. This results in an offset of a few percent of the power spectra in the Monte Carlo samples. Since our main focus is on the manner with which the estimates of the aperture statistic change in the presence of gaps, we correct for this small offset by relating all estimates to the average of "I" from the non-gap case instead of the theoretical, mathematically correct values. For future work, however, the sampling inaccuracy should be removed.

The effect of gaps is strikingly visible in Fig. 3.8, right column, and Fig. 3.9, middle row. Clearly, the ensemble average for "II", obtained by placing apertures into the field, suffers by loosing signal for $\langle N^2 \rangle$, $\langle N M_{\rm ap} \rangle$ and artificially gaining signal for $\langle M_{\rm ap}^2 \rangle$. The signal can be biased as much as $60\%, 30\%, 20\%$ for $\langle N^2 \rangle$, $\langle N M_{\rm ap} \rangle$ and $\langle M_{\rm ap}^2 \rangle$, respectively, if the presence

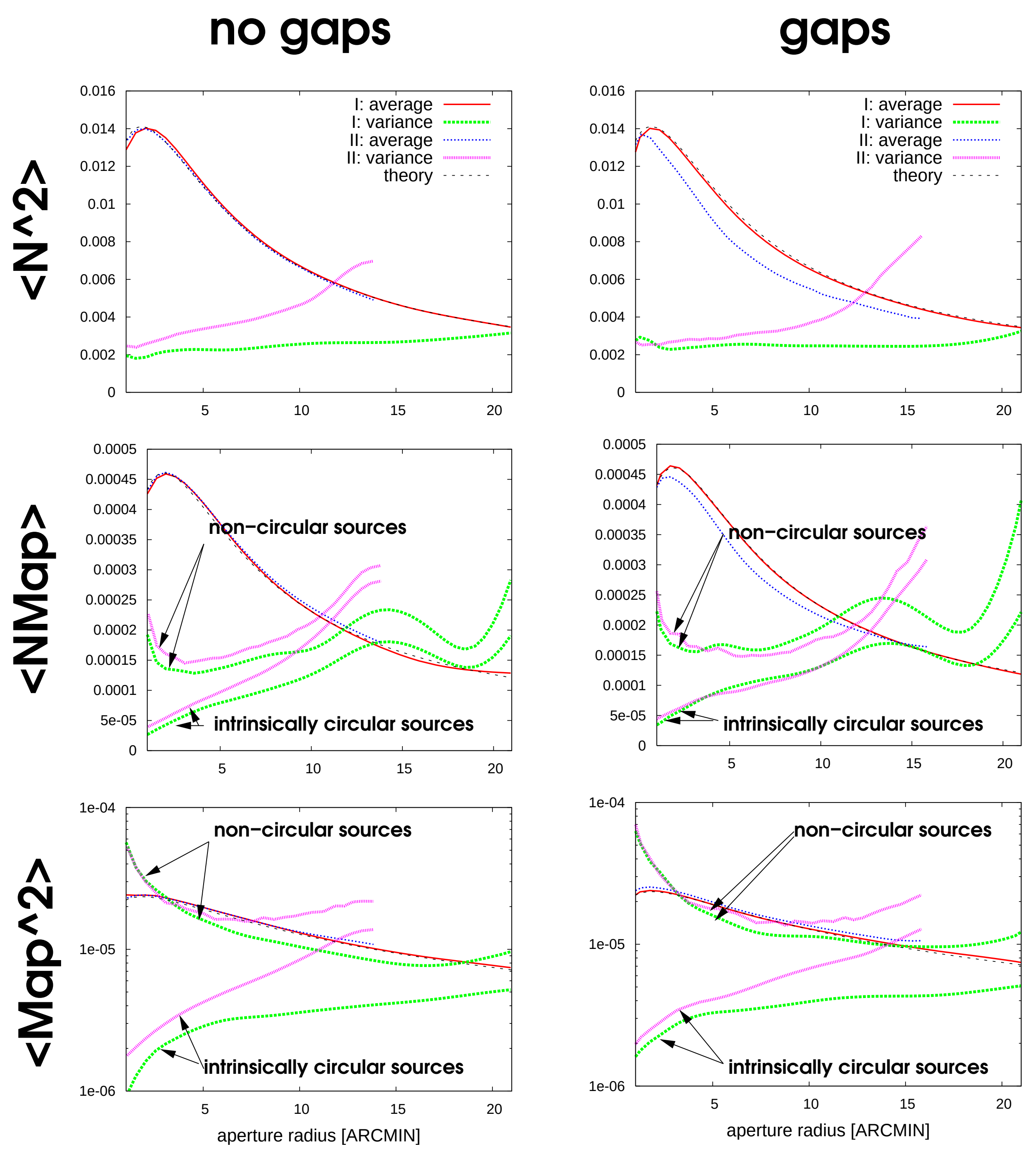

Figure 3.8.: *Ensemble average* $\langle x(\theta_i)\rangle$ *and field-to-field variance* $\Delta x(\theta_i) \equiv \sqrt{\langle x^2(\theta_i)\rangle - \langle x(\theta_i)\rangle^2}$ *of estimates for* $x = N^2, NM_{\rm ap}, M_{\rm ap}^2$ *(top to bottom row), respectively, based upon* 500 *Monte Carlo samples; estimator "I" uses two-point correlators, while "II" places apertures into the field.* ***left column****: without gaps, the gap tolerance of "II" is* 0%. ***right column****: with gaps (about* 15% *coverage, the gap tolerance of "II" is* 20%. *The sudden stop of the curves belonging to "II" occurs beyond apertures radii where no more apertures complying with the tolerance level can be found (left column:* 14.0 *arcmin, right column:* 16.0 *arcmin). Variances involving the aperture mass are plotted twice in the same line style: once with intrinsically circular source galaxies and one with intrinsically elliptical source galaxies* $(\sigma_\epsilon = 0.3)$.

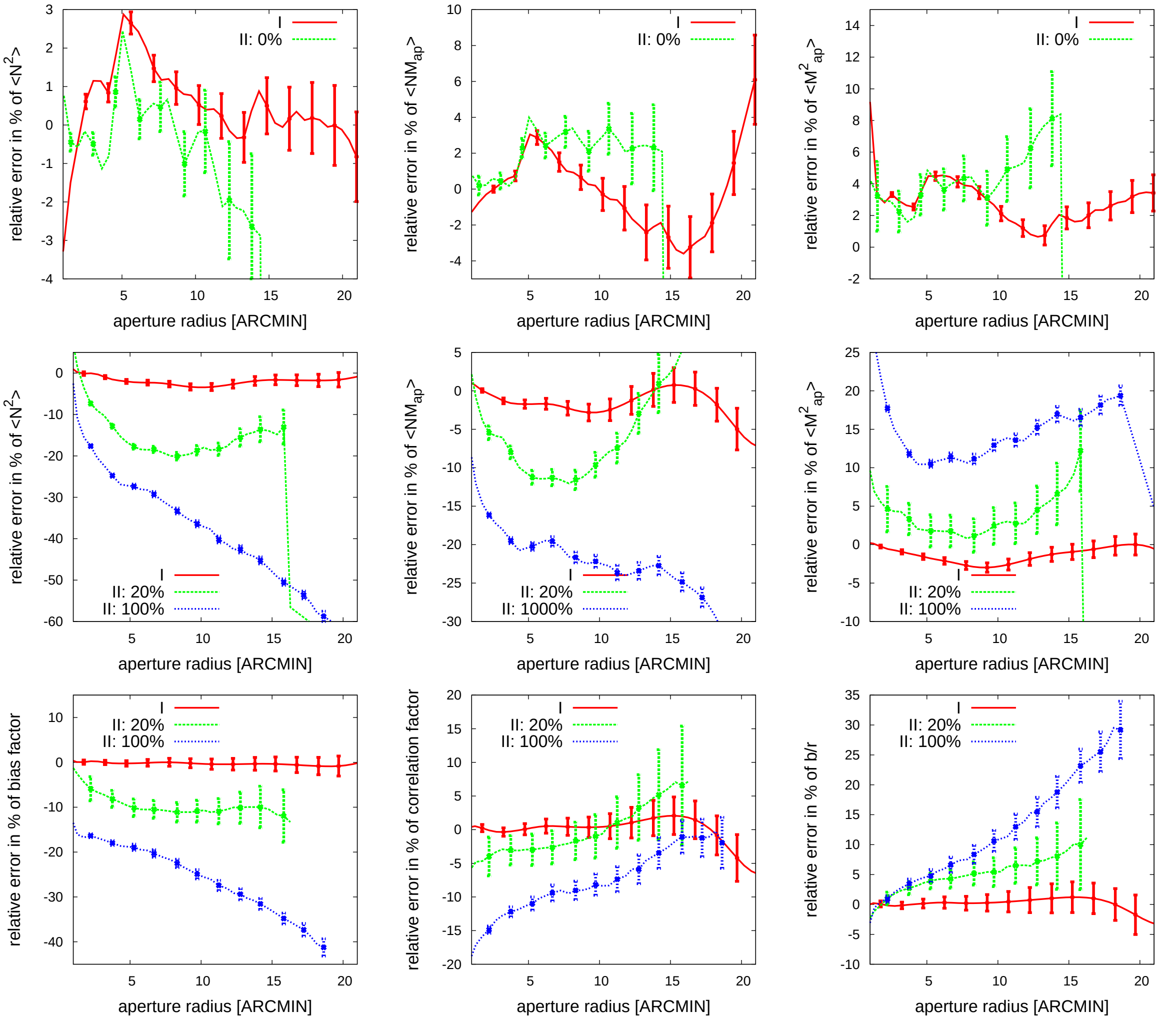

Figure 3.9.: ***top and middle row**: Comparison of Monte Carlo averaged estimates of $\langle N^2\rangle$, $\langle NM_{\rm ap}\rangle$ and $\langle M^2_{\rm ap}\rangle$ (left to right) obtained with the estimators "I" and "II". The figures show the relative deviation $(x-\hat{x})/\hat{x}$ of the estimates x with respect to the expected theoretical value $\hat{x}$. The top row has been calculated from fields without gaps, while the middle row is based upon simulated fields covered by the mask in Fig. 3.7; the percentage values denote the gap tolerance threshold of method "II". **bottom row**: Deviation from theory of the estimated linear stochastic bias between the aperture number count and aperture mass maps for data with gaps using the estimators "I" and "II". The percentage values denote the gap tolerance threshold of method "II". From left to right: bias factor $b=\sqrt{\langle N^2\rangle/\langle M^2_{\rm ap}\rangle}$, correlation factor $r=\langle NM_{\rm ap}\rangle/\sqrt{\langle N^2\rangle\langle M^2_{\rm ap}\rangle}$ and the ratio $b/r=\langle NM_{\rm ap}\rangle/\langle N^2\rangle$. **all figures**: The error bars (1σ) indicate the remaining statistical uncertainty due to the finite number of Monte Carlo samples (500).*

of the gaps is completely ignored. If we, however, discard apertures with a gap overlap of more than 20%, the bias in the estimator "II" is reduced to 20%, 10% and 10%, respectively. The estimates from "I" are obviously much less affected by the presence of gaps. Here the bias is always less than 3% with a maximum bias on intermediate scales, $\sim 10'$. Like for "II" the signal decreases for $\left\langle N^2\right\rangle$ and $\langle NM_{\rm ap}\rangle$ but also becomes lower for $\left\langle M_{\rm ap}^2\right\rangle$.

Why are "I" and "II" so differently biased although they both work on the same data and are both closely related to each other? The problem is that a gap region overlapping with the aperture disk (method "II") in general immediately means a violation of the assumption underlying Eq. (3.4) which relates the aperture mass to the tangential shear about the aperture centre. The underlying assumptions for this relation are: a) a compensated filter $U_{\theta_{\rm ap}}(\vec{\vartheta}\,)$, and b) a radial symmetry of the filter. As a gap can be expressed as a function $f_{\rm gap}(\vec{\vartheta}\,)$ which assumes the value 1 where are no gaps and 0 where are gaps, an overlap modifies the effective filter used to $U'_{\theta_{\rm ap}}(\vec{\vartheta}\,)=U_{\theta_{\rm ap}}(\vec{\vartheta}\,)\,f_{\rm gap}(\vec{\vartheta}\,)$. Usually this new, effectively used filter is neither compensated nor radially symmetric. Therefore, relation (3.4) is no longer true. By ignoring this fact, however, we pretend that it still is which introduces a bias in $\langle NM_{\rm ap}\rangle$ and $\left\langle M_{\rm ap}^2\right\rangle$. Another cause for an estimator bias is given for $\left\langle N^2\right\rangle$ and $\langle NM_{\rm ap}\rangle$ because both estimators "II" for these statistics depend on $\bar{N}_{\rm f}$. The average number of foreground galaxies, $\bar{N}_{\rm f}$, certainly becomes smaller if the aperture is obscured by a gap. As we have not accounted for this fact, we underestimate $\left\langle N^2\right\rangle$ and $\langle NM_{\rm ap}\rangle$ by dividing by a too large $\bar{N}_{\rm f}$ in the case of apertures overlapping with gap regions. For $\langle NM_{\rm ap}\rangle$, the bias is smaller compared to $\left\langle N^2\right\rangle$ for two reasons: first, $\bar{N}_{\rm f}$ enters the estimator linearly and not quadratically, and second the bias due to $U'_{\theta_{\rm ap}}(\vec{\vartheta}\,)$ causes an overestimation, as clearly seen in $\left\langle M_{\rm ap}^2\right\rangle$, which counteracts the underestimation caused by a too large $\bar{N}_{\rm f}$.

We now turn to estimators based on method "I". These estimators rely on the two-point correlators which are derived just from pairs of points in the random fields; the definitions do not care about gaps possibly being between these points. But yet, we observe that the aperture statistics is underestimated. This may be partially understood by the following discussion. Mathematically, the correlators probe a random field that is multiplied with a selection function $f_{\rm gap}(\vec{\vartheta}\,)$. In the absence of phase correlations between the cosmic shear and galaxy number density fields with the mask $f_{\rm gap}(\vec{\vartheta}\,)$ (*cf.* Feldmann *et al.* 1994), this has the effect that we actually observe the convolved power spectrum

$$P'(\ell)=(P*|\tilde{f}_{\rm gap}|^2)(\ell)\;, \tag{3.88}$$

where $P(\ell)$ the power spectrum without gaps and $\tilde{f}_{\rm gap}(\ell)$ the Fourier transform of the mask. To have a quantitative estimate of the relative change, $\Delta P(\ell)/P(\ell)=(P'(\ell)-P(\ell))/P(\ell)$, caused by the gap pattern we computed two power spectra of the foreground galaxy number density for various field realisations: one spectrum without gaps, $P(\ell)$, and one from fields with gaps, $P'(\ell)$. The power spectrum was estimated by means of the dispersion of the Fourier coefficient moduli in bins of $|\vec{\ell}\,|$. Finally, we averaged the relative change, $\Delta P(\ell)/P(\ell)$, for all field realisations. The result can be seen Fig. 3.10. On the one hand, one can see that the power is indeed reduced by applying the gap mask to the random field. Moreover, the relative decrease is scale-dependent with a maximum decrease on intermediate scales. On the other hand, the amplitude of the decrease is larger by a factor ~ 2 compared to Fig. 3.9 (very left panel in the middle row) which may mean that we have not found the reason for the power decrease yet. A definite answer to this problem is therefore left to future work.

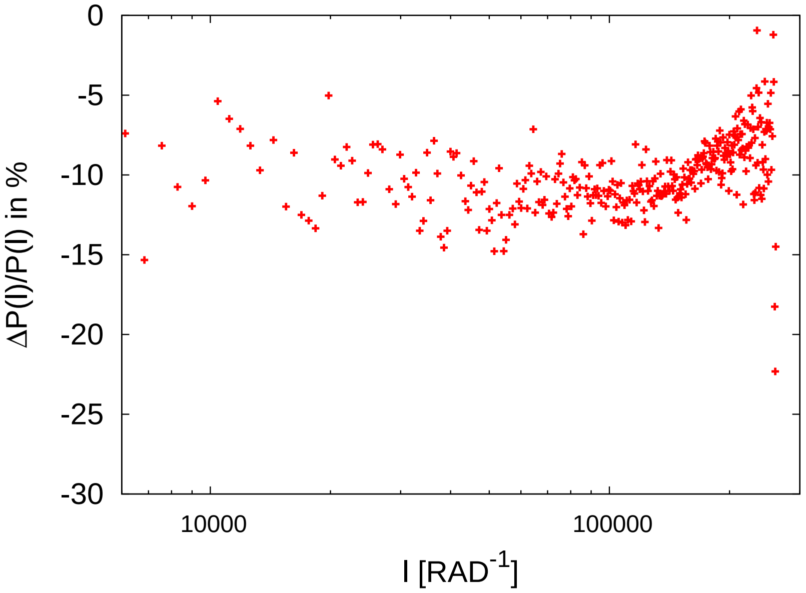

Figure 3.10.: *Relative change in the number density power spectrum of the foreground galaxies if our gap mask is applied. The plotted data points are the average of five random field realisations.*

Fig. 3.9, bottom row, translates the estimator averages fore the aperture statistics into the linear stochastic bias between the aperture number count and aperture mass map. They can be employed to study the linear stochastic bias between the foreground galaxies and the total matter distribution. As for the bias parameters obtained with the estimator "II", the accuracy is about 10% and 5% for the bias factor and correlation factor, respectively, if a gap tolerance of 20% is used. For "I", we see no systematics in the bias parameter estimates within the statistical uncertainties of a few percent. Obviously, in the estimates for the linear stochastic bias parameter the systematics of the individual second-order moments partly compensate each other. This means that even under realistic conditions we can principally recover the galaxy bias parameters with high accuracy.

In order to quantify the estimators' noise properties we plotted the field-to-field variance of the estimates as a function of aperture radius in Fig. 3.8. Contributions to the total noise come from a) the positional shot noise of the foreground and background galaxies, b) the cosmic variance and c) from intrinsically non-circular source galaxies, $\sigma_\epsilon \leq 0$, wherever weak lensing is involved (van Waerbeke 1998; Schneider 1998). There are two curves for both "I" and "II" in the diagrams for $\langle NM_{\rm ap}\rangle$ and $\langle M^2_{\rm ap}\rangle$: one without, $\sigma_\epsilon = 0$, and one with, $\sigma_\epsilon = 0.3$, intrinsic ellipticities of the source galaxies. This shows, not surprisingly, how the noise is increased by intrinsically non-circular source galaxies. To quantify this increase and for a comparison with the literature, we plot in Fig. 3.11, bottom row, the function

$$\rho(X) = \frac{\sigma(X, \sigma_\epsilon = 0)}{\sigma(X, \sigma_\epsilon \neq 0) - \sigma(X, \sigma_\epsilon = 0)} \,, \tag{3.89}$$

where $\sigma(X, \sigma_\epsilon = 0)$ and $\sigma(X, \sigma_\epsilon \neq 0)$ denote the field-to-field variance of the estimates of $X \in \{\langle NM_{\rm ap}\rangle, \langle M^2_{\rm ap}\rangle\}$ for circular and non-circular sources, respectively. The function $\rho(X)$

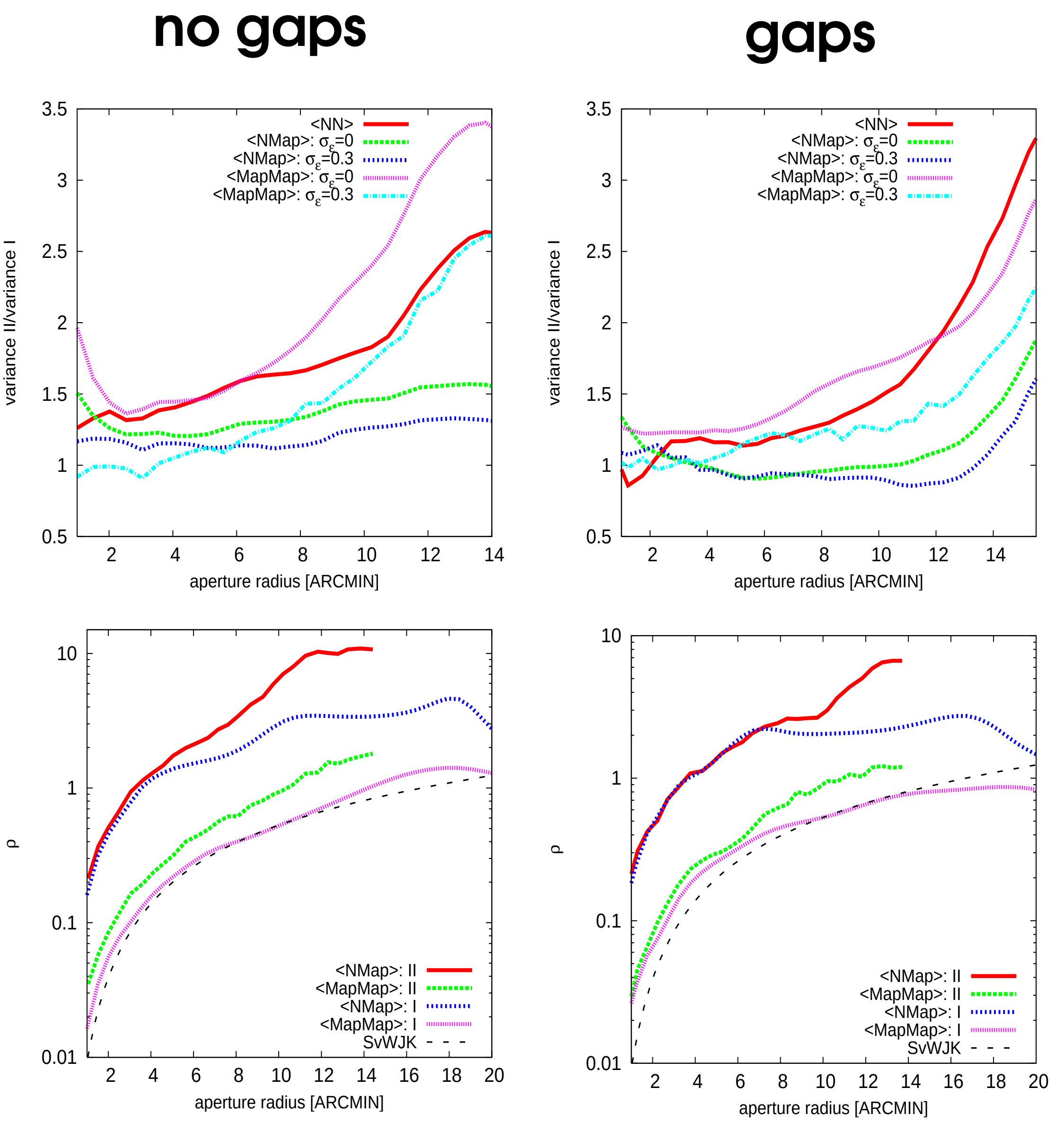

Figure 3.11.: ***top row:*** *Ratio II/I of the field-to-field variances of the statistical errors of* $\langle N^2 \rangle$, $\langle N M_{\rm ap} \rangle$ *and* $\langle M_{\rm ap}^2 \rangle$, *respectively. The result for the Monte Carlo samples without gaps is plotted in the left panel, with gaps in the right panel.* ***bottom row****: Monte Carlo average of* ρ *- Eq. (3.89) - for the estimators "I" and "II" of* $\langle N M_{\rm ap} \rangle$ *and* $\langle M_{\rm ap}^2 \rangle$. *The left panel is for the data set without gaps, the right panel for data with gaps. The curve indicated by "SvWJK" is the theoretical* $\rho(M_{\rm ap}^2)$ *for estimator "I", thus Eq. (3.91), divided by* 3.

was introduced in Schneider *et al.* (1998, SvWJK hereafter) for the estimator of $\langle M_{\rm ap}^2\rangle$, type "II", for the following reason. According to SvWJK the variance of the $\langle M_{\rm ap}^2\rangle$-estimate is for fields with negligible kurtosis (like for our Gaussian convergence fields):

$$\sigma(\langle M_{\rm ap}^2\rangle) \approx \frac{\sigma_\epsilon^2 G}{\sqrt{2}\pi\theta_{\rm ap}^2\bar{n}} + \sqrt{2}\,\langle M_{\rm ap}^2\rangle \ , \tag{3.90}$$

where $G = 6/5$ for our polynomial filter,[12] $\theta_{\rm ap}$ is the aperture radius and $\bar{n}$ the mean galaxy number density. The first term on the RHS is the shot noise due to non-circular sources, the second term is noise due to cosmic variance. The variance due to positional shot noise of the sources is subdominant and can be neglected (SvWJK). Therefore, $\rho(\langle M_{\rm ap}^2\rangle)$ quantifies the ratio between the σ_ϵ-term and cosmic variance term:

$$\rho(\langle M_{\rm ap}^2\rangle) \approx \frac{2\,\langle M_{\rm ap}^2\rangle\,\pi\theta^2\bar{n}}{G\sigma_\epsilon^2} \ . \tag{3.91}$$

If $\rho \ll 1$ the distribution of the intrinsic ellipticities of the source galaxies mostly contributes to the variance, whereas in the opposite case cosmic variance is the dominating source of the statistical uncertainty. As noted in Schneider *et al.* (2002a), a type "I" estimator for $\langle M_{\rm ap}^2\rangle$ has, in absence of a kurtosis in the convergence field, the same ρ but lower by a factor of 3. This corresponds to the curve "SvWJK" plotted in Fig. 3.11, in the two bottom panels. Our Monte Carlo average for $\rho(\langle M_{\rm ap}^2\rangle)$, type "I", agrees very well with this prediction. The curve of ρ but for estimator "II" is found to be larger in amplitude, but not by a factor of 3 as in SvWJK. This can be explained, however, by the fact that we placed the aperture centres at the grid points of a 128×128 grid. This leads for our range of aperture radii to an overlap of neighboured apertures, while the expression for ρ in SvWJK is strictly only for the case of non-overlapping, in fact statistically independent, apertures. The presence of gaps (bottom right panel) appears to tilt $\rho(\langle M_{\rm ap}^2\rangle)$, estimator "I", by a small amount compared to SvWJK. However, the impact of gaps seems to be small so that more Monte Carlo samples are needed to obtain more significant results. Plotted in the same panels are $\rho(\langle NM_{\rm ap}\rangle)$ for the gap and non-gap case. They have roughly the same shape as $\rho(\langle M_{\rm ap}^2\rangle)$ but are larger in amplitude. Although detailed expressions remain to be worked out, we expect that the analytic expression of $\sigma(\langle NM_{\rm ap}\rangle)$ is similar to $\sigma(\langle M_{\rm ap}^2\rangle)$, Eq. (3.90), however with an additional noise term related to the positional shot noise of the foreground galaxies. In direct comparison (top row of Fig. 3.11), the variance of estimator "II" is always higher than the variance of "I" (roughly by a factor between 1 and 3). This also favours the usage of estimators "I".

The impact of noise on a single measurement is illustrated by Fig. 3.13 (for the "I" estimator). Realistic measurements on $30' \times 30'$ fields are obviously far from looking like the expected theoretical curve, at least for the measurements involving the aperture mass. Even the B-mode signals in $\langle NM_{\rm ap}\rangle$ and $\langle M_{\rm ap}^2\rangle$, usually employed as indicator for systematics in the PSF-correction of the lensing catalogues, scatter heavily about zero. Thus, there is no point in using the B-mode signal of a single field of this size as a quality indicator for PSF-correction. Such a decision can only be found by averaging the B-mode signal over many fields.

Figs. 3.14 and 3.15 display the correlations, $r(\theta_1,\theta_2)$, of the estimates belonging to different aperture radii, θ_1 and θ_2. Note that the correlation matrices are based on the Monte Carlo

[12] According to SvWJK one has $G = \pi\theta_{\rm ap}^2 \int {\rm d}\theta\, Q^2(|\vec{\theta}|^2) = 2\pi^2 \int_0^1 {\rm d}x\, x\, q^2(x)$.

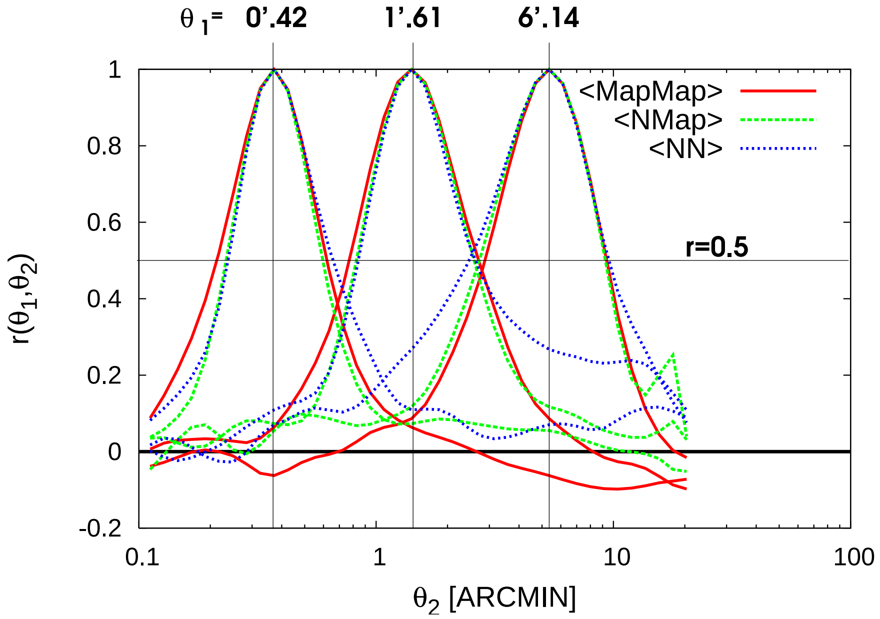

Figure 3.12.: *Correlation coefficient $r(\theta_1,\theta_2)$ of the estimators $\langle N^2\rangle$, $\langle NM_{\rm ap}\rangle$ and $\langle M^2_{\rm ap}\rangle$, type "I", with no gaps, with $\theta_1=0'.42,1'.61,6'.14$ fixed. The curves present cuts through the matrices in Fig. 3.14, left column.*

samples without intrinsic ellipticities of the background source galaxies in order to obtain a better signal-to-noise for the matrices. We observe several things: a) On scales where measurements from both estimators "I" and "II" are accessible, the estimator correlations of both methods are basically the same (in areas where the correlation is larger than $r\approx 0.25$), b) our gap pattern has but little effect on the correlations, and c) the correlations are essentially only large, $r\gtrsim 0.5$, within a strip about the diagonal. Cuts, *i.e.* keeping θ_1 fixed while varying θ_2, through the correlation matrices $r(\theta_1,\theta_2)$ are plotted in Fig. 3.12. We find that almost independent of θ_1 the correlation decreases to $r\simeq 0.5$ once a certain ratio $\theta_1/\theta_2=f$ or $\theta_2/\theta_1=f$ is reached, namely $f\simeq 1.78, 1.74, 1.77$ for $\langle M^2_{\rm ap}\rangle$, $\langle NM_{\rm ap}\rangle$ and $\langle N^2\rangle$, respectively. For the case of $\langle M^2_{\rm ap}\rangle$, this is in good agreement with Schneider *et al.* (2002a), see their Fig. 3.

Although the presented results are for a very specific set of parameters (field size, cosmology, redshift bins, galaxy number density, gap pattern, *etc.*), we think that they are roughly representative for the general picture. The general conclusion is that the estimators "I" should be the first choice, while "II" can only reach an accuracy of about $10\%-20\%$ under realistic circumstances. However, the approach "II" has a technical advantage compared to "I" due to which it should not be completely banned: it is easily extended to higher-order statistics as, for example, the estimator for $\langle M^3_{\rm ap}\rangle$ in Schneider *et al.* (1998) shows. General estimators for $\langle N^nM^m_{\rm ap}\rangle$ surely can equally easily be written down. This is not the case for the approach "I", where, first of all, a sensible definition for n-point correlators between shear and galaxy number density has to be found; not mentioning the transformation to the aperture statistics that has to be worked out in the second step. To get an idea of this effort, we refer the reader to Schneider & Watts (2005), Schneider, Kilbinger & Lombardi (2004), Jarvis *et al.* (2004) and Schneider & Lombardi (2003). Most of these references involve even only the third-order statistics.

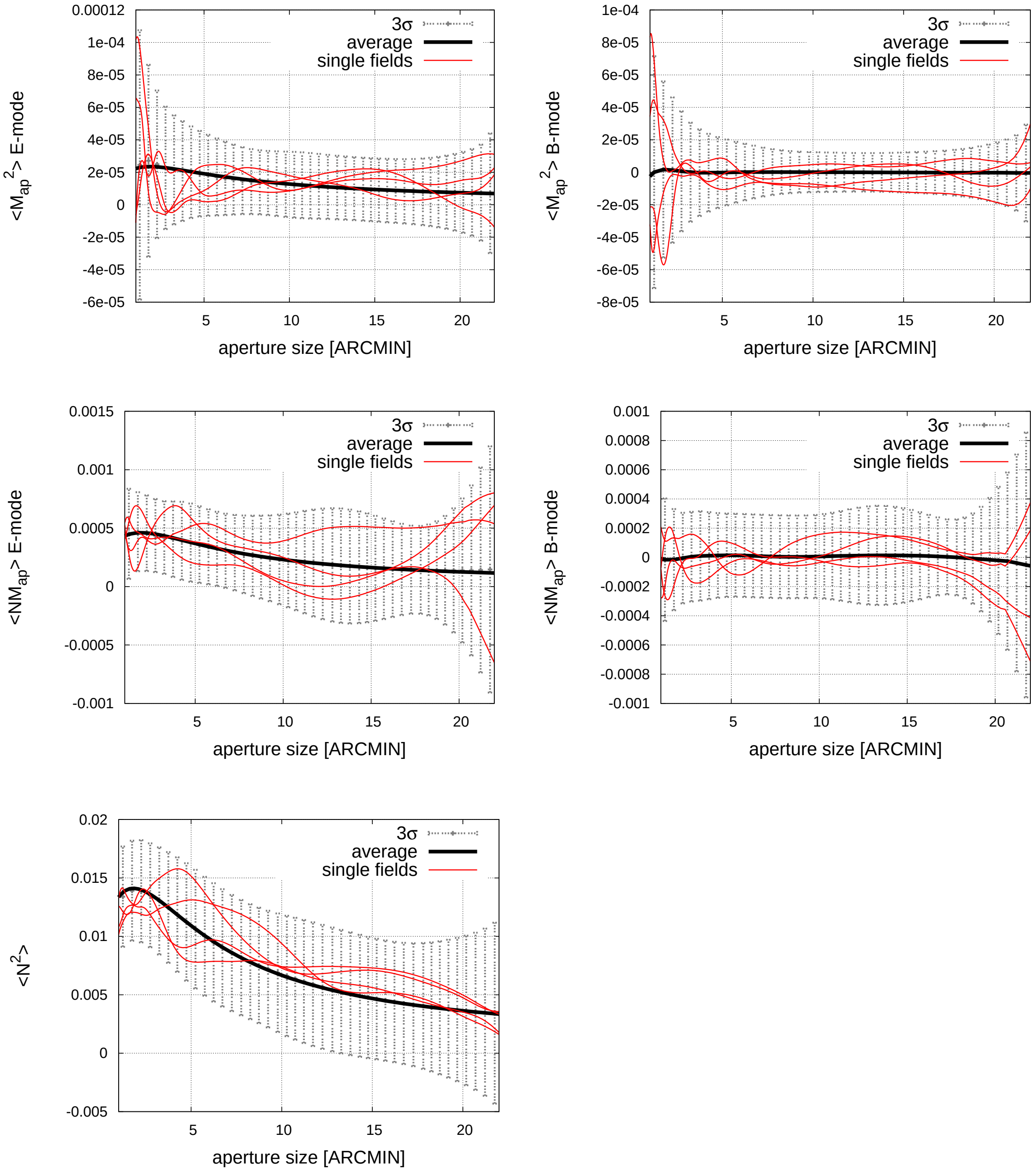

Figure 3.13.: *Compilation of some individual simulated measurements of* $\langle M_{\rm ap}^2 \rangle$, $\langle N M_{\rm ap} \rangle$ *and* $\langle N^2 \rangle$ *(top to bottom row) in the mock data applying the estimator method "I" only; the fields have been covered by a mask to mimic realistic conditions. The source galaxies are intrinsically elliptical with a variance of* $\sigma_\epsilon = 0.3$*. The right column displays the B-modes of the quantities involving the aperture mass. Note that the B-modes in individual fields are by no means vanishing compared to the E-mode, but are expected to scatter symmetrically about zero so that they are on average vanish.*

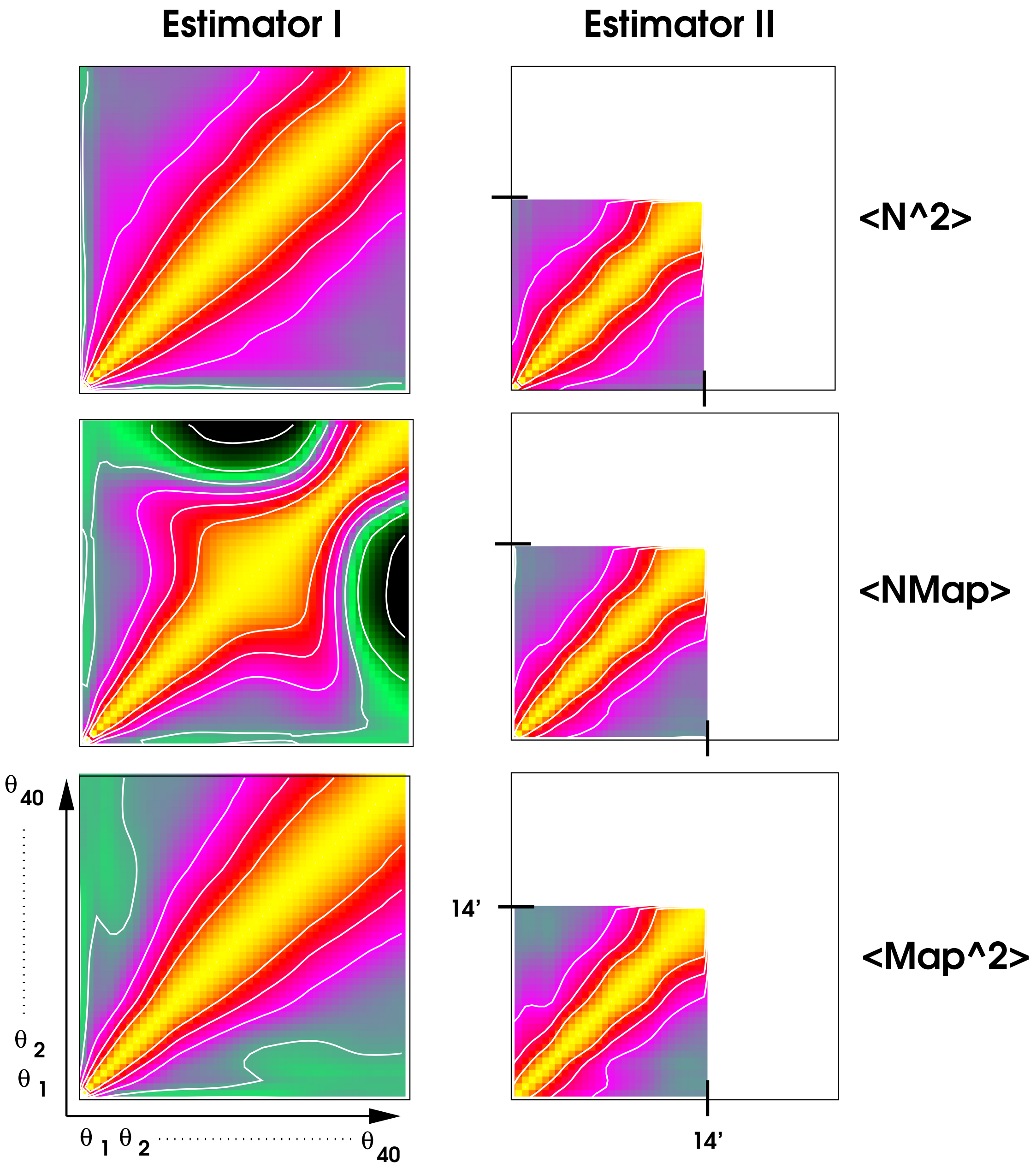

Figure 3.14.: *Correlations (**without gaps in the field**)* $r_{ij} = \langle x(\theta_i)\, x(\theta_j)\rangle\, \Delta x(\theta_i)^{-1}\, \Delta x(\theta_j)^{-1}$ *of the estimates for* $\langle x(\theta_i)\rangle$ *between different angular bins* $\theta_i = 1.0, 1.5, \ldots, 21.0$ arcmin *(*40 *bins); x denotes* $N^2, NM_{\rm ap}, M_{\rm ap}^2$ *(top to bottom row), respectively,* $\Delta x(\theta_i) \equiv \sqrt{\langle x^2(\theta_i)\rangle - \langle x(\theta_i)\rangle^2}$ *denotes the variance of x. The matrices in the left column are for estimates based upon method "I", the matrices in the right column are for estimates based upon method "II" (gap tolerance* 0%*). For each matrix, the angular size θ_i of the aperture is increasing from left to right and θ_j is increasing from bottom to top; the overlaid contours are for the levels* $r_{ij} = 0.75, 0.5, 0.25, \ldots, -0.5$. *The matrices in the right column are smaller than the matrices in the left column because apertures with radii greater than* 14.0 arcmin *could not be found in the field. The intrinsic ellipticities of the source galaxies were set to zero* ($\sigma_\epsilon = 0$)*.*

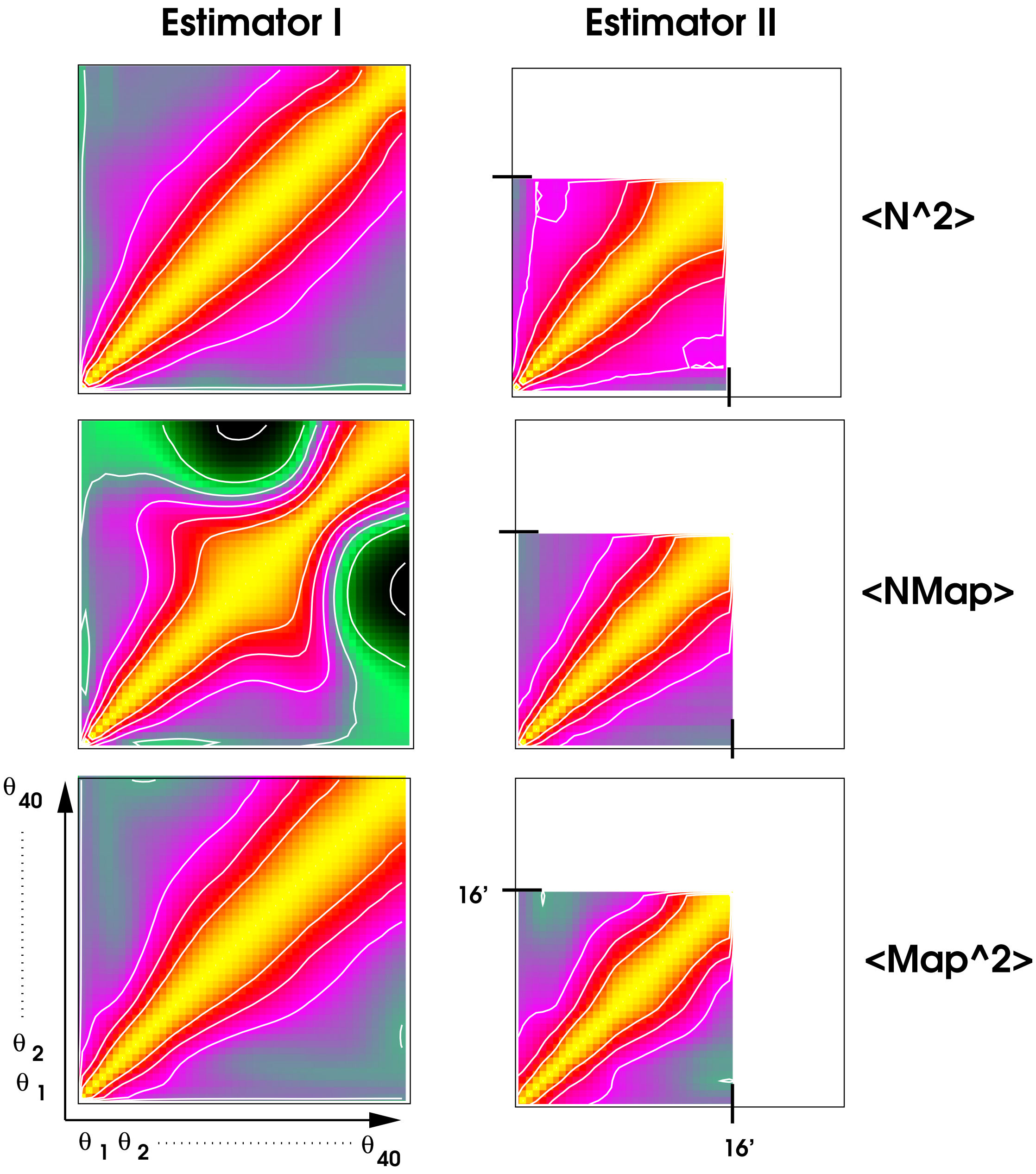

Figure 3.15.: *As in Fig. 3.14 except that the correlation matrix is obtained from fields that are obscured by a mask. The adopted gap tolerance for estimator "II" is 20%. The impact of the gap mask on the correlation matrix is relatively small.*

CHAPTER 4

Galaxy bias in GaBoDS

4.1. Introduction

In this chapter, we use the technique outlined and tested in detail in the foregoing Chapter 3 to probe the galaxy distribution relative to the dark matter distribution in the Garching-Bonn Deep Survey. The applied technique analyses fluctuations of the projected galaxy number and dark matter density within circular apertures. The galaxy sample for which the galaxy bias is measured is split into three magnitude bins. The bins have increasingly fainter median R-band magnitudes and thus represent different typical redshifts. So far, this type of analysis has been applied only once in the VIRMOS-DESCART survey and the Red-Sequence Cluster Survey (Hoekstra *et al.* 2001; Hoekstra *et al.* 2002, H02 hereafter).

The following Sect. 4.2 introduces the Garching-Bonn Deep Survey which is used for the analysis. Technical details of our analysis are summarised in Sect. 4.3, such as used aperture filter and the calibration of the galaxy bias estimates. We discuss our results, presented in Sect. 4.4, in the final Sect. 4.5.

4.2. GaBoDS: The Garching-Bonn Deep Survey

Here we will give only a brief account of the GaBoDS. For details concerning the GaBoDS and its data reduction we refer the reader to Schirmer *et al.* (2003).

4.2.1. The GaBoDS fields and their reduction

The GaBoDS comprises roughly 20 deg^2 of high-quality data (seeing better than one arcsec) in R-band taken with the Wide Field Imager (WFI) mounted on the 2.2m telescope of MPG/ESO at La Silla, Chile; the $34' \times 33'$ field of view, subject to the dither pattern applied, is covered with 8 CCD chips. The data set was compiled by Mischa Schirmer and Thomas Erben mostly from archival ESO data (for which the archive utility `querator` has been developed), partly with about 4 square degree coming from own observations. The positions of the fields were chosen randomly from regions of small stellar densities at high galactic latitudes. The limiting magnitudes of the fields is inhomogeneous, ranging between 25.0 mag and 26.5 mag (5σ) in the

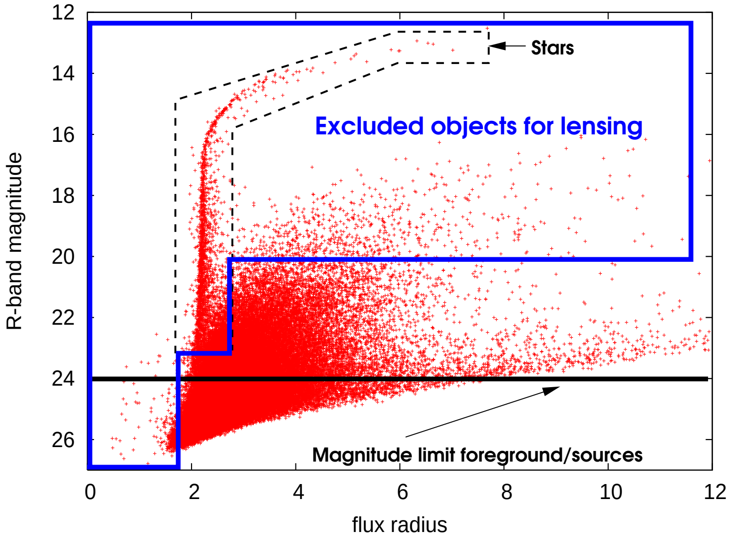

Figure 4.1.: *Magnitude vs. half-light radius plot of objects found by* `SExtractor` *in one particular field. Stars appear as almost vertical branch and can be separated from galaxies with high confidence. The solid and dashed box roughly encircles objects excluded for the lensing catalogue (for details, see Schirmer* et al. *2003). Going to the faint bottom of the diagram one finds more and more noise peaks misidentified as objects. Therefore, we do not take into account objects fainter than* 24 mag*. For the classification of foreground objects, the* `SExtractor` *CLASS-STAR parameter is used.*

R-band depending on the observation time and during what fraction of this time the seeing was acceptable for gravitational lensing applications. The data set can roughly be categorised into a shallow ($t \leq 7$ ksec, total 9.6 deg^2), medium (7 ksec $< t \leq 10$ ksec, total 7.4 deg^2) and deep (10 ksec $< t \leq 56$ ksec, total 2.6 deg^2) set depending on the total usable integration time t for each field (the fields are co-additions from single observational frames obtained according to a certain dither pattern). For this chapter, we used only the deep and medium deep part of GaBoDS amounting in total to about 10 deg^2. Note that due to the dithering, the co-added image of one field can be larger than the WFI field of view.

For the data reduction [involving overscan correction, debiasing, flat fielding, weighted co-adding using the `drizzle` package (Fruchter & Hook 2002), creation of a superflat, defringing, astrometric calibration, determination of the photometric zero point], the data imposed new, high demands which resulted into the development of a data reduction pipeline whose usage is not restricted to the aforementioned instrument only; it has successfully been tested on data from various other instruments (Erben *et al.* 2005).

4.2.2. Selection of the lens and object catalogues

After the data reduction process, `SExtractor` (Bertin & Arnouts 1996) was used to compile a catalogue of *source galaxy candidates* needed for the shear analysis. For the rather conservative selection of source candidates, the final co-added science frames are first smoothed with a Gaussian kernel of 4 pixel FHWM. One pixel corresponds to $0''.238$. A source candidate further needs to consist of at least 5 contiguous pixels with a total flux greater than 2.5σ

Table 4.1.: *Fields belonging to the deep (upper half) and medium (lower half) part of the GaBoDS. Note that the listed numbers of objects are based upon specific* `SExtractor` *parameters (Sect. 4.2.2) which are different for background and foreground galaxies. Fields indexed with a dagger*† *(5 fields) are not considered for the estimation of* $\langle M_{\rm ap}^2 \rangle$*; the asterisks** *fields are heavily contaminated by stars and are therefore not taken into account for* $\langle N^2 \rangle$ *(2 fields). For* $\langle N M_{\rm ap} \rangle$ *neither asterisks** *nor dagger*† *fields are used (7 fields).* α *and* δ *denote the equatorial coordinates of the fields' centres in degree, latitude and longitude, respectively.*

Field	α(2000.0)	δ(2000.0)	[ksec]	#total	#FORE-I	#FORE-II	#FORE-III	#BACK-I
A1347_P1	175.25702	−25.51474	13.5	34949	242	468	1732	6639
A901	149.07771	−10.02734	18.1	47150	729	1168	3146	15617
AXAF	53.13344	−27.82255	57.2	62277	445	1060	3388	17125
CAPO_DF	186.03787	−13.10764	13.0	29712	794	1372	3174	4630
FDF	16.44541	−25.85742	11.8	33964	668	1236	3061	15168
NDF	181.36237	−7.65226	21.8	22840	634	1204	2713	11138
S11	175.74860	−1.73458	21.5	45313	645	1157	3346	15444
SGP	11.49852	−29.61047	20.0	47072	630	1293	3537	16051
SHARC2	76.3333	−28.81805	11.4	37576	669	1336	3431	14684
F4_P3	322.32389	−39.72689	10.0	32832	672	1254	3123	10789
F17_P1*	216.41916	−34.69460	10.0	30662	2000	2848	4701	9210
F17_P3*	217.02611	−34.69463	10.0	35722	1276	2061	4826	12476
A1347_P2	175.79254	−25.50918	7.5	46439	646	1516	4633	6435
A1347_P3	175.23976	−25.00933	7.0	27107	809	1429	3356	12236
A1347_P4	175.79459	−24.99836	8.0	27166	1094	1683	3485	10717
AM1	58.81181	−49.667762	7.5	27478	682	1409	3105	11207
B8p0†	340.34886	−9.59009	7.2	23208	789	1195	2624	10586
Deep1e	341.96679	−39.52874	9.0	27157	1008	1555	3288	9076
Deep2e†	53.12291	−27.30467	7.5	25939	794	1413	3111	13413
Deep2f	53.66995	−27.32400	7.0	23263	1044	1583	3311	11789
Deep3b	170.66159	−21.70969	9.3	30624	861	1549	3392	5235
Deep3c	170.01909	−21.69960	9.0	30529	912	1562	3510	12629
Deep3d	169.42875	−25.85742	9.3	31188	945	1555	3317	13042
Deep1a	343.79506	−40.19886	7.2	28852	987	1384	3348	12503
Deep3a	171.24559	−21.68289	7.2	27472	990	1503	3266	11945
F4_P1†	321.65611	−40.25193	9.5	29424	1165	1839	3937	13177
F4_P2†	321.71942	−39.76761	7.0	26540	1207	1791	3632	11163
F4_P4†	322.32389	−39.72689	7.5	22706	1223	1678	3257	9977
$\sum$ 28 fields				9×10^5	3×10^4	4×10^4	1×10^5	3×10^5

Foreground object catalogue

sample	bin limits [mag]	#objects	$\langle z \rangle$
FORE-I	$19.5 \leq \mathrm{R} < 21.0$	2.5×10^4	0.34 ± 0.09
FORE-II	$21.5 \leq \mathrm{R} < 22.0$	4.1×10^4	0.49 ± 0.12
FORE-III	$22.5 \leq \mathrm{R} < 23.0$	9.5×10^4	0.65 ± 0.14

Background source catalogue

sample	bin limits [mag]	#objects	$\langle z \rangle$
BACK-I	$21.5 \leq \mathrm{R} < 24.0$	3.2×10^5	0.67 ± 0.15
BACK-II	$22.0 \leq \mathrm{R} < 24.0$	2.9×10^5	0.69 ± 0.15
BACK-III	$23.0 \leq \mathrm{R} < 24.0$	1.8×10^5	0.74 ± 0.15

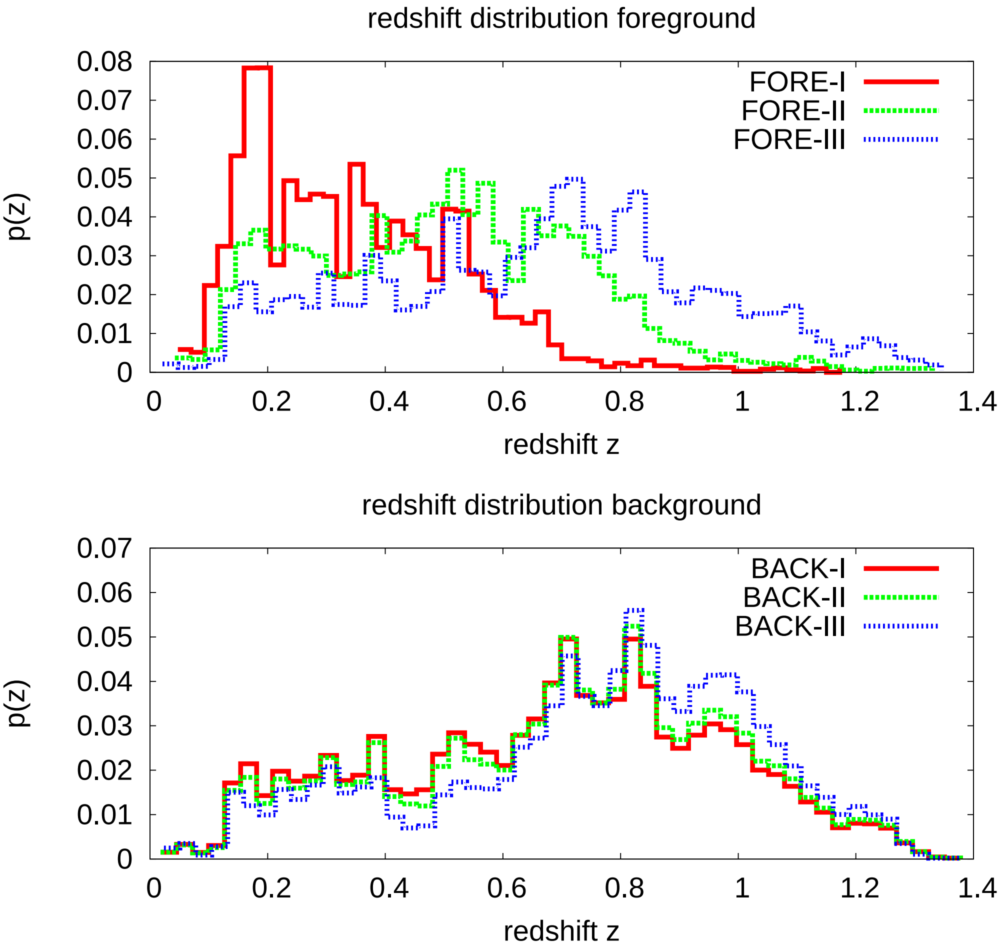

Figure 4.2.: *Redshift distribution of the foreground and background galaxy R-band bins as estimated from the photometric redshifts in the COMBO-17 fields A901, AXAF (CDFS) and S11 (Wolf et al. 2004). The upper table lists the limits of the magnitude bins, the total number of objects for all* 28 *fields (deep and medium deep fields in GaBoDS), the mean redshift and the* 1σ*-variance inside each bin.*

above the background noise level, and it has to possess a clearly defined quadrupole moment ($cl \neq 0$, `analyseldac`) and position (USNO-A2 as reference catalogue, Mario Radovich's `astrometrix`). Stars and galaxies are distinguished in a magnitude vs. half-light radius plot of the selected objects (see Fig. 4.1 for an example). In this scatter plot, stars that are not too faint are clearly identified as a column of objects with roughly identical half-light radius $r_\star$. Objects with a half-light radius smaller than $r_\star$ plus some safety offset are rejected as source candidates. An exception are objects in the faint part (fainter than 23.5 mag in R-band) near this column.

As accurate measurements of galaxy shapes are the key in a weak lensing analysis, the quadrupole moments in the galaxy light profiles of the source candidates have to be corrected for PSF effects: atmospheric turbulence and instrumental effects also distort the galaxy images. This is done using the KSB method (Kaiser *et al.* 1995) by its implementation in the `imcat` software package. A detailed description of the PSF correction procedure may be found in Erben *et al.* (2001). The PSF fitting polynomial used is of order 2.

In the estimators of the aperture statistics, every source galaxy is weighted with a statistical weight. This weight, w_i, is defined by the variance σ_ϵ^2 in ellipticity of the 12 nearest neighbours of a galaxy i in the magnitude vs. half-light radius diagram: $w_i = 1/\sigma_\epsilon^2$. In the case that the ellipticity of a galaxy exceeds $|\epsilon| = 0.8$ it automatically is attributed the weight zero and is hence not considered further in the analysis. Applying this cut removes outliers with unrealistic ellipticities, produced by the KSB technique, which can strongly affect the final results. Since this removes real high ellipticities as well, we also can expect to slightly bias the final result, but only on a level smaller than the remaining statistical errors (Marco Hetterscheidt, private communication). The final lensing catalogue is split into three magnitude bins BACK-I, BACK-II and BACK-III, see Fig. 4.2.

The actual *foreground objects*, of which the bias parameters are measured, are selected with less conservative `SExtractor` parameters; only their positions not the shapes are of interest. For them, we demand a minimum of 3 contiguous pixel for being an object candidate and a flux larger than 2σ above the flux noise background in the field. Foreground galaxies are finally selected if they have a `SExtractor` CLASS_STAR parameter less than 0.92 and are brighter than 24 magnitudes.

For the final analysis, we consider only the medium and deep part of the GaBoDS comprising in total 28 WFI fields corresponding to an area of about 10 deg^2. In order to select for the bias analysis different mean redshifts of the object (foreground) catalogues we subdivide the object catalogue into the three different R-band bins FORE-I, FORE-II and FORE-III as stated in the table in Fig. 4.2.

To estimate the redshift distribution of the galaxies –both foreground objects and background sources– we average the photometric redshift distribution in the different magnitude bins of the fields A901, AXAF and S11 (see Fig. 4.2). These three fields are contained in the deep part of the GaBoDS and were observed as part of the COMBO-17 Survey (Wolf *et al.* 2004, see Sect. 5.2) in 17 colours yielding quite accurate photometric redshifts with an uncertainty of $\delta z \approx 0.02\ (1+z)$ for objects brighter than $R = 24$ mag; their redshift distribution is assumed to be representative for our whole catalogue.

For the source galaxies carrying the $M_{\rm ap}$ signal, the magnitude bin BACK-I is used throughout. As can be seen in the table of Fig. 4.2, by varying only the lower limit, but keeping the upper limit of the magnitude bin fixed to $R = 24$ mag, one cannot shift the median of the background redshift distribution to much higher values than $z \approx 0.7$; essentially, only the number of sources in the bin decreases. A large median redshift of the source galaxies is desired to achieve a good lensing efficiency. Since we do not use objects fainter than 24 mag in order to maintain good accuracy in the estimate for the redshift distribution of the background, the bin BACK-I for all three foreground bins FORE-I, FORE-II and FORE-III is the best choice.

Table 4.1 summarises the number of foreground galaxies and sources found in the individual fields and magnitude bins.

4.3. Method details

The method for measuring the linear stochastic bias with aperture statistics is described in detail in Sects. 3.2.3 and 3.2.4. Based on the conclusion in Chapter 3, we follow H02 who prefer the estimators based on two-point correlation functions of the galaxies' spatial clustering, galaxy-galaxy lensing and cosmic shear. For the GaBoDS analysis, we bin the three correlators into 7300 linear bins spanning a range between $0' < \theta \leq 48'$ (the diagonal of a single WFI field). In order to reduce the computation time for the correlations, a binary tree data structure as in Pen & Zhang (2003) is used. See also Moore *et al.* (2001) and Jarvis *et al.* (2004).

4.3.1. Aperture filter functions

To weight density fluctuations inside apertures we use a compensated polynomial filter (H02; Schneider *et al.* 1998)

$$u\,(x) \;=\; \frac{9}{\pi}\left(1-x^2\right)\left(\frac{1}{3}-x^2\right)\,H(1-x)\,, \tag{4.1}$$

$$q\,(x) \;=\; \frac{6}{\pi}x^2\left(1-x^2\right)\,H(1-x)\,, \tag{4.2}$$

which by definition vanishes for $x \geq 1$. See also Sect. 3.4.2. The filter has the effect that only dark matter or galaxy number density fluctuations from a small range of angular scales contribute to the N- or $M_{\rm ap}$-signal as can be seen in Fig. 4.3; it acts as a narrow-band filter for the angular modes with highest sensitivity[1] to $l_{\rm c} \sim 4.5/\theta_{\rm ap} \approx 0.7 \times \frac{2\pi}{\theta_{\rm ap}}$ (Schneider *et al.* 1998). Apertures with radius $\theta_{\rm ap}$ therefore effectively probe a comoving physical scale of $f_{\rm K}(\bar{w})\theta_{\rm ap}/0.7$, if $\bar{w}$ is the median comoving radial distance of the galaxy sample under examination. For the effective scales quoted in the following we ignore the small shift due to the factor 0.7 and take simply $f_{\rm K}(\bar{w})\theta_{\rm ap}$.

4.3.2. Calibration of the bias estimators

The linear stochastic galaxy bias is estimated according to Eqs. (3.13). The presence of the calibration factors $f_{1/2}$ in these equations has a simple explanation. Imagine the idealised case that the foreground galaxies are located at one redshift, $z_{\rm f}$. The source galaxies, needed to infer the matter distribution at the redshift of the foreground galaxies by means of lensing, shall also

---

[1] At higher spatial frequencies beyond $l_{\rm c}$ the filter shows wiggles which are due to the finite support of the polynomial filter. This could be avoided, for instance, by using the exponential filter proposed by van Waerbeke (1998) which, however, does not have a finite support, *i.e.* it has no clearly defined aperture radius.

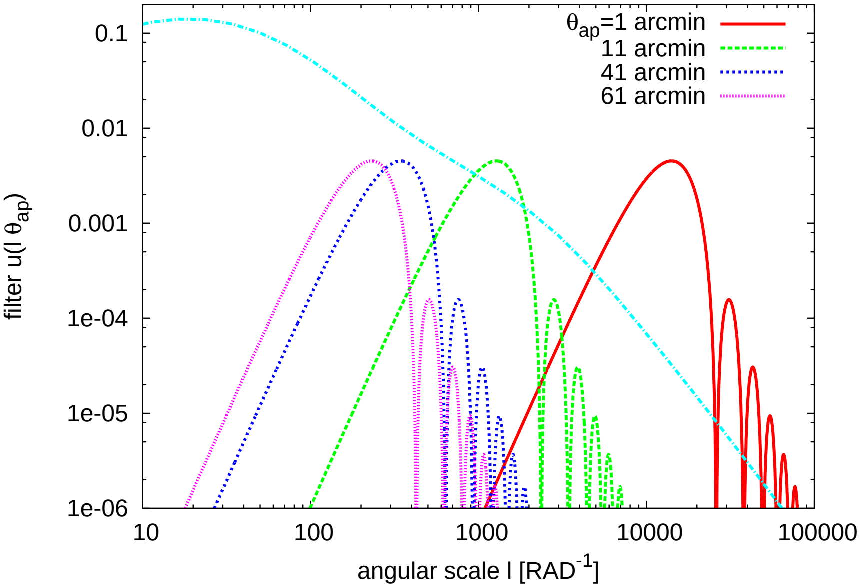

Figure 4.3.: *Sensitivity of $M_{\rm ap}\left(\theta_{\rm ap}\right)$ and $N\left(\theta_{\rm ap}\right)$ to dark matter and galaxy number density fluctuations, respectively, as a function of angular scale ℓ using the polynomial filter in Eq. (4.1). Most sensitivity is given to the scales $\ell_{\rm c}\sim 4.5/\theta_{\rm ap}$ where $\theta_{\rm ap}$ is the aperture radius. For illustration, we have plotted the power spectrum of the expected galaxy number density fluctuations, P_{nn}, of an unbiased galaxy population with a mean redshift of $\langle z\rangle=0.28$ (see Eq. 3.58).*

be located at one redshift, $z_{\rm b}$, but farther away than the foreground, $z_{\rm b}>z_{\rm f}$. Now, the aperture number count, N, of the foreground contains information on the galaxy distribution at one redshift only, while the aperture mass $M_{\rm ap}$ –or convergence κ– contains contributions from the matter density field of all redshifts up to $z_{\rm b}$ (see Eq. 3.61). Quantifying the galaxy bias of the foreground requires the comparison of the random field N with the dark matter distribution at $z_{\rm f}$, $\Delta M_{\rm ap}$, which is contained in $M_{\rm ap}$ but only as part of the total signal $M_{\rm ap}=M^\prime_{\rm ap}+\Delta M_{\rm ap}$. Most of the signal in the aperture mass originates from dark matter inhomogeneities outside $z_{\rm f}$, $M^\prime_{\rm ap}$. Moreover, $M_{\rm ap}$ is not a density contrast, as N is, but proportional to it by some number depending on the fiducial cosmology. Naively identifying N with the galaxy number density contrast, $\delta_{\rm g}$, and $M_{\rm ap}$ with the matter density contrast, $\delta_{\rm m}$, at redshift $z_{\rm f}$ therefore gives the wrong linear stochastic bias parameters (1.49). The bias parameters have to be corrected, and this is done by means of the calibration factors $f_{1/2}$.

Since $M^\prime_{\rm ap}$ and $\Delta M_{\rm ap}$ are related to the dark matter field at different redshifts, they are only very weakly correlated $\left\langle M^\prime_{\rm ap}\Delta M_{\rm ap}\right\rangle\approx 0$. According to H02, the calibration factors $f_{1/2}$ can therefore be calculated by means of

$$
\begin{aligned}
f_1\left(\theta_{\rm ap}\right) &= \sqrt{\frac{\left\langle M^2_{\rm ap}\left(\theta_{\rm ap}\right)\right\rangle}{\left\langle N^2\left(\theta_{\rm ap}\right)\right\rangle}}\,, \qquad (4.3)\\
f_2\left(\theta_{\rm ap}\right) &= \frac{\sqrt{\left\langle N^2\left(\theta_{\rm ap}\right)\right\rangle\left\langle M^2_{\rm ap}\left(\theta_{\rm ap}\right)\right\rangle}}{\left\langle N\left(\theta_{\rm ap}\right)M_{\rm ap}\left(\theta_{\rm ap}\right)\right\rangle}\,,
\end{aligned}
$$

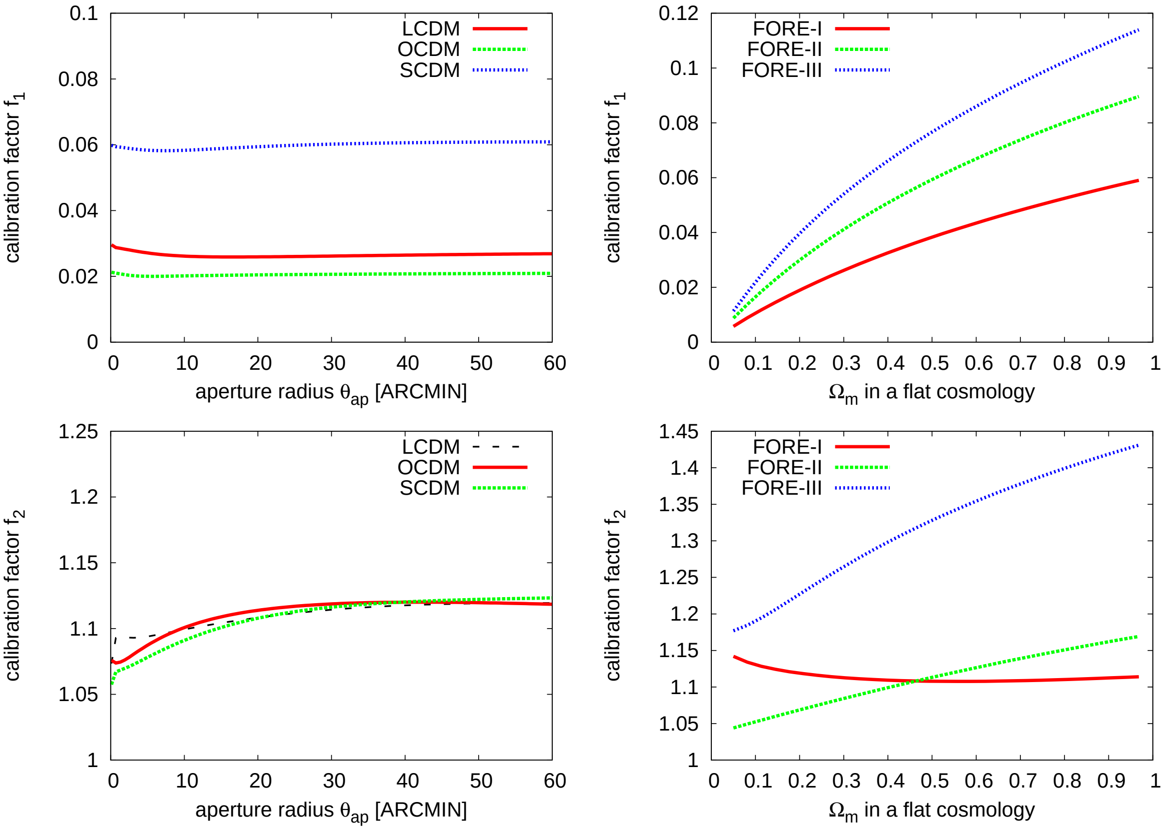

Figure 4.4.: ***left column***: *Scale-dependence of the calibration factors* f_1 *and* f_2 *in Eqs. (3.13) for three different cosmological models* (Ω_m,Ω_Λ, Γ, σ_8, h) *with adiabatic CDM: LCDM(0.3,0.7,0.21,0.9,0.7), OCDM(0.3,0.0,0.21,0.9,0.7) and SCDM(1.0,0.0,0.7,0.6,0.7). For the redshift distributions of the foreground and source galaxies, we assume the distribution in FORE-I and BACK-I, respectively (see Fig. 4.2). The dependence on scale is very weak and mostly in the non-linear clustering regime.*
right column: *Depicted is the over a range of* $10' \leq \theta_{ap} \leq 60'$ *averaged value of* $f_{1/2}$ *for* $\Omega_m+\Omega_\Lambda = 1$, $\Gamma = \Omega_m h$ *(Efstathiou, Bond & White 1993),* $\sigma_8 = 0.55\,\Omega_m^{-0.56}$ *(White, Efstathiou & Frenk 1993) and* $h = 0.7$. *All three curves for* f_1 *are fairly well fitted by* $f_1\,(\Omega_m) = a + b\,\Omega_m^c$, *namely* $(a = -0.006, b = 0.067, c = 0.6)$, $(-0.013, 0.105, 0.55)$, $(-0.020, 0.137, 0.508)$ *for foreground redshift distributions as in FORE-I, FORE-II and FORE-III, respectively. Except for FORE-I,* f_2 *can be fitted with the same generic function, namely* $(1.029, 0.145, 0.790)$ *and* $(1.122, 0.321, 0.661)$ *for FORE-II and FORE-III respectively. FORE-I requires an additional term:* $f_2\,(\Omega_m) = 3.654 - 2.565\,\Omega_m^{0.007} + 0.027\,\Omega_m^2$. *The deviation from a constant* f_1 *is in all three cases less than* 1.5 *percent only rising to* 3.5 *percent for* $\Omega_m < 0.1$*; for* f_2 *it is always lower than* 1.5 *percent.*

where $\left\langle N^n(\theta_{\rm ap})M_{\rm ap}^m(\theta_{\rm ap})\right\rangle$, $n+m=2$, in these equations have to be evaluated by Eqs. (3.14), (3.58), (3.62) and (3.64), specifically for the redshift distributions of foreground and background galaxies in the data and for a fiducial cosmological model *assuming that galaxies are not biased with respect to the dark matter, i.e.* $b_i = r_i = 1$. The values $f_1^{-1}(\theta_{\rm ap})$ and $f_2^{-1}(\theta_{\rm ap})$ are consequently the theoretical values of the uncalibrated $b(\theta_{\rm ap})$ and $r(\theta_{\rm ap})$, respectively, for the case that galaxies are not biased.

Importantly, it turns out (H02; van Waerbeke 1998) that the calibrations f_1 and f_2 vary only slightly for realistic aperture radii $\theta_{\rm ap}$ within a fixed fiducial cosmological model. For examples, see left column diagrams in Fig. 4.4 where $f_{1/2}(\theta_{\rm ap})$ are plotted for three fiducial cosmological models assuming the redshift distribution of FORE-I and BACK-I. The calibration factors show very little variance with $\theta_{\rm ap}$. Hence, a scale-dependence of the uncalibrated measurements already indicates an real scale-dependence in the bias parameter *without* fixing the fiducial cosmology.

We calculated the calibration factors $f_{1/2}$ for a range of spatially flat fiducial cosmologies, $\Omega_{\rm m} + \Omega_\Lambda = 1.0$, using the redshift distribution in our data set (right column in Fig. 4.4), assuming constraints on σ_8 from cluster abundances and $\Omega_{\rm b} \approx 0$. Predicting the power spectra functions requires a model for the redshift evolution of the 3-D power spectrum. For that purpose, a scale-invariant ($n=1$, Harrison-Zel'dovich) spectrum of the (adiabatic) primordial fluctuations is assumed. We use the fitting formula of Bardeen *et al.* (1986) for the transfer function (CDM), and the Peacock and Dodds (1996) prescription for evolution in the non-linear regime.

It becomes clear from Fig. 4.4 that in particular the interpretation of the bias factor, b (calibration f_1), depends on $\Omega_{\rm m}$. For the final calibration of the GaBoDS measurements we assume as fiducial cosmological model $\Omega_{\rm m} = 0.3, \Omega_\Lambda = 0.7, \sigma_8 = 0.9, \Gamma = 0.21, h = 0.7$, which is in concordance with constraints from the CMB, weak lensing and the Lyman-α forest (*cf.* Seljak *et al.* 2004; Tegmark *et al.* 2004).

4.3.3. Combining measurements from different fields

Signal average and variance

The whole data set taken into account for the analysis consists of 28 fields from the medium and deep part of the GaBoDS. For each field, we compute the two-point correlation estimates as in Sect. 3.2.4 and transform them according to the integrals Eqs. (3.22)-(3.24) to the second-order aperture statistics for radii $\theta_{{\rm ap},i} \in \{1.18', 3.45', ..., 23.85'\}$ (overall 11 linear bins). For every *individual field*, j, we make 100 bootstrap samples of the foreground and background object catalogues to estimate the statistical error of the measurements for

$$x_i^{(j)} \in \left\{\left\langle N^2(\theta_{{\rm ap},i})\right\rangle, \left\langle N(\theta_{{\rm ap},i})M_{\rm ap}(\theta_{{\rm ap},i})\right\rangle, \left\langle M_{\rm ap}^2(\theta_{{\rm ap},i})\right\rangle\right\} \tag{4.4}$$

for the various aperture radii. The aperture moments x_i from all fields are combined to one final result by the weighted average

$$\bar{x}_i = \frac{\sum_{j=1}^{N_p} x_i^{(j)}\, w_i}{\sum_{i=1}^{N_p} w_i}\;. \tag{4.5}$$

As weight we use the bootstrapping variance of $x_i^{(j)}$ in the individual fields, $w_i = 1/\sigma^2(x_i^{(j)})$. This weighting scheme yields the minimum-variance average of the statistically independent variables $x_i^{(j)}$. In the following results, the assigned 1σ-error bars Δx_i of the combined x_i account for the *cosmic variance* which is estimated from the variance among the N_p GaBoDS fields:

$$(\Delta x_i)^2 = \frac{1}{N_\mathrm{p}\left(N_\mathrm{p}-1\right)} \sum_{j=1}^{N_\mathrm{p}} \left(x_i^{(j)} - \bar{x}_i\right)^2 \ . \tag{4.6}$$

Error covariance

To assess the goodness of our fiducial cosmological model and the redshift distribution estimate of the sources we compute the reduced χ^2 of the field averages of $\left\langle M_\mathrm{ap}^2\right\rangle$ with respect to the theoretical model. This requires the knowledge of the covariances between the errors in the different angular bins, not only the statistical variance inside a bin. We use the covariance, $C_{kl}^{(j)} = \langle\Delta^{(j)}x_k\Delta^{(j)}x_l\rangle$, of the bootstrapping errors, $\Delta^{(j)}x_k$, in every individual field j to estimate the correlation between the statistical errors of the estimates for different aperture radii:

$$R_{kl}^{(j)} = C_{kl}^{(j)}/\sqrt{C_{kk}^{(j)}C_{ll}^{(j)}} \ . \tag{4.7}$$

In a second step, we average the correlation matrices from the different fields yielding a combined $\bar{R}_{kl} = \frac{1}{N_\mathrm{p}}\sum_j R_{kl}^{(j)}$. The final covariance is obtained by means of $\bar{C}_{kl} = \bar{R}_{kl}\sqrt{(\Delta x_k)^2(\Delta x_l)^2}$ with $(\Delta x_k)^2$ from the cosmic variance error (4.6). The resulting covariance matrix has the cosmic variance errors on the diagonal.

We evaluate the χ^2 per degree of freedom n by

$$\chi^2/n = \frac{1}{N_\mathrm{bins}} \sum_{i,k=1}^{N_\mathrm{bins}} \left(\bar{x}_i - \hat{x}_i\right)\left[\bar{C}^{-1}\right]_{i,k}\left(\bar{x}_k - \hat{x}_k\right) \ , \tag{4.8}$$

where $\hat{x}_i$ denotes the theoretically expected value for the measurement x_i and $\bar{C}^{-1}$ the inverse of the error covariance. N_bin is the number of aperture radii bins (here: 11).

4.4. Aperture statistics results

The combined measurements for $\left\langle N^2\right\rangle$, $\langle NM_\mathrm{ap}\rangle$ and $\left\langle M_\mathrm{ap}^2\right\rangle$ can be found in Fig. 4.5 and Fig. 4.7, respectively. According to the method described in Sect. 3.2.4 they are based upon the two-point correlators ω, $\langle\gamma_\mathrm{t}\rangle$ and $\xi_\pm$; the combined measurement of the last two is plotted in Fig. 4.6.

4.4.1. Aperture number count dispersion

The aperture number count dispersion, $\left\langle N^2\right\rangle$, is, except for the lowest angular bin, well described by a power law for the angular clustering $\omega\left(\theta\right)$ (Eq. 3.28) with a slope of -0.8, see Fig. 4.5. A power-law behaviour with similar slopes is also observed in other surveys (*e.g.* Zehavi *et al.* 2002). The galaxy clustering in FORE-I, a sample roughly comparable to the foreground sample of H02, is in agreement with H02. Furthermore, we clearly observe a dependence of the clustering amplitude on the mean magnitude of the galaxies: the fainter the samples' median magnitude, the smaller the clustering. Note that $\left\langle N^2\right\rangle$ is insensitive to the integral constraint

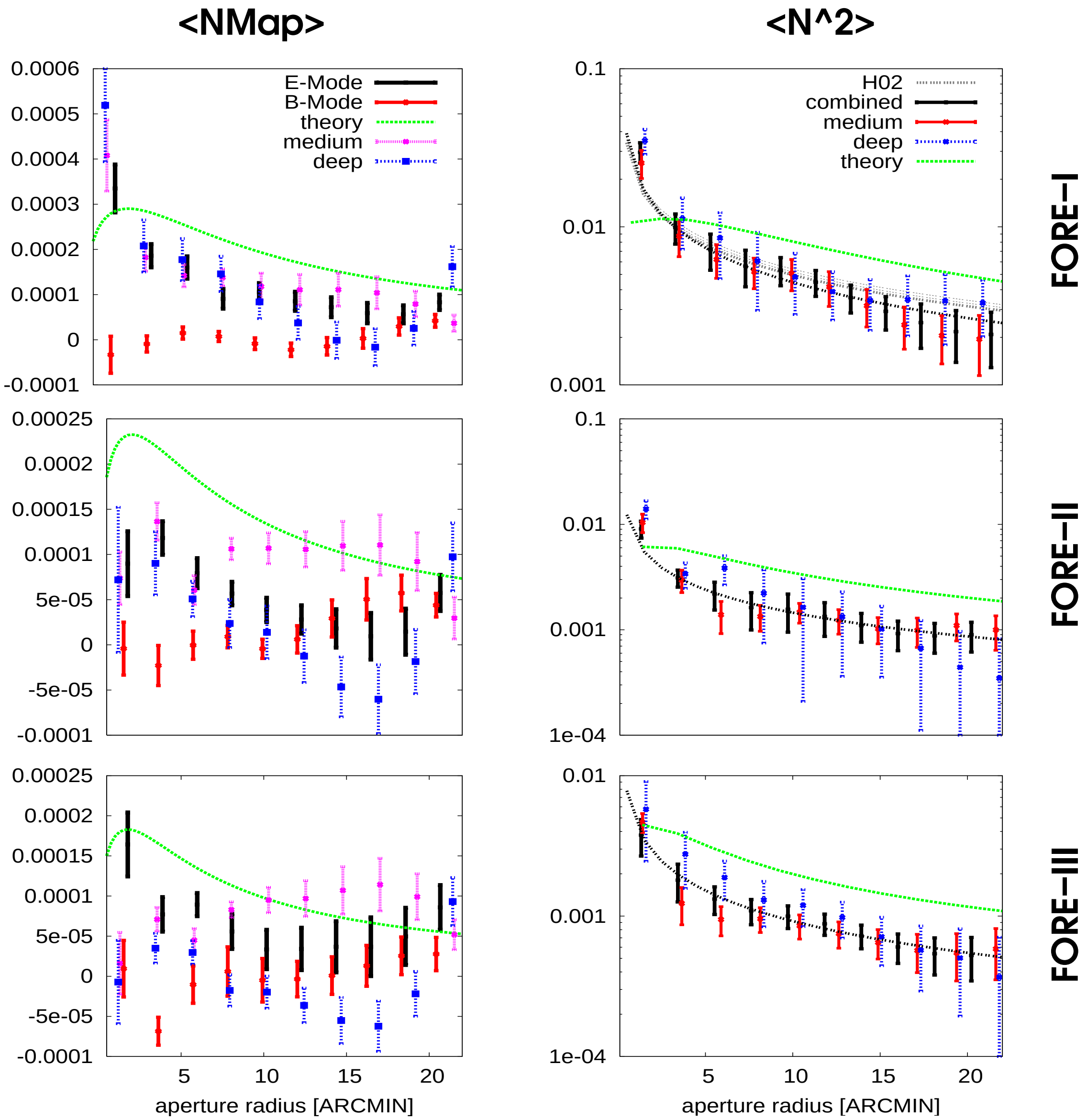

Figure 4.5.: *Plots of the measured* $\langle NM_{\rm ap}\rangle$ *(left column:* 1σ *errors) and* $\langle N^2_{\rm ap}\rangle$ *(right column:* 2σ *errors) for different aperture radii and magnitude bins for the foreground galaxies (top to bottom: FORE-I, FORE-II and FORE-III). The theoretical curves assume concordance* ΛCDM *(Sect. 4.3.2), the redshift distributions in Fig. 4.2 and the foreground galaxies being unbiased with respect to the dark matter. Deviations of the E-modes from the "theory" in the left column indicate a biased galaxy population which is clearly observed. Note that we plotted also the E-modes for the deep and medium data set separately. The B-modes are consistent with zero on a* χ^2/n *level of* $0.87, 0.98$ *and* 2.68 *for FORE-I, FORE-II and FORE-III respectively. Deviations of the aperture number count dispersion (right) from the theory also indicates a biased galaxy population on a particular scale. In the upper right panel, we plotted the best fit* $\omega(\theta) = (0.115 \pm 0.005)\,\theta^{-0.7}$ *to the measurement result for* $\langle N^2\rangle$ *of H02, who studied the same magnitude bin we as in FORE-I. Our measurement is roughly consistent with H02, but declines a bit faster on larger scales preferring a power law which is a bit steeper; the same steeper slope is also found in the two other bins (middle and lower panel in right column). Our best-fit parameters for a power law* $\omega(\theta) = A\,\theta^{\beta}$ *are* $\beta = -0.8$ *and* $A = 0.096, 0.030, 0.019$ *for FORE-I, FORE-II and FORE-III, respectively.*

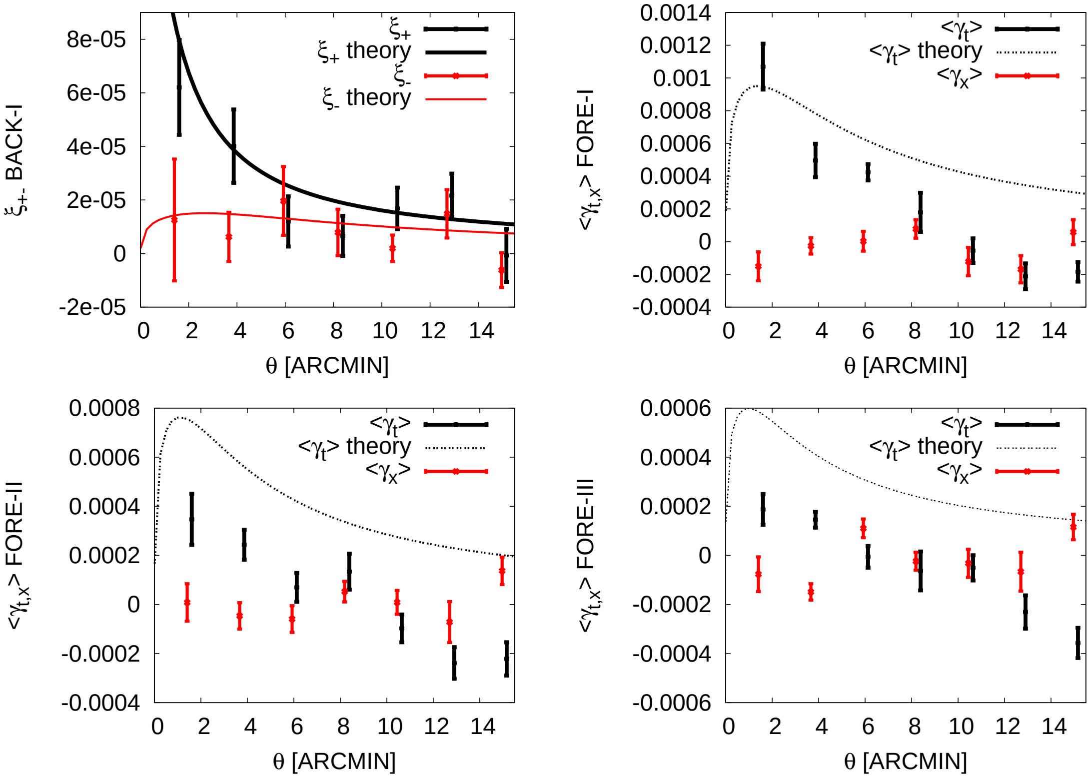

Figure 4.6.: *Combined estimate, deep and medium set, of the two-point correlators $\xi_\pm$ (beyond 6 arcsec) and $\langle\gamma_{\rm t,\times}\rangle$ (Eqs. 3.30 and 3.29). Underlying the theoretical curves are the redshift distributions in Fig. 4.2 and the fiducial cosmological model in Sect. 4.3.2. Note that the theoretical curve for the galaxy-galaxy lensing signal assumes a galaxy population unbiased with respect to the dark matter.*

which usually hampers the interpretation of angular clustering measurements (H02), so that already for the investigation of the spatial clustering alone $\langle N^2\rangle$ is a very useful statistic. This will be discussed in more detail in the following Sect. 5.3.6.

4.4.2. Aperture mass dispersion

The aperture mass dispersion for the galaxy background sources is depicted in Fig. 4.7. In the first attempt for this measurement, we observed a very steep increase in the signal, both E-mode and B-mode, below aperture radii of about $5'$ in all fields. We traced this effect back to the estimates for the shear-shear correlations, $\xi_\pm$, which have a sharp peak for bins smaller than 6 arcsec. It seems that this artificially high correlation in ellipticities of very close galaxies (up to a value of about 0.4 for both ξ_+ and ξ_-) is related to the data reduction (`drizzle`) as it is not seen in data reprocessing currently performed by Marco Hetterscheidt (private communication). In order to circumvent this problem, we start the binning of $\xi_\pm$ from 6 arcsec and reject all signal on smaller scales (see Fig. 4.8).

The correlations between the statistical errors of $\langle M_{\rm ap}^2\rangle$ for both E-mode and B-mode signals can be found in Fig. 4.10 at the end of this chapter. The correlation matrices are comparable to

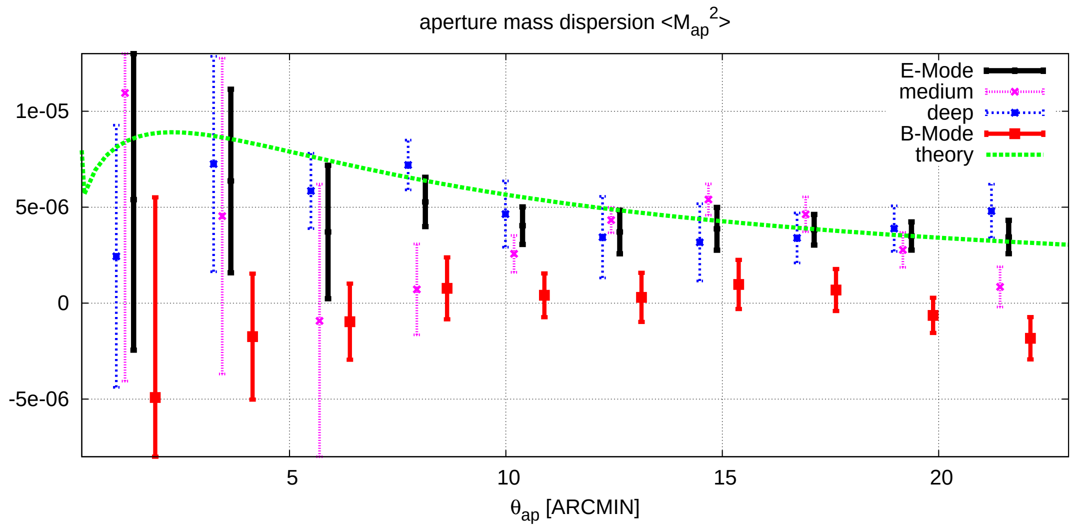

Figure 4.7.: *Aperture mass dispersion determined as weighted average over all considered fields (Sect. 4.3.3). The theoretical curve assumes the concordance parameters stated in Sect. 4.3.2. Assuming correlations of the statistical errors as in Fig. 4.10 the data points yield* $\chi^2/n = 0.37, 0.66$ *(reduced) for the E-mode and B-mode, respectively; the latter is assumed to be scattered about zero. We also plotted the E-mode signals of the two data sets "medium" and "deep" separately.*

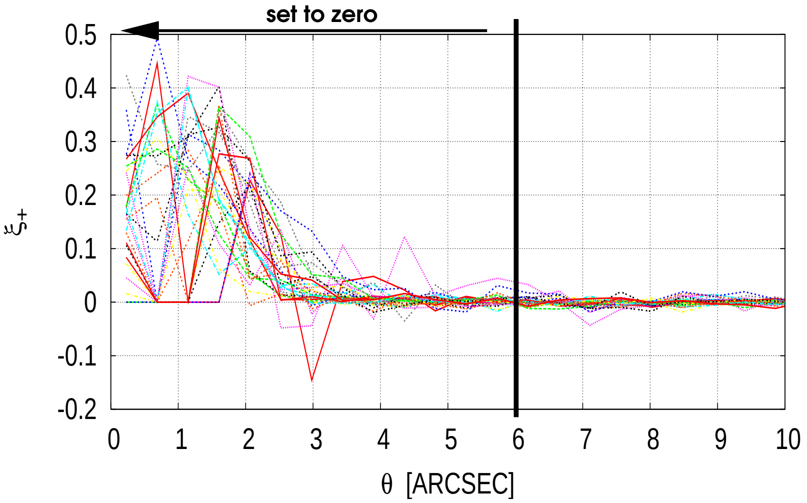

Figure 4.8.: *Plot of measured* ξ_+ *for all fields in the deep and medium deep GaBoDS. The shear correlations of all fields rise below 6 arcsec to a level that is orders of magnitude larger than what is expected by theory (*$\xi_+ \approx 10^{-5}$*), probably hinting at a problem in the data reduction pipeline; the same behaviour is observed for* ξ_- *(not plotted). We circumvent this problem by ignoring all correlations smaller than 6 arcsec setting them to zero.*

the matrices found by means of Monte Carlo simulations (Fig. 3.14 and 3.15). The data points of the E-mode are consistent with the theoretical curve but are less scattered than the error bars actually imply ($\chi^2/n = 0.37$). This could mean that the cosmic variance estimated from the signal variance between the fields overpredicts the true statistical error of the data points. However, we conclude that the agreement is fair enough to make a reasonable calibration of the bias parameters. The B-modes of $\left\langle M_{\rm ap}^2 \right\rangle$ are consistent with zero ($\chi^2/n = 0.66$) which implies that remaining systematics in the shear data are small.

4.4.3. Galaxy-matter cross-correlation

The cross-correlation between the N-maps and the $M_{\rm ap}$-maps is plotted in Fig. 4.5 (left column). The B-modes of the signal are all fairly consistent with zero ($\chi^2/n = 0.87, 0.98, 2.68$) –possibly with some remaining systematics in the faintest bin FORE-III. The correlation of the statistical errors for the B-mode signal, used for χ^2/n, can be found in Fig. 4.10. As to the striking difference in the E-mode signal of $\langle N M_{\rm ap} \rangle$ between the deep and medium data set on intermediate scales we note that the statistical errors are highly correlated over some arcmin, especially in the intermediate range (see Fig. 4.10).

The data points (E-mode) are below the theoretical prediction for $\langle N M_{\rm ap} \rangle$ which is based on a unbiased galaxy population. This already indicates that the (biasing) correlation parameter differs from unity. On the largest and smallest scales considered in these measurements, the data points for FORE-I become consistent with the theoretical curve.

4.4.4. Galaxy bias

The final result of our effort is comprised in Fig. 4.9. The bias parameters calculated from the aperture statistics, Eqs. (3.13), have been calibrated, and the aperture radii have been converted into a typical physical scale based on the mean redshift of the foreground galaxies inside the various magnitude bins (see figure caption). Over the investigated range of (comoving) physical scales, between about $0.42\,h^{-1}$Mpc $\leq r \leq 8.9\,h^{-1}$Mpc, the bias factor stays remarkably constant, possibly rising on the smallest scales. Here the errors are largest, however. Averaging the measurements for the bias over the range $4' \leq \theta_{\rm ap} \leq 18'$, weighting with the cosmic variance error, yields $b = 0.89 \pm 0.05, 0.79 \pm 0.05, 0.89 \pm 0.05$ for FORE-I, FORE-II and FORE-III, respectively. Galaxies are thus less clustered than the dark matter on that particular scales (anti-biased). The weighted average of r, the correlation factor, over the same range as before is $r = 0.8 \pm 0.1, 0.8 \pm 0.1, 0.5 \pm 0.1$ for FORE-I, FORE-II and FORE-III, respectively. This means that on average, on these scales, the galaxy distribution is not perfectly correlated to the dark matter distribution. We are going to discuss our results in the following section.

4.5. Discussion and conclusions

Observationally, the galaxy-dark matter bias can be probed by means of various methods, see Sect. 1.4. Gravitational lensing provides a promising new method in this respect. It is special because it allows for the first time to map the total matter content (mainly dark matter) with a minimum of assumptions and independent from the galaxy distribution. Such a map can be compared to the distribution of galaxies or special types of galaxies in order to investigate the galaxy bias. In particular, correlations between galaxy and dark matter density become

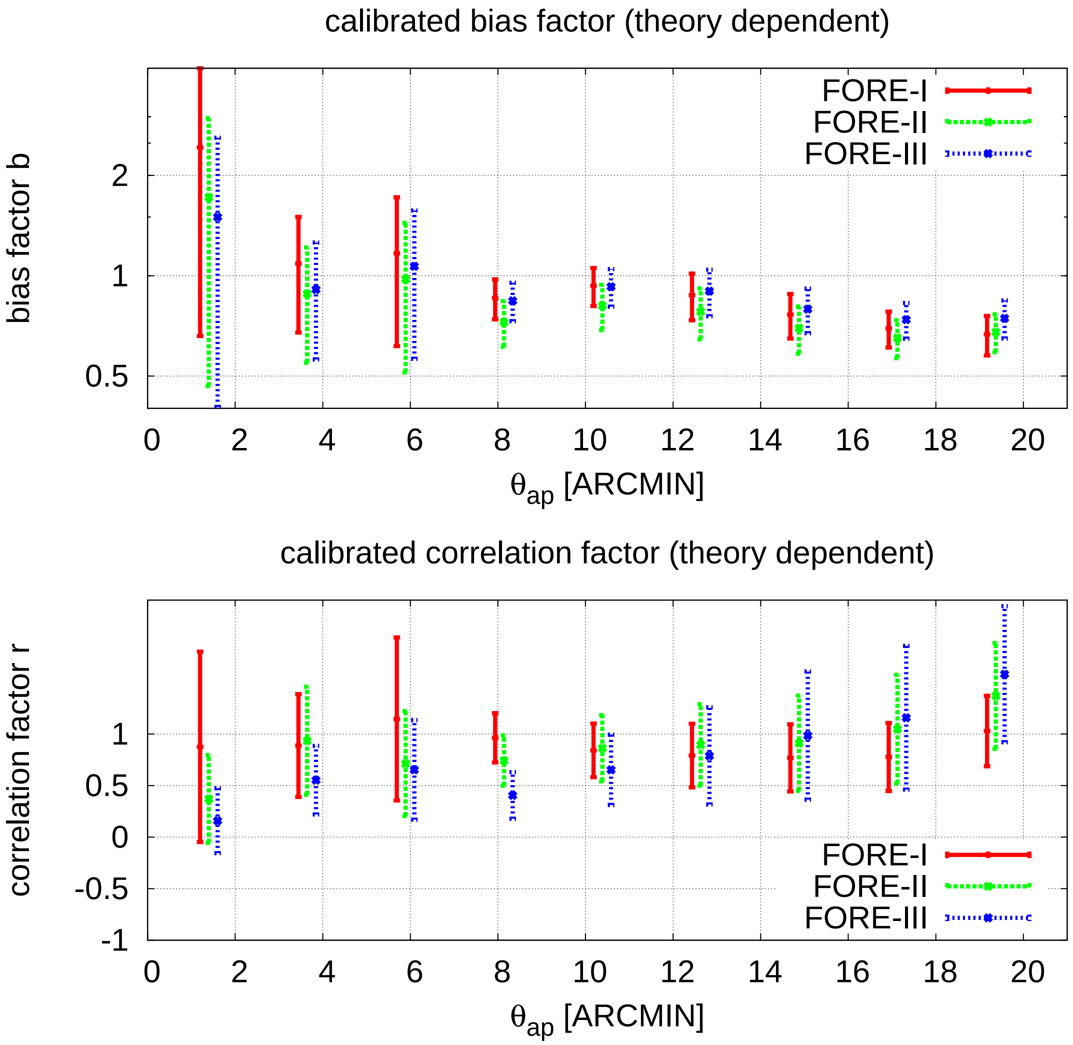

Figure 4.9.: *The linear bias factor (top panel) and correlation factor (lower panel) for the magnitude bins FORE-I, FORE-II and FORE-III (1σ error bars for cosmic variance). The effective comoving physical scale spanned by the aperture radii, $\theta_{\rm ap}$, can be estimated by the mean redshift of the galaxies in the foreground magnitude bins:* $2.66\,h^{-1}{\rm Mpc}\times(\theta_{\rm ap}/10')$, $3.71\,h^{-1}{\rm Mpc}\times(\theta_{\rm ap}/10')$ *and* $4.64\,h^{-1}{\rm Mpc}\times(\theta_{\rm ap}/10')$ *for FORE-I, FORE-II and FORE-III respectively.*

directly visible. For working out the galaxy-dark matter bias, older methods need as basis assumptions regarding the lowest-order perturbation terms for structure growth, the peculiar velocities of galaxies and their correlation to the dark matter density. Moreover, they often only allow to measure the bias on large (linear) scales, $\gtrsim 8\,h^{-1}$Mpc, whereas the non-linear regime is also accessible with lensing. However, gravitational lensing has the disadvantage that it is not equally sensitive at all redshifts. The background galaxies used for mapping the matter field is most sensitive to matter fluctuations roughly half-way between $z = 0$ and the mean redshift of the background. This defines a natural best-working regime for the method at a redshift of about $z \approx 0.5$, mostly even a bit lower, considering the depth of current galaxy surveys. It can be expected that the best-working regime will be shifted towards higher redshifts by future space-based lensing surveys. Lensing observables are quite noisy so that for a good signal-to-noise large survey areas are required.

In this chapter, we employed aperture statistics to quantify the relation between the dark matter and galaxy density. The data used is the GaBoDS with restriction to fields having total integration times larger than 7 ksec (the medium and deep set, overall about 10 $\deg^2$); this allowed us to estimate the redshift distribution of the galaxies on the basis of three COMBO-17 fields (A901, AXAF/CDFS and S11) for which accurate photometric redshifts are available (Fig. 4.2). For all the other fields, only R-band magnitudes can be used to select galaxies. For this selection, we made foreground galaxy samples by choosing galaxies from three R-band magnitude bins that have increasingly higher median magnitudes. The sample FORE-I is comparable to the foreground selection in H02. By means of the photometric redshifts of the COMBO-17 fields we can translate the magnitude information into redshift information. However, only as distribution for the whole sample. The fainter the bin gets, the broader the redshift distribution becomes, while the mean redshift moves to larger values. Therefore, only FORE-I has a rather sharp peak in redshift, while FORE-III stretches between redshifts of about $z = 0.1$ and $z \approx 0.9$ giving almost equal weight to all redshifts. Hence, FORE-II and FORE-III are averages over a wide range of redshifts. In order to get narrower distributions in redshifts with the aim to reconstruct the redshift evolution of biasing, multi-colour surveys are required.

The second-order aperture statistics are estimated from the angular clustering of the foreground galaxies, the mean tangential ellipticity of background galaxies about foreground galaxies (galaxy-galaxy lensing) and the shear-shear correlations of background galaxies. Those two-point correlators are then transformed into $\left\langle N^2\right\rangle$, $\langle NM_{\rm ap}\rangle$ and $\left\langle M_{\rm ap}^2\right\rangle$ by numerical integration. We tested the evaluation software against Monte Carlo simulated WFI fields, assuming an unbiased galaxy population, and found that the software is working to at least a few percent accuracy.

The B-modes of the aperture statistics $\langle NM_{\rm ap}\rangle$ and $\left\langle M_{\rm ap}^2\right\rangle$ are used as an indicator for systematics in the PSF-corrected shapes of the background galaxies (Figs. 4.7 and 4.5); they cannot be produced by gravitational lensing and should therefore be pure noise. Intrinsic alignments or spatial clustering of the background source galaxies can give rise to B-modes on small scales, though. We find that the B-modes are fairly consistent with zero, maybe there are remaining systematics in the $\langle NM_{\rm ap}\rangle$ signal in FORE-III. The fit of a theoretical $\left\langle M_{\rm ap}^2\right\rangle$ constructed from our fiducial cosmology and redshift distribution of source galaxies to the measured $\left\langle M_{\rm ap}^2\right\rangle$ is an important test for the calibration of the bias parameter; $\left\langle M_{\rm ap}^2\right\rangle$ is independent of the galaxy bias. Our data points are consistent with the fiducial cosmological model on a level of $\chi^2/n = 0.37$. We interpret the somewhat low value for χ^2/n as an indication that we may be overestimating the actual statistical errors of the data points but accept the fiducial cosmological model and the estimated redshift distributions as sufficiently accurate for our purposes.

The result of the galaxy bias measurement is plotted in Fig. 4.9. Overall, the galaxy bias factor and the correlation are smaller than unity. This means that galaxies are less clustered than dark matter and that the correlation of the dark matter and galaxy distribution is not perfect. A possible scale-dependence is indicated at small scales for the bias and correlation factor, and at large scales for the correlation factor only. An anti-bias on the scales considered here is in concordance with numerical simulations of dark matter structure formation (*cf.* Jenkins *et al.* 1998), although a rise of the bias factor at about our largest scales –also a theoretical prediction– is not visible in the data. Such a rise of the bias factor, or characteristic "dip" in the functional form of the bias factor (see Fig. 1.11), is however observed by H02 and Pen *et al.* (2003) using the same or a similar lensing technique. By looking at the results of H02 –comparable to the FORE-I sample results– we notice that the rise of the bias factor is just about to start at scales where our measurement stops, in particular if the statistical uncertainties in H02 are taken in to account. Therefore, it may be that we needed just slightly larger aperture radii to find the predicted behaviour. This would be possible for adjacent fields in the survey so that galaxies belonging to different fields could be correlated. As some fields in GaBoDS are indeed close to each other, we intend to repeat the bias analysis for this subset of fields in order to estimate the galaxy bias on even larger scales. For the linear correlation parameter, we observe as H02 a slight increase towards $r \sim 1$ in the last angular bin. However, the statistical uncertainties are large. Comparing the average bias, $b \sim 0.9$, and correlation factor, $r \sim 0.8$, of FORE-I to H02 near the minimum of the bias "dip" we conclude that our results are consistent.

Within the uncertainties of our measurement we do not see a difference in the biasing parameters between the three foreground bins. As the three different foreground bins represent different median redshifts of the galaxies, we conclude that on the scales considered the redshift dependence of the linear bias for $0.3 \leq z \leq 0.65$ has to be smaller than $\Delta b \lesssim 0.1$ and $\Delta r \lesssim 0.2$ (2σ confidence).

The figures for the correlation parameter –r is smaller than unity– show that the galaxies on intermediate scales are either stochastically or non-linearly biased, or a mixture of both. Discriminating between these two cases requires the additional measurement of the non-linear stochastic bias parameter $\tilde{b}$ or $\sigma_{\rm b}$, Sect. 1.4.3. To achieve this, using approaches similar to ours where statistical moments of the joint PDF of matter and galaxies are measured, one needs to invoke higher-order statistics (cumulants), see Appendix A.4. As the currently ongoing research is working on the three-point statistics of the aperture mass and the aperture number count (*e.g.* Schneider & Watts 2005; Schneider, Kilbinger & Lombardi 2004; Schneider & Lombardi 2003; Jarvis *et al.* 2004) we can expect to be capable of such task quite soon.

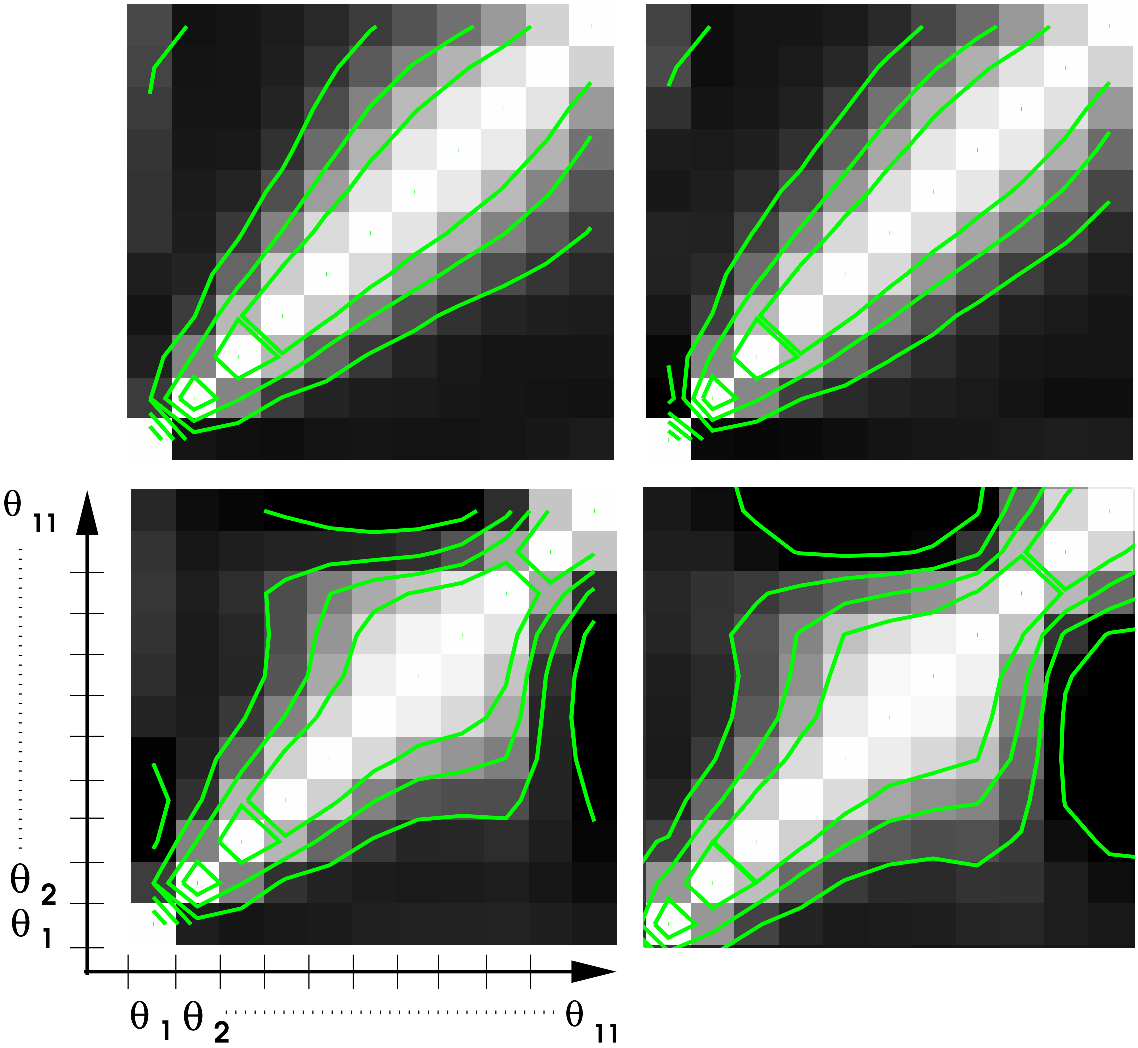

Figure 4.10.: ***top row***: *The correlation of the errors of* $\langle M_{\rm ap}^2 \rangle$ *(Fig. 4.7) as estimated by combining the bootstrap covariances of all individual fields (Sect. 4.3.3). The left panel depicts the correlation between the E-mode errors of different aperture radii; the correlation,* R*, of the B-mode errors is plotted in the right panel. The angular radius of the aperture,* $\theta_{\rm ap}$*, increases per pixel from left to right and bottom to top in the following equally spaced steps:* $\theta_{\rm ap} = 1'.18, 3'.41, ..., 23'.85$ *(overall 11 linear bins); the values on the diagonal correspond to the correlation of the error in the same bin and are consequently* $R = 1$*. The grey scale is linearly stretching from* $R = -0.1$ *to* $R = 1.0$*; the contours denote* $R = 0.73, 0.45, 0.18, -0.1$*. Note that the contours crossing the diagonal in the lower left corner is a plot artefact.*
bottom row: *Same as in the top row, but this time for the E-modes and B-modes (left to right) of* $\langle N M_{\rm ap} \rangle$ *in FORE-I. For FORE-II and FORE-III the correlation matrices look similar.*

CHAPTER 5

Galaxy bias in COMBO-17

5.1. Introduction

A long-standing question is the origin of the diversity in physical properties of galaxies. Morphologically, galaxies fall into two broad classes: early-type galaxies, with almost spheroidally appearance and none or only very small disk component, and late-type galaxies, with a small central bulge and a dominating stellar disk exhibiting different degrees of spiral structure. Within the framework of the cold dark matter paradigm for cosmological structure formation, galaxies grow and evolve by participating in a hierarchical merging process (*e.g.* Cole *et al.* 2000). The hierarchical model predicts that early-type galaxies –formed by mergers– are on average more massive, more luminous and have an older stellar population than late-type galaxies because they have lost most of their gaseous component by at least one major merger event. This is in rough agreement with observations. But doubts remain. It seems, for example, that individual early-type galaxies formed relatively quickly at high redshift and not quite recently, $z \sim 1$, as expected by hierarchical scenarios (see introduction of Bell *et al.* 2004 and references therein), although alternative interpretation of the observations leading to this conclusion are possible (van Dokkum & Franx 2001). An important source of information hinting to the nature of late-type and early-type galaxies is their spatial distribution. Early-type, reddish, galaxies are preferentially found in the cores of rich galaxy clusters where their fraction is about 90 percent, whereas outside of galaxy clusters about 70 percent of the field galaxies are bluish late-type galaxies (*e.g.* Goto *et al.* 2003; Dressler *et al.* 1997; Postman & Geller 1984; Dressler 1980).

One traditional way to study the spatial distribution of galaxies has been to look at correlations in the galaxy distribution, in particular the angular two-point correlation function (*e.g.* Peebles 1980; Davis *et al.* 1977; Totsuji & Kihara 1969). This can be translated into the correlations of the large-scale matter distribution if one knows the relation between matter and galaxy distribution, which is commonly known as galaxy bias (*e.g.* Dekel & Lahav 1999). In the local Universe, galaxies seem to be unbiased on large scales $\gtrsim 10\ h^{-1}$Mpc (Verde *et al.* 2002). This cannot be true, however, for all scales and all individual populations of galaxies. Analyses revealed that galaxy clustering depends on the properties of the galaxy population like morphology, colour, luminosity or spectral type, see Sect. 1.4.4 for more details. Therefore, different galaxy populations are differently biased with respect to the total matter component and with respect to each other. The detailed dependence of this relative bias on galaxy characteristics, scale and redshift is a window of opportunity to learn more about the formation and evolution history of galaxies. For example, the relative clustering and the galaxy-matter bias can be interpreted in terms of a physical model (Zehavi *et al.* 2004; Seljak *et al.* 2004a).

The aim of this chapter is to measure the bias –the relative bias and bias with respect to dark matter– of early-type and late-type galaxies as function of scale and redshift. For this purpose, the COMBO-17 Survey (Wolf *et al.* 2001a) offers an unique opportunity. It provides the so-far largest galaxy sample in the regime $0.2 \leq z \leq 1.1$ covering an area of ~ 0.78 deg^2, observed in 5 broad-band and 12 narrow-band filters (*cf.* Wolf *et al.* 2004). Based on the photometry, photometric redshifts of galaxies brighter than $m_R \leq 24$ mag have been derived within a few percent accuracy as well as absolute rest-frame luminosities and colours. The survey has also been designed to fit the requirements of gravitational lensing applications (Kleinheinrich *et al.* 2004; Heymans *et al.* 2004; Brown et al. 2003; Gray *et al.* 2002). The coherent shear distortions of images of COMBO-17 background galaxies can therefore be used to infer the total matter distribution in the survey using the weak gravitational lensing technique (*cf.* Gray *et al.* 2002).

By correlating fluctuations of the matter density, encoded in the image shear distortions, with fluctuations in the galaxy number density of a selected galaxy population, the weak lensing technique has become a relatively new tool to study the galaxy-matter bias (*e.g.* Sheldon *et al.* 2004; Seljak *et al.* 2004a; Pen *et al.* 2003; Hoekstra *et al.* 2002, 2001; McKay *et al.* 2001; Wilson *et al.* 2001; Fisher *et al.* 2000). The COMBO-17 Survey allows one to apply the bias analysis to galaxies from a narrow redshift interval searching for a possible redshift dependence. Furthermore, one has the option to further subdivide the galaxy sample by making cuts using the available photometric information. This is done in this chapter to distinguish between a red and a blue galaxy population in the same way as Bell *et al.* (2004). Out to at least $z \sim 1$, the distribution of galaxies in a $U-V$ vs. M_V colour-magnitude diagram (CMD) is bimodal exhibiting a red and blue peak (Bell *et al.* 2004). The red mode is the well-known colour-magnitude relation (CMR) of early-type galaxies. The standard interpretation of the CMR is that more luminous early-type galaxies have more metals and appear therefore redder. In order to make an approximate cut between early-types and late-types in the CMD a division line along the CMR is defined. In adopting this division line about 80% of the selected red galaxies have morphologies earlier than or equal Hubble type Sa (Bell *et al.* 2004 and references therein), if $z \lesssim 1$.

The machinery that is applied here to study the matter-galaxy bias is the aperture statistics (Hoekstra *et al.* 2002; van Waerbeke 1998; Schneider 1998). It is useful for analysing weak lensing data and, in particular, to measure the linear stochastic galaxy bias (Hoekstra et al. 2002) as a function of scale. In order to have a compatible statistical quantity that quantifies the relative bias between red and blue galaxies the formalism is slightly extended.

The structure of this chapter is as follows. In the following Sect. 5.2, the object and lens catalogue and their selection criteria are explained. Thereafter in Sect. 5.3 method details including estimators and used aperture filter are summarised. Conclusions on the results for the aperture statistics and galaxy bias, Sect. 5.4, are drawn in Sect. 5.5.

5.2. Galaxy catalogue selection

5.2.1. COMBO-17

The observations and data reduction of the COMBO-17 Survey is described in detail in Wolf *et al.* (2001a) and Wolf *et al.* (2003). Overall the survey consists of four different, non-contiguous fields observed in 17 optical filters[1], spanning a spectral range from $364 - 914$ nm, with the Wide Field Image (WFI) mounted on the MPG/ESO 2.2m telescope in La Silla, Chile. With a WFI field-of-view of about $33' \times 34'$ and $0''.238$ pixel resolution the total survey area amounts to approximately $1\,\mathrm{deg}^2$. The four fields are A901, AXAF (or CDFS), S11 and SGP. For the total exposure time and positions of the fields see Table 4.1 [the R-band images reduced with the GaBoDS pipeline (Erben *et al.* 2005) are also part of the Garching-Bonn Deep Survey].

A901 was primarily chosen for a weak lensing analysis of the Abell 901a, Abell 901b and Abell 902 supercluster (Gray *et al.* 2002). The AXAF field was selected because it contains the Chandra Deep Field South previously studied in the X-ray band and several other wavebands. SGP is in direction of the Galactic South Pole, whereas S11 was chosen randomly and, by coincidence, partly overlaps with the Two Degree Field Galaxy Survey (2dFGS).

The fields were observed as sets of several single exposures with ten different telescope pointings (dithering patterns) and co-added by the data reduction pipeline developed at the MPIA, Heidelberg. The data reduction process includes bias subtraction, creation of a mosaic image, flatfielding, super-flatfielding, removal of "cosmics", defringing, an astrometric and photometric calibration.

Galaxies were detected in the R-band frames using `SExtractor` (Bertin & Arnouts 1996) (12 contiguous pixels with S/N greater than 3 above the noise background level). The detected objects are photometrically subdivided into three classes: stars, galaxies and quasars (AGN). As no morphological information was used misidentifications of the objects are possible. For example, double stars could be confused with galaxies or compact galaxies with quasars. Statistical uncertainties of the measured total magnitudes (Vega normalised) are $\delta m_R \sim 0.01$ mag, $\delta m_{B,V,I} \sim 0.05$ mag, $\delta_U \sim 0.3$ mag and values increasing from $\delta \sim 0.03$ mag (red end) to $\delta \sim 0.2$ mag (blue end) for the medium passband filters (Bell *et al.* 2004).

The photometric information has been used to derive for A901, AXAF and S11 photometric redshifts of galaxies with $m_R \leq 24$ mag, based on a set of galaxy spectrum templates (see references in Wolf *et al.* 2004). The quality of the estimate depends primarily on the apparent magnitude of the object (Wolf *et al.* 2001b). For bright galaxies, $m_R < 20$ mag, the accuracy is $\delta z \sim 0.01(1 + z)$. At median magnitudes, $m_R \sim 22$ mag, the accuracy is $\delta z \sim 0.02(1 + z)$, whereas for the faintest galaxies the photometric redshift has an accuracy of $\delta z \gtrsim 0.05(1 + z)$. The combined galaxy redshift distribution of all three fields is plotted in Fig. 4.2 (curve for data set BACK-I).

Based on photometry, rest-frame colours with accuracy $\delta m \sim 0.1$ mag and absolute luminosities with accuracies $\delta m \sim 0.1$ mag (0.2 mag) for redshifts $z \gtrsim 0.5$ (~ 0.3) were calculated.

Our object catalogue consists of galaxies from A901, AXAF and S11 with reliable photometric redshifts. Galaxies are only contained in the object catalogue if both spectral classification and estimation of the photometric redshift has been successful. Therefore there is a certain probability with which a galaxy of some absolute magnitude, M_{tot}, redshift, z, and template spectrum (SED) cannot be identified. This means that the comoving number density,

---

[1] The filters include UBVRI and 12 medium-band filters.

Table 5.1.: *Number of galaxies for all redshift bins and survey fields. Only the median redshifts of the redshift bins* $0.2 \leq z < 0.4$*,* $0.4 \leq z < 0.6$*,* $0.6 \leq z < 0.8$ *and* $0.8 \leq z < 1.0$ *are quoted. The quoted fractions are red and blue galaxies relative to the total number of galaxies in the corresponding redshift bin. The statistical error on the last digit in the brackets is an estimate assuming Poisson errors for the absolute galaxy numbers. The meaning of the notation is for example* $0.22(1) = 0.22 \pm 0.01$*. The last column contains the number of source galaxies, with* $21.5 \leq R < 24.5$ *mag, used for the lensing analysis. The source galaxies have a median redshift of* $\langle z \rangle = 0.76$*.*

Field	$\langle z \rangle$	#RED	Fraction[RED]	#BLUE	Fraction[BLUE]	#Sources
A901	0.31	297	0.22(1)	1045	0.78(5)	22099
	0.50	416	0.24(1)	1305	0.76(4)	
	0.70	413	0.17(1)	2046	0.83(4)	
	0.90	376	0.13(1)	2421	0.87(5)	
AXAF	0.31	118	0.16(2)	621	0.84(8)	21730
	0.50	352	0.18(1)	1573	0.82(5)	
	0.70	433	0.16(1)	2323	0.84(4)	
	0.90	154	0.11(1)	1263	0.89(8)	
S11	0.31	280	0.25(2)	843	0.75(5)	21256
	0.50	418	0.21(1)	1552	0.79(4)	
	0.70	393	0.18(1)	1832	0.82(5)	
	0.90	367	0.14(1)	2334	0.86(5)	

$\phi_0(M_{\rm tot}, z, SED)$, of COMBO-17 galaxies is incomplete. The completeness of COMBO-17 has been studied using extensive Monte Carlo simulations (Wolf *et al.* 2003) and has been found to be a complex function of galaxy type, and redshift. Roughly, the completeness is about 90% for $m_R \lesssim 23$ mag and about 50% near $m_R \approx 23.8$ mag (blue, late-type galaxies) or near $m_R \approx 23.5$ mag (red, early-type galaxies).

5.2.2. Object catalogue of red and blue galaxies

We split the total object catalogue into four distinct redshift bins, namely a) $0.2 \leq z < 0.4$, b) $0.4 \leq z < 0.6$, c) $0.6 \leq z < 0.8$ and d) $0.8 \leq z < 1.0$. The median redshifts of galaxies belonging to a)-d) are $\langle z \rangle = 0.31, 0.50, 0.70, 0.90$, respectively. The sizes of the samples are listed in Table 5.1.

The galaxy samples are subdivided further by applying a cut in the rest-frame $U - V$ vs. $M_V - 5\,\log_{10} h$ colour magnitude diagram (Johnson filter) along the line

$$(U - V)(M_V, z) = 1.15 - 0.31\,z - 0.08(M_V - 5\log_{10} h + 20)\ . \tag{5.1}$$

Galaxies above $(U - V)(M_V, z)$ are dubbed “red galaxies”, “blue galaxies” otherwise. This model-independent, empirical cut has been chosen by Bell *et al.* (2004) to study red galaxies near the galaxy red-sequence. It slices the bimodal distribution of galaxies in the colour-magnitude diagram between the two modes. For the redshifts considered here, most of the red galaxies selected this way are morphologically early-type with dominant old stellar populations

Table 5.2.: *Median rest-frame magnitudes and colours (Johnson filter) of different galaxy samples for different redshift bins with median redshift* $\langle z \rangle$. *Values in brackets denote the variance between the three fields,* e.g. $+0.41(1) \equiv +0.41 \pm 0.01$. *The values for* M_V *assume* $h = 1$.

		RED		BLUE		ALL	
Field	$\langle z \rangle$	$\langle M_{\rm V} \rangle$	$\langle U-V \rangle$	$\langle M_{\rm V} \rangle$	$\langle U-V \rangle$	$\langle M_{\rm V} \rangle$	$\langle U-V \rangle$
A901	0.3	−19.88	+1.35	−18.62	+0.46	−18.90	+0.65
	0.5	−20.02	+1.30	−18.90	+0.38	−19.16	+0.60
	0.7	−20.35	+1.18	−18.93	+0.20	−19.13	+0.34
	0.9	−19.96	+1.13	−18.59	−0.01	−18.73	+0.10
AXAF	0.3	−20.05	+1.25	−18.48	+0.34	−18.73	+0.49
	0.5	−19.87	+1.24	−18.72	+0.27	−18.92	+0.45
	0.7	−19.78	+1.10	−18.79	+0.19	−18.94	+0.32
	0.9	−19.23	+1.06	−18.34	−0.03	−18.46	+0.11
S11	0.3	−19.91	+1.34	−18.56	+0.44	−18.90	+0.66
	0.5	−20.13	+1.29	−19.02	+0.37	−19.26	+0.57
	0.7	−20.06	+1.18	−18.80	+0.25	−19.00	+0.39
	0.9	−19.82	+1.11	−18.70	+0.09	−18.83	+0.21
COMBINED	0.3	−20.0(1)	+1.31(1)	−18.55(1)	+0.41(1)	−18.84(2)	+0.60(2)
	0.5	−20.0(1)	+1.28(2)	−18.88(4)	+0.34(1)	−19.11(6)	+0.54(1)
	0.7	−20.1(2)	+1.15(2)	−18.84(2)	+0.21(1)	−19.02(2)	+0.35(1)
	0.9	−19.7(4)	+1.10(1)	−18.54(7)	+0.02(1)	−18.67(7)	+0.14(1)

(Bell *et al.* 2004 and references therein). As we took only galaxies with reliable photometric redshifts, we have as further selection rule $m_{\rm R} \leq 24\,{\rm mag}$.

The distribution of our samples in a rest-frame CMD is plotted in Fig. 5.1. Obviously, in the lowest redshift bin CMD (top row) galaxies populate faint regions in the diagram that are excluded in the other redshift bins due to the survey flux-limit. We estimate that in the three deeper redshift bins galaxies have roughly to be brighter than $M_{\rm V} - 5\log_{10} h \approx -17\,{\rm mag} - ({\rm U}-{\rm V})$ in order to be included (see steep black lines in Fig. 5.1). To obtain comparable galaxy samples at all redshifts we artificially apply this limit as cut to all redshift bins. After applying this cut, the galaxy samples of all redshift bins have comparable absolute M_V luminosities. The average rest-frame luminosities and colours of the various galaxy samples are compiled by Table 5.2. The red and blue sample both become bluer towards larger redshifts. This is partly due to incompleteness effects and partly due to ageing of the star population building up the galaxies (Bell *et al.* 2004).

The number of red and blue galaxies found after all cuts in the individual survey fields are listed in Table 5.1. The AXAF field catches one's eye as to the fraction of red galaxies. Compared to the two other fields AXAF contains significantly fewer red galaxies. A possible explanation is that the volume seen in the light-cone of AXAF is low in density and contains only few galaxy clusters. In such a volume, the fraction of red galaxies is low according to the morphology-density relation (*e.g.* Dressler et al. 1997). That there are only few galaxy clusters in AXAF is supported by the fact that the total number of sources (21730) found in AXAF is comparable to S11 and A901 despite the extremely long exposure time, $t \sim 52\,{\rm ksec}$. For comparison, S11 and A901 have $t \sim 18\,{\rm ksec}$ and $t \sim 22\,{\rm ksec}$ (Table 4.1).

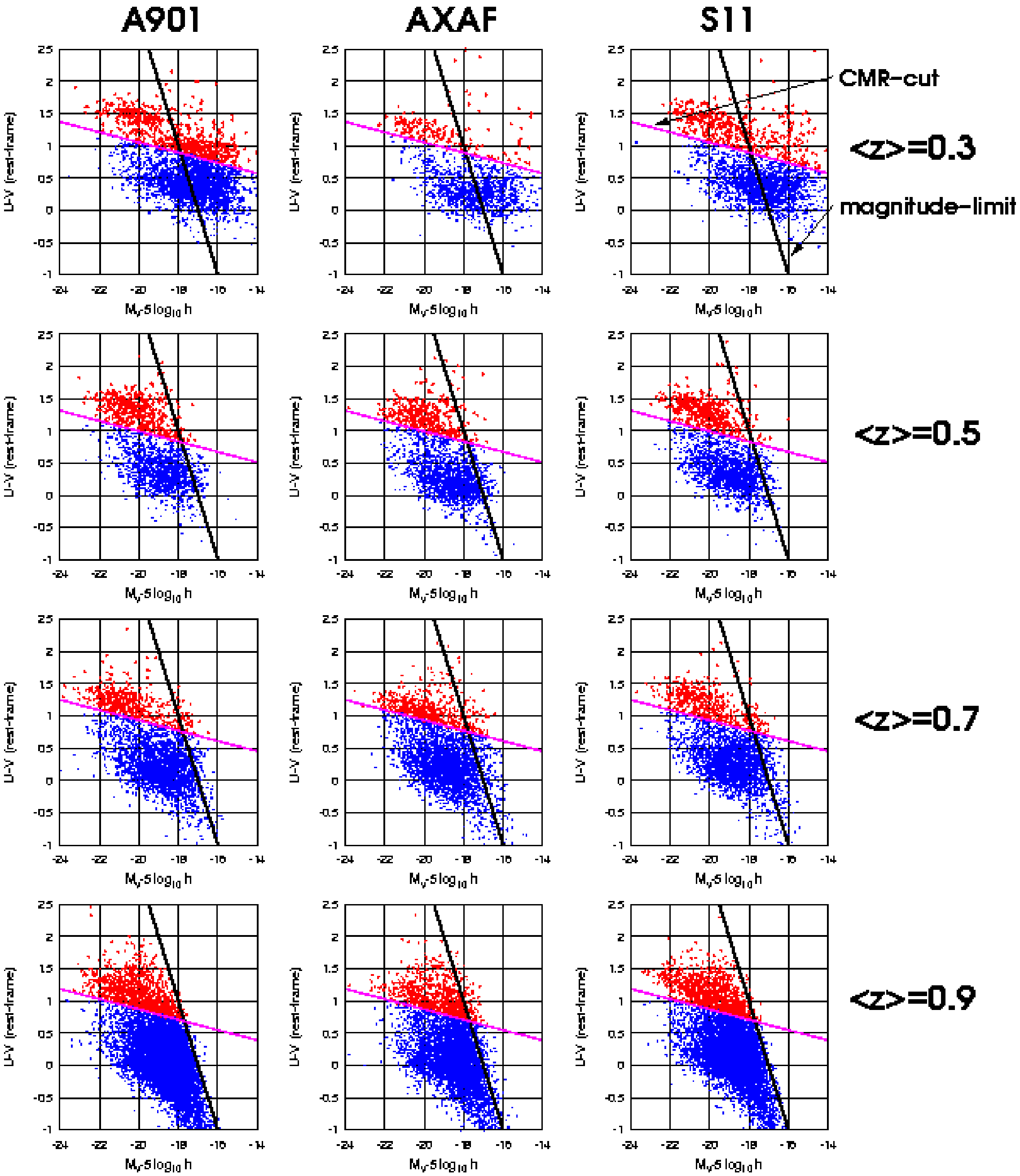

Figure 5.1.: *Rest-frame U-V colour vs. absolute magnitude in V-band,* $M_V - 5\log_{10} h$*, for COMBO-17 galaxies inside redshift bins with median redshift* $\langle z \rangle = 0.3, 0.5, 0.7, 0.9$ *(upper to lower row) and for the three fields A901, AXAF and S11 (left to right column). The galaxy sample is split into a red and blue population by a division line (light-gray) along* $(U-V)(M_V, z) = 1.15 - 0.31\,z - 0.08(M_V - 5\log_{10} h + 20)$*. The steep black line is an additional cut applied to obtain comparable magnitude-limits in all bins.*

S11 and A901 additionally exhibit a significant increase in the fraction of blue galaxies from about 80% to 87% as one goes from low to high redshift. This trend remains even after correction for incompleteness effects so that it is real (Bell *et al.* 2004). This increase is not observed in AXAF.

For illustration, the estimator for the aperture number count, $\hat{N}$ in Eq. (3.11), is used to map the galaxy number density contrast of the red and blue sample for different redshift bins, see Figs. 5.2 and 5.3. Note that the maps are noisy due to positional shot noise of the galaxies. In order to measure the linear stochastic bias for each field and redshift bin, these maps –for a wide range of aperture radii– will in the following be correlated with each other and with the aperture mass maps.

5.2.3. Lensing catalogue

The three COMBO-17 fields as observed in R-band are included in the GaBoDS (Schirmer *et al.* 2003); they have been reduced with the GaBoDS data reduction pipeline (Erben *et al.* 2005). For the lensing analysis here, the corresponding GaBoDS lens catalogues are used. The general selection criteria and data reduction steps are listed in detail in Sect. 4.2. For the final lensing catalogue, galaxies with R-band magnitudes between $21.5 \leq R < 24.5$ are chosen. We allow for a deeper lensing catalogue as in Chapter 4 to increase the yield of source galaxies, because we now have just ~ 0.78 deg^2 survey area. Indeed, a comparison of Table 5.1 and Table 4.1 shows the the number of source galaxies has grown by a factor of about 1.36. With the chosen limits in magnitude, however, we are no longer able to reliably estimate the redshift distribution of the source galaxies using the photometric redshifts of COMBO-17 galaxies. But the median redshift of the lensing catalogue can still be estimated using the median R-band magnitude of the sample. This is found to be $\langle m_R \rangle = 23.4$. According to Brown *et al.* (2003)[2] one has in the COMBO-17 Survey

$$\langle z \rangle = 2.53 - 0.3427 \, \langle m_R \rangle + 0.0114 \, \langle m_R \rangle^2 \ , \tag{5.2}$$

and as redshift distribution for the flux-limited sample

$$p(z)\mathrm{d}z = \frac{1.5z^2}{z_*^3} \, \exp\left[-\left(\frac{z}{z_*}\right)^{1.5}\right]\mathrm{d}z \ , \tag{5.3}$$

where $z_* = \langle z \rangle / 1.412$. Together with our value for $\langle m_R \rangle$ we obtain $\langle z \rangle = 0.76$.

For illustration, the aperture mass distribution in the three COMBO-17 fields based on the lensing catalogue is plotted in Fig 5.4. For this plot, the estimator (3.8) has been used. For A901, the Abell clusters A901a and A901b near the field centre clearly stick out. They have been studied by Gray *et al.* (2001) in detail using a weak lensing mass reconstruction technique. These maps in Fig. 5.4 are, however, very noisy so that not every peak is significant.[3]

---

[2] The coefficients in the fitting formula Eq. (29) in Brown *et al.* (2003) have not enough digits to fit the data points in their Table 2 with sufficient accuracy. To have a better accuracy, we fit a second-order polynomial to the values in their Table 2, taking into account the statistical uncertainties of "$z_{\rm m}$". Thereby we found the formula quoted here.

[3] The significance of the $M_{\rm ap}$-maps can be estimated by the signal-to-noise ratio $S/N = M_{\rm ap}/\sigma(M_{\rm ap})$, where the noise, $\sigma(M_{\rm ap})$, is obtained using –extended by a weighting scheme– the estimator

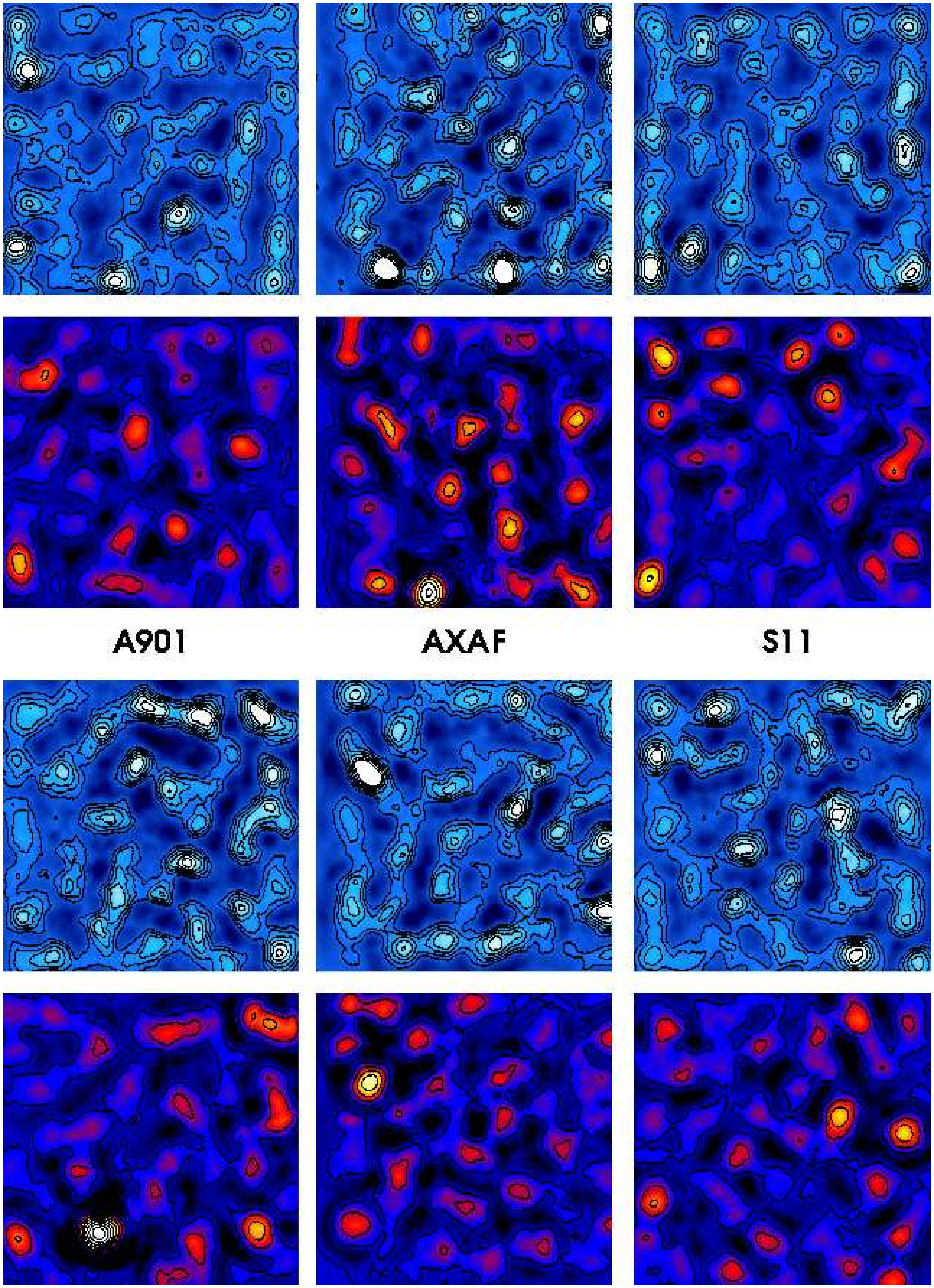

Figure 5.2.: *Aperture number count maps of red and blue galaxies belonging to different redshift bins (upper two rows: $\langle z\rangle = 0.3$, lower two rows: $\langle z\rangle = 0.5$) and fields. The first and third row are blue galaxies (contours: $N \in \{0, 0.1, 0.2, \dots, 0.5\}$), second and forth row are red galaxies (contours: $N \in \{0, 0.5, 1.0, \dots, 4\}$). The aperture radius of $3'.8$ corresponds to comoving scales of $0.9\,h^{-1}\mathrm{Mpc}$ (top) and $1.5\,h^{-1}\mathrm{Mpc}$ (bottom). The fields have a size of $22' \times 21'$ (cropped).*

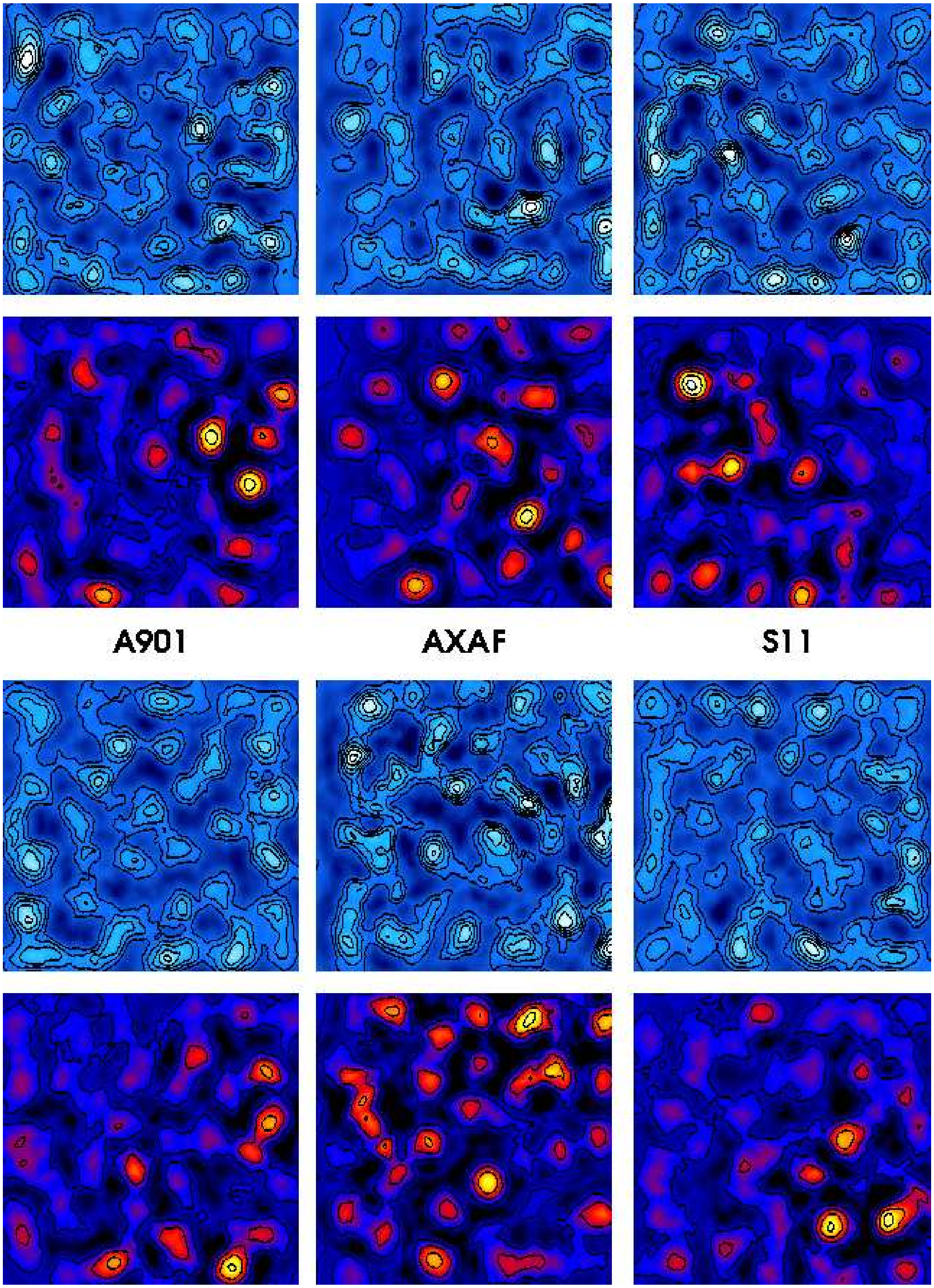

Figure 5.3.: *As in Fig. 5.2 except that the redshift bins are now* $\langle z \rangle = 0.7$ *(two top rows) and* $\langle z \rangle = 0.9$ *(two bottom rows). The aperture radius* $3'.8$ *corresponds to effective comoving scales of* $1.9\,h^{-1}\mathrm{Mpc}$ *and* $2.3\,h^{-1}\mathrm{Mpc}$*, respectively.*

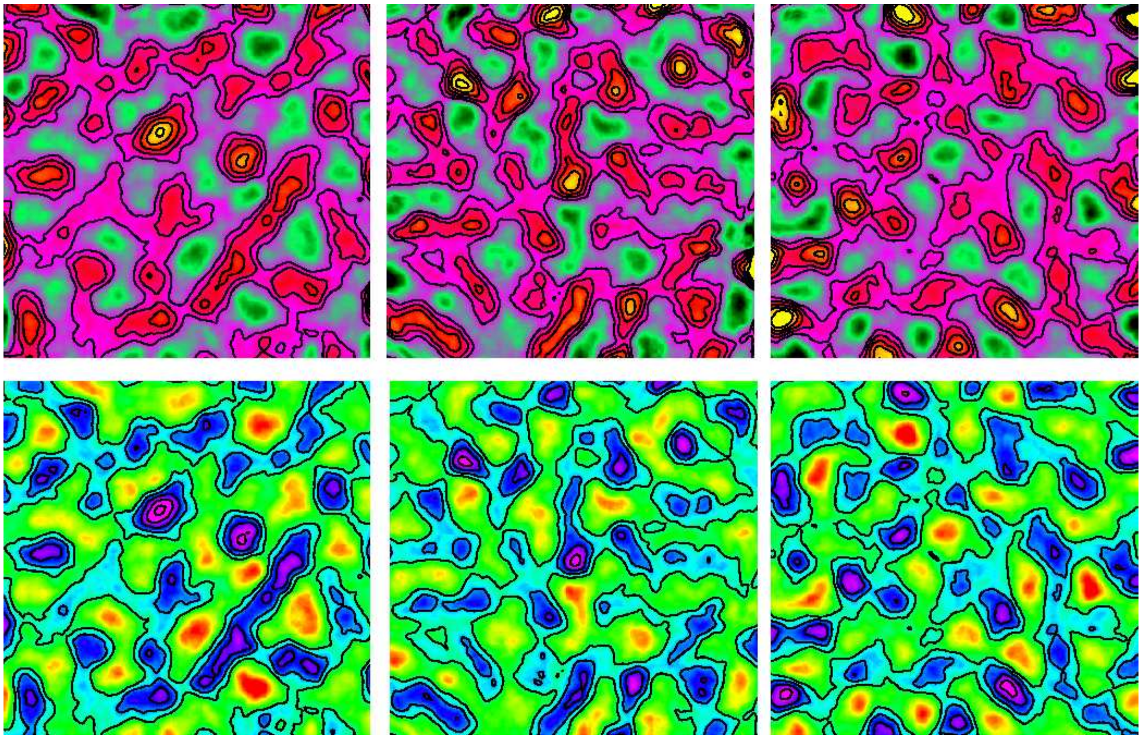

Figure 5.4.: *Aperture mass maps (upper row, contours* $M_{\rm ap} = 0.0, 0.1, 0.2, 0.3, 0.4$*) and signal-to-noise maps (lower row, contours* $S/N = 0, 1, 2, 3, 4$*) of the aperture mass of the three COMBO 17 fields A901, AXAF and S11 (left to right). The aperture radius is* $3'.8$*, the aperture filter a polynomial filter, Eq. (4.1). The fields have a size of* $22' \times 21'$ *(cropped).*

(Kruse & Schneider 1999; Schneider 1996)

$$\sigma(M_{\rm ap})(\vec{\theta}, \theta_{\rm ap}) = \frac{\pi}{2} \left[\sum_{i=1}^{N_{\rm b}} w_i \right]^{-1} \sqrt{\sum_{i=1}^{N_{\rm b}} [q(|\vec{\theta}_i - \vec{\theta}|/\theta_{\rm ap})]^2 \, w_i^2 \, |\epsilon_i|^2} \;, \tag{5.4}$$

where $N_{\rm b}$ is the number of galaxies with positions $\vec{\theta}_i$ within the aperture, $\vec{\theta}$ and $\theta_{\rm ap}$ the aperture centre and radius, respectively. w_i are the statistical weights of the individual galaxies used for the $M_{\rm ap}$-maps, and ϵ_i denotes the complex ellipticities of the source galaxies. The vectors $\vec{\theta}_i$ denote the galaxy positions and σ_ϵ the dispersion of the galaxy ellipticities. Similarly, the significance of the aperture number count maps may be worked out using as (shot) noise map $S/N = N/\sigma(N)$:

$$\sigma(N)(\vec{\theta}, \theta_{\rm ap}) = \pi \left[\sum_{i=1}^{N_{\rm f}} w_i \right]^{-1} \sqrt{\sum_{i=1}^{N_{\rm f}} [u(|\vec{\theta}_i - \vec{\theta}|/\theta_{\rm ap})]^2 \, w_i^2} \;, \tag{5.5}$$

where $N_{\rm f}$ is the number of foreground galaxies inside the aperture, and w_i are statistical weights –usually $w_i = 1$— of the foreground galaxies.

5.2.4. Merging of object and lensing catalogues

As the object catalogues with red and blue galaxies are the output from a different data reduction pipeline (MPIA Heidelberg, COMBO-17) than the lens catalogues (IAEF Bonn, GaBoDS), the spatial pixel coordinate systems are different. In particular, the complex galaxy ellipticities in the GaBoDS lens catalogue are relative to a coordinate system different than COMBO-17. We therefore have to either transform the GaBoDS lens catalogue positions (and ellipticities) into the COMBO-17 coordinate frame or vice versa. We have chosen the second option by performing the following steps. Galaxy positions in GaBoDS and COMBO-17 are, besides from their specific pixel coordinates, also given in equatorial coordinates based on the astrometry in the data reduction pipelines. First, by fitting a fifth-order polynomial as a function of the equatorial coordinates –α and δ– to the pixel coordinates x and y of the GaBoDS galaxies,

$$x(\alpha,\delta)=\sum_{n+m\leq 5}c_{nm}\alpha^n\delta^m\;,\qquad y(\alpha,\delta)=\sum_{n+m\leq 5}d_{nm}\alpha^n\delta^m \tag{5.6}$$

with coefficients c_{nm} and d_{nm}, we find the transformations, $x(\alpha,\delta)$ and $y(\alpha,\delta)$, that translate between equatorial and GaBoDS pixel coordinates (see Appendix A.2 for details). Second, the transformations $x(\alpha,\delta)$ and $y(\alpha,\delta)$ are then employed to transform equatorial coordinates of COMBO-17 galaxies to GaBoDS pixel coordinates.

5.3. Method details

5.3.1. Linear stochastic galaxy bias

The technique applied in this chapter to study the galaxy clustering and the linear stochastic bias is the same as in the foregoing Chapter 4, Sect. 4.3, and Chapter 3, Sect. 3.2.4. We refer the reader to these sections for details. The program codes performing the measurements on the data were validated using mock catalogues described in Chapter 3.

5.3.2. Estimation of the aperture statistics' errors

A small difference to the methodology of the foregoing chapter is, however, in the way how we estimate the errors of our measurements. Analogous to the method described in Sect. 4.3.3 we combine the measurements from the three fields weighted with the statistical error, Δx_i^2, which are estimated by bootstrap resampling (100 times) of the data in every field i. The expression x has to be understood in this context as a placeholder for $\langle N^2\rangle$, $\langle NM_{\rm ap}\rangle$ or $\langle M_{\rm ap}^2\rangle$ which are estimated for each field. The bootstrapping procedure estimates for every individual field the statistical error of x due to the positional shot noise of the galaxies and the intrinsic ellipticity distribution of the source galaxies. As we have in total only three fields, $N_{\rm p}=3$, we take as total error of the combined value (4.5) the combined statistical error

$$\Delta x^2=\left[\sum_{i=1}^{N_{\rm p}}1/\Delta x_i^2\right]^{-1} \tag{5.7}$$

instead of the field-to-field variance (4.6) of x. In general, this underestimates the actual error because the cosmic variance –the variance in the measurement due to observing different parts

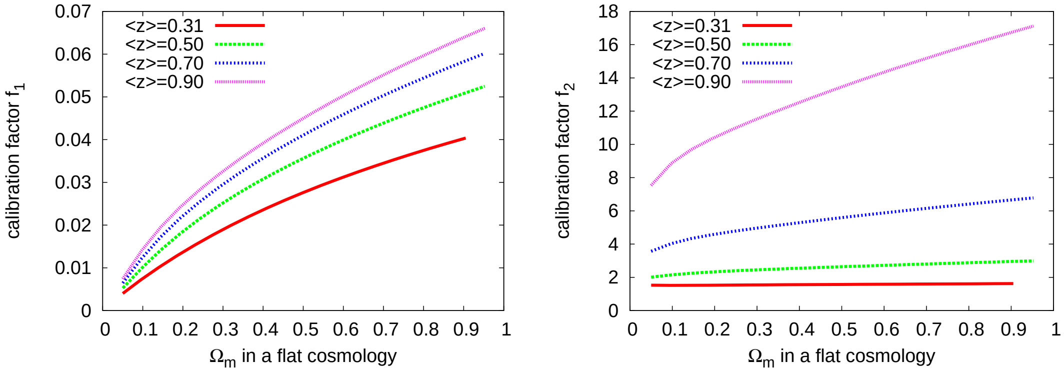

Figure 5.5.: *Calibration factors, Eqs. (4.3), for the bias estimators (3.13) applied to our four redshift bins. The median redshifts of the bins are quoted. The calibration factors assume a spatially flat* Λ*CDM cosmology and adiabatic density fluctuations for the dark matter. The shape parameter,* Γ*, assumes a universe with negligible baryon density,* $\Omega_{\rm b} \ll \Omega_{\rm m}$*, and* σ_8 *is constrained by the observed abundance of galaxy clusters. See text for more details. The curves for* f_1 *are reasonably well fitted by* $f(\Omega_{\rm m}) = a + b\,\Omega_{\rm m}^c$ *with* $(a = -0.005, b = 0.0485, c = 0.580)$, $(-0.009, 0.0633, 0.510)$, $(-0.010, 0.0722, 0.496)$ *and* $(-0.010, 0.0777, 0.503)$ *for* $\langle z\rangle = 0.31, 0.5, 0.7, 0.9$*, respectively.*

of the Universe– is not contained in Δx^2. We changed the way of estimating the errors of our measurements compared to GaBoDS because the field-to-field variance between just three fields gives sometimes very small, unreliable errorbars. By comparing the combined statistical error, Eq. (5.7), and the cosmic variance error, Eq. (4.6), in the GaBoDS data analysis we found the cosmic variance error is usually larger by a factor varying between $1-2$. Therefore, the errors quoted in this chapter are lower limits of the 1σ-variance; the true error including cosmic variance may be larger by up to a factor of roughly 2.

5.3.3. Aperture filter functions

As radial weight for the convergence and galaxy density contrast inside apertures the polynomial filter (4.1) is used. The auxiliary functions $T_\pm(x)$ and $F(x)$ required for the transformation from two-point correlators to the aperture statistics are summarised by Eqs. (3.87). The effective physical scale, in comoving coordinates, that is probed by an aperture with radius $\theta_{\rm ap}$ is approximately $f_{\rm K}(\bar{w})\theta_{\rm ap}$ where $\bar{w}$ corresponds to the median comoving distance of the analysed galaxy sample. This relation is used in the following to estimate the physical scale for which bias parameters are measured.

5.3.4. Estimators for galaxy bias and their calibration

As explained in Sect. 4.3.2 the estimators for the linear stochastic bias parameters, quantifying the difference between the galaxy and dark matter distribution, need calibration factors, $f_{1/2}$, that depend on the redshift distribution of the galaxies and the fiducial cosmological model. They are required because matter inhomogeneities contributing to $M_{\rm ap}$ have in general a different distribution in redshift than galaxies contributing to N. Fig. 5.5 is a plot of $f_{1/2}$ for the four chosen redshift bins as a function of the matter density parameter $\Omega_{\rm m}$ assuming the galaxy redshift distribution in COMBO-17, a spatially flat fiducial cosmology, $\Omega_{\rm m} + \Omega_\Lambda = 1$, with adiabatic CDM density fluctuations (Bardeen *et al.* 1986), $h = 0.7$ and a primordial power law index of $n = 1$. Furthermore, we use for the shape parameter $\Gamma = \Omega_{\rm m} h$ (Efstathiou, Bond & White 1993) and for the power spectrum normalisation $\sigma_8 = 0.55\ \Omega_{\rm m}^{-0.56}$ (White, Efstathiou & Frenk 1993). The following results are calibrated assuming $\Omega_{\rm m} = 0.3$ but can be rescaled to a different matter density according to Fig. 5.5. For example, the galaxy bias "increases" for $\Omega_{\rm m} > 0.3$ and "decreases" in the opposite case.

5.3.5. Estimating relative galaxy bias

The aperture statistics in Sect. 3.2.3 is extended here to also quantify the relative bias between two galaxy populations, in this case the relative bias between red and blue galaxies. The linear stochastic bias, Eq. (1.49), between two different galaxy populations can be defined in analogy to Eq. (3.13)

$$\begin{aligned} b_{\rm rel}\left(\theta_{\rm ap}\right) &= \sqrt{\frac{\left\langle N^2_{\rm red}\left(\theta_{\rm ap}\right)\right\rangle}{\left\langle N^2_{\rm blue}\left(\theta_{\rm ap}\right)\right\rangle}}\ , \qquad (5.8)\\ r_{\rm rel}\left(\theta_{\rm ap}\right) &= \frac{\left\langle N_{\rm red}\left(\theta_{\rm ap}\right) N_{\rm blue}\left(\theta_{\rm ap}\right)\right\rangle}{\sqrt{\left\langle N^2_{\rm red}\left(\theta_{\rm ap}\right)\right\rangle \left\langle N^2_{\rm blue}\left(\theta_{\rm ap}\right)\right\rangle}}\ , \end{aligned}$$

where $N_{\rm red}$ and $N_{\rm blue}$ are the aperture number count maps of red and blue galaxies. In difference to (3.13) no further calibration is necessary if both galaxy populations have the same selection probability in comoving radial distance; this is assumed in the following.

Chapter 3 discusses two estimator approaches for $\left\langle N^n M^m_{\rm ap}\right\rangle$, $n + m = 2$, required for a measurement of the dark matter-galaxy bias. One approach is based on placing apertures into the field, the other approach is based on two-point correlation functions that are estimated from pairs of galaxies. Both estimator approaches can be extended to also estimate the aperture number count correlation

$$\left\langle N_1\left(\theta_{\rm ap}\right) N_2\left(\theta_{\rm ap}\right)\right\rangle = 2\pi \int_0^\infty {\rm d}s\, s\, P^{(12)}_{\rm nn}\left(s\right) \left[I\left(s\theta_{\rm ap}\right)\right]^2\ , \qquad (5.9)$$

where the integral kernel $I(x)$ is defined in Eq. (3.14). Here $P^{(12)}_{\rm nn}\left(s\right)$ corresponds to the cross-correlation power spectrum of the number densities of two galaxy populations; for an analytical expression of $P^{(12)}_{\rm nn}$ see Eq. (3.59).

In the previous chapters, we have come to the conclusion that the estimator approach based on two-point correlation functions is most robust against gaps in the data field. Therefore, we employ the same technique here. For this task, we require the angular correlation between two galaxy populations, thus

$$\omega_{12}\left(\theta\right) = \left\langle \delta n_1\left(x + \theta\right) \delta n_2\left(\theta\right)\right\rangle = \int_0^\infty \frac{{\rm d}s\, s}{2\pi}\, P^{(12)}_{\rm nn}\left(s\right) J_0\left(s\theta\right)\ , \qquad (5.10)$$

where δn_1 and δn_2 are the number density contrasts of the galaxies on the sky. In the same way as for $\left\langle N^2\right\rangle$, Sect. 3.2.4, we can invert (5.10) with respect to $P^{(12)}_{\rm nn}$ and insert the expression for $P^{(12)}_{\rm nn}$ into (5.9). This results in

$$\left\langle N_1\left(\theta_{\rm ap}\right) N_2\left(\theta_{\rm ap}\right)\right\rangle = \int_0^\infty {\rm d}x\, x\, \omega_{12}\left(x\theta\right) T_+\left(x\right)\ . \qquad (5.11)$$

The auxiliary function $T_+(x)$ is defined in Eq. (3.25). Therefore, we can find $\langle N_1 N_2 \rangle$ by integration over the angular cross-correlation $\omega_{12}(\theta)$. As practical estimator for $\omega_{12}(\theta)$ we use:

$$\widehat{\omega_{12}}\,(\theta) = \frac{D_1 D_2}{R_1 R_2} - \frac{D_1 R_2 + D_2 R_1}{R_1 R_2} + 1\ . \tag{5.12}$$

This is a generalisation of $\widehat{\omega}(\theta)$, Eq. (3.28), which is used in this thesis to estimate the angular auto-correlation function of galaxies. This notation has to be understood in the following way: D_1 and D_2 are catalogues of galaxy positions of two different samples. The mock catalogues R_1 and R_2 are obtained from D_1 and D_2, respectively, by randomising the positions of the galaxies taking into account the geometry of the fields. In the next step, the number of pairs of galaxies with distances between θ and $\theta + \delta\theta$ are counted. The number of pairs between catalogue D_1 and D_2 is denoted by $D_1 D_2$. Similarly, $D_1 R_2$, $D_2 R_1$ and $R_1 R_2$ are the number of pairs between the other possible combinations of catalogues. In our analysis, we repeat this procedure 25 times and take the average of all iterations.[4]

5.3.6. Clustering correlation function

Here we outline how the aperture number count dispersion can be used to estimate the angular clustering correlation of galaxies without the need for knowing the so-called integral constraint. This will be needed for comparison of our intermediate results to the literature.

The two-point angular correlation function $\omega(\theta)$ is commonly defined as

$$\mathrm{d}P = \bar{n}^2\,[1 + \omega(\theta)]\mathrm{d}\Omega_1 \mathrm{d}\Omega_2\ , \tag{5.14}$$

where $\bar{n}$ is the mean number density of galaxies on the sky, dP the excess probability compared with a random distribution of observing two galaxies within two solid angles dΩ_1 and dΩ_2 separated by the distance θ. In an estimate of $\omega(\theta)$, *e.g.* $\hat{\omega}(\theta)$ in Eq. (3.28), there is always an uncertainty about the mean galaxy density $\bar{n}$ which is the larger the smaller the area of the field under consideration. This introduces a bias in $\hat{\omega}(\theta)$, known as the *integral constraint* (Groth & Peebles 1977), that systematically reduces, $\langle \hat{\omega} \rangle = \omega - C$, the angular correlation by a constant value

$$C = \frac{1}{\Omega^2} \int_\Omega \mathrm{d}^2\theta_1 \mathrm{d}^2\theta_2\, \omega(|\vec{\theta}_1 - \vec{\theta}_2|)\ , \tag{5.15}$$

---

[4] The estimator approach involving placing apertures is quoted here for the sake of completeness. Similar to the estimator $\hat{N}^2(\vec{\theta}, \theta_{\rm ap})$, Eq. (3.11), we define an estimator for $\langle N_1 N_2 \rangle$ that is obtained for one single aperture

$$\widehat{N_1 N_2}(\vec{\theta}, \theta_{\rm ap}) = \frac{\pi^2}{\bar{N}_{\rm f}^{(1)} \bar{N}_{\rm f}^{(2)}} \sum_i^{\mathrm{N}_{\rm f}^{(1)}} \sum_j^{N_{\rm f}^{(2)}} u_i^{(1)} u_j^{(2)}\ , \tag{5.13}$$

where $N_{\rm f}^{(1)}$ and $N_{\rm f}^{(2)}$ are the numbers of galaxies of two distinct populations inside the aperture. The aperture centre is placed at $\vec{\theta}$ and has the radius $\theta_{\rm ap}$. The filter values $u_i^{(1)}, u_j^{(2)}$ are defined as in Chapter 3, $u_i = u(|\vec{\theta}_i - \vec{\theta}|/\theta_{\rm ap})$, but are here restricted to the positions of either galaxy population. Similar to the estimator $\widehat{N^2}$, $\bar{N}_{\rm f}^{(i)}$ denotes the mean number of galaxies inside the aperture, thus $\bar{N}_{\rm f}^{(i)} = \pi\theta_{\rm ap}^2 \bar{n}_{\rm f}^{(i)}$ where $\bar{n}_{\rm f}^{(i)}$ is the mean galaxy number density. By averaging over many positions $\vec{\theta}$, one obtains a combined, final estimate for $\langle N_1 N_2 \rangle$.

where Ω is the area of the field from which $\omega(\theta)$ is estimated.[5]

In this and the foregoing chapter, the angular correlation is used to estimate the dispersion of the galaxy aperture number count by integrating over $\hat{\omega}(\theta)$, Eq. (3.24). As pointed out by Hoekstra *et al.* (2002) $\left\langle N^2 \right\rangle$ is independent of the integral constraint when the aperture filter $u(x)$ is compensated because

$$\int_0^\infty \mathrm{d}x\, x\, C\, T_+(x) = C \int_0^\infty \mathrm{d}x\, x\, T_+(x) = 0\;. \tag{5.16}$$

Therefore the estimator bias C does not make any contribution to $\left\langle N^2 \right\rangle$ and $\langle N_1 N_2 \rangle$. This makes the aperture statistics with compensated filter a convenient tool to study galaxy clustering.

Traditionally, however, galaxy clustering is studied using $\omega(\theta)$. For a comparison of our results for the two-point statistics of galaxy clustering in COMBO-17 with the literature it would be convenient to have $\omega(\theta)$ cleaned from the integral constraint. Already from early studies on galaxy clustering (*e.g.* Davis & Peebles 1983) up to recent studies (Norberg *et al.* 2001; Zehavi *et al.* 2002) it is known that $\omega(\theta)$ is close to a power law over many scales up to $\sim 10 - 20h^{-1}$Mpc (Zehavi et al. 2004 and references therein). The scales considered here are below $\sim 10h^{-1}$ Mpc so that we can assume to good accuracy that

$$\omega(\theta) = A_\omega \left(\frac{\theta}{1'}\right)^{-\delta}\;, \tag{5.17}$$

where A_ω and δ are the clustering amplitude at $1'$ and the clustering power law index, respectively. Assuming this power law we can calculate the aperture number count dispersion for our polynomial aperture filter (see Eqs. 3.87 for $T_+(x)$)

$$\left\langle N^2 \right\rangle(\theta) = \int_0^2 \mathrm{d}x\, x\, \omega(\theta\, x)\, T_+(x) = f(\delta)\, A_\omega \left(\frac{\theta}{1'}\right)^{-\delta}\;, \tag{5.18}$$

where the following definition has been used (obtained by `Mathematica`[6])

$$\begin{aligned} f(\delta) \equiv{} & \frac{1}{25} 2^{3+\delta} \times \\ & \left(\frac{30}{2+\delta} - \frac{900}{4+\delta} + \frac{15\,\Gamma(\frac{3+\delta}{2})}{\sqrt{\pi}\,\Gamma(3+\frac{\delta}{2})} - \frac{30\left((2+\delta)\sqrt{\pi} - \frac{2\,\Gamma(\frac{3+\delta}{2})}{\Gamma(1+\frac{\delta}{2})}\right)}{(2+\delta)^2\sqrt{\pi}} + \frac{1160\,\Gamma(\frac{5+\delta}{2})}{\sqrt{\pi}\,\Gamma(4+\frac{\delta}{2})} + \right. \\ & \left. \frac{900\left((4+\delta)\sqrt{\pi} - \frac{2\,\Gamma(\frac{5+\delta}{2})}{\Gamma(2+\frac{\delta}{2})}\right)}{(4+\delta)^2\sqrt{\pi}} - \frac{1508\,\Gamma(\frac{7+\delta}{2})}{\sqrt{\pi}\,\Gamma(5+\frac{\delta}{2})} + \frac{1056\,\Gamma(\frac{9+\delta}{2})}{\sqrt{\pi}\,\Gamma(6+\frac{\delta}{2})} - \frac{288\,\Gamma(\frac{11+\delta}{2})}{\sqrt{\pi}\,\Gamma(7+\frac{\delta}{2})} \right)\;. \end{aligned} \tag{5.19}$$

Thus, $\left\langle N^2 \right\rangle(\theta)$ obeys the same power law as $\omega(\theta)$ just with a different amplitude, but independent of the integral constraint. Note that the same holds for $\langle N_1 N_2 \rangle(\theta)$. In the regime $\delta \in [0, 1.6]$, the somewhat bulky function $f(\delta)$ can be approximated by

$$f(\delta) \approx 0.0051\,\delta^{11.55} + 0.2769\,\delta^{3.95} + 0.2838\,\delta^{1.25} \tag{5.20}$$

---

[5] The integral constraint is the expected dispersion of the mean galaxy number density contrast inside Ω in excess of the dispersion due to shot noise, divided by Ω^2.

[6] Wolfram Research: `http://www.wolfram.com`.

Table 5.3.: *Assuming a shifted power law,* $\omega(\theta) = A_\omega\,\theta^{-\delta} + const$*, for the spatial clustering of the galaxies, the clustering amplitude at* $\theta = 1'$*,* A_ω*, and the slope,* δ*, can be determined from* $\langle N^2 \rangle$*.* ***Upper half of table****: summary of results obtained this way considering values for* $\langle N^2 \rangle$ *out of* $\theta \in [0'.6, 20']$ *for red and blue galaxies and the combined data set for different median redshifts,* $\langle z \rangle$*. The quoted values of* χ^2/n *assume uncorrelated errors.* ***Lower half of table****: the fit for* $\omega(\theta)$ *has been transformed into the 3D-galaxy clustering function* $\xi(r) = (r/r_0)^{-\gamma}$ *using Limber's equation (*$\Omega_{\rm m} = 0.3$*,* $\Omega_\Lambda = 0.7$*). The clustering length* r_0 *is in units of* h^{-1}Mpc*;* $\xi_{\rm 1Mpc}$ *denotes* $\xi(r)$ *at a comoving length of* $r = 1\,h^{-1}$Mpc*. The numbers in brackets are the statistical errors of the last significant digit.* e.g. $0.12(1) \equiv 0.12 \pm 0.01$.

	ALL			RED			BLUE		
$\langle z \rangle$	A_ω	δ	χ^2/n	A_ω	δ	χ^2/n	A_ω	δ	χ^2/n
0.31	0.12(1)	0.82(4)	0.5	0.50(7)	0.85(8)	1.0	0.09(3)	0.7(2)	1.0
0.50	0.14(2)	0.84(5)	2.6	0.21(6)	0.96(9)	3.7	0.11(3)	0.7(1)	3.0
0.70	0.11(2)	0.70(6)	2.5	0.37(8)	0.93(6)	2.5	0.07(2)	0.7(1)	2.1
0.90	0.06(2)	0.74(6)	1.6	0.25(6)	1.04(7)	1.5	0.04(1)	0.8(1)	1.6
$\langle z \rangle$	r_0	γ	$\xi_{\rm 1Mpc}$	r_0	γ	$\xi_{\rm 1Mpc}$	r_0	γ	$\xi_{\rm 1Mpc}$
0.31	3(1)	1.82(4)	5(4)	5(2)	1.85(8)	21(10)	2.3(8)	1.7(2)	4(3)
0.50	3(1)	1.84(5)	8(4)	5(1)	1.96(9)	28(15)	3.0(9)	1.7(1)	6(4)
0.70	3(1)	1.70(6)	7(4)	5(2)	1.93(6)	24(14)	2.4(8)	1.7(1)	4(3)
0.90	2(1)	1.74(6)	4(3)	4(1)	2.04(7)	18(11)	1.7(6)	1.8(1)	3(2)

within a few percent accuracy, which covers the commonly observed range of values for the power law index. Based on this notion we estimate in the following the clustering amplitude, A_ω, and the index, δ, of $\omega(\theta)$ by fitting a power law to $\widehat{N^2}(\theta) = A'_\omega\,\left(\frac{\theta}{1'}\right)^{-\delta}$ and by using the transformation $A_\omega = A'_\omega/f(\delta)$.

5.4. Results and discussion

5.4.1. Aperture number count dispersion

The aperture number count dispersion for the red, blue and the combined data set is plotted in Fig. 5.6, and the best-fit power-law parameters are summarised by Table 5.3. How the clustering amplitude and slope are derived from the aperture number count dispersion is described in Sect. 5.3.6. All measurements are reasonably well fitted by a power law over the whole observed range. Clearly visible in Fig. 5.6 is that the two-point correlations of the galaxy sets are different compared to the correlation function expected if galaxies trace the dark matter distribution (solid line). This suggests that there are two regions in the observed range $\theta \lesssim 20'$: one region at small scales where all galaxies together are more clustered than dark matter and a region on larger scales where galaxies are less clustered than the dark matter.

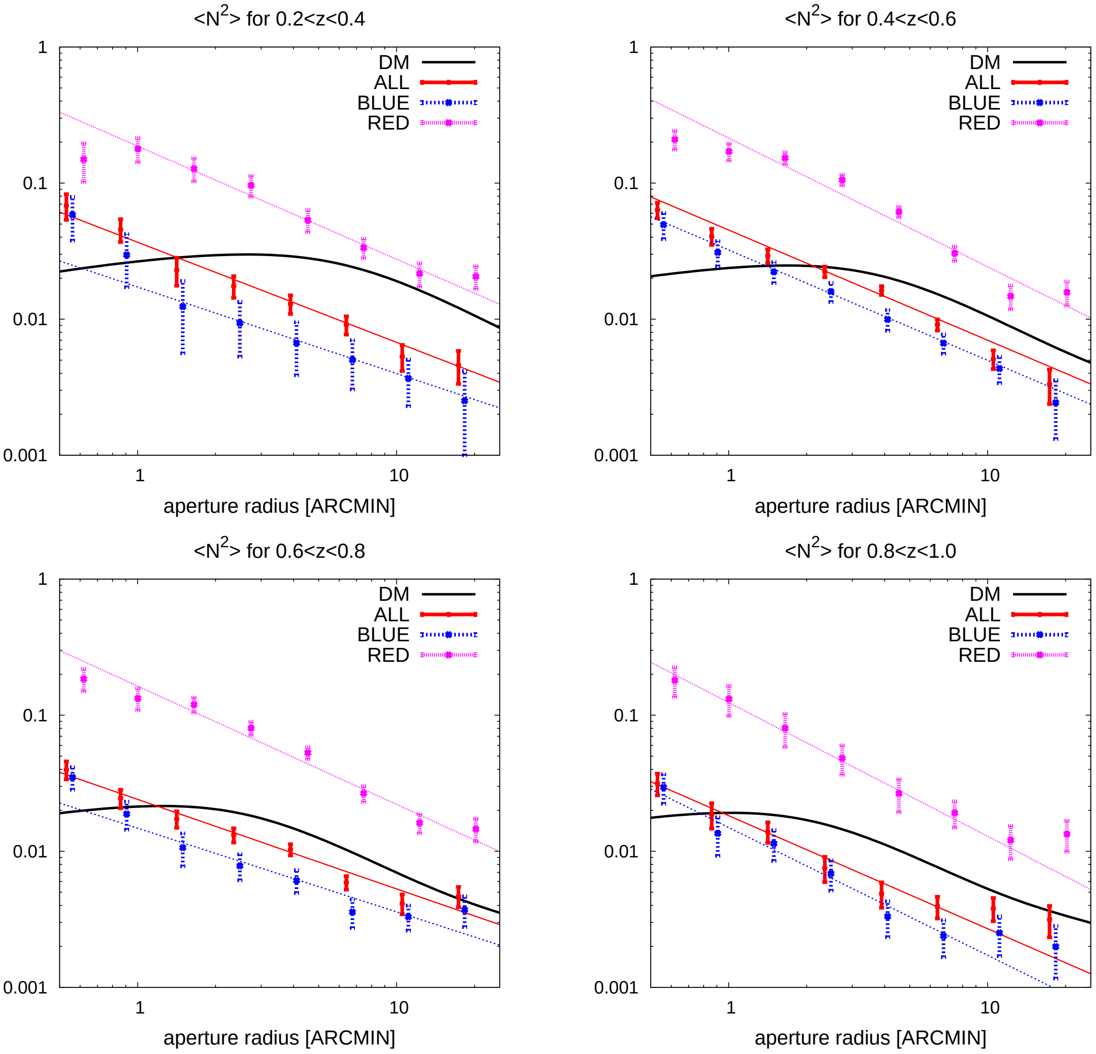

Figure 5.6.: *Dispersion of the aperture number count, $\langle N^2 \rangle$, for red, blue galaxies and the complete data set. The straight lines are the best-fitting power laws to the measurements. "DM" denotes the theoretical dispersion $\langle N^2 \rangle$ for galaxies unbiased to the dark matter assuming concordance ΛCDM. For redshift bins in increasing order, apertures with radii $10'$ correspond to an effective comoving physical scale of $2.43\,h^{-1}\mathrm{Mpc}$, $3.85\,h^{-1}\mathrm{Mpc}$, $5.13\,h^{-1}\mathrm{Mpc}$ and $6.17\,h^{-1}\mathrm{Mpc}$ for the smallest to largest redshift bins respectively.*

Comparison with earlier studies

In the following, we would like to compare the best-fit parameters A_ω and δ, thus clustering amplitude at $1'$ and slope respectively, to the results of other papers. Since the data sample selections between different surveys are in general not equal, we can only make a *crude comparison* to other results.

In the literature, it is common to quote galaxy clustering in terms of the three-dimensional two-point correlation function

$$\xi(r) = \left(\frac{r}{r_0}\right)^{-\gamma}\,, \tag{5.21}$$

where r is the comoving distance of two galaxies and r_0 the clustering length, all in units of h^{-1}Mpc. In order to be able to compare our measurements for the clustering of galaxies to these papers we transform $\omega(\theta)$ to $\xi(r)$ by the following procedure. The projected angular clustering of galaxies, $\omega(\theta)$, is related to $\xi(r)$ by means of Limber's equation (*cf.* Hildebrandt *et al.* 2005),

$$\omega(\theta) = \int_0^\infty \mathrm{d}\bar{w}\, p^2(\bar{w}) \int_{-\infty}^\infty \mathrm{d}\Delta w\, \xi(\sqrt{(\bar{w}\theta)^2 + \Delta w^2}) \tag{5.22}$$

in which $\bar{w}$ and Δw are the mean and difference of the comoving distances of two galaxies seen with angular separation θ on the sky. $p(\bar{w})$ is the PDF of the galaxies in comoving distance. According to the Limber equation, a power law $\xi(r)$ results in a power law $\omega(\theta)$, Eq. (5.17), with

$$r_0^\gamma = A_{\omega;rad}\,\frac{\Gamma(\gamma/2)(2-\gamma)}{\Gamma(1/2)\Gamma(\gamma/2-1/2)}\,\frac{(1-a/b)^2}{1-(a/b)^{2-\gamma}}\,b^\gamma\,, \tag{5.23}$$

where $\gamma = \delta + 1$, and $A_{\omega;rad}$ is the amplitude of $\omega(\theta)$ at a scale of one radian. This formula assumes that galaxies contributing to $\omega(\theta)$ have a flat distribution within the comoving radial distance interval $a \le w \le b$; this is roughly the case for our narrow redshift bins. We employed this equation for r_0 to convert the measurements for A_ω and δ, Sect. 5.3.6, into r_0.

Typical values for the clustering of galaxies at low redshifts are $r_0 = 4 - 6\,h^{-1}$Mpc and $\gamma = 1.6 - 1.9$ (*cf.* Hawkins *et al.* 2003; Norberg *et al.* 2002; Zehavi *et al.* 2001 and references therein). Compared to these values our results are consistent within 1σ statistical uncertainty, although we seem to have somewhat lower values for r_0. Hoekstra *et al.* (2002) quote a value of $A_\omega = 0.115 \pm 0.005$ for their foreground galaxy sample selected by $19.5 < R < 21.5$, $\langle z\rangle = 0.35$, from the RCS. The redshift distribution of this sample is roughly comparable to the lowest COMBO-17 redshift bin ($0.2 \le z < 0.4$, see distribution of FORE-I in Fig. 4.2). Our value of $A_\omega = 0.12 \pm 0.01$ is thus in agreement with Hoekstra *et al.*

Subdividing the galaxy sample of COMBO-17 into red and blue galaxies yields different clustering properties: red galaxies are more strongly, $r_0 \sim 5h^{-1}$Mpc and $\gamma \sim 0.9$, clustered than blue galaxies, $r_0 \sim 2.5h^{-1}$Mpc and $\gamma \sim 0.7$. At low redshifts, other authors obtain similar results (*e.g.* Zehavi *et al.* 2004; Budavari *et al.* 2003; Madgwick *et al.* 2003; Norberg et al. 2002; Shepherd *et al.* 2001), in detail depending on how the samples are selected, *i.e.* spectroscopically, morphologically or by colour. Again, our values for r_0 are somewhat lower than the values of other authors, whereas the values for γ are in good agreement.

We now turn to the redshift dependence of clustering. There are not many papers on the redshift evolution of galaxy clustering to compare with (Phleps & Meisenheimer 2003; Wilson 2003; Firth *et al.* 2002; Shepherd *et al.* 2001; Carlberg *et al.* 2000b; Le Févre *et al.* 1996).

Our observation is that the amplitude A_ω for all galaxies is a decreasing function with median redshift. If translated into the three-dimensional comoving clustering function, $\xi(r)$, assuming $\Omega_\mathrm{m} = 0.3$ and $\Omega_\Lambda = 0.7$, however, the results are consistent with a non-evolution of r_0 and γ within the statistical errors. For the complete galaxy sample, we find $r_0 = (3 \pm 1)\, h^{-1}$Mpc and $\gamma = 1.8 \pm 0.1$ over the whole redshift range. Carlberg *et al.* (2000b) and Shepherd *et al.* (2001) measured in CNOC2 (median redshift $\langle z \rangle \sim 0.4$) a correlation length of $r_0 = (4.9 \pm 0.1)\ h^{-1}$Mpc for redshifts between $0 < z < 0.65$ which is somewhat larger than our value for r_0. Note, however, that the authors assume a fiducial cosmology of $\Omega_\mathrm{m} = 0.2$ and $\Omega_\Lambda = 0$ which increases r_0 slightly. Using the data of the Las Campas IR Survey, Firth *et al.* (2002) found that the value for A_ω decreases from ~ 0.12 down to ~ 0.07 for a galaxy sample with median redshift $\langle z \rangle \sim 0.4$, $18 < H < 19$, to a sample with median redshift $\langle z \rangle \sim 0.6$, $19.5 < H < 0.5$, respectively. This is close to our observations if one considers that fainter magnitude bins broaden the redshift distribution, whereas our samples have narrow distributions in redshift. Phleps & Meisenheimer (2003) investigated the clustering of galaxies in the Calar Alto Deep Imaging Survey (CADIS) up to redshifts $z = 1$. This is a range comparable to our work, albeit the mean redshift of COMBO-17 is with $\langle z \rangle = 0.86$ (Brown *et al.* 2002) clearly deeper than in CADIS, $\langle z \rangle \approx 0.6$. Although we are in agreement with their clustering amplitude for the total galaxy sample at the lower redshifts, we probably –the statistical uncertainties are large– disagree on the strong evolution of ξ_1Mpc observed in CADIS.

As in the low-redshift Universe the clustering of galaxies at higher redshifts also depends on colour. We find for the whole redshift range $r_0 = 4 - 5\, h^{-1}$Mpc and $\gamma = 1.8 - 2.0$, $r_0 = 2 - 3\, h^{-1}$Mpc and $\gamma \sim 1.7$ for the red and blue galaxy sample, respectively. This allows at most only a moderate evolution with redshift. Shepherd *et al.* (2001) find for the comoving correlation length an almost linear increase with redshift for the red and blue sample in CNOC2 which is not observed here. This increase, however, may be due to SED misclassifications at larger redshifts, as is pointed out by the authors themselves. In another paper by Phleps & Meisenheimer (2003), the authors quote slopes for their early-type and late-type sample that are smaller than ours, namely $\gamma \sim 1.5$ and $\gamma \sim 1.7$ for late-type and early-types, respectively. Moreover, they find, in contrast to Shepherd *et al.*, in their data a decrease in clustering amplitude, from $\xi_\mathrm{1Mpc} = 15 \pm 1$ at $z \sim 0.3$ to $\xi_\mathrm{1Mpc} = 9^{+7}_{-3}$ at $z \sim 0.9$, of the early-type galaxies towards higher redshifts which appears to be in conflict with our data. Independent of whether there is an evolution of the clustering of red and blue galaxies or not, we agree with Shepherd *et al.* and Phleps & Meisenheimer on the statement that red and blue galaxies are biased with respect to each other up to redshift $z \sim 1$. This disagrees with Le Févre *et al.* (1996) who found that in the Canadian-France Redshift Survey at high redshifts, $0.5 < z < 0.8$, the clustering between red and blue galaxies (spectroscopically selected) on comoving scales $100h^{-1}$kpc $\lesssim r \lesssim 2h^{-1}$Mpc is indistinguishable, which would suggest an evolution of their relative bias.

Finally, we compare our results to Wilson (2003) who studied the clustering evolution of red L_*-galaxies in the UH8K Survey. The galaxy sample was selected on the basis of a cut in a $V - I$ vs. I diagram taking only galaxies brighter than $M_* + 1$. His observed correlation amplitudes are $A_\omega \sim 0.44, 0.28, 0.34, 0.52$ for median redshifts of $\langle z \rangle = 0.3, 0.5, 0.7, 0.9$, respectively, see his Table 9. Note that we obtained these values for A_ω by averaging over three adjacent redshift bins in his Table 9 to account for the fact that our redshift bins are wider ($\Delta z = 0.2$ instead of $\Delta z = 0.1$). Except for the highest redshift our results for the clustering of the red galaxy sample are consistent with these measurements.

Table 5.4.: *Parameters of the best-fitting power-law* $\langle\gamma_{\rm t}\rangle(\theta) = A_\xi\,(\theta/1')^{-\delta}$ *to measured galaxy-galaxy lensing signal. Lens galaxy samples are binned in redshift and colour (Fig. 5.8). For the fit only data points within* $\theta \in [0.'4, 10']$ *are taken into account. "SIS" denotes a fixed power-law slope, namely* $\delta = 1$*, which corresponds to the shear profile about an overdensity peak with singular isothermal sphere density profile. "x" indicates that the fitting algorithm did not converge. "*χ^2/n*" denotes the residual scatter per degree of freedom for statistically independent data points.*

	ALL			RED			BLUE		
$\langle z\rangle$	A_ξ	δ	χ^2/n	A_ξ	δ	χ^2/n	A_ξ	δ	χ^2/n
0.3	0.003(2)	1.7(9)	1.61	0.008(2)	1.5(7)	0.89	0.002(2)	2(2)	1.40
0.3	0.003(2)	SIS	1.57	0.007(2)	SIS	0.92	0.002(2)	SIS	1.30
0.5	0.001(1)	SIS	1.20	0.002(2)	SIS	1.30	x	x	x
0.7	x	x	x	0.005(2)	1.2(8)	1.09	x	x	x
0.7	0.001(1)	SIS	1.20	0.005(2)	SIS	0.96	x	x	x
0.9	x	x	x	x	x	x	x	x	x

We conclude, that at low redshift our results are in good agreement with other surveys. At the high redshifts, however, there are both discrepancies and consistencies with other surveys. This demonstrates that inferences on the clustering of galaxies at high redshift are probably still hampered by not fully understood selection effects.

5.4.2. Galaxy-Galaxy lensing

The measured cross-correlation between aperture number count and aperture mass for the red and blue galaxy sample is plotted in Fig. 5.7. We note that the B-mode of $\langle NM_{\rm ap}\rangle$ –an indicator for remaining statistical noise and systematics– is consistent with zero. Probably due to the limited survey area and the small number of galaxies in each redshift bin there is almost no significant detection above the noise background (B-mode, right panels) except at the smallest scales.

The solid lines in the left panels of Fig. 5.7 indicate the signal one would expect if galaxies perfectly traced mass given our redshift distributions of lens, source galaxies and concordance ΛCDM as fiducial cosmological model. As we already know from the last chapter (Fig. 4.5) the actual signal for the complete galaxy sample is, except for the smallest scales below about $3'$, actually even lower.

Only for the red galaxy sample on scales smaller than $\sim 3'$ there are detections on a level of $1\sigma - 2\sigma$ above the noise level, which is not visible in the blue galaxy sample. This signal is particularly strong for the lowest redshift bin where we expect the strongest galaxy-galaxy lensing signal for source galaxies with $\langle z\rangle = 0.76$.

Comparison with earlier studies

In order to compare our results to other studies we go one step back and look at the mean tangential shear about the lens galaxies, $\langle\gamma_{\rm t}\rangle$, which is used to estimate $\langle NM_{\rm ap}\rangle$ (Sect. 3.2.4). The mean tangential shear is a frequently used quantity to analyse the galaxy-dark matter correlation (*cf.* Seljak *et al.* 2004b; Sheldon *et al.* 2004; Kleinheinrich *et al.* 2004; Hoekstra

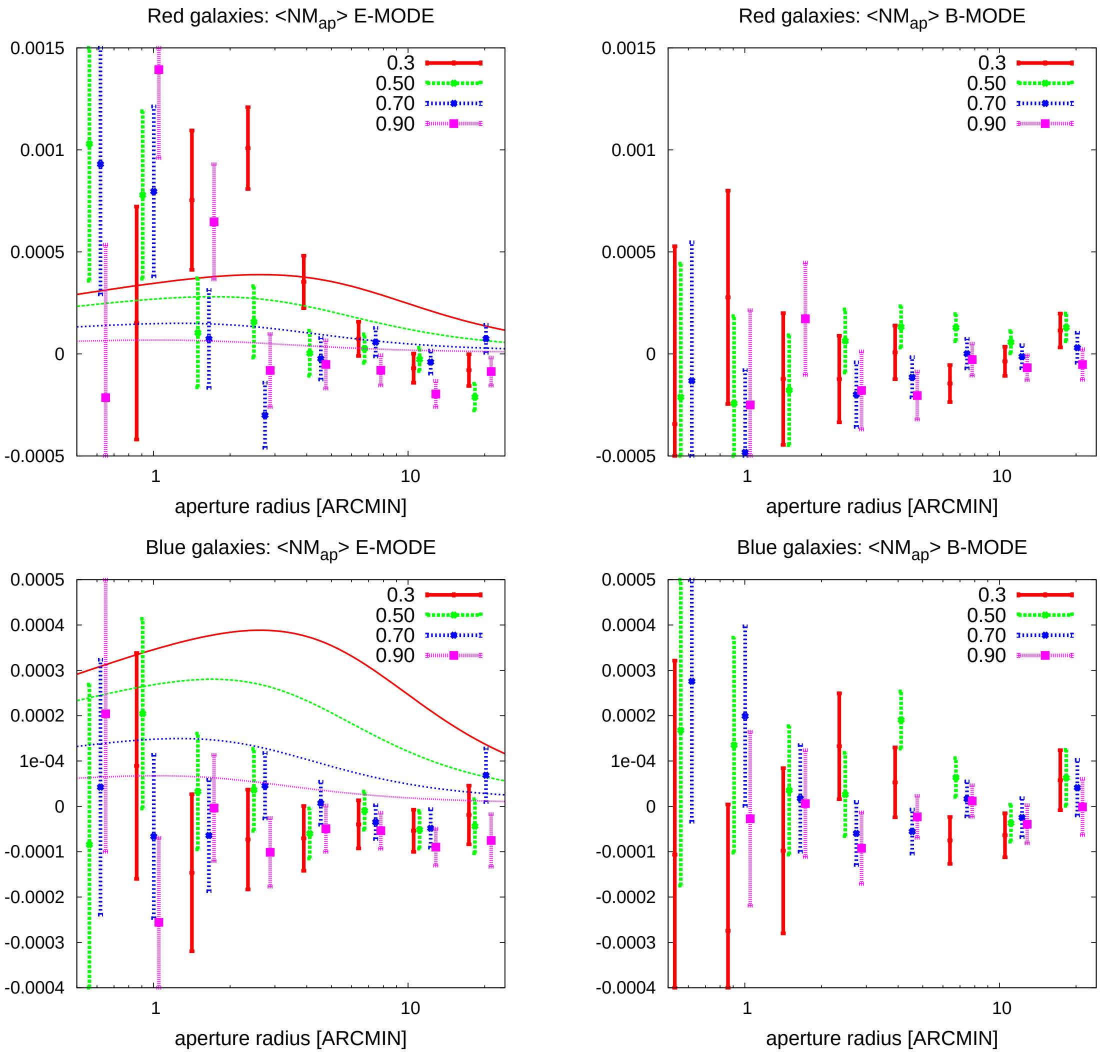

Figure 5.7.: *Cross-correlation between aperture number count of galaxies and aperture mass map for red galaxies (top) and blue galaxies (bottom) for four redshift bins. The signals' E-modes are in the left column, B-modes in the right column. The lines are the theoretically expected signal for galaxies being unbiased with respect to the dark matter assuming concordance* Λ*CDM and a median source galaxy redshift of* $\langle z \rangle = 0.76$*. The only significant signals detected with respect to the residual background noise (B-mode) are for red galaxies on scales smaller than* $\sim 3'$*.*

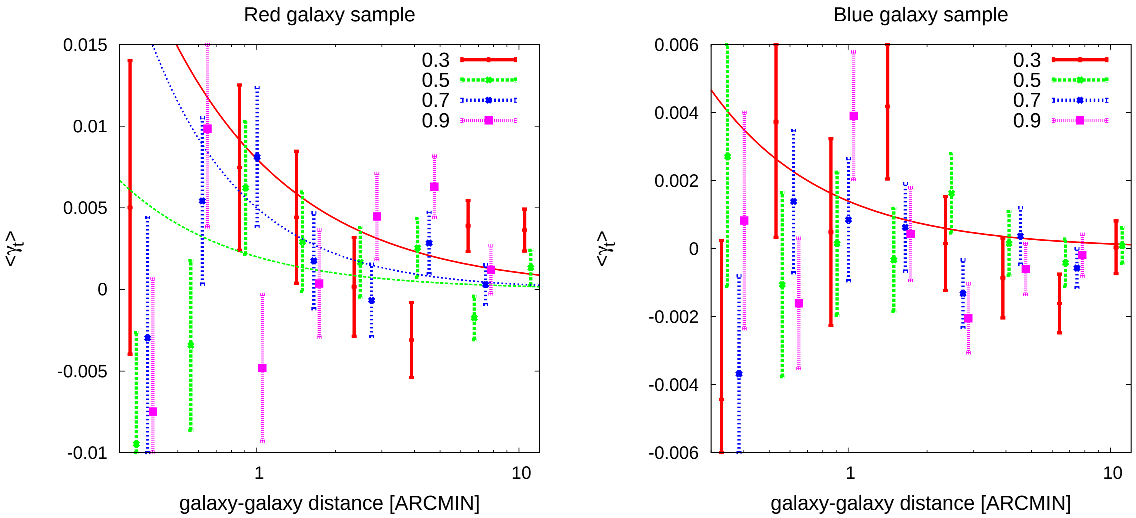

Figure 5.8.: *Mean tangential shear about lens galaxies binned in redshift and colour. The solid lines are best-fit power-laws to the data points; they are only present if sensible fits are possible. The best-fit parameters can be found in Table. 5.4.*

et al. 2003; Guzik & Seljak 2001; McKay *et al.* 2001; Fisher *et al.* 2000; Hudson *et al.* 1998; Brainerd *et al.* 1996). Our measurements for $\langle\gamma_{\rm t}\rangle$ are shown in Fig. 5.8. Where possible we fit a power law to the data points. The best-fit parameters can be found in Table 5.4.

Kleinheinrich (2003) and Kleinheinrich *et al.* (2004) already studied galaxy-galaxy lensing in COMBO-17. We do not want to repeat the detailed analysis of Kleinheinrich *et al.* (2004) for the sanity check in this section. Instead, we consider only the galaxy-galaxy lensing signal obtained by Kleinheinrich (2003) by means of a simple R-band magnitude binning. In Chapter 7 of her thesis, the galaxy sample is divided into lens and source galaxies using R-magnitudes bins, namely $18 < R < 22.5$ and $22.5 < R < 24$ for the lens and source catalogue, respectively. To crudely estimate the median redshifts of those magnitude bins we use the results from the Chapter 4. The bins of lens and source galaxies correspond roughly to the sample FORE-I/FORE-II (combined) and BACK-II, respectively. From Fig. 4.2 we estimate $\langle z\rangle \approx 0.4$ (average of FORE-I and FORE-II weighted with the number of galaxies) for the median redshift of her lens galaxy sample and $\langle z\rangle \approx 0.7$ for the median redshift of the source galaxy sample. The foreground sample hence has about the same median redshift as our two lowest redshift bins combined, whereas the source galaxy sample is in our case slightly deeper, $\langle z\rangle = 0.76$. A quick and dirty calculation yields that the lensing efficiency,

$$W(w,w') = \frac{f_{\rm K}(w-w')f_{\rm K}(w')}{f_{\rm K}(w)} \tag{5.24}$$

with w and w' being the comoving radial distances corresponding to the median redshifts of the lens and source sample respectively and $f_{\rm K}(w)$ being the angular diameter distance, is in our sample a bit larger by about 10%. For that reason, we can expect to find a slightly larger galaxy-galaxy lensing signal. Furthermore, since we are discarding galaxies fainter than $M_{\rm v} - 5\log_{10} h \approx -17\,$mag the signal should be enhanced even more (McKay *et al.* 2001).

By fitting an isothermal sphere profile, $\langle\gamma_{\rm t}\rangle(\theta) = A_\xi/(\theta/1')$, Kleinheinrich obtained a value of $\langle\gamma_{\rm t}\rangle = (6 \pm 2) \times 10^{-4}$ for a lens-source separation of $\theta = 1'$; we combined the results for the fields A901, AXAF and S11 from her Table 7.3 only. Our value of $A_\xi = (14 \pm 8) \times 10^{-4}$, the average of the first two redshift bins weighted with the statistical error, is consistent with that measurement.

We would like to note here that a signal of $\langle NM_{\rm ap}\rangle$ indistinguishable from noise beyond aperture radii $\theta \sim 3'$ is no contradiction to Kleinheinrich (2003) and Kleinheinrich *et al.* (2004). In these studies, only the smallest scales out to about $2'$ are investigated by means of galaxy-galaxy lensing with the intention to constrain the dark matter environment in direct vicinity to a galaxy. At these scales we also find a galaxy-galaxy lensing signal. In our study, however, we are also interested in the large-scale environment of galaxies, up to $24'$, which for an acceptable signal-to-noise obviously requires a survey area larger than $0.78\,{\rm deg}^2$, as can be seen in Chapter 4.

For a further crude comparison we consider the observed galaxy-galaxy lensing in CNOC2 (Hoekstra *et al.* 2003). Among other things the authors measured the mean tangential shear of galaxies out of $20 < R < 23$ (faint sample). As value for the median redshift of the lenses the authors mention $\langle z\rangle = 0.46$. Using the "β-parameter" in Hoekstra *et al.*,

$$\beta = f_{\rm K}(w - w')/f_{\rm K}(w) = W(w, w')/f_{\rm K}(w')\ , \tag{5.25}$$

we estimate that the lensing efficiency is about 15% larger than in our measurement. According to the fit in their Fig. 4 the value for the mean tangential shear in their data is $\langle\gamma_{\rm t}\rangle \approx (1.0 \pm 0.3) \times 10^{-3}$ at $\theta = 1'$. This is in agreement with our value of $A_\xi = (1 \pm 1) \times 10^{-3}$ for a median redshift $\langle z\rangle = 0.5$. For their bright galaxy sample, $17.5 < R < 21.5$ and $22 < R < 26$ for lenses and source respectively, Hoekstra *et al.* obtain a larger value at $\theta = 1'$, $\langle\gamma_{\rm t}\rangle \approx (16 \pm 4) \times 10^{-4}$. The median redshift of the lens sample is in that case $\langle z\rangle = 0.34$ and hence comparable to our lowest redshift bin; the lensing efficiencies are more or less the same. We therefore can compare their measurement directly with our result of $A_\xi = (28 \pm 15) \times 10^{-4}$ which is in good agreement.

As to the relative strength of the galaxy-galaxy lensing signal for blue and red galaxies we compare our results to Sheldon *et al.* (2004). For blue galaxies, we only found a signal in the lowest redshift bin. In our sample, at lowest redshift the signal for red galaxies is higher by a factor of approximately 4 compared to the blue sample signal, whereas Sheldon *et al.* finds in SDSS a ratio between $3-4$ depending whether the galaxy sample is subdivided morphologically in early and late types or by colour in red and blue samples. McKay *et al.* (2001) find similar values in SDSS. Considering the statistical errors attached to our measurements the results are in good agreement.

5.4.3. Aperture mass dispersion

The aperture mass dispersion based on our lens catalogue is plotted in Fig. 5.9, lower right panel. We find a clear and significant E-mode signal that is slightly above the dispersion expected from our fiducial cosmological model and a median source redshift of $\langle z\rangle = 0.76$. Considering that cosmic variance is not included in the errors bars, see Sect. 5.3.2, the measurement is consistent with the theory. Some systematics indicated by the B-mode remain, which are, however, always smaller in absolute amplitude with respect to the E-mode beyond

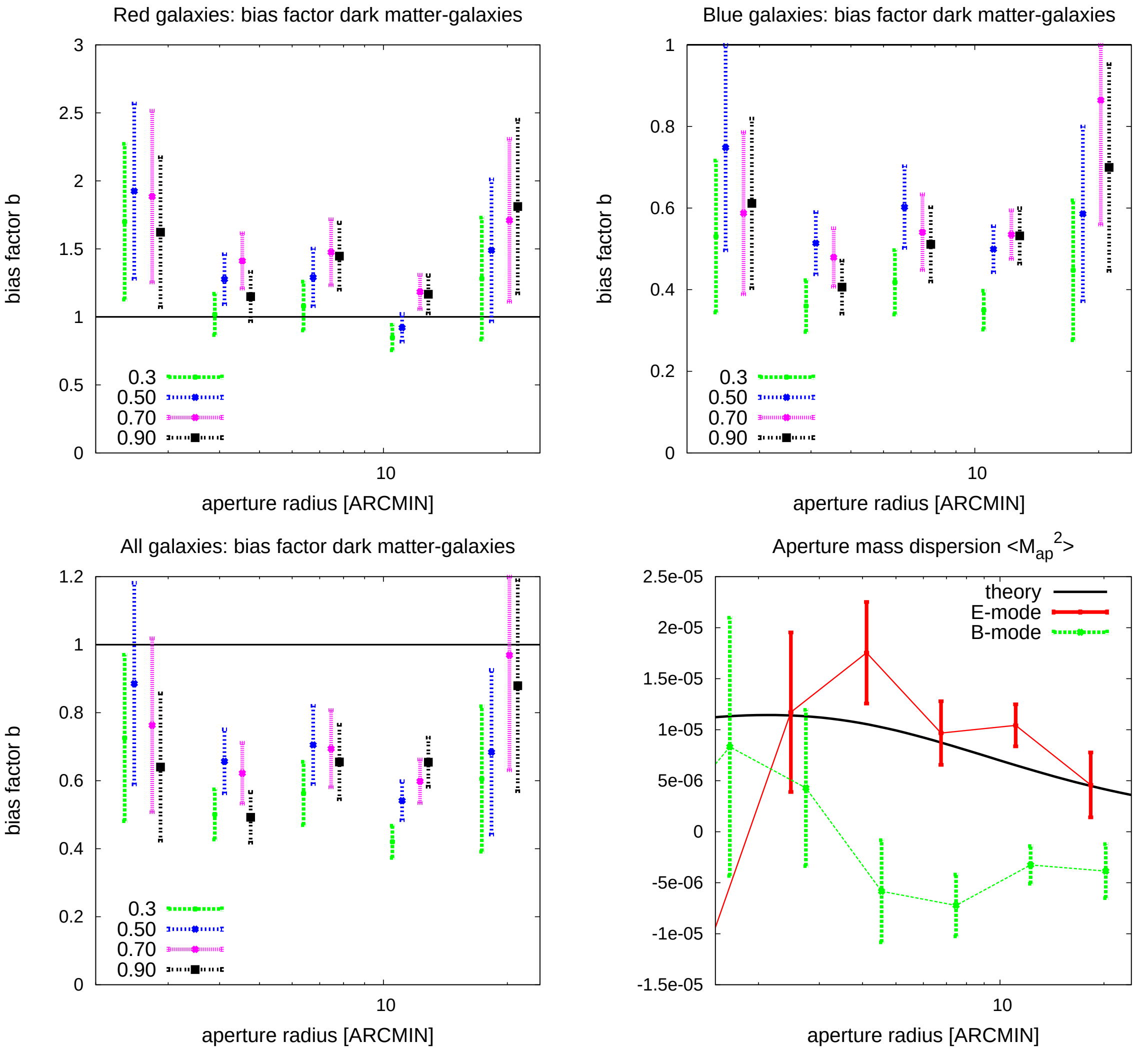

Figure 5.9.: *Linear bias factor relative to the dark matter of the red, blue and combined galaxy sample in the upper left, upper right and bottom left panel, respectively. For redshift bins in increasing order, the apertures with radii* $10'$ *correspond to an effective comoving physical scale of* $2.43\,h^{-1}\mathrm{Mpc}$, $3.85\,h^{-1}\mathrm{Mpc}$, $5.13\,h^{-1}\mathrm{Mpc}$ *and* $6.17\,h^{-1}\mathrm{Mpc}$, *respectively. The panel in the lower right is the dispersion of the aperture mass which is used to calculated the bias parameters. Note that the E-mode signal becomes consistent with zero on scales smaller than about* $2'$. *Therefore, the bias factor can only be inferred for aperture radii larger than* $2'$. *The solid line is the theoretically expected aperture mass dispersion assuming concordance* Λ*CDM and a mean redshift of the galaxy sources of* $\langle z\rangle = 0.76$.

Table 5.5.: *Best-fit parameters to the data points, $\theta < 15'$, of the linear bias factor, Fig. 5.9, as measured for the red, blue and complete galaxy sample binned in redshift. The values in the column $\bar{b}$ are the average bias factor (constant line fit), while b_0 and b' are the parameters of the best-fitting line $b(\theta_{\rm ap}) = b_0 + b'\,\theta_{\rm ap}$ where $\theta_{\rm ap}$ is the aperture radius. Note that the bias factor calibration assumes a flat ΛCDM with $\Omega_{\rm m} = 0.3$. Statistical errors do not include cosmic variance and the uncertainty concerning the redshift distributions of lens and source catalogue.*

	ALL			RED			BLUE		
$\langle z\rangle$	$\bar{b}$	b_0	b'	$\bar{b}$	b_0	b'	$\bar{b}$	b_0	b'
0.3	0.47(3)	0.58(3)	−0.010(2)	0.95(6)	1.1(1)	−0.017(8)	0.36(3)	0.45(3)	−0.008(3)
0.5	0.62(5)	0.82(3)	−0.018(4)	1.2(1)	1.6(3)	−0.04(2)	0.55(7)	0.7(2)	−0.02(1)
0.7	0.70(3)	0.66(9)	+0.004(8)	1.39(8)	1.6(2)	−0.02(2)	0.58(3)	0.50(4)	+0.08(4)
0.9	0.63(3)	0.59(7)	+0.004(6)	1.36(3)	1.42(8)	−0.005(6)	0.52(3)	0.50(8)	+0.001(8)

an aperture radius of $3'$. Below $\sim 3'$ E-mode and B-mode become comparable and consistent with zero so that we cannot use the measurements on the these scales.

A large contribution to the $\langle M_{\rm ap}^2\rangle$ signal comes from the A901 field (not shown). This was already observed by Brown *et al.* (2001). Note that the aperture mass dispersion is essentially the shear power spectrum seen through a narrow band filter. By looking at the shear power spectra of the fields A901, AXAF (or CDFS) and S11 in their paper, Fig. 15, we expect that a combined shear power spectrum would yield more power than expected for a cosmic average. Therefore their measurements for the cosmic shear fluctuations are in qualitative agreement with our measurement for $\langle M_{\rm ap}^2\rangle$, despite the fact that their source catalogue is somewhat deeper, $\langle z\rangle = 0.86$ instead of $\langle z\rangle = 0.76$, and the data reduction was done independently with another pipeline.

5.4.4. Galaxy-dark matter bias

The separate measurements of the aperture statistics are now combined to draw conclusion about the relative clustering between galaxies and the total matter (mainly dark matter), that is to say about galaxy bias. On the level of second-order statistics, we are only able to obtain answers about the linear stochastic bias coefficients, Eqs. (1.54), which are the ratio of the rms-values of the aperture number count and aperture mass, and the correlation between both.

For transforming the aperture statistics into linear stochastic bias as function of scale, *i.e.* aperture radius, we employ Eqs. (3.13).

Linear bias factor

The linear bias factor is plotted for the red, blue and complete galaxy sample in Fig. 5.9. The calibration, Sect. 5.3.4, assumes a spatially flat ΛCDM as fiducial cosmological model with $\Omega_{\rm m} = 0.3$; the bias values need to be scaled up or down for smaller or larger $\Omega_{\rm m}$, respectively (Fig. 5.5). Based on these data points the average bias factor, $\bar{b}$, on the scale range $\theta \in [3', 20']$ is calculated, and linear models, $b(\theta) = b_0 + b'\,\theta$, are fitted to parameterise a possible scale-dependence (Table 5.5); b_0 and b' are constants. The angular range corresponds to effective comoving physical scales of $730\,h^{-1}$kpc $\lesssim r \lesssim 12\,h^{-1}$Mpc, somewhat smaller for the low-redshift sample and a bit larger for the high-redshift sample.

For all redshift bins, rms-fluctuations in number density of the complete galaxy sample are smaller than fluctuations in the dark matter density field, $\bar{b} = 0.5-0.7$. This was also seen in the Garching-Bonn Deep Survey (GaBoDS), foregoing chapter, although with a larger value, $\bar{b} = 0.8-0.9$. This small discrepancy may be explained by the fact that the redshift distribution in GaBoDS has only approximately been estimated, whereas here accurate photometric redshifts of the individual foreground galaxies are given which makes the calibration more accurate. Our measurements in the lowest redshift bin are consistent with the results of Hoekstra *et al.* (2002) who applied the same technique to the combined VIRMOS-DESCART/RCS survey finding for aperture radii $3' \lesssim \theta \lesssim 20'$ a bias factor of $b \sim 0.7$. Furthermore, the result of Hoekstra *et al.* and ours are consistent with ΛCDM predictions assuming $\Omega_{\rm m} \sim 0.3$. An galaxy anti-bias on intermediate scales is a theoretical necessity in order to reconcile the theoretical dark matter correlation function with the (nearly) power-law correlation function of the galaxies (*e.g.* Jenkins *et al.* 1998; Jing *et al.* 1998).

Numerical simulations (Weinberg *et al.* 2004; Yoshikawa *et al.* 2001; Somerville *et al.* 2001; Blanton *et al.* 2000; Cen & Ostriker 2000) predict an increase of the linear bias factor (all galaxies) by a factor of ~ 1.5 within $0 < z < 1$ at scales of about $1-8\,h^{-1}$Mpc. In our data, we may see an overall growth of the bias factor for all galaxy samples, when going to higher redshifts, that is consistent with this factor . Due to the remaining statistical uncertainties, however, a non-evolution cannot be ruled out.

In COMBO-17, red galaxies are more or equally clustered than dark matter, $\bar{b} = 1.0-1.4$, at all redshifts, whereas the blue sample is clearly anti-biased with $\bar{b} = 0.4-0.6$. This agrees quite well with simulations that assume the same fiducial cosmological model as adopted here. Specifically, Yoshikawa *et al.* (2001) split the simulated galaxy sample into galaxies formed early, $z > 1.5$, and recently formed galaxies, $z < 1.5$; the samples were denoted as "early types" and "late types". The implicit assumption of the authors is that "early-type" galaxies form earlier than late-type galaxies.[7] This division line was chosen to obtain a galaxy number ratio of early- and late-type galaxies of 1/3 at $z = 0$ which corresponds to the observed ratio (Loveday *et al.* 1995). The authors argue that age-splitting is similar to a colour-splitting and therefore comparable to subdividing the galaxy sample into red and blue galaxies like in our analysis. Yoshikawa *et al.* find, for $z = 0$, $b_{\rm red} \approx 1.4$ and $b_{\rm blue} \approx 0.7$ for the red (old) and blue (young) sample near $\sim 3\,h^{-1}$Mpc, respectively. Weinberg *et al.* (2004) quote $b_{\rm red} \approx 1.3$ and $b_{\rm blue} \approx 0.7$ at about the same scale, adopting age-splitting as well. Somerville *et al.* (2001) find qualitatively the same result but less bias/anti-bias because the scales studied are larger, $r \sim 8\,h^{-1}$Mpc, and the result is slightly different for morphologically selected samples and samples chosen by colour (bias and anti-bias are larger for the case of colour selection). The common theoretical explanation (*cf.* Zehavi *et al.* 2004; Somerville *et al.* 2001) for the red(blue) bias(anti-bias) is that the mean dark matter halo mass occupied by red (early-type) galaxies is larger than the mean halo mass occupied by blue (late-type) galaxies. As low-mass haloes are less clustered and high-mass haloes are more clustered than the overall dark matter density field (Mo & White 1996), blue galaxies are anti-biased, whereas red galaxies

---

[7] The terminology of "early-type" and "late-type" galaxies in astronomy, however, has purely historical reasons. At the time of coining these terms nothing was known about the origin of the morphology of galaxies (Hubble 1936).

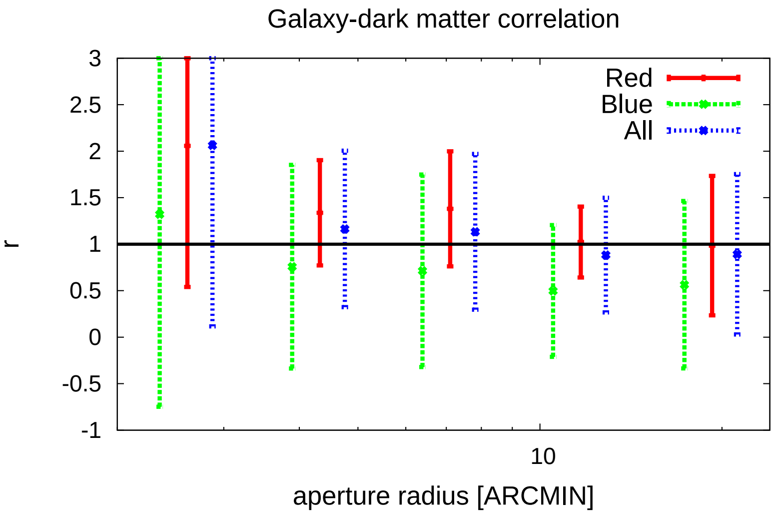

Figure 5.10.: *Correlation between dark matter and red, blue and complete galaxies sample, respectively, in the lowest redshift bin, $\langle z\rangle = 0.3$. The data points assume a SIS-profile for the mean tangential shear about a foreground galaxy.*

are positively biased with respect to the dark matter.

For all samples, there is for $z \lesssim 0.5$ a significant scale-dependence of the bias factor that is increasing towards smaller scales (Table 5.5). The increase is stronger for the red sample which is due to their steeper slope of $\omega(\theta)$, $\delta \sim 0.95$, compared to the blue sample, $\delta \sim 0.7$. We do not observe a significant scale-dependence below $20'$ at higher redshift, $\langle z\rangle \gtrsim 0.5$. In the last bin at about $20'$, we may see an increase of the bias factor for all samples which, however, is not very significant. The scale-dependence of the bias factor depends very weakly on the assume fiducial cosmological model (van Waerbeke 1998) since the calibration virtually only affects the overall amplitude. A scale-dependence of bias has also been observed by Pen *et al.* (2003) and Hoekstra *et al.* (2002). It is a generic prediction of the CDM paradigm (*e.g.* Zehavi *et al.* 2004; Weinberg *et al.* 2004; Blanton *et al.* 1999; Jing *et al.* 1998; Jenkins *et al.* 1998).

Linear correlation factor

For the correlation parameter $r(\theta_{\rm ap})$, Eq. (3.13), we require both $\langle N M_{\rm ap}\rangle$ and $\left\langle M_{\rm ap}^2\right\rangle$ which are not, as outlined above, available for an overlapping range of aperture radii: we have significant detections for $\left\langle M_{\rm ap}^2\right\rangle$ only for aperture radii larger than $3'$, whereas $\langle N M_{\rm ap}\rangle$ only for aperture radii smaller than $\sim 3'$ and almost only for the red galaxy sample. A larger survey area is necessary to achieve the require signal-to-noise for performing the full analysis in the sense of Hoekstra *et al.* (2002).

The situations improves a bit, however, if we assume that the galaxy-galaxy lensing signal can be approximated by a power law, $\langle \gamma_{\rm t}\rangle = A_\xi\,(\theta/1')^{-\delta}$. This seems, at least on small scales, to be a good approximation (*cf.* McKay *et al.* 2001). By adding this extra piece of information we can nevertheless draw some conclusions about the correlation between dark matter and galaxy distribution. The parameters of the best-fitting power law to the measured mean tangential are listed in Table 5.4. Additionally in a second fit, we assume a singular isothermal sphere model (SIS), thus a power law with exponent $\delta = -1$, because the power law slope cannot be very well constrained for our data. The parameters of the SIS-fit are the only ones used in the following analysis. We trust only fits for the lowest redshift bin, which is the bin where we find the most significant signal. The signal for the blue sample seems to be rather weak so that we consider the corresponding fit just as an upper limit.

The best-fitted SIS-profile for $\langle\gamma_{\rm t}\rangle$ is transformed to $\langle NM_{\rm ap}\rangle$ by virtue of Eq. (3.24). For the statistical error of $\langle NM_{\rm ap}\rangle$ we take into account the uncertainties of the slope and amplitude for $\langle\gamma_{\rm t}\rangle$. Together with $\left\langle N^2\right\rangle$ and $\left\langle M_{\rm ap}^2\right\rangle$ we are then able to compute the correlation parameter. Note, however, that the SIS-profile for all scales is a very strong assumption which is likely to fail on galaxy group and cluster scales. Fig. 5.10 shows the correlation parameters of the red, blue and complete sample in the lowest redshift bin. Similar to the bias factor estimate, the correlation factor depends on the fiducial model used for the calibration (Fig. 5.5): the plotted correlation factor increases for $\Omega_{\rm m} > 0.3$ and decreases otherwise. For a median redshift $\langle z\rangle = 0.3$, this dependence is very weak, though, because most of the signal contributing to the aperture mass is from the redshift range $0.2 < z < 0.4$ where the galaxies are located in.

We find that, despite the strong assumption about the profile of $\langle\gamma_{\rm t}\rangle$, the correlation parameters of the samples are only poorly constrained. Being very optimistic we take the error-weighted average of the data points of the red sample, which has the most significant galaxy-galaxy lensing signal, and estimate that the mean correlation factor of the red sample over the plotted range is $r_{\rm red} = 1.1 \pm 0.2$. This value suggests that the correlation factor of red galaxies is close to unity which means that the red sample is highly correlated to the dark matter distribution. Wilson et al. (2001) arrive at a similar conclusion for a selected sample of bright red galaxies.

5.4.5. Relative galaxy bias

We now turn to the relative bias between the red and blue samples. Here we do not need the information on the dark matter clustering provided by weak gravitational lensing. We employ the estimators in Eqs. (5.8) to convert the aperture number count dispersion, $\langle N^2_{\rm red/blue}\rangle$, and aperture number count cross-correlation, $\langle N_{\rm red}N_{\rm blue}\rangle$, of the red and blue sample into the relative linear stochastic bias.

Relative linear bias factor

As already seen in Fig. 5.9 red and blue galaxies are differently biased with respect to the dark matter and therefore have also to be differently biased relative to each other. This difference is equivalent to a relative bias factor of about $b = 2 - 3$ which is slightly rising in the regime $1' < \theta < 10'$ towards smaller scales (Fig. 5.11). The rise stems from the different power-law slopes of $\langle N^2\rangle$ for the two samples (Sect. 5.4.1); red galaxies obey a steeper power-law than blue galaxies. At $\theta_{\rm ap} = 1'$ we find a bias of $b \approx 3$ which drops to $b \approx 2.2$ at $\theta = 20'$. For the lowest redshift bin, this is in good agreement with Madgwick et al. (2003), their Fig. 4. Furthermore, the observed scale-dependence explains why we find an overall larger value for the red/blue bias than other authors who determined the relative bias with various different methods on larger scales, *e.g.* Conway *et al.* (2005), $b \approx 1.3$ at $15\,h^{-1}$Mpc, Wild *et al.* (2005), $b \approx 1.8$ at $10\,h^{-1}$Mpc, Willmer *et al.* (1998), $b \approx 1.2$ at $8\,h^{-1}$Mpc, or Guzzo *et al.* (1997), $b \approx 1.7$.

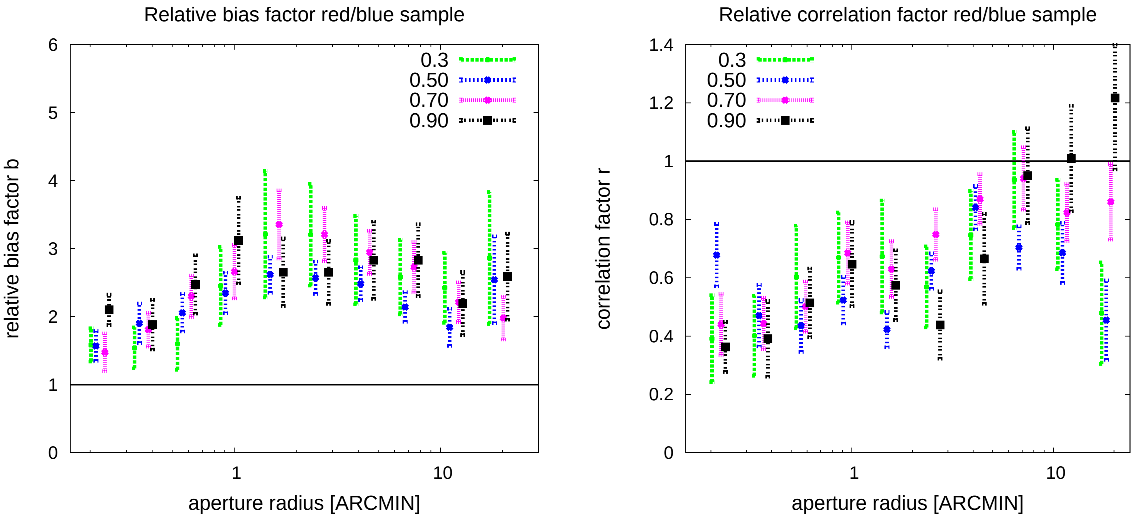

Figure 5.11.: *Relative linear stochastic bias between the red and blue galaxy sample for four median redshifts. For redshift bins in increasing order, apertures with radii* $10'$ *correspond to an effective comoving physical scale of* $2.43\,h^{-1}$Mpc, $3.85\,h^{-1}$Mpc, $5.13\,h^{-1}$Mpc *and* $6.17\,h^{-1}$Mpc *for the smallest to the largest redshift bin, respectively.*

Within the errors we do not see an evolution of the relative bias with redshift as, for example, has been reported by Le Fèvre *et al.* (1996). This confirms the finding of Phleps & Meisenheimer (2003). On scales smaller than $1'$, we find that the relative bias decreases again down to a value of $b \sim 1.5 - 2$ at $\sim 0'.5$.

Relative linear correlation factor

The correlation between red and blue galaxies for four median redshifts is shown in Fig. 5.11. We can make out a clear trend of decorrelation, $r < 1$, between the two samples towards small scales starting from about $10'$, which corresponds to comoving $\sim 3 - 6\,h^{-1}$Mpc depending on the median redshift. We estimate that the correlation factor drops to a minimum of $r = 0.57 \pm 0.06, 0.52 \pm 0.02, 0.56 \pm 0.02, 0.56 \pm 0.05$ for the median redshifts $\langle z \rangle = 0.3, 0.5, 0.7, 0.9$, respectively. These values were obtained by averaging all data points between $[0'.3, 2']$ using the errors as weights; errors were assumed to be uncorrelated. An evolution with redshift exceeding the statistical errors is not visible. We note that cosmic variance is particularly strong on the larger scales which explains the large scatter of the data points beyond $10'$. As many authors find a correlation close to unity on large scales (*e.g.* Wild *et al.* 2004; Conway *et al.* 2004; Blanton 2000; Tegmark & Bromley 1995) that is decreasing towards smaller scales (*e.g.* Wild *et al.* 2004), we expect our data points to be actually consistent with $r \sim 1$ beyond $10'$.

The decorrelation is probably intimately related to the well established morphology-density relation of galaxies (*e.g.* Goto *et al.* 2003; Narayanan *et al.* 2000; Dressler *et al.* 1997; Dressler 1980), according to which the fraction of red galaxies increases in regions of high galaxy densities while the fraction of blue galaxies is high in regions of low galaxy density. This relation defines a mapping, probably with a random component (see next section), between the density field of all galaxies and the number density field of red and blue galaxies, respectively. It is likely that this mapping can be translated into our observed scale-dependence of the correlation factor. If this is the case, we can conclude from our observation that the density-morphology relation has to be present up to $z \sim 0.9$.

Relative non-linear stochastic bias

Is the decorrelation between the density fluctuations of red, $\delta_{\rm red}$, and blue, $\delta_{\rm bue}$, galaxies a result of a deterministic non-linear mapping or the result of a real stochastic scatter between $\delta_{\rm blue}$ and $\delta_{\rm red}$, or both? In the non-linear stochastic bias scheme, see Sect. 1.4.3, one can disentangle contributions to the correlation factor, r, caused by non-linearity, $\epsilon_{\rm nl}$, or stochasticity, $\epsilon_{\rm scatt}$,

$$r_{\rm rel} = (1 + \epsilon^2_{\rm scatt} + \epsilon^2_{\rm nl})^{-1/2} \,, \tag{5.26}$$

if we know the joint PDF $P(\delta_{\rm red}, \delta_{\rm blue})$. Wild *et al.* (2004) argue that number densities of galaxies are well modelled by a lognormal distribution and $P(\delta_{\rm blue}, \delta_{\rm red})$ by a bivariate lognormal distribution. In this case we have (see Appendix A.4):

$$\begin{aligned} \epsilon^2_{\rm nl} &= \frac{1}{r^2_{\rm rel}} \frac{\left\langle [f(\delta_{\rm red})]^2 \right\rangle}{\left\langle \delta^2_{\rm blue} \right\rangle} - 1 \,, \\ \epsilon^2_{\rm scatt} &= \frac{1}{r^2_{\rm rel}} \left(1 - \frac{\left\langle [f(\delta_{\rm red})]^2 \right\rangle}{\left\langle \delta^2_{\rm blue} \right\rangle} \right) \,, \end{aligned} \tag{5.27}$$

where

$$\frac{\left\langle [f(\delta_{\rm red})]^2 \right\rangle}{\left\langle \delta^2_{\rm blue} \right\rangle} = \frac{1}{\left\langle \delta^2_{\rm blue} \right\rangle} \left(\exp\left[\frac{\ln^2\left(\langle \delta_{\rm blue}\delta_{\rm red} \rangle + 1 \right)}{\ln\left(\langle \delta^2_{\rm red} \rangle + 1 \right)} \right] - 1 \right) \,. \tag{5.28}$$

The aperture number count, N, is a projection of the density contrast smoothed to some scale depending on the aperture radius, see Eqs. (3.56) and (3.9). Therefore, $\langle N^n_{\rm red} N^m_{\rm blue} \rangle$ with $n + m = 2$, which have been measured in this study, are equivalent to $\langle \delta^n_{\rm red} \delta^m_{\rm blue} \rangle$ smoothed to some effective scale and averaged over some redshift range. Thus, we can employ (5.27), (5.28) and our measurement for the second-order aperture number count statistics of red and blue galaxies to estimate $\epsilon_{\rm scatt}$ and $\epsilon_{\rm nl}$. This has been done for Fig. 5.12.

We find that both $\epsilon_{\rm scatt}$ and $\epsilon_{\rm nl}$ are decreasing with smoothing scale but are, at equal scales, indistinguishable between the different redshift bins, meaning that we do not see a redshift dependence. The ratio $\epsilon_{\rm scatt}/\epsilon_{\rm nl}$ has a value roughly between $5 - 15$ for all scales. This means that stochasticity in the relation between red and blue galaxies contributes most to the correlation factor. Wild *et al.* (2004) find in the 2dFGRS $\epsilon_{\rm scatt} = 0.45 \pm 0.05$ and $\epsilon_{\rm nl} = 0.055 \pm 0.005$ at a scale of $10\,h^{-1}$Mpc, which is in agreement with our largest aperture radii corresponding to $\sim 6\,h^{-1}$Mpc for the lowest redshift bin. Our measurement thus shows that the trend observed by Wild *et al.* (2004), namely that $\epsilon_{\rm scatt}$ and $\epsilon_{\rm nl}$ are increasing towards smaller scales, continues below $10\,h^{-1}$Mpc.

Constraining the correlation between blue galaxies and dark matter

Finally, with our measurement for the red/blue correlation and our crude estimate for the correlation between red galaxies and dark matter, $r_{\rm red} = 1.1 \pm 0.2$ (foregoing section), at a

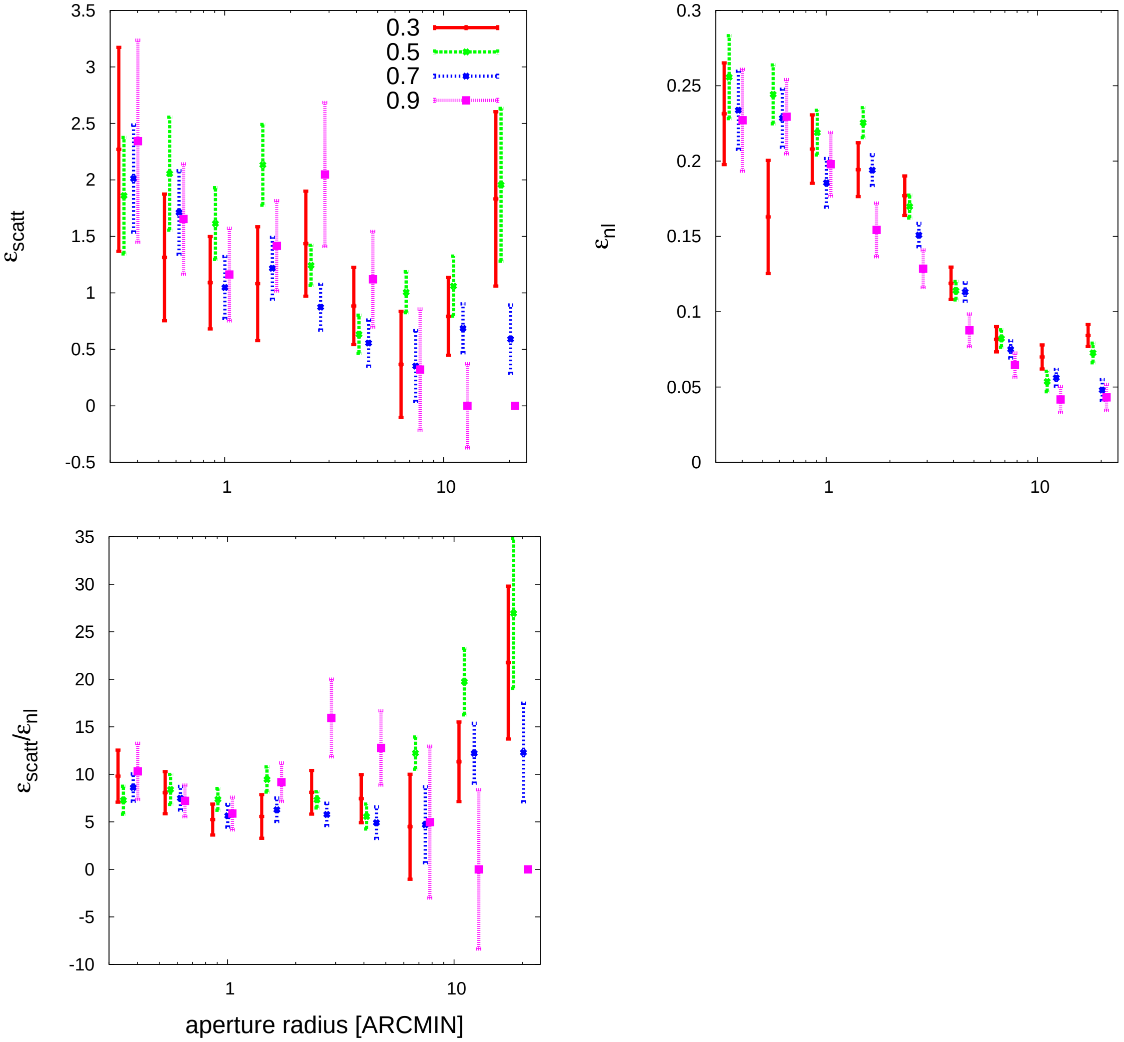

Figure 5.12.: *Separation of non-linear,* $\epsilon_{\rm nl}$*, and stochastic,* $\epsilon_{\rm scatt}$*, contributions to the relative linear correlation factor,* $r_{\rm rel} = (1+\epsilon^2_{\rm scatt}+\epsilon^2_{\rm nl})^{-1/2}$*, of red and blue galaxies by assuming a bivariate lognormal joint PDF* $P(\delta_{\rm red}, \delta_{\rm blue})$*. Both contributions show an increase towards smaller scales (upper left and upper right panel). The largest fraction is due to stochasticity with* $\epsilon_{\rm scatt}/\epsilon_{\rm nl} \gtrsim 5-15$ *(lower left). Indicated are the median redshifts of the samples. For redshift bins in increasing order, apertures with radii* $10'$ *correspond to an effective comoving physical scale of* $2.43\,h^{-1}{\rm Mpc}$, $3.85\,h^{-1}{\rm Mpc}$, $5.13\,h^{-1}{\rm Mpc}$ *and* $6.17\,h^{-1}{\rm Mpc}$ *for the smallest to largest redshift bin respectively.*

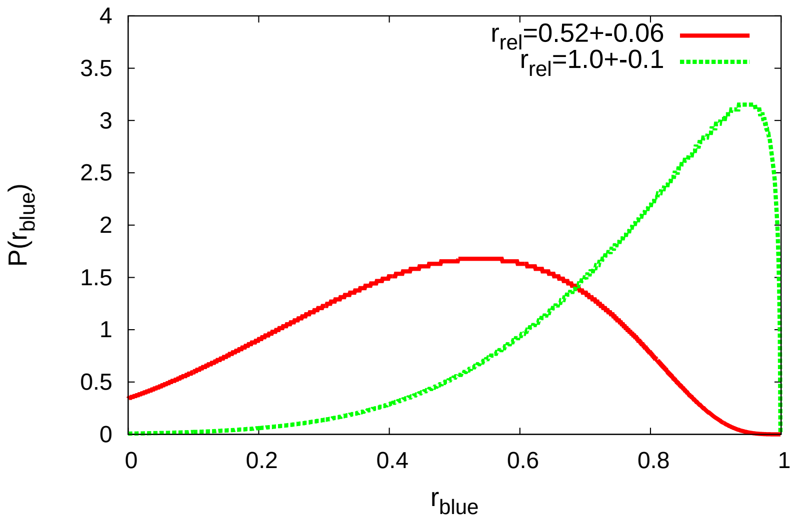

Figure 5.13.: A-posteriori *probability distribution of the correlation between the blue galaxy sample and dark matter at median redshift* $\langle z\rangle = 0.3$ *and a effective physical scale of* $\sim 200\,h^{-1}\mathrm{kpc}$ *based on* $r_{\rm red} = 1.1 \pm 0.2$ *(Gaussian PDF) and* $r_{\rm rel} = 0.52 \pm 0.06$ *(Gaussian PDF). As additional prior all correlation factors are assumed to be positive. For comparison, the* a-posteriori *PDF of* $r_{\rm blue}$ *assuming* $r_{\rm rel} = 1.0 \pm 0.1$ *is plotted as well. Such a value for* $r_{\rm rel}$ *is typically found on larger scales.*

median redshift $\langle z\rangle = 0.3$ we can constrain the correlation between blue galaxies and dark matter. That supplements the discussion of the foregoing section where $r_{\rm blue}$ could not be deduced from the cross-correlation $\langle NM_{\rm ap}\rangle$ alone. Let $r_{\rm red}$, $r_{\rm blue}$ and $r_{\rm rel}$ be the correlation between red galaxies and dark matter, blue galaxies and dark matter, and red and blue galaxies, respectively. We noted earlier on in this thesis, Eq. (2.37), that the triple $\{r_{\rm red}, r_{\rm blue}, r_{\rm rel}\}$ cannot assume any conceivable combination of values. Instead, they have to fulfil the condition

$$2r_{\rm red}\,r_{\rm blue}\,r_{\rm rel} \ge r_{\rm red}^2 + r_{\rm blue}^2 + r_{\rm rel}^2 - 1\;, \tag{5.29}$$

because the covariance matrix of the density fluctuations of the three fields has to be positive definite. Apart from $r_{\rm red}$, we also have $r_{\rm rel} = 0.57 \pm 0.06$ at $\sim 200h^{-1}$kpc. The correlation factors $r_{\rm red}$ and $r_{\rm rel}$ plus the inequality in combination constrain the allowed parameter range of $r_{\rm blue}$ at the same scale as can be seen by the following argument. For a given $r_{\rm red}$ and $r_{\rm rel}$, (5.29) defines an interval $[r_{\rm min}, r_{\rm max}]$ of possible values for $r_{\rm blue}$. Since we do not have any other constraints on $r_{\rm blue}$, we assume for fixed values $r_{\rm blue}$ and $r_{\rm rel}$ a uniform conditional *a-posteriori* probability distribution,

$$P(r_{\rm blue}|r_{\rm red}, r_{\rm rel}) \propto \begin{cases} 1 & r_{\rm blue} \in [r_{\rm min}, r_{\rm max}] \\ 0 & \text{otherwise} \end{cases}\;, \tag{5.30}$$

of $r_{\rm blue}$ inside this interval. Furthermore, in order to account for the fact that $r_{\rm red}$ and $r_{\rm rel}$ are not exactly known we marginalise $P(r_{\rm blue}|r_{\rm red}, r_{\rm rel})$:

$$P(r_{\rm blue}) = \int_0^1 {\rm d}r_{\rm red}{\rm d}r_{\rm rel}\, P(r_{\rm blue}|r_{\rm red}, r_{\rm rel})\, P(r_{\rm red})\, P(r_{\rm rel})\;, \tag{5.31}$$

where we assume that the errors of $r_{\rm red}$ and $r_{\rm rel}$ have both a Gaussian PDF, $P(r_{\rm red})$ and $P(r_{\rm rel})$, and are not correlated. For the level of accuracy we are working on here this is a reasonable assumption. As additional prior we demand that all correlation factors have to be positive; negative galaxy-galaxy lensing signals are ruled out on a high confidence level by other studies (*e.g.* McKay *et al.* 2001). Using these arguments we conclude from the marginalised $P(r_{\rm blue})$, Fig. 5.13, that $r_{\rm blue} = 0.5 \pm 0.2$. Thus, blue galaxies are less correlated to dark matter than red galaxies, either due to non-linearity, stochasticity or both. Applying the same technique, we find $r_{\rm blue} = 0.8 \pm 0.2$ for $r_{\rm rel} = 1.0 \pm 0.1$, for the typical correlation found on scales beyond $10'$ corresponding to $\sim 2.4\,h^{-1}$Mpc for $\langle z \rangle = 0.3$.

5.5. Conclusions

We use accurate photometric redshifts to study the linear stochastic bias of galaxies in the COMBO-17 Survey as a function of scale and median redshift, $0.3 \lesssim z \lesssim 0.9$. This comprises the bias in the clustering of red and blue galaxies with respect to the total matter (dark matter) content, on comoving scales $730(1800)\,h^{-1}$kpc $\lesssim r \lesssim 6(12)\,h^{-1}$Mpc for $\langle z \rangle = 0.3(0.9)$, and the relative bias between red and blue galaxies, on comoving scales from $200(600)\,h^{-1}$kpc $\lesssim r \lesssim 6(12)\,h^{-1}$Mpc.

The red and blue galaxy subsample are selected by a redshift dependent red-sequence cut in a rest-frame colour magnitude diagram, $M_{\rm V}$ vs. $U - V$. Morphologically, the red sample consist mainly of elliptical galaxies, the blue sample mainly of (star-forming) spiral and irregular galaxies. In addition, galaxies are chosen to have apparent magnitudes brighter than $m_{\rm R} = 24\,$mag, which guarantees the photometric redshift accuracy, and absolute magnitudes brighter than $M_{\rm V} - 5\log_{10} h = -17\,{\rm mag} - (U - V)$ in order to obtain galaxy samples comparable in median absolute magnitude at all redshifts. The effective area that can be used for this work is about $0.78\,{\rm deg}^2$, distributed among three fields: A901, AXAF and S11.

In A901 and S11, the fraction of red galaxies is a decreasing function with median redshift: $\sim 23\%$ at $\langle z \rangle = 0.3$ down to $\sim 14\%$ at $\langle z \rangle = 0.9$. In AXAF, the fraction is significantly lower, and no clear evolution is visible. We interpret the fact that the total number of galaxies in AXAF is relatively low considering the total observation time as an indication that AXAF is under-abundant in galaxies and therefore poor in galaxy clusters. In this case, the fraction of red galaxies has to be small according to the morphology-density relation.

The clustering of galaxies and dark matter is investigated using second-order aperture statistics. This statistics probes density fluctuations inside circular apertures weighted with a polynomial compensated filter. It is applied to the projected galaxy number density, the so-called aperture number count, and dark matter density, the so-called aperture mass. The aperture mass is inferred from gravitational shear distortions of images of faint background galaxies. The linear stochastic bias is estimated using three individual statistical quantities: i) the aperture number count dispersion, ii) the aperture mass dispersion and iii) the cross-correlation between aperture number count and aperture mass. In order to calibrate the estimates of bias between galaxies and dark matter we have to assume a fiducial cosmological model. We choose for the following results a spatially flat ΛCDM with $\Omega_{\rm m} = 0.3$, $\Omega_\Lambda = 0.7$, $\Gamma = 0.21$, $\sigma_8 = 0.9$. The background galaxies used for the lensing analysis are taken from the Garching-Bonn Deep Survey; they do not have photometric redshifts since they go deeper than $m_{\rm R} = 24\,$mag.

The obtained aperture number count dispersion is almost consistent with a power law for the angular correlation function, $\omega(\theta)$, of galaxies; red galaxies obey a power law with a slope, $\delta \approx 0.9$, steeper than for blue galaxies, $\delta \approx 0.7$, and exhibit a stronger clustering, A_ω, than blue galaxies, by about a factor of 5. Our results for $\omega(\theta)$ are in agreement with earlier studies based on different surveys. The amplitude of angular clustering decreases with median redshift for the red, the blue and the complete galaxy sample. When converted to the clustering in three-dimensional comoving space by deprojecting $\omega(\theta)$ with Limber's equation our measurements are compatible with a non-evolution of clustering. However, statistical uncertainties are large.

We find that red and blue galaxies are differently biased to the dark matter. Red galaxies are equally or more clustered than dark matter for all redshifts, while blue galaxies are less clustered than the dark matter. For $z \lesssim 0.5$, we see a scale-dependence of the bias factor which is slightly increasing towards smaller scales; the increase is stronger for the red sample. For the largest aperture radius we also find a possible increase of the bias factor for all redshifts. Averaging the bias factor over all observed scales, $\theta < 15'$, yields $\bar{b} = 0.95 \pm 0.06, 1.2 \pm 0.1, 1.39 \pm 0.08, 1.36 \pm 0.03$ (red) and $\bar{b} = 0.36 \pm 0.03, 0.55 \pm 0.07, 0.58 \pm 0.03, 0.52 \pm 0.03$ (blue) for the median redshifts $\langle z \rangle = 0.3, 0.5, 0.7, 0.9$, respectively. The figures allow a moderate bias increase with redshift by a factor of $1 - 2$. An increase by a factor of ~ 1.5 and a scale-dependent bias is expected by the currently favoured ΛCDM model and therefore is consistent with our measurements. Moreover, the absolute values of $\bar{b}$ for red (biased) and blue (anti-biased) galaxies are also in agreement with cosmological simulations of galaxy formation and evolution assuming the fiducial cosmology adopted here.

Due to the relatively small survey area, the aperture mass dispersion, $\langle M_{\rm ap}^2 \rangle$, and aperture mass/aperture number count cross-correlation, $\langle N M_{\rm ap} \rangle$, do not yield significant signals on a common range of scales. Therefore, the measurement of the dark matter/galaxy correlation factor is not directly possible. To get at least some answers we assume a template function (SIS-profile) with one degree of freedom that is fitted to the galaxy-galaxy lensing signal. This is possible for the samples at lowest median redshift. The signal for red galaxies is strongest which suggests that red galaxies (early-types) are situated inside dark matter halos that are on average more massive than the hosts of blue galaxies (mainly late-types). Using the template-fit we can extrapolate $\langle N M_{\rm ap} \rangle$ to scales where significant data points of $\langle M_{\rm ap}^2 \rangle$ have been found. This crude estimate yields a correlation between dark matter and red galaxies of $r_{\rm red} = 1.1 \pm 0.2$ averaged over the observed range of scales, which implies that red galaxies are highly correlated to the dark matter distribution; similar constraints for blue galaxies are poor.

Using only the aperture number count statistics of blue and red galaxies we investigated the relative bias, $b_{\rm rel}$, between these two samples. We find that the relative bias factor is a decreasing function with scale beyond an aperture radius of $\sim 1'$: $b_{\rm rel} \approx 3$ at $\sim 240(610)\,h^{-1}$kpc and $b_{\rm rel} \approx 2.2$ at $\sim 2.4(6.2)\,h^{-1}$Mpc for a median redshift of $\langle z \rangle = 0.3(0.9)$. For smaller aperture radii than $\sim 1'$, the bias factor decreases. The decrease on scales $< 1'$ might be a systematic effect of the used estimators for $\omega(\theta)$, Eq. (3.28). Within the statistical uncertainties we do not find a clear evolution with redshift on all scales.

The relative correlation factor relating the distributions of red and blue galaxies is clearly scale-dependent. It drops from a value close to unity for large aperture radii, $\gtrsim 5(12)\,h^{-1}$Mpc (comoving), to $r_{\rm rel} = 0.55 \pm 0.05$ on scales of about $\sim 250(600)\,h^{-1}$kpc for the sample with median redshift $\langle z \rangle = 0.3(0.9)$. A redshift evolution is not observed within the statistical errors. These values may be a new constraint for models of galaxy formation. We expect that the scale-dependence is intimately related to the well known morphology-density relation of galaxies. If so, then our results show that there is such a relation present up to median redshifts of $\langle z \rangle = 0.9$. This needs further investigation.

Specifically, the result for $r_{\rm rel}$ demonstrates that blue galaxies are not correlated the same way to the dark matter distribution as red galaxies. In fact, our measurement at $\langle z \rangle = 0.3$ for $r_{\rm red}$, which is based on galaxy-galaxy lensing, and for $r_{\rm rel}$ can be combined to constrain $r_{\rm blue}$. We find $r_{\rm blue} = 0.5 \pm 0.2$ at $\sim 500\,h^{-1}$kpc and $r_{\rm blue} = 0.8 \pm 0.2$ at $\sim 5\,h^{-1}$Mpc. Assuming a bivariate lognormal joint PDF for the smoothed density contrasts of red and blue galaxies, we can estimate the contributions of stochasticity, $\epsilon_{\rm scatt}$, and non-linearity, $\epsilon_{\rm nl}$, to the correlation factor $r_{\rm rel}$ within the framework of the non-linear bias scheme. We find that although both variables $\epsilon_{\rm scatt}$ and $\epsilon_{\rm nl}$ increase from large to small aperture radii their ratio is roughly constant between $5-15$ on all scales at all redshifts. Consequently, a random scatter between the local densities of red and blue galaxies, $\epsilon_{\rm scatt}$, mostly contributes to $r_{\rm rel}$. Accepting that red galaxies are highly correlated to the dark matter distribution, this result means that blue galaxies also have to some degree to be randomly scattered with respect to the dark matter field as expected by some numerical models of galaxy formation (*e.g.* Blanton *et al.* 2000, 1999).

CHAPTER 6

Constraints on cosmology using shear tomography correlations

6.1. Introduction

The statistics of the distorted images of distant galaxies, gravitationally lensed by the tidal gravitational field of intervening matter inhomogeneities, contain a wealth of information about the power spectrum of the dark and luminous matter in the Universe, and the underlying cosmological parameters. The importance of "cosmic shear" as a cosmological tool was proposed in the early 1990s by Blandford *et al.* (1991), Miralda-Escudé (1991) and Kaiser (1992). Further analytic and numerical work (*e.g.*. Kaiser 1998; Schneider et al. 1998; White & Hu 2000) took into account the increased power on small scales, resulting from the non-linear evolution of the power spectrum (Hamilton *et al.* 1991; Peacock & Dodds 1996).

The feasibility of cosmic shear studies was demonstrated in 2000, when four teams announced the first observational detections (Bacon *et al.* 2000; Kaiser *et al.* 2000; van Waerbeke *et al.* 2000; Wittman *et al.* 2000). Upcoming surveys will cover much larger areas, and multicolour observations will enable photometric redshift estimates for the galaxies to be obtained. For example, the CFHT Legacy survey[1] will cover 172 deg^2 in 5 optical bands, with a smaller area to be observed in J and K bands.

In order to compare these observations with predictions for various cosmological models and matter power spectra, different two-point statistics of galaxy ellipticities can be employed, all of which are filtered versions of the convergence power spectrum. Here, we focus on the gravitational shear correlation functions, which can be directly obtained from the data as described in Sect. 6.2.2.

This quest for the parameters describing the matter content and geometry of the Universe is limited by several sources of error, dominated by the dispersion in the intrinsic ellipticities of galaxies and by cosmic (sampling) variance. The covariance (error) matrix is thus an essential ingredient in the extraction of parameters from data, or in parameter error estimate predictions. Schneider *et al.* (2002a) provide analytical approximations for the contributions to the covariance matrix. They consider the case when the mean redshift of the population is known, and data taken in a single contiguous area. Kilbinger & Schneider (2004) use a numer-

---

[1] `http://www.cfht.Hawaii.edu/Science/CFHLS`

ical approach to investigate the impact of survey geometry on parameter constraint. Using a Fisher matrix approach, which provides a lower-bound estimate of covariance, Hu (1999) has shown that even crude redshift information enables much tighter constraints to be placed on cosmological parameters, compared with the case when only the mean redshift of the population is known. This study concentrated on the convergence power spectrum as the vehicle of cosmological information.

Motivated by these studies, in this chapter we demonstrate how numerical simulations can be used to estimate the full covariance matrix for the shear correlation functions in the presence of redshift information, and for arbitrary survey geometries. We consider auto- and cross-correlations for redshift bins (as in Hu 1999) and in addition allow for cross-correlations between measurements of the shear signal at different angular scales. With covariance matrices at hand, we then investigate the improvement in parameter estimates due to redshift binning.

6.2. Power spectra and correlation functions

Access to cosmological parameters is provided through the *observable* two-point statistics of the ellipticities of distant galaxies. In this section, we describe how these are related to the matter power spectrum, and to the underlying density field.

6.2.1. The convergence power spectrum

The power spectrum $P_\kappa(\ell)$ of the effective convergence (see Eq. 1.72), or equivalently of the shear $P_\gamma(\ell)$ (*e.g.* Bartelmann & Schneider 2001), is related to that of the density fluctuations, $P_\delta(k, w)$, through the Limber equation (Eq. 1.38):

$$\begin{aligned} P_\kappa(\ell) &= \frac{9H_0^4\Omega_\mathrm{m}^2}{4c^4}\int_0^{w_\mathrm{h}} \mathrm{d}w\,\frac{\bar{W}^2(w)}{a^2(w)}\,P_\delta\left(\frac{\ell}{f_\mathrm{K}(w)}, w\right) && (6.1)\\ \bar{W}(w) &\equiv \int_w^{w_\mathrm{h}} \mathrm{d}w'\,p(w')\,\frac{f_\mathrm{K}(w'-w)}{f_\mathrm{K}(w')}\,, && (6.2)\end{aligned}$$

where ℓ is the angular mode, Fourier space conjugate to the angle θ; w is the comoving radial distance. The function $\bar{W}(w)$ accounts for the sources being distributed in redshift, where $p(w')dw'$ is the comoving distance probability distribution for the sources. $a\,(w)$ is the scale factor normalised to $a\,(w=0)=1$ and H_0 is the Hubble constant.

Splitting up the weak lensing survey in redshift, as in Fig.6.2, defines a set of effective convergence and shear maps instead of a single one, giving more information on the evolution of the dark matter fluctuations and therefore enabling tighter constraints to be placed on cosmological parameters. Auto- and cross-correlation of these maps introduce a whole set of power spectra, generalising Eq. (6.1):

$$\begin{aligned} P_\kappa^{(ij)}(\ell) &= \frac{9H_0^4\Omega_\mathrm{m}^2}{4c^4}\int_0^{w_\mathrm{h}} \mathrm{d}w\,\frac{\bar{W}^{(i)}(w)\,\bar{W}^{(j)}(w)}{a^2(w)}P_\delta\left(\frac{\ell}{f_\mathrm{K}(w)}, w\right) && (6.3)\\ \bar{W}^{(i)}(w) &\equiv \int_{w_{i-1}}^{w_i} \mathrm{d}w'\,p^{(i)}(w')\,\frac{f_\mathrm{K}(w-w')}{f_\mathrm{K}(w')}\,, &&\end{aligned}$$

with $p^{(i)}(w)$ being the normalised galaxy distribution in comoving distance inside the i-th bin, where i runs between 1 and the number of redshift bins N_z. $P_\kappa^{(ii)}$ are auto-correlation power spectra, whereas $P_\kappa^{(ij)}$ with $i \neq j$ are cross-correlation cosmic shear power spectra.

6.2.2. Shear correlation functions

Constraints can be placed on cosmological parameters using the *directly observable* shear correlation functions, which we now turn to.

The basis which underpins the use of the distorted images of distant galaxies in weak lensing studies is a transformation relating the source, $\epsilon^{(\mathrm{s})}$, and image, ϵ, (complex) ellipticities to the tidal gravitational field of density inhomogeneities (see Sect. 1.5.2). We focus on the non-critical regime where

$$\epsilon \approx \epsilon^{(\mathrm{s})} + \gamma \; . \tag{6.4}$$

Empirically the probability distribution function (PDF) of the galaxies' intrinsic ellipticities is a truncated Gaussian like in Eq. (3.83).

As in Schneider *et al.* (2002b), the shear correlation functions are defined as

$$\xi_\pm(\theta) = \langle \gamma_\mathrm{t}\gamma_\mathrm{t} \rangle \pm \langle \gamma_\times \gamma_\times \rangle = \int_0^\infty \frac{\mathrm{d}\ell\,\ell}{2\pi}\,\mathrm{J}_{0,4}(\ell\theta)\;P_\kappa(\ell) \; , \tag{6.5}$$

where J_n are n-th order Bessel functions of the first kind; γ_t and $\gamma_\times$ are the tangential and cross shear components respectively. From now on we focus on ξ_+, since this contains most of the cosmological information on the scales of interest.

6.2.3. Choice of cosmology and matter power spectrum

Unless otherwise stated, our cosmology throughout is a ΛCDM model with $\Omega_\mathrm{m} = 0.3$, $\Omega_\Lambda = 0.7$ and $H_0 = 70\,\mathrm{km\,s^{-1}\,Mpc^{-1}}$. A scale-invariant ($n = 1$, Harrison-Zel'dovich) spectrum of primordial fluctuations is assumed. Predicting the shear correlation functions requires a model for the redshift evolution of the 3-D power spectrum. We use the fitting formula of Bardeen *et al.* (1986; BBKS) for the transfer function, and the Peacock and Dodds (1996) prescription for evolution in the non-linear regime. The power spectrum normalisation is parameterised with $\sigma_8 = 0.9$, and $\Gamma = 0.21$. Quantities calculated for this fiducial cosmology/power spectrum will be super-scripted with a "t".

6.3. Simulating cosmic shear tomography

6.3.1. Outline of the technique

Since we consider only the two-point cosmic shear statistics in an area of relatively small angular size, we can represent the cosmic shear by random Gaussian fields in a flat-sky approximation. This allows us to reduce the computational effort by expressing the fields of the shear and convergence as random Gaussian fields having the same power spectrum as the corresponding fields from the N-body approach. In the weak lensing regime, ray-tracing is well described by the Born approximation which ignores the effects of lens-lens coupling and deviations of light rays from the fiducial path (see White & Hu 2000). The task of calculating the required power spectra then becomes relatively straightforward, because these can be shown to be linear

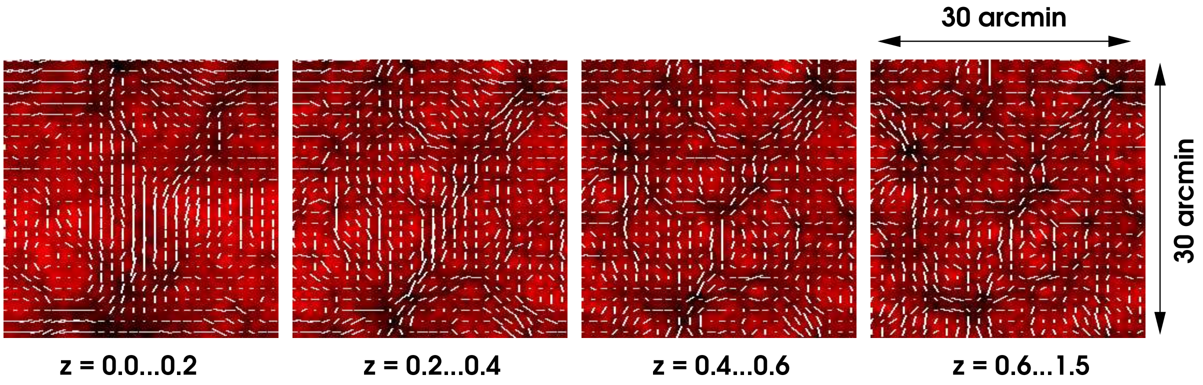

Figure 6.1.: *Realisation of a simulated cosmic shear tomography. Plotted are the shear (white sticks) and the convergence fields (grey intensity scale in the background) acting on the shape of source galaxies that are binned in redshift z (four bins). See text for simulation details.*

functions of the three-dimensional evolving dark matter power spectrum. The accuracy of the results depends on how accurately that three-dimensional power spectrum is known.

The simulation algorithm is essentially described in Sect. 3.3. However, we downsize this algorithm slightly, by restricting ourself to the convergence (shear) fields only neglecting the number density fields of the galaxies which are used to mimic the spatial clustering of the galaxies; here the positions of the galaxies are completely random without any clustering (white noise). This is justified, because we solely focus on the cosmic shear correlations which are only little affected by the clustering of the source galaxies.

This restriction has the effect that the vector $\vec{R}\,(\theta)$ in Eq. (3.65) no longer contains the density contrasts $\delta n\,(\theta)$ of the galaxy number density fields but only the convergence fields $\kappa\,(\theta)$. Equally, the power matrix in Eq. (3.67) determining the realisation process of the fields in Fourier space only consists of the correlation power spectra of and between the convergence fields, thus only of $\mathbf{A}_{\kappa\kappa}\,(\ell)$. These correlation functions are defined by the Eqs. (6.3). See Fig. 6.1 for one simulation output.

6.3.2. Simulation parameters

Each galaxy in the mock galaxy catalogue is defined by an angular position, an ellipticity ϵ and a redshift bin it belongs to. The ellipticity of the iso-photes of a galaxy is determined by the intrinsic shape of a galaxy $\epsilon_i^{(\mathrm{s})}$ and the reduced shear g at the position of the galaxy. The reduced shear is a function of the convergence κ and shear γ which have to be simulated for each redshift bin as a map covering the simulated area. Here we assume that the galaxies are binned into N_z pairwise adjacent redshift bins, chopping off the redshift distribution

$$p\,(z) = \frac{1}{z_0^3}\frac{1}{\Gamma\,(3/\beta)\,\beta}z^2\exp\left[-\left(\frac{z}{z_0}\right)^{\beta}\right] \tag{6.6}$$

as in Fig. 6.2. This empirical distribution with $\beta = 1.5$ and $z_0 = 1.0$ is based on deep field surveys (see *e.g.* Smail *et al.* 1995). The total number of galaxies inside the field, with chosen size of $5^\circ \times 5^\circ$, is set to be $\approx 2.7 \times 10^6$, to get an average of 30 galaxies per arcmin^2. Moreover, the galaxies are assumed to be randomly distributed over the field of view.

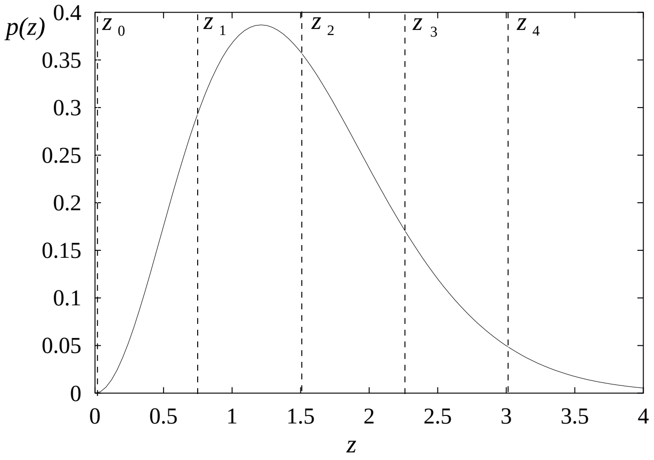

Figure 6.2.: *Galaxies are binned together according to their redshift, the boundaries of the pairwise adjacent redshift bins are* w_i *with* $i = 0...N_z$ *(here as an example* $N_z = 4$*). For every redshift bin the reduced shear field is calculated, averaging over the redshift distribution inside the bin.*

The method of the last subsection is used to work out the shear and convergence maps in Fourier space on a grid of 2048 × 2048 pixels. For every galaxy, shear and convergence are then combined with the intrinsic ellipticity $\epsilon_i^{(\mathrm{s})}$, randomly drawn from the PDF (3.83) using $\sigma_\epsilon^{(\mathrm{s})} = 0.3$, to compute the final ellipticity of the galaxy via Eq. (6.4).

Both angular size Δ and number of pixels N_P along one axis –the sampling size– limits the number of fluctuation modes accounted for in the simulated data. This means, since we are lacking fluctuations on scales outside of $5^\circ/(2N_P) \leq \Theta \leq 5^\circ$, equivalent to $\ell_{\min} \leq \ell \leq \ell_{\max}$, that we have less correlation in the cosmic shear fields than expected (Eq. 6.5)

$$\xi_\pm(\theta) = \int_{\ell_{\min}}^{\ell_{\max}} \frac{\mathrm{d}\ell\,\ell}{2\pi}\,\mathrm{J}_{0,4}(\ell\theta)\,P_\kappa(\ell) \tag{6.7}$$

$$\ell_{\min} = \frac{\pi}{\sqrt{2}\Delta}\,;\;\; \ell_{\max} = N_P\,\ell_{\min}\,. \tag{6.8}$$

The values for the limits are estimates for a square field. The limits are not clearly defined, because the number of ℓ-modes in the FFT matrix becomes very small near the cutoffs. One solution to this problem is to artificially set a clearly defined range within the interval $[\ell_{\min}, \ell_{\max}]$, or, as we have done, to find a best-fit cutoff. This is found by varying the cutoffs to obtain closest agreement between the theoretical two-point correlation and the ensemble average of all Monte Carlo realisations.

In total, we simulated two data sets. The first data set consists of $N_f = 795$ independent realisations each 5° × 5°. The redshift distribution of the galaxies was split into 2 bins at a redshift cut $z_{\mathrm{cut}} = 1.25$, and the distribution is truncated at $z = 3$. For our fiducial surveys, we randomly selected 10 sub-fields, each of $1.25^\circ \times 1.25^\circ$, from different large realisations. This was done for two reasons: 1. to reduce the computation time, since for 10 shear maps we require only one realisation, and 2. sub-fields are less affected by $\ell_{\min}$ that necessarily enters the simulations due to the finite realisation area.

Table 6.1.: *The final column denotes the name given to a particular binning of data. The entries in the columns z_i show the corresponding cuts in redshift.*

z_0	z_1	z_2	z_3	z_4	Name
0	0.75	1.5	2.25	3.0	4bins
0	1.5	2.25	3.0		3binsI
0	0.75	2.25	3.0		3binsII
0	0.75	1.5	3.0		3binsIII
0	2.25	3.0			2binsI
0	1.5	3.0			2binsII
0	0.75	3.0			2binsIII
0	1.25	3.0			2binsIV
0	3.0				onebin

The second data set has 4 redshift bins, with $z_{\mathrm{cut}} = 0.75, 1.5, 2.25, 3.0$ where the last value is the truncation redshift. It has $N_f = 266$ independent realisations. The fiducial surveys from this data set consist of single sub-fields of size $1.25° \times 1.25°$.

For both data sets, ξ_+ was estimated (see next section) for $N_{\Delta\theta} = 65$ angular separation bins, ranging from about $2\overset{\prime}{.}0$ to $40\overset{\prime}{.}0$. For the first (second) data set, the correlation functions were subsequently averaged for 10 (1) sub-fields in order to simulate cosmic shear surveys consisting of 10 (1) independent data fields.

In a further step, the cross- and auto-correlation of the cosmic shear between the shear maps were, according to Appendix C.1, combined to yield the cosmic shear correlations for a coarser redshift binning; in each step the number of redshift bins was reduced by one by combining two neighbouring bins. This process gave for the first data set, apart from the original data, the shear correlation of one redshift bin with boundaries $z = 0$ and $z = 3$. The second data set allows more freedom of choice for combining redshift bins, so that we are able to construct several data sets with three and two redshift bins. Table 6.1 lists the different redshift bins and reference names, all extracted from the two original data sets.

Below, this data is used to study the improvement in the statistical uncertainties of the cosmological parameter estimates, if one has more information on the redshifts of the galaxies.

6.4. Estimating ξ_+

To estimate the two-point correlator ξ_+ between the galaxy ellipticities ϵ_i –depending on position $\vec{\Theta}_i$ and redshift bin– inside of the sub-fields we use the estimator in Eq. (3.30). Since we are dealing with simulated data here, there is no need to weight galaxies with respect to their ellipticity. Therefore, we set $w_i = 1$ for every galaxy.

Although mathematically simple, it takes quite a time to evaluate the estimator due to the large number of galaxy pairs. To speed up the whole procedure we put a grid of rectangular cells of size $\Delta\theta \times \Delta\theta$ over the sub-field in question and compute the number N_{ij} of galaxies and the mean of their ellipticities $\bar{\epsilon}_{ij}$ inside every cell. The index ij indicates the position of the cell inside the grid. This means we are representing galaxies inside the same cell by a single data point with weight N_{ij} and ellipticity $\bar{\epsilon}_{ij}$. In particular, all galaxies inside this cell are assumed to be placed at the same position. The estimator of ξ_+ for this rearranged data set can be shown to be

$$\begin{aligned} \hat{\xi}_+(\theta) &= \frac{1}{N_p(\theta)} \sum_{ij,kl} N_{ij} N_{kl} \left(\bar{\epsilon}_{ij\mathrm{t}} \bar{\epsilon}_{kl\mathrm{t}} + \bar{\epsilon}_{ij\times} \bar{\epsilon}_{kl\times} \right) \Delta_\theta \left(\left| \vec{\Theta}_{ij} - \vec{\Theta}_{kl} \right| \right) \\ N_p(\theta) &= \sum_{ij,kl} N_{ij} N_{kl} \Delta_\theta \left(\left| \vec{\Theta}_{ij} - \vec{\Theta}_{kl} \right| \right) \qquad (6.9) \\ \Delta_\theta(\phi) &\equiv \begin{cases} 1 & \text{for } \theta - \Delta\theta/2 < \phi \le \theta + \Delta\theta/2 \\ 0 & \text{otherwise} \end{cases}, \qquad (6.10) \end{aligned}$$

where $\vec{\Theta}_{ij}$ represents the angular position of cell ij.

The advantage of this approach is obvious: instead of considering N^2 pairs (N is the number of galaxies) we have to consider only N_c^2 pairs, where N_c is the number of grid cells. Thus, the number of pairs depends only on the cell size and not on the number of galaxies. Hence, this method pays off once the cell size becomes large enough, making the number of cells smaller than the number of galaxies. Moreover, in order to find all galaxies at some distance from a certain cell we no longer have to check all galaxies, but only neighbouring cells which are easy to find by the grid index.

The approach becomes inaccurate, however, for small angular bins, because for these the assumption that cell-galaxies are essentially concentrated into one single point is particularly inaccurate. By comparing the ensemble average of $\hat{\xi}_+$ with the theoretical ξ_+ we find that after the third angular bin this approximation becomes accurate enough. For our purposes, this approach is completely sufficient. A better and more sophisticated approach can be found in Pen & Zhang (2003).

For the case with $N_z = 2$, with the division at $z_{\mathrm{cut}} = 1.25$ (2binsIV), Fig. 6.3 shows the close agreement between the correlation and cross-correlation functions, averaged over 7950 sub-fields, with the analytical prediction for the fiducial ΛCDM cosmological model, obtained from Eq. (6.5). Shown are comparisons for the lower (L) and upper (U) redshift bins, and cross-correlation (LU). To account for finite field size in our numerical work, $\ell_{\mathrm{min}} = 2\pi/14.9°$ in the integration. As noted above, since there is no well-defined cut-off, this value of ℓ_{min} was determined by allowing it to vary while performing a least-squares fit of $\xi^{\mathrm{t}}_{\mathrm{L,U,LU}}$ to $\left\langle \hat{\xi}_{\mathrm{L,U,LU}} \right\rangle$, so obtaining the inverse variance weighted mean ℓ_{min}. A cut-off at high ℓ is not critical since in this regime the power-spectrum amplitude is much lower.

6.5. Estimating the covariance of $\hat{\xi}_\pm$

We now outline how the covariance matrix of $\hat{\xi}_\pm$ is estimated, for the case of $N_z = 2$ redshift bins, with the division at $z_{\mathrm{cut}} = 1.25$ (2binsIV). As described above, our mock survey consists of 10 uncorrelated fields. An angle bracket denotes averaging over all 7950 sub-fields. Note that we may drop the L, U and LU sub-scripts for ease of notation.

When no redshift binning is assumed, it is computationally advantageous to determine the shear correlation function by combining those determined for the case with redshift binning:

$$\hat{\xi} = n_{\mathrm{L}}^2 \hat{\xi}_{\mathrm{L}} + 2 n_{\mathrm{L}} n_{\mathrm{U}} \hat{\xi}_{\mathrm{LU}} + n_{\mathrm{U}}^2 \hat{\xi}_{\mathrm{U}}\,, \qquad (6.11)$$

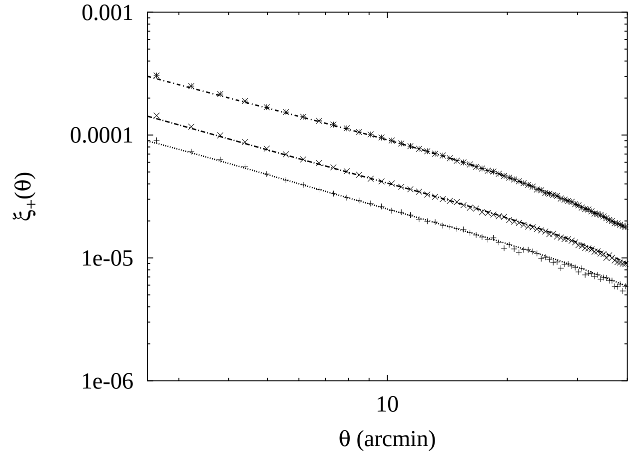

Figure 6.3.: *Comparison of the analytical (lines) and numerical (symbols) shear correlation and cross-correlation functions* $\xi_{\rm L,LU,U}$ *(lower, middle and upper lines/symbols).*

where $n_{\rm L,U}$ are the fraction of sources in the lower and upper bins respectively. A more general relation between $\hat{\xi}$ and the cross- and auto-correlations of the shear from more than two redshift bins can be found in Appendix C.1.

The impact of cosmic variance is taken into account by determining correlation functions for each of the $N_f = 795$ independent surveys. The covariance matrix between bin i and j is determined using

$$\mathbf{C}_{ij} = \left\langle \left(\hat{\xi} - \left\langle\hat{\xi}\right\rangle\right)_i \left(\hat{\xi} - \left\langle\hat{\xi}\right\rangle\right)_j \right\rangle_{N_f} , \qquad (6.12)$$

where the outer average is performed over the $N_f = 795$ surveys. If redshift binning is considered, there are $N_z\left(N_z+1\right)/2$ combinations of correlation and cross-correlation functions and hence $\mathbf{C}$ is a matrix composed of $\left[N_z\left(N_z+1\right)/2\right]^2$ blocks. Fig. 6.4 illustrates this for the simplified case where $N_z = 2$ and $N_{\Delta\theta} = 5$; for example the block in the upper left of the matrix corresponds to elements $\mathbf{C}_{ij} = \langle[\hat{\xi}_{\rm L} - \langle\hat{\xi}\rangle_{\rm L}]_i[\hat{\xi}_{\rm L} - \langle\hat{\xi}\rangle_{\rm L}]_j\rangle$, and the shaded entry to $\mathbf{C}_{2,3}$. The block in the middle row, left column, corresponds to covariance elements between the cross-correlation and the lower redshift bin, with the shaded entry being $\mathbf{C}_{8,2}$. The bins denoted by i and j extend over $\Delta\theta$ bins, repeated for each redshift auto- and cross-correlation bin.

A representation of the covariance matrix determined from our simulations with $N_z = 4$ is shown in Fig. 6.5. Note that $\mathbf{C}$ has a strong diagonal, although it is not strictly diagonally dominant.

Our covariance matrix for the case of no redshift binning is consistent ($< 10\%$ difference) with the treatment of Schneider et al. (2002a), and with Kilbinger & Schneider (2004) who adopted the same assumption of Gaussianity.

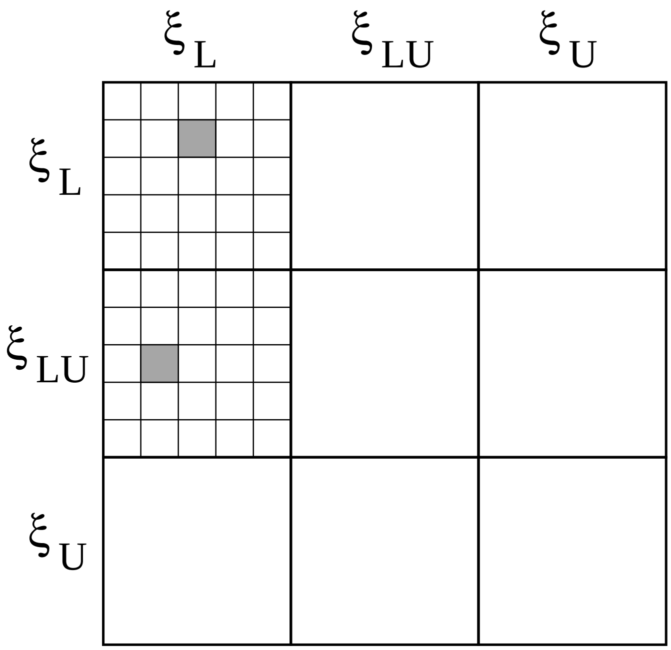

Figure 6.4.: *Schematic illustration of the symmetric covariance matrix* $\mathbf{C}$ *for the case where there are* $N_z = 2$ *source redshift bins and* $N_{\Delta\theta} = 5$ *angular separation bins. Combinations of* $\xi_{\rm L,U,LU}$ *identify covariance terms of the form given in Eq. (6.12).*

6.6. Constraints on cosmological parameters

The rather featureless two-point shear correlation function $\xi_+(\theta)$ or corresponding convergence (shear) power spectrum $P_\kappa(\ell)$ leads to strong degeneracies amongst the parameters that can be derived from cosmic shear surveys. An indication of the degree of degeneracy is the behaviour of the partial derivatives of ξ_+ with respect to each parameter π_i (see King & Schneider 2003 for such a comparison), or using a Fisher matrix analysis as in Sect. 6.6.2.

External sources of information often provide complementary constraints: for example, confidence regions in the $\Omega_{\rm m} - \sigma_8$ plane derived from weak lensing are almost orthogonal to those from the analysis of CMB data (*e.g.* van Waerbeke *et al.* 2002), lifting this well known degeneracy (*e.g.* Bernardeau, van Waerbeke & Mellier 1997).

In this section we consider the extent to which crude redshift information for sources used in a lensing analysis decreases the expected errors in the $\Omega_{\rm m} - \sigma_8$, $\Omega_{\rm m} - \Gamma$ and $\sigma_8 - \Gamma$ planes. Since we are interested in the influence of redshift binning on parameter degeneracies, hidden parameters are assumed to be perfectly known. As described above, we focus on the information provided by the shear two-point correlation function ξ_+ (we may drop the "+" subscript). We restrict this application to the case of $N_z = 2$ (2binsIV). A larger parameter space is then explored using the covariance matrix derived from simulations in a Fisher analysis for the cases $N_z = 2, 3, 4$.

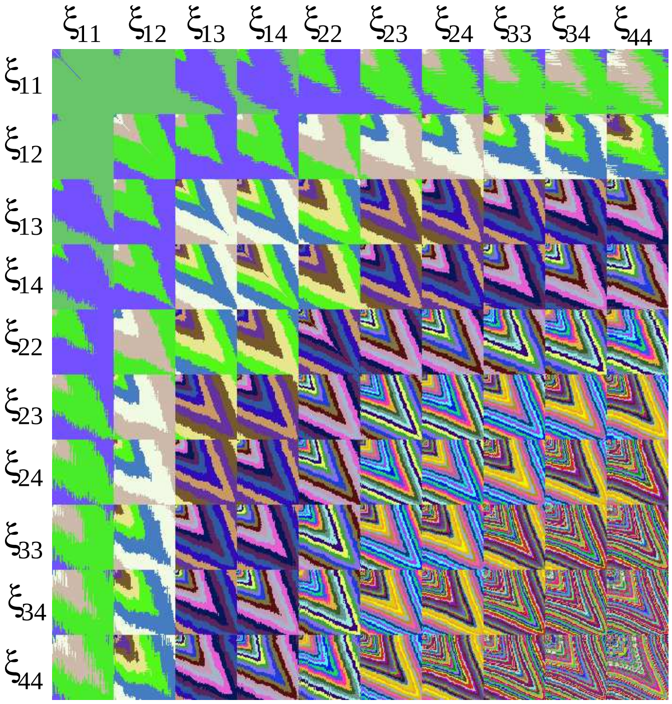

Figure 6.5.: *The covariance matrix* $\mathbf{C}$ *determined from our simulations, for* $N_z = 4$, $N_{\Delta\theta} = 65$ *and a survey consisting of 1 sub-field. Different blocks correspond to auto- and cross-correlations between the redshift bins. Inside these blocks are auto-and cross-correlations for angular separation bins.*

6.6.1. Obtaining confidence regions in parameter space

We now determine and compare the likelihood contours in the $\Omega_\mathrm{m} - \sigma_8$, $\Omega_\mathrm{m} - \Gamma$ and $\sigma_8 - \Gamma$ planes for the cases with and without redshift binning. The likelihood function is given by

$$\mathcal{L}(\pi) \quad = \quad \frac{1}{(2\pi)^{n/2}|\mathbf{C}|^{1/2}} \prod_{ij} \exp\left[-\frac{1}{2}\left(\xi^\mathrm{t} - \xi(\pi)\right)_i \left[\mathbf{C}^{-1}\right]_{ij} \left(\xi^\mathrm{t} - \xi(\pi)\right)_j\right] , \qquad (6.13)$$

where n is the number of rows (or columns) of the covariance matrix $\mathbf{C}$ and $\xi(\pi)$ are theoretical correlation functions determined on a grid in parameter space.

The log-likelihood function is distributed as $\chi^2/2$ so that

$$\chi^2(\pi) = \sum_{ij} \left(\xi^\mathrm{t} - \xi(\pi)\right)_i \left[\mathbf{C}^{-1}\right]_{ij} \left(\xi^\mathrm{t} - \xi(\pi)\right)_j \, . \qquad (6.14)$$

Confidence contours can be drawn in this χ^2-surface, relative to the minimum (zero) at $\xi(\pi) \equiv \xi^\mathrm{t}$. In Figs. 6.6-6.8 the confidence contours are shown for each of the $\Omega_\mathrm{m} - \sigma_8$, $\Omega_\mathrm{m} - \Gamma$ and $\Gamma - \sigma_8$ planes, with and without redshift binning. Note that while Ω_m is varied, we keep $\Omega_\mathrm{m} + \Omega_\Lambda = 1$. To highlight the difference and avoid confusion, we plot contours for a single value of $\Delta\chi^2 = 4.61$ (90% confidence).

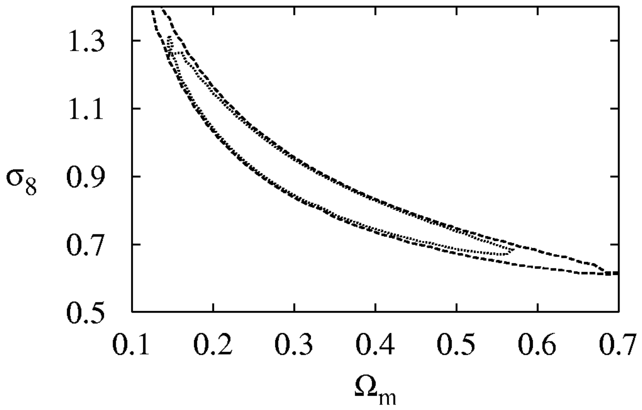

Figure 6.6.: *Expected constraints in the* $\Omega_{\rm m} - \sigma_8$ *plane plotted for* $\Delta\chi^2 = 4.61$ *(90% confidence) with (inner contour) and without (outer contour) redshift binning. The survey consists of 10 square uncorrelated sub-fields, each* 1.25° *on a side. The redshift distribution and binning are described in the text.*

6.6.2. Fisher Information

The Fisher matrix (Fisher 1935) gives a handle on the question as to how accurately model parameters can be estimated from a given data set. It is helpful to get a *lower limit* for the statistical errors of the inferred model parameters underlying the observed set of data points (*posterior* probability) other than tediously evaluating the likelihood function $\mathcal{L}$ on a fine grid in some volume of the parameter space.[2]

In this section, we will use this method to examine quantitatively the increase of information on the cosmological parameters $\Omega_{\rm m}$, Ω_Λ, σ_8 and Γ when the number of redshift bins, thus the knowledge of the three-dimensional distribution of the galaxies, is increased. Note that we no longer impose the condition $\Omega_{\rm m} + \Omega_\Lambda = 1$. After a brief introduction to this topic we apply the Fisher statistics to our simulated data.

Fisher Formalism

In general, one uses data points ξ_i from a measurement to infer parameters π_i based on a theoretical model. As the measurements are polluted by noise, we cannot expect to exactly obtain the data points $\xi\,(\pi)$ predicted by our model. Instead, one obtains $\xi_i = \xi_i(\pi) + \epsilon_i(\pi)$ where $\epsilon_i(\pi)$ is random noise, $\langle\epsilon_i(\pi)\rangle = 0$. The noise can in principle depend on the parameters of the theoretical model. One calls the probability distribution for the data points based on theoretical model parameters the likelihood function $\mathcal{L}[\pi, \xi]$ which is essentially the PDF of the data noise $\epsilon(\pi)$. We may not be able to find from the data ξ_i the true model parameters, but we can try to find a combination of model parameters $\hat{\pi}_i$ that predict data points as close as possible to the actual measurement. The closeness is decided on the grounds of a statistical estimator. It is clear, that due to the noise a new realisation of data points yields a new

---

[2] More advanced techniques use Markov chain methods based on the Metropolis-Hastings algorithm to sample the *posterior* probability; they are getting more and more applied in cosmology (*cf.* Tereno *et al.* 2004; Lewis & Bridle 2002; Christensen et al. 2001).

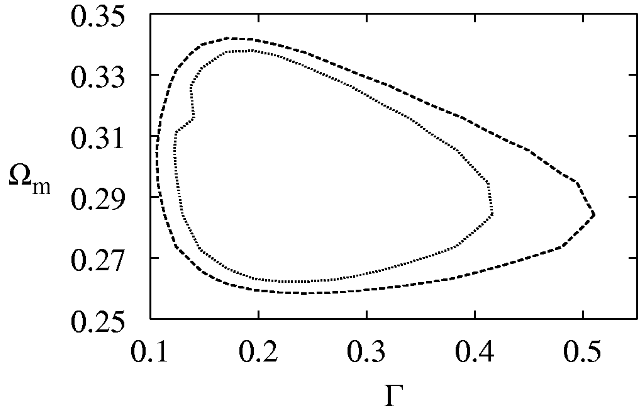

Figure 6.7.: *Expected constraints in the* $\Gamma - \Omega_{\rm m}$ *plane plotted for* $\Delta\chi^2 = 4.61$ *(90% confidence) with (inner contour) and without (outer contour) redshift binning. The survey is the same as in Fig. 6.6.*

estimate of the model parameters, so that as a consequence the estimates for π_i are random variables as much as the data points are.

Imagine we have got a concrete measurement $\hat{\xi}$. The *maximum likelihood estimator* takes the most likely set of parameters $\hat{\pi}$ inferred from $\hat{\xi}$ to be at the position where $\mathcal{L}[\hat{\pi}, \hat{\xi}]$ has a maximum, or equivalently where the log-likelihood $L[\hat{\pi}, \xi] \equiv -\log \mathcal{L}[\hat{\pi}, \xi]$ has a minimum. This means we have to solve $\frac{\partial L[\hat{\pi}, \hat{\xi}]}{\partial \hat{\pi}_i} = 0$ with $\hat{\xi}$ as given parameters. Note that one assumes here as a working hypothesis that the particular measurement $\hat{\xi}$ is actually the most likely.

Of course, not only the most likely model parameters are of interest but also the statistical uncertainty

$$\sigma_i \equiv \left(\left\langle \hat{\pi}_i^2 \right\rangle - \langle \hat{\pi}_i \rangle^2 \right)^{1/2} \tag{6.15}$$

of our estimates, or, put in a more general way, the *covariance of the model parameter estimates*

$$Q_{ij} \equiv \Big\langle (\hat{\pi}_i - \langle \hat{\pi}_i \rangle)(\hat{\pi}_j - \langle \hat{\pi}_j \rangle) \Big\rangle = \langle \Delta\hat{\pi}_i \Delta\hat{\pi}_j \rangle \ , \tag{6.16}$$

where $\Delta\hat{\pi}_i \equiv \hat{\pi}_i - \langle \hat{\pi}_i \rangle$. Interpreting $\mathcal{L}$ as a Bayesian PDF in parameter space (*e.g.* Tegmark *et al.* 1997), one can show that

$$\left[\mathbf{Q}^{-1}\right]_{ij} = \left.\frac{\partial^2 L[\pi, \hat{\xi}]}{\partial \pi_i \partial \pi_j}\right|_{\pi = \hat{\pi}} \ , \tag{6.17}$$

which is the Hessian of $L[\pi, \xi]$ at the position of the maximum-likelihood parameters $\hat{\pi}$. The covariance $\mathbf{Q}$ is a function of the concrete set of data points $\hat{\xi}$.

The important tool in this context is the *Fisher information matrix*, defined by

$$F_{ij} \equiv \left\langle \frac{\partial^2 L[\pi, \hat{\xi}]}{\partial \pi_i \partial \pi_j} \right\rangle_{\hat{\xi}} = \left\langle \left[\mathbf{Q}^{-1}\right]_{ij} \right\rangle_{\hat{\xi}} \ . \tag{6.18}$$

Note that the Fisher matrix is defined as the expected average, over all possible measurements $\hat{\xi}$, of the Hessian matrix of $L[\pi, \hat{\xi}]$ at the position of the *true model parameters* π in parameter

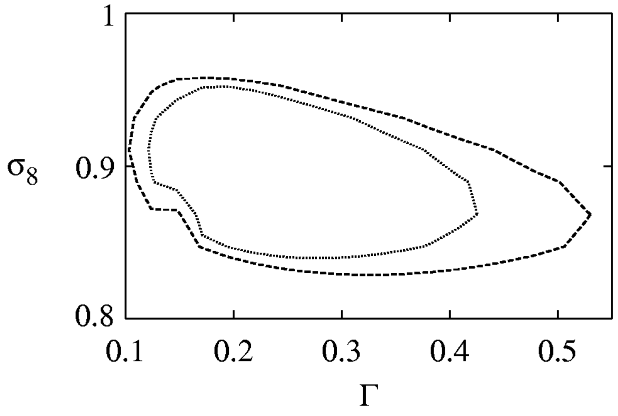

Figure 6.8.: *Expected constraints in the* $\Gamma - \sigma_8$ *plane plotted for* $\Delta\chi^2 = 4.61$ *(90% confidence) with (inner contour) and without (outer contour) redshift binning. The survey is the same as in Fig. 6.6.*

space, whereas Q_{ij} is the Hessian matrix at the position of the *maximum likelihood parameters* $\hat{\pi}$. On average $\mathbf{F}$ and $\mathbf{Q}^{-1}$ are identical, however, so that one can use the inverse of the Fisher matrix as an estimate for the parameter covariance. This is an important conclusion for our following analysis.

It follows from theory that the 1σ-scatter of the estimated parameters is (Crámer-Rao inequality)

$$\sigma_i \geq \sqrt{\left[\mathbf{F}^{-1}\right]_{ii}}\,, \tag{6.19}$$

where commonly the lower limit is taken to be the estimate for $\Delta\hat{\pi}_i$. To quantify the degeneracies in the parameter estimate, we evaluate the correlation of the estimate's uncertainty contained in $\mathbf{F}$:

$$r_{ij} \equiv \frac{\langle\Delta\hat{\pi}_i\Delta\hat{\pi}_j\rangle}{\sigma_i\sigma_j} = \frac{\left[\mathbf{F}^{-1}\right]_{ij}}{\sqrt{\left[\mathbf{F}^{-1}\right]_{ii}\left[\mathbf{F}^{-1}\right]_{jj}}} \tag{6.20}$$

as, for example, in Huterer (2002). Highly correlated or anti-correlated $\Delta\hat{\pi}_i$ and $\Delta\hat{\pi}_j$ are called degenerate, whereas no correlation means no degeneracy (for the adopted fiducial model). Another piece of information that can be extracted from the Fisher matrix is the orientation of the error ellipsoid in parameter space, which is defined by the eigenvectors of $\mathbf{F}$. This corresponds to the directions of degeneracies.

In the application of this formalism below, we will look at situations where some of the model parameters are assumed to be known *a-priori*. In this case, they are no longer free parameters that have to be estimated from measured data points, so that the size of the Fisher matrix reduces according to the number of parameters fixed. This amounts to removing rows and columns from the general Fisher matrix, one for each fixed parameter, so that these cases can be considered by simply looking at sub-matrices of the largest Fisher matrix. Taking all conceivable sub-matrices enables the exploration of all possible combinations of fixed (strong prior) and free parameters.

Since the log-likelihood $L[\pi,\xi]$ is usually not exactly known, one Taylor expands $L[\pi,\xi]$ near its local maximum, $L[\pi,\xi(\pi)]$, taking only the two leading terms. These are the zeroth and the second order, because the first order vanishes for a local extremum: the likelihood $\mathcal{L}[\pi,\xi] \propto \exp\left(-L[\pi,\xi]\right)$ is therefore approximated by a multivariate Gaussian, Eq. (6.13)[3]. The covariance of the likelihood $\mathcal{L}$ is $C_{ij}(\pi) = \langle \epsilon_i(\pi)\epsilon_j(\pi)\rangle$, which is the covariance of the data noise $\epsilon(\pi)$. Employing this approximation the Fisher information matrix is (Tegmark *et al.* 1997)

$$F_{ij} = \frac{1}{2}\mathrm{tr}\left(\mathbf{A}_i\mathbf{A}_j + \mathbf{C}^{-1}(\pi)\mathbf{M}_{ij}\right) \,, \tag{6.21}$$

where "tr" denotes the trace of a matrix; as further definitions we have

$$\begin{aligned} \mathbf{A}_i &\equiv \mathbf{C}^{-1}(\pi)\,\frac{\partial \mathbf{C}(\pi)}{\partial \pi_i}\,, && (6.22)\\ \mathbf{M}_{ij} &\equiv \frac{\partial \xi\,(\pi)}{\partial \pi_i}\left[\frac{\partial \xi\,(\pi)}{\partial \pi_j}\right]^{\mathrm{t}} + \frac{\partial \xi\,(\pi)}{\partial \pi_j}\left[\frac{\partial \xi\,(\pi)}{\partial \pi_i}\right]^{\mathrm{t}}\,. && (6.23) \end{aligned}$$

The superposed index$^{\mathrm{t}}$ in $\mathbf{M}_{ij}$ denotes the transpose. The expression for the Fisher matrix simplifies if we can neglect, as in our work here, the derivatives of the covariance matrix $\mathbf{C}$. This leaves us with the well known result

$$F_{ij} = \frac{1}{2}\mathrm{tr}\left(\mathbf{C}^{-1}\mathbf{M}_{ij}\right) = \sum_{kl}\left[\frac{\partial \xi\,(\pi)}{\partial \pi_i}\right]_k \left[\mathbf{C}^{-1}\right]_{kl}\left[\frac{\partial \xi\,(\pi)}{\partial \pi_j}\right]_l\,. \tag{6.24}$$

Again, $\mathbf{C}$ is the covariance of the data noise and $\xi\,(\pi)$ the vector of modelled data points in absence of noise.

Application of the Fisher formalism

Now we use the Fisher formalism to estimate constraints on various combinations of parameters, with different degrees of redshift binning. First, we evaluate Eq. (6.24) using the covariance matrix from our fiducial survey consisting of 10 independent sub-fields, $N_z = 2$ (with $z_{\mathrm{cut}} = 1.25$), and $N_{\Delta\theta} = 65$. The procedure is repeated for the covariance matrix for the coarser $N_z = 1$ binning. Table 6.2 shows the percentage error for $N_z = 2$ as opposed to $N_z = 1$ for the same set of free and fixed parameters.

We extend the treatment to a larger number of redshift bins, in the context of the survey consisting of 1 sub-field. Again Eq. (6.24) is calculated, this time using the covariance matrices from the simulations with $N_z = 4$, and those from coarser binning ($N_z = 3, 2, 1$) of this data set. Table 6.3 lists the errors for $N_z = 4, 3, 2$ as a percentage of the $N_z = 1$ error.

In order to investigate the degeneracies of the parameter estimates, we concentrate on the case that no priors are given. For this particular situation, the gain by introducing redshift binning is largest (see Tables 6.2 and 6.3). In Fig. 6.9 we plot the correlations of the errors in the parameter estimates for different pairs of parameters and different numbers of redshift bins. If more than one redshift binning for the same number of redshift bins is available in our data set, we indicate the scatter of correlation coefficients by error bars. Some scatter indicates that the correlations can be changed slightly by varying the bin limits. The strong correlation between the estimates of Ω_{m} and σ_8 is only marginally affected by redshift binning. This is also the case for fixed Γ and/or Ω_Λ (not shown).

---

[3] We would like to stress the slight change in notation: $\xi = \xi^{\mathrm{t}}$ here.

Table 6.2.: *Uncertainties in the parameter estimates according to the Fisher formalism, for our fiducial survey of 10 uncorrelated sub-fields. The first data set (2binsIV) with $N_z = 2$ and $z_{\rm cut} = 1.25$ is used. Columns with dots "." denote fixed parameters (strong priors). Uncertainties in the top half are absolute values for a single redshift bin. Those in the lower half are for $N_z = 2$, quoted as a percentage of the single redshift bin ($N_z = 1$) case. For instance, with no fixed parameters, $\Delta\Omega_\Lambda = 0.26$ with $N_z = 2$ (*i.e.* 13% of the $N_z = 1$ error). $|\mathbf{F}^{-1}|$ denotes the determinant of the inverse of the Fisher matrix; its square root is proportional to the volume of the error ellipsoid in parameter space. The n-th root, with n being the number of free parameters, defines a typical size of the error ellipsoid; this size is proportional to the geometric mean of the lengths of the principal ellipsoid axes.*

$\Delta\Omega_m$	$\Delta\Omega_\Lambda$	$\Delta\sigma_8$	$\Delta\Gamma$	$\sqrt{\lvert\mathbf{F}^{-1}\rvert}^{1/n}$
0.9	2.0	1.2	0.4	0.16
.	0.5	0.1	0.1	0.09
0.2	.	0.4	0.2	0.04
0.09	0.7	.	0.08	0.08
0.3	1.0	0.3	.	0.13
0.06	0.5	.	.	0.09
0.08	.	0.1	.	0.05
0.02	.	.	0.07	0.03
.	0.3	0.06	.	0.09
.	0.1	.	0.06	0.08
.	.	0.03	0.07	0.04
0.02	.	.	.	0.15
.	0.10	.	.	0.10
.	.	0.02	.	0.02
.	.	.	0.06	0.06
13%	13%	17%	26%	47%
.	52%	57%	64%	72%
53%	.	52%	49%	73%
43%	38%	.	68%	65%
32%	24%	46%	.	57%
50%	45%	.	.	64%
86%	.	85%	.	88%
89%	.	.	81%	85%
.	65%	71%	.	76%
.	80%	.	81%	81%
.	.	87%	80%	84%
85%	.	.	.	85%
.	81%	.	.	81%
.	.	89%	.	89%
.	.	.	82%	82%

Table 6.3.: *The notation is identical to Table 6.2. The second data set was used to obtain these values, with various binnings in redshift denoted by the final column, and with covariance matrices calculated for 1 sub-field. Uncertainties are again quoted as a percentage of that for $N_z = 1$.*

$\Delta\Omega_m$	$\Delta\Omega_\Lambda$	$\Delta\sigma_8$	$\Delta\Gamma$	$\sqrt{\lvert\mathbf{F}^{-1}\rvert}^{1/n}$	data set
16%	14%	19%	26%	41%	2binsI
17%	14%	21%	32%	42%	2binsII
21%	18%	30%	53%	49%	2binsIII
85%	.	84%	.	88%	2binsI
80%	.	80%	.	85%	2binsII
88%	.	89%	.	91%	2binsIII
74%	.	.	70%	79%	2binsI
75%	.	.	74%	82%	2binsII
92%	.	.	91%	92%	2binsIII
.	.	67%	63%	76%	2binsI
.	.	71%	69%	79%	2binsII
.	.	90%	87%	91%	2binsIII
13%	11%	16%	23%	34%	3binsI
13%	12%	16%	22%	36%	3binsII
14%	11%	18%	27%	36%	3binsIII
73%	.	75%	.	79%	3binsI
73%	.	73%	.	79%	3binsII
72%	.	73%	.	78%	3binsIII
68%	.	.	65%	73%	3binsI
67%	.	.	64%	74%	3binsII
69%	.	.	67%	74%	3binsIII
.	.	62%	58%	70%	3binsI
.	.	61%	57%	70%	3binsII
.	.	65%	61%	72%	3binsIII
11%	9%	14%	19%	31%	4bins
65%	.	67%	.	71%	4bins
61%	.	.	57%	66%	4bins
.	.	55%	51%	63%	4bins

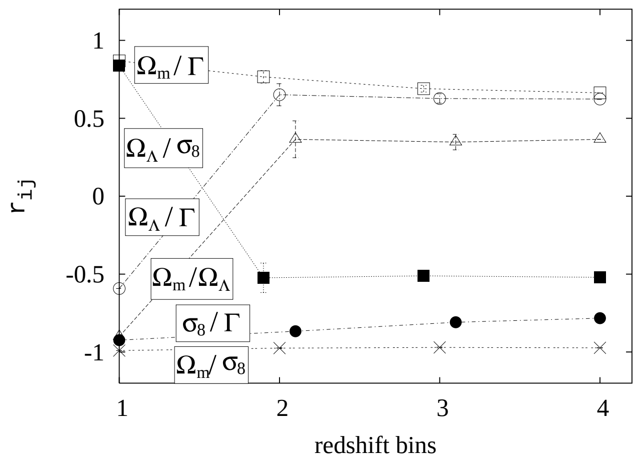

Figure 6.9.: *Correlations of the errors in the parameter estimates for different pairs of parameters and numbers of redshift bins as derived from the Fisher matrix; only the case with no fixed priors is considered. Error bars denote the variance in the correlations for the different redshift binnings for the same number of bins (only for 2 and 3 bins). The data points are slightly shifted to avoid overlapping.*

6.7. Discussion

The average shear correlation functions obtained from our numerical simulations are in good agreement with those obtained analytically, as was illustrated in Fig. 6.3. We also pointed out that their covariance is compatible with Schneider *et al.* (2002a), SvWK02 hereafter, and Kilbinger & Schneider (2003).

Our treatment is only strictly valid for Gaussian density fields and is hence a good approximation for scales greater than $\sim 10'$, but giving a lower limit on the covariance at smaller scales (*e.g.* van Waerbeke *et al.* 2002). A more accurate covariance matrix may be possible, though. According to SvWK02 (Section 4 therein), the covariance matrix of ξ_+ can be decomposed into three terms

$$C_{ij} = \sigma_\epsilon^2 X_{ij} + \sigma_\epsilon^4 Y_{ij} + Z_{ij} \ , \tag{6.25}$$

where X, Y and Z are some functions. X is a function of the two-point correlation of cosmic shear while Y depends on the weights of the data points. Consequently, X and Y are insensitive to non-Gaussian features of the field. Z, however, depends linearly on the four-point correlation of cosmic shear which in SvWK02 is worked out by assuming a Gaussian field; this factorises Z into a sum of products of two-point correlators only. In the hierarchical clustering regime, the four-point correlation of the random field differs from that value only by a constant scale-independent factor Q, the so-called hierarchical amplitude (see *e.g.* Bernardeau *et al.* 2002). Thus, hierarchical clustering increases the component Z simply by the factor Q. This could be included in C_{ij} by the following two steps: i) calculating $C_{ij} \equiv C_{ij}^{(1)}$ by setting the intrinsic noise $\sigma_\epsilon = 0$, ii) recalculating $C_{ij} \equiv C_{ij}^{(2)}$, this time with the intrinsic noise turned on. The final covariance matrix C_{ij}, accounting for Q, is obtained by

$$C_{ij} = C_{ij}^{(1)} \left(Q - 1\right) + C_{ij}^{(2)} \ . \tag{6.26}$$

As an illustration of the use of numerically derived covariance matrices, we have considered to what degree redshift information tightens the confidence regions on cosmological parameters. Note that we required rather crude redshift information: photometric redshift estimates for sources can be obtained from multi-colour observations, with typical accuracies in σ_z of ~ 0.1 or better (*e.g.* Bolzonella *et al.* 2000).

We have investigated the information contained in ξ_+, rather than the shear (or equivalently convergence) power spectrum P_κ since it is directly obtained from the statistics of the distorted images of distant galaxies. Various estimators of P_κ have been proposed, requiring the *spatial* distribution of the shear (*e.g.* Kaiser 1998; Hu & White 2001) or the shear correlation functions (SvWK02). Note that a calculation similar to ours but using $\hat{P}_\kappa$ would formally require one to use the full covariance matrix for the associated estimator. However, as noted in SvWK02, the band-power estimates for $\hat{P}_\kappa$ do decorrelate rather quickly.

The first data set consists of 2 redshift bins, and covariance matrices estimated with and without binning for a survey with 10 uncorrelated (1.25° on a side) sub-fields (*i.e.* selected from different realisations). Constraints on pairs of cosmological parameters using a likelihood treatment, with and without redshift information, are shown in Figs. 6.6-6.8. Since our goal here is to study the benefit of redshift information in cosmic shear studies, we do not adopt priors from WMAP or other probes of large scale structure which might confuse the issue. In both cases the redshift *distribution* is assumed to be known. Assigning sources to 2 redshift bins tightens the confidence regions in all cases.

Noteworthy are the tightened upper limits on Γ in the $\Gamma - \sigma_8$ and $\Omega_\mathrm{m} - \Gamma$ planes when binning is employed. The constraints on Γ in both planes are rather asymmetric, with the confidence regions being more extended towards high Γ values. Γ determines the location of the peak in the matter power spectrum, and having extra redshift information places tighter constraints on this –there is a degeneracy between Γ and the mean source redshift $\langle z \rangle$ such that a larger Γ would be compensated for by a smaller $\langle z \rangle$. Recall that Γ is not a fundamental quantity; in the limit of zero baryons, $\Gamma = \Omega_\mathrm{m} h$, which is modified to $\Gamma = \Omega_\mathrm{m}\, h \exp\left(-\Omega_\mathrm{b}\left(1 + \sqrt{2h}/\Omega_\mathrm{m}\right)\right)$, if Ω_b, the present baryon density, is accounted for in the transfer function (Sugiyama 1995). With our strong priors (hence fairly tight constraint on Ω_m or σ_8), the error in Γ roughly translates into an error in h, so redshift binning decreases the upper limit on h.

In the $\Omega_\mathrm{m} - \sigma_8$ plane we obtain the familiar "banana" shaped confidence regions, tightened with the inclusion of redshift binning. It is difficult to directly compare our constraints to real surveys with different observational conditions; however, our confidence regions are roughly compatible with those of van Waerbeke *et al.* (2001) allowing for these differences.

To explore a wider range of parameter combinations, we employed the Fisher formalism since this allows one to easily obtain error estimates and investigate degeneracies. We used the covariance matrices estimated from the first data set, again for 10 sub-fields as described above. Table 6.2 shows to what extent the errors on various parameters are improved for $N_z = 2$ compared with $N_z = 1$. Note that these results depend on the cosmological model and power spectrum of our fiducial model. Redshift binning is particularly helpful when fewer strong priors are assumed, compared with the case when only one or two of the parameters are allowed to vary. In the case where Ω_m, Ω_Λ, σ_8 and Γ are free, errors are a factor of roughly 4 to 8 smaller when $N_z = 2$. As we adopt more strong priors, redshift binning becomes progressively less beneficial. For example, if we consider parameter combinations where either Ω_m or σ_8 are assumed to be perfectly known, this breaks a strong degeneracy otherwise present; the decrease in errors when $N_z = 2$ are therefore not so great as one might have anticipated.

Another interesting trend is that the constraint of Ω_Λ seems to be most favourably affected by redshift binning, perhaps because it is important to the growth rate of structure at redshifts $z \sim 1$.

How does Fisher analysis compare with the likelihood treatment? Fisher analysis should be seen as a way to estimate errors and investigate degeneracies, but does not propose to reveal the detailed behaviour of confidence regions far from the fiducial model –for instance the asymmetric constraints in the $\Gamma - \Omega_\mathrm{m}$ or $-\sigma_8$ planes, or the "banana" shaped constraints in the $\Omega_\mathrm{m} - \sigma_8$ plane. Nevertheless, the differences in the constraints on the parameter pairs drawn from Ω_m, σ_8 and Γ are roughly consistent with the full likelihood treatment discussed above.

Using the second data set consisting of 4 redshift bins, for a survey consisting of 1 sub-field, we obtained covariance matrices corresponding to various redshift cuts for 2 and 3 redshift bins. Parameter constraints are again tightened going from $N_z = 1$ to $N_z = 4$. Considering again for example the case where all parameters are free, the most dramatic change is already seen going from $N_z = 1$ to $N_z = 2$. In the case of $N_z = 2$, with the lowest redshift cut $z_\mathrm{cut} = 0.75$ (2binsIII), parameter constraints are weakest. When higher redshift sources are isolated ($z_\mathrm{cut} = 1.5, 2.25$) the constraints are similar, and which is the better choice depends on the combination of parameters considered. For 3 redshift bins, the combinations of cuts in redshift lead to very similar error estimates.

At some point further sub-division into redshift bins does not lead to improved constraints on parameters (Hu 1999). This limit must be determined for the survey and cosmological parameters in question. For simplicity consider the case of $N_z = 2$: ξ_L and ξ_U are correlated since sources in the upper redshift bin are also sensitive to lensing by structure at $z < z_\mathrm{cut}$. A measure of this correlation is provided by a correlation parameter, $p = \xi_\mathrm{LU} / \left(\xi_\mathrm{L} \xi_\mathrm{U}\right)^{0.5}$, also used by Hu (1999) in the context of power spectra. $p = 1$ and $p = 0$ indicate complete correlation and lack of correlation respectively. For our simulations, $0.83 < p < 0.93$ for the range over which the correlation functions are calculated, with $\bar{p} = 0.87$ taking the mean over all $\Delta\theta$ bins.

The improvement of the parameter constraints is clearly also a function of how the redshift intervals are set. This can already be seen in Table 6.3 where we calculated different binnings with two and three redshift bins. We expect that there is an optimal way to bin the data. The intention of this chapter, however, is to present a fast method for calculating the covariance matrix of the cosmic shear correlation estimator. This issue will be explored in a forthcoming publication. In practise, this question probably does not arise anyway, because there one would take as many redshift bins as possible, their number being determined by the accuracy of the redshift estimator.

As described above, one of our fiducial surveys is composed of 10 uncorrelated sub-fields. Another possibility is that a single contiguous patch of sky is targeted primarily for another science goal; such a survey might consist of 10 sub-fields drawn from the same large field. The sub-fields might in that case be selected so as to avoid bright stars, chip boundaries or defects. These sub-fields would be correlated to some extent, meaning that taking m rather than $n(< m)$ sub-fields does not decrease the covariance by a factor of m/n, which would be the case if they were independent. The degree to which the sub-fields are correlated is accounted for directly in the covariance matrix. However, it is instructive to have an estimate of this, using the (ensemble average) covariance matrix for a survey composed of 10 *correlated* as opposed to 10 *uncorrelated* sub-fields. The ratio of the diagonal elements of the correlated and uncorrelated geometry covariance matrices ranges between $\approx 1.1 - 1.4$, from the lower to upper redshift bin. Of course, the amount of correlation between sub-fields also depends on their geometry, so this has to be estimated for the survey in question.

6.8. Conclusions

In preparation for upcoming cosmic shear surveys, the main purpose of this paper was to demonstrate that it is possible to rapidly simulate surveys using a Monte Carlo method. This enables one to obtain accurate *full* covariance matrices for the shear two-point correlation function ξ_+, estimated from arbitrary survey geometries and with the sources binned in redshift. Averaging over many independent realisations enables us to take into account cosmic variance. As a first application, we estimated the extent to which redshift information for sources used in a cosmic shear analysis improves constraints on parameters derived from the estimated shear two-point correlation function $\hat{\xi}_+$.

A likelihood analysis in the $\Omega_\mathrm{m} - \sigma_8$, $\Omega_\mathrm{m} - \Gamma$ and $\Gamma - \sigma_8$ planes shows that separating the sources into two redshift bins enables tighter constraints to be placed on parameters. Considering a wider range of parameter combinations in the context of a Fisher analysis reveals that redshift information is particularly advantageous in cases where few strong priors are assumed. When Ω_m, σ_8, Γ and Ω_Λ are free parameters, having 2 (4) redshift bins tightens errors on parameters by a factor of $\sim 4 - 8$ ($\sim 5 - 10$). Most improvement on error estimates occurs going from $N_z = 1$ to $N_z = 2$. In general, for the combinations of free and fixed parameters explored, Ω_Λ seems to benefit most from redshift binning,

One might ask why cosmic shear is of interest, in the light of the recent WMAP results (*e.g.* Bennett *et al.* 2003), which suggest that the era of precision cosmology is already upon us; there are several facets to consider. Cosmic shear has the power to break degeneracies inherent to CMB data (*e.g.* Hu & Tegmark 1999), for instance the angular diameter distance degeneracy (*e.g.* Efstathiou & Bond 1999). It also provides a completely independent cross-check of cosmological parameters, based on equally well understood but different physical principles. Besides this, as is the case with the CMB, the interpretation of results requires no assumption about the bias between luminous tracers and the underlying dark matter distribution which plagues, for example, galaxy redshift surveys. In addition, with redshift estimates for sources in upcoming large cosmic shear surveys, lensing has the potential to see beyond the radially projected convergence power spectrum, becoming sensitive to the evolution and growth of structure in the Universe.

Summary

In the following, a summary of the individual foregoing chapters is given.

Chapter 1: Scientific framework

The chapter briefly reviews the standard model of cosmology. Cosmic structure grows by purely gravitational collapse from initially tiny density perturbations in an almost homogeneous universe. The observed fluctuations in the matter density require that the largest mass fraction is only interacting gravitationally and has non-relativistic velocities. Only a small fraction of mass is given as baryonic matter in gas, dust and galaxies. This is the cornerstone of the cold dark matter (CDM) models. Relatively simple physics is sufficient to describe the growth of density perturbations. Explicit solutions to the equations modelling structure growth are currently only found by computationally expensive N-body simulations. Approximate analytical solutions are also available, however, only for scales where fluctuations are small, for linear or quasi-linear scales.

Commonly, cosmological structure is measured in terms of correlation functions (real space) or polyspectra (Fourier mode representation). Cosmic fields, such as the distribution of matter or galaxies, are pictured as realisations of a random process. Relevant statistical quantities to describe random processes, in particular random fields, are introduced. A statistical quantity of great interest is the power spectrum. It completely determines the so-called second-order statistics of random fields, *e.g.* the dispersion of field values smoothed to some arbitrary scale or the probability to find a given pair of values with a given distance in a random field. The power spectrum of fluctuations in the dark matter density field is presented for ΛCDM-type models.

The correlations of galaxy number densities are in general different compared to the correlations of the dark matter densities. This difference is called galaxy bias. The standard explanation for galaxy bias is that galaxies require special conditions in order to form and evolve in the dark matter field. Parameters –bias parameters– that quantify the difference between two random fields are introduced. In the linear stochastic bias scheme, two parameters, the bias factor b and correlation factor r, are defined. The bias factor can be pictured as the ratio of the clustering strengths of two fields, whereas the correlation parameter, broadly speaking, measures how strongly the peaks and valleys of two density fields coincide. Both parameters are completely determined by second-order statistics and are the most frequently measured bias parameters in practice. Almost everywhere in this thesis, the linear stochastic bias parameters are used. The linear stochastic bias scheme has a shortcoming because it cannot distinguish whether a bias is non-linear or stochastic. This distinction may be important to constrain models of galaxy formation. The shortcoming is removed by the non-linear stochastic bias scheme which involves three different bias parameters. However, for a measurement these parameters require either the knowledge of higher-order correlations in the random fields, or assumptions about higher-order correlations that relate them to second-order statistics.

Further on, the chapter compiles measurements and predictions for the galaxy bias as found in the literature. Essentially, galaxy bias depends on galaxy type, redshift and scale. Depending on the applied method for measuring the galaxy bias, the results often depend on strong assumptions on the dark matter component. The effect of gravitational lensing allows us to map the dark matter distribution and thus to measure galaxy bias without strong assumptions. The principles and formalism of gravitational lensing are explained at the end of this chapter.

Chapter 2: Evolution of galaxy bias on linear scales

The time dependent bias model of Tegmark & Peebles (1998) is extended. The extended model now makes predictions on the large-scale evolution of the linear stochastic bias of different galaxy populations with respect to both the dark matter and each other. The model equations contain a general expression, coined the “interaction term”, accounting for the destruction or production of galaxies. This term may be used to model couplings between different populations that lead to an increase or decrease of the number of a galaxies belonging to a population, *e.g.* passive evolution or merging processes. This is explored in detail using toy models. Strictly speaking, a non-linear interaction term cannot be treated within the framework of this model because it requires in general the knowledge of the bias parameters on non-linear scales. This is demonstrated by assuming a quadratic interaction term. If, however, the number densities or small-scale bias parameters of non-linearly coupled galaxy populations that are given as a constraint, the model equations can still be used for predicting the large-scale bias evolution. According to the model if no interactions are present, meaning the number of galaxies is conserved, a debiasing of a biased galaxy population with time is to be expected due to the gravitational pull of the dark matter field. After a sufficiently long time galaxies become unbiased perfect tracers of the total matter density. It is shown that the presence of interactions, that change the number of galaxies, can modify the evolution of the bias parameters compared to an interaction-free evolution. It is argued that the observation of the evolution of the large-scale bias and galaxy number density with wide-field surveys may be used to infer fundamental interaction parameters between galaxy populations, possibly giving an insight in their formation and evolution. It is argued on the basis of this model that early-type galaxies, known to be more clustered than late-type galaxies, are not likely to have formed by passive evolution from late-type galaxies. Non-linear interaction terms like the considered quadratic interaction (“collision” or “merging”) are required.

The core of this chapter has been published in Simon (2004a).

Chapter 3: Studying two estimators for the linear stochastic bias

This chapter introduces a new statistical measure –the aperture statistics– that is used in weak gravitational lensing. It can be employed to examine the distribution of galaxies on the sky, the projected dark matter density and the cross-correlation of both. Therefore, the aperture statistics provide means to probe the galaxy bias. This technique basically averages the fluctuations in the projected density of dark matter and galaxies over the area of a circular aperture. The (second-order moments of the) joint probability distribution of aperture-averages are the quantities being looked at. "Joint" in this context means that aperture-averages of different density fields but for the same apertures are analysed. The size of the aperture determines the effective physical scale that is probed. In order to apply this technique in practice to weak lensing surveys, estimators for the rms-fluctuations and cross-correlations of the aperture-averages are required. In the recent years, authors have proposed and used two classes of estimators. One class, nicknamed here "I", first of all measures the probability to obtain a certain pair of values with a given relative distance in the density fields. These so-called two-point correlation functions are then transformed to obtain the rms-fluctuations as a function of aperture radius. Another class, nicknamed here "II", explicitly places aperture into the field and averages over the field values within the aperture. Each aperture gives one average. The scatter of averaged values for different aperture positions yields also an, maybe more intuitive, estimate of the rms-fluctuations. However, for Class II, it is not clear how to cope with cases where parts of the data field within the aperture are missing due to masking (gaps). Both estimator approaches are presented in detail and compared by applying them to simulated weak lensing surveys. The algorithm for generating the mock data is developed here and explained. The chosen parameters of the simulated data fields are inspired by real wide-field image galaxy surveys. Considering one particular survey geometry we find that estimators from Class I yield the most reliable results with an inaccuracy of less than 3%. In the presence of gaps, estimators from Class II are inaccurate by up to 60%. However, if only apertures are taken whose area has at most 20% overlap with a gap region the inaccuracy is reduced to about $10\% - 20\%$. Moreover, the variance of the statistical noise of estimators Class I is lower by a factor of $1 - 3$ compared to Class II. The results are therefore clearly in favour of estimators of Class I. Class I estimators are applied to real data in the following two chapters of this thesis. For the future, higher-order moments of the aperture statistics, such as the skewness or kurtosis, will become important. This may make an improvement of estimators of Class II worthwhile. Estimators of Class II are namely easily extended to higher-order statistics, while estimators of Class I require a lot more effort for an extension. Finally, a minor but important conclusion is that the program code implementations of the estimators, used further on in this thesis, yield computational results that are accurate within at least $1\% - 2\%$.

Chapter 4: Galaxy bias in GaBoDS

The GaBoDS comprises roughly 20 deg^2 of high-quality data in R-band taken with the Wide Field Imager at the 2.2m telescope of MPG/ESO at La Silla, Chile. Fields with long exposure times, total area about 10 deg^2, are chosen for the analysis in this chapter. The bias and correlation factor, b and r respectively, of galaxies with respect to the dark matter is measured using the aperture statistics as described in Chapter 3. This includes the aperture mass from weak gravitational lensing. The analysis is performed for three galaxy samples selected by R-band magnitudes; the median redshifts of the samples are $\langle z\rangle = 0.34, 0.49$ and 0.65, respectively. The brightest sample has the strongest peak in redshift and can therefore be most accurately represented by a single redshift. The COMBO-17 Survey is used for an accurate estimate of the redshift distribution of the galaxies. Assuming the currently favoured ΛCDM model as fiducial cosmology, in particular $\Omega_{\rm m} = 0.3$ and $\Omega_\Lambda = 0.7$, values for the linear stochastic galaxy-dark matter bias on angular scales $1' \le \theta \le 20'$ are obtained. At $10'$, the median redshifts of the samples correspond to a effective physical scale of $2.66, 3.71, 4.64\ h^{-1}$Mpc, respectively. Over the investigated range of physical scales the bias factor b stays almost constant, possibly rising on the smallest scales. Here the errors are largest, however. Averaging the measurements for the bias factor over the range $4' \le \theta_{\rm ap} \le 18'$, weighting with the cosmic variance error, yields $b = 0.89 \pm 0.05$, 0.79 ± 0.05, 0.89 ± 0.05, respectively (1σ). Galaxies are thus less clustered than the total matter on that particular range of scales (anti-biased). As for the correlation factor, r a slight increase to $r = 1$ in the last angular bin from an almost constant value on smaller scales is found; the weighted average over the same range as before is $r = 0.8 \pm 0.1$, 0.8 ± 0.1, 0.5 ± 0.1, respectively. Therefore, on these scales a degree of stochasticity or/and non-linearity in the relation between dark matter and galaxy density has to be inferred. On the largest scales considered, the correlation between dark matter and galaxy distribution is high. Within the measurement uncertainties and over the redshift range represented by the galaxy samples no evolution with redshift of the bias is observed. It is concluded that on the scales considered the redshift dependence of the linear bias for $0.3 \le z \le 0.65$ has to be smaller than $\Delta b \lesssim 0.1$ and $\Delta r \lesssim 0.2$ (2σ confidence).

A shortened version of this chapter been published in Simon *et al.* (2004b).

Chapter 5: Galaxy bias in COMBO-17

In this chapter the bias –the relative bias and bias with respect to dark matter– of red and blue galaxies as function of scale and redshift is measured. For this purpose, the COMBO-17 Survey offers an unique opportunity. It provides the so-far largest galaxy sample in the regime $0.2 \le z \le 1.1$ covering an area of ~ 0.78 deg^2, observed in 5 broad-band and 12 narrow-band filters. Based on the photometry, photometric redshifts of galaxies brighter than $m_R \le 24$ mag have been derived within a few percent accuracy as well as absolute rest-frame luminosities and colours.

The full galaxy sample with photometric redshift information is split into a red and a blue sample by applying a redshift-dependent cut in a $U-V$ vs. M_V (rest-frame) colour-magnitude diagram. In adopting this specific cut about 80% of the selected red galaxies have morphologies earlier than or equal to Hubble type Sa. Most of the blue galaxies are (star-forming) late-type galaxies. In addition, galaxies are chosen to have apparent magnitudes brighter than $m_{\rm R} = 24\,$mag, which guarantees the photometric redshift accuracy, and absolute magnitudes brighter than $M_{\rm V} - 5\log_{10} h \simeq -17\,{\rm mag} - (U-V)$ in order to obtain galaxy samples comparable in median absolute magnitude at all redshifts. The aperture statistics as described in Chapter 3 is employed to measure the linear stochastic bias of the red and blue galaxy sample as a function of scale and redshift. In order to have a compatible statistical quantity that quantifies the relative bias between red and blue galaxies the formalism is slightly extended, estimators for the relative bias are explained. The data set is subdivided into four redshift bins with median redshifts $\langle z \rangle = 0.3, 0.5, 0.7, 0.9$ and widths $\Delta z = 0.2$. The effective comoving physical scales probed at $10'$ aperture radius are $2.43\,h^{-1}$Mpc, $3.85\,h^{-1}$Mpc, $5.13\,h^{-1}$Mpc and $6.17\,h^{-1}$Mpc, respectively. Aperture radii between $0'.5 \lesssim \theta_{\rm ap} \lesssim 24'$ are used.

Except for the red sample with $\langle z \rangle = 0.3$ it is found that red and blue galaxies are differently biased with respect to the dark matter, $b \neq 1$, at all analysed redshifts. Averaging the bias factor over all observed scales yields $\bar{b} = 0.95 \pm 0.06, 1.2 \pm 0.1, 1.39 \pm 0.08, 1.36 \pm 0.03$ (red) and $\bar{b} = 0.36 \pm 0.03, 0.55 \pm 0.07, 0.58 \pm 0.03, 0.52 \pm 0.03$ (blue) for $\langle z \rangle = 0.3, 0.5, 0.7, 0.9$, respectively. The figures allow a moderate bias increase with redshift by a factor of $1 - 2$ in concordance with ΛCDM predictions. Moreover, a small increase of the bias factor towards smaller scales is seen in the data for the red and blue sample. A scale-dependence of galaxy bias is also a prediction of the ΛCDM model. Due to the relatively small survey area the measurement of the dark matter-galaxy correlation factor is not directly possible because the signal-to-noise on the scales of interest becomes too small. By assuming a singular isothermal sphere profile for the so-called galaxy-galaxy lensing signal, on which the dark matter-galaxy correlation factor is based, it is crudely estimated that for $\langle z \rangle = 0.3$ red galaxies are on all scales highly correlated, $r_{\rm red} \sim 1.1 \pm 0.2$, to the dark matter field while blue galaxies may be less correlated with $r_{\rm blue} = 0.5 \pm 0.2$ for $\theta_{\rm ap} \sim 1'$ and $r_{\rm blue} = 0.8 \pm 0.2$ for $\theta_{\rm ap} \sim 20'$.

As to the relative bias factor, $b_{\rm rel}$, between red and blue galaxies it is found that red galaxies are more clustered than blue galaxies. The relative bias factor is scale-dependent: $b_{\rm rel} \simeq 3.0 \pm 0.5$ for $\theta_{\rm ap} \sim 1'$ decreasing to $b_{\rm rel} \simeq 2.2 \pm 0.5$ for $\theta_{\rm ap} \sim 22'$. For scales smaller than $\theta_{\rm ap} \sim 1'$, the bias factor is decreasing again down to $b_{\rm rel} = 1.5 \pm 0.2$. The relative correlation factor, $r_{\rm rel}$, of the distributions of red and blue galaxies is clearly scale-dependent. It drops from a value close to unity for large aperture radii to $r_{\rm rel} = 0.55 \pm 0.05$ on scales of about $\theta_{\rm ap} \sim 1'$. The scale-dependence of $r_{\rm rel}$ is probably intimately related to the well known morphology-density relation of galaxies. If so, the results show that there is such a relation present up to $\langle z \rangle = 0.9$. This needs further investigation. To address the question whether $r_{\rm rel} < 1$ is due to a non-linear relation between the red and blue galaxy density or mainly due to a random scatter, we assume a bivariate lognormal model for the probability to obtain a joint pair of values for the densities of red and blue galaxies. This is a common assumption for galaxy number densities in the literature. With this assumption and the measurements for the aperture statistics we can disentangle non-linearity, $\epsilon_{\rm nl}$, and stochasticity, $\epsilon_{\rm scatt}$, contributions to the correlation factor, $r_{\rm rel} = (1 + \epsilon^2_{\rm nl} + \epsilon^2_{\rm scatt})^{-1/2}$. On all analysed scales, the major contributor to $r_{\rm rel}$ is a stochastic scatter with $\epsilon_{\rm scatt}/\epsilon_{\rm nl} \simeq 5 - 15$. Therefore, the bias between red and blue galaxies is clearly non-deterministic. If red galaxies are highly correlated to the dark matter field, as indicated by the galaxy-galaxy lensing signal, then blue galaxies have, on small scales, not only to be randomly scattered with respect to red galaxies but also with respect to the dark matter density field. This poses a new constraint on models for galaxy formation. Within the statistical uncertainties we do not find a clear evolution with redshift for $r_{\rm rel}$, $b_{\rm rel}$, $\epsilon_{\rm nl}$ and $\epsilon_{\rm scatt}$.

Chapter 6: Constraints on cosmology using shear tomography correlations

Cosmological weak lensing by the large scale structure of the Universe, cosmic shear, is coming of age as a powerful probe of the parameters describing the cosmological model and matter power spectrum. It complements Cosmic Microwave Background studies, by breaking degeneracies and providing a cross-check. Furthermore, upcoming cosmic shear surveys with photometric redshift information will enable the evolution of dark matter to be studied, and even a crude separation of sources into redshift bins leads to improved constraints on parameters. The evolution of structure can be constrained using so-called cosmic shear tomography, which is performed by binning the galaxies carrying the lensing signal in redshift. Every redshift bin yields a different cosmic shear field because source galaxies sitting at different redshifts preferentially probe the matter distribution at different cosmic times. An important measure of the cosmic shear signal are the shear correlation functions; these can be directly calculated from data, and compared with theoretical expectations for different cosmological models and matter power spectra. However, taking subsets of galaxies decreases the lensing signal-to-noise of the shear correlation functions so that a natural question to ask is how much does redshift information improve confidence in cosmological parameter estimates? A Monte Carlo method to quickly simulate mock surveys of the shear tomography is presented. One application of this method is in the determination of the full covariance matrix for the correlation functions; this includes redshift binning and is applicable to arbitrary survey geometries. Terms arising from shot noise and cosmic variance (dominant on small and large scales respectively) are accounted for naturally. As an illustration of the use of such covariance matrices, it is considered to what degree confidence regions on parameters are tightened when redshift binning is employed. The parameters considered are those commonly discussed in cosmic shear analyses –the matter density parameter $\Omega_{\rm m}$, dark energy density parameter (classical cosmological constant) Ω_Λ, power spectrum normalisation σ_8 and shape parameter Γ. The computed covariance matrices are incorporated into a likelihood treatment, and also use the Fisher formalism to explore a larger region of parameter space. Parameter uncertainties can be decreased by a factor of $\sim 4-8$ ($\sim 5-10$) with 2 (4) redshift bins.

The core of this chapter has been published in Simon, King & Schneider (2004).

Outlook

Weak gravitational lensing is a tool with great potential for studying galaxy bias. Chapter 3 shows that with lensing the parameters of the linear stochastic bias can in principle be measured accurately. Moreover, also with lensing (Chapter 6) the clustering of dark matter can be analysed separately from the galaxy distribution to put constraints on parameters of cosmological models. At the moment practical limits mainly originate from statistical noise due to the relatively small area of available surveys. Ongoing lensing surveys –such as the Subaru Survey, CFHT Legacy Survey or OmegaCAM Survey– and surveys planned for the near future –as surveys with SNAP, PANSTARS, VST or LSST– are going to change this situation completely. Survey areas will comprise hundreds of square degrees observed in multiple colours. Even higher-order correlations of cosmic shear will be measured with reasonable signal-to-noise ratios providing independent new constraints for cosmological parameters. We are on the brink of a very exciting time for observational cosmology.

A galaxy bias analysis like in Chapters 4 and 5 will be possible over a wider range of length scales with a good resolution in redshift. The expectedly small evolution of bias in the redshift range accessible with lensing, that is not properly resolved in GaBoDS or COMBO-17, should then become visible. The bias model in Chapter 2 encourages us that new constraints on galaxy evolution will be found. However, this model, as being based on linear perturbation theory, offers only a limited view on the evolution of galaxy bias. Its description is only valid on linear scales. An improved evolutionary bias model is required, particularly for modelling the scale-dependence of bias. Currently the most successful analytical model for cosmic large-scale structure is the halo model. It predicts correlations, including higher-order correlations, even on non-linear scales. Another advantage is that it relates density correlations to physical parameters such as dark matter halo profiles and galaxy halo occupation numbers. For an evolutionary bias model based on the halo model, however, the redshift evolution and, for practical applications, a translation between halo model parameters and bias parameters needs to be worked out.

As pointed out in Sect. 1.4.3, the linear stochastic bias scheme does not distinguish between a non-linear and stochastic bias. Therefore, we cannot tell whether the observed decorrelation, $r < 1$, between galaxy number density and dark matter density as measured in GaBoDS (Chapter 4) and COMBO-17 (Chapter 5) is due to the fact that the galaxy density is random with respect to the dark matter density, or due to the fact that the number of galaxies at some position is actually a deterministic but non-linear function of the underlying dark matter density. If the galaxy-dark matter relation was completely random, say, we would have to conclude that dark matter is irrelevant for galaxy formation. Therefore, the distinction between non-linearity and stochasticity is important for our understanding of galaxy formation. The non-linear stochastic bias scheme makes this distinction so that the next step should be to measure its parameters using weak gravitational lensing. How can this be done? Appendix A.4 suggests two general possibilities. One way is to specify the type of statistics relating two biased fields, *i.e.* specifying the joint PDF for pairs of densities in the smoothed random fields, and to measure its remaining free parameters. This option is applied in Chapter 5 for obtaining the relative (non-linear stochastic) bias of red and blue galaxies in COMBO-17. The assumed model of the joint PDF allows us to estimate the non-linear bias parameters already from the second-order statistics of the aperture galaxy number count. Lognormal statistics might also be a valid assumption for the joint PDF of galaxy/dark matter densities, however so far no observational constraints for this PDF –apart from the second-order cumulants– are available. A lognormal model is suggested by N-body simulations (*e.g.* Kayo *et al.* 2001). Another possibility is to approximate the joint PDF by its cumulants, for example by means of a Edgeworth expansion. This seems to be the most practical approach for measuring the non-linear stochastic galaxy-dark matter bias. For this purpose, one has to find an adaption of the method in Chapter 3 to third-order aperture statistics. Most of this work has already been done (Schneider & Watts 2005; Schneider, Kilbinger & Lombardi 2004; Schneider & Lombardi 2003; Jarvis *et al.* 2004) using estimators of correlations of cosmic shear and galaxy positions in triangle configurations. However, the remaining details for an explicit application to galaxy bias still need to be done. In this context, halo model predictions for the non-linear stochastic bias parameters are also something worth considering. Maybe even an analytical model for the evolution of the non-linear bias can be found. First steps have already been made (Taruya & Suto 2000; Taruya & Soda 1999).

The upcoming generation of cosmic shear surveys will also greatly improve the derived constraints on cosmological parameters since also measurements of third-order statistics of cosmic shear will become feasible. In addition, multi-colour information of the source galaxies will confine the redshifts of individual galaxies. As for second-order shear tomography correlations (Chapter 6) third-order correlations are also very likely to further increase the confidence on cosmological parameters. The expected gain from these improvements is addressed by ongoing studies. With these advances we may soon hope to learn more about the mysterious dark energy that is challenging modern theoretical physics and cosmology.

APPENDIX A

Appendix: Miscellaneous

A.1. Fast Hankel transformations

This Appendix briefly summarises a method (in detail: Hamilton 2000) that can be used to tackle integrals numerically, like the biased Hankel transformation

$$a\left(r\right) = \int_0^\infty \mathrm{d}k\ r\ \left(rk\right)^{-q}\ J_\mu\left(kr\right)\hat{a}\left(k\right) \tag{A.1}$$

$$\hat{a}\left(k\right) = \int_0^\infty \mathrm{d}r\ k\ \left(rk\right)^{+q}\ J_\mu\left(kr\right)a\left(r\right)\ . \tag{A.2}$$

$a\left(r\right)$ and $\hat{a}\left(k\right)$ are a Hankel transformation pair, q and μ real numbers. $q = 0$ indicates a so-called unbiased Hankel transformation. The integrals are numerically troublesome since the integration kernel –a spherical Bessel function J_μ of μ-th order– is an oscillating function.

Siegmann (1977) noted that this integral transformation, taking $a\left(r\right)$ to $\hat{a}\left(k\right)$ and back, can actually be pictured as a convolution on a log-scale, $\ln r$ and $\ln k$ respectively. As this not only holds for integrals of the kind above, we conduct the following derivation for a slightly more general class of integrals, namely

$$\hat{f}\left(k\right) = \int_0^\infty \mathrm{d}r\ k\ \mathrm{K}\left(kr\right)\ f\left(r\right)\ , \tag{A.3}$$

where $K\left(x\right)$ is some arbitrary function. In the case of the Hankel transformations, we have $K\left(x\right) = x^{+q}\,J_\mu\left(x\right)$ or $K\left(x\right) = x^{-q}\,J_\mu\left(x\right)$.

Going from the linear scale to the logarithmic scale, $x \equiv \ln r$ and $y \equiv \ln k$, Eq. (A.3) becomes

$$\hat{f}_{\log}\left(y\right) = \int_{-\infty}^{+\infty} \mathrm{d}x\ \mathrm{e}^{x+y}\ \mathrm{K}\left(\mathrm{e}^{x+y}\right)\ f_{\log}\left(\mathrm{e}^{x}\right) \tag{A.4}$$

$$\equiv \int_{-\infty}^{+\infty} \mathrm{d}x\ \hat{\mathrm{K}}\left(x+y\right)\ f_{\log}\left(x\right) \tag{A.5}$$

$$= \left(\hat{K} * f_{\log}\right)\left(y\right)\ , \tag{A.6}$$

where $f_{\log}(x) \equiv f(\mathrm{e}^x)$ and $\hat{f}_{\log}(x) \equiv \hat{f}(\mathrm{e}^x)$ are f and $\hat{f}$ on a logarithmic scale. This transformation shows clearly that the Eq. (A.3) is a convolution on a log-scale with the convolution kernel

$$\hat{\mathrm{K}}(x) \equiv \mathrm{e}^x\,\mathrm{K}(\mathrm{e}^x) \;. \tag{A.7}$$

From the numerical point of view, convolutions, $f * g$, are convenient because in Fourier space they reduce to the simple product, $\tilde{f} \times \tilde{g}^*$, of the Fourier transforms $\tilde{g}$ and $\tilde{f}$ according to the convolution theorem; a Fourier transform is easily implemented using the FFT algorithm (*cf.* Press *et al.* 1992). Thus, the numerical recipe for Eq. (A.3) is

1. Evenly sample $f(r)$ on a logarithmic scale by $f_i = f(r_{\rm c}\,\mathrm{e}^{(i-N_{\rm c})\Delta\ln r})$ where $\ln r_{\rm c} = (\ln r_{\max} + \ln r_{\min})/2$, $N_{\rm c} = (N-1)/2$ and $\Delta\ln r = (\ln r_{\max} - \ln r_{\min})/N$. N is the number of sampling points of the log-scale with index $i \in \{0, 1, \ldots, N-1\}$ stretching from $\ln r_{\min}$ to $\ln r_{\max}$ about the centre $r_{\rm c}$.

2. FFT transform f_i to obtain $\tilde{f}_i$.

3. Multiply every $\tilde{f}_i$ by $\tilde{u}_i \equiv \mathrm{F}^*[\hat{\mathrm{K}}](k_i)$ where k_i are the k-modes corresponding to $\tilde{f}_i$; these are usually integral multiples of the Nyquist frequency $\pi/(N\Delta\ln r)$ depending on the conventions of the FFT algorithm. $\mathrm{F}^*[\hat{\mathrm{K}}]$ denotes the complex conjugate of the Fourier transform of $\hat{\mathrm{K}}$.

4. Owing to the peculiarities of the FFT, there are usually Fourier coefficients $\tilde{f}_i$ and $\tilde{f}_j$ with $k_j = -k_i$ in the FFT array that share the same elements; they are transformed in a special way since the transformed $f(r)$ has to be real: set $\mathrm{Im}\;\tilde{f}_i = \mathrm{Im}\;\tilde{f}_j = 0$ and $\mathrm{Re}\;\tilde{f}_i = \mathrm{Re}\;\tilde{f}_j = \mathrm{Re}\;\tilde{f}_i \times \mathrm{Re}\;u_i$ [real $f(x)$ obey the constraint $\tilde{f}(k) = \tilde{f}^*(-k)$].

5. Re-FFT the product $\tilde{f}_i \times \tilde{u}_i$ to obtain $\hat{f}(k)$ (Eq. A.3) sampled on a log-scale with $k_i = 1/r_{\rm c}\,\mathrm{e}^{(N_{\rm c}-i)\Delta\ln r}$ (the exponent has switched sign).

Ways to reduce the systematics –aliasing and ringing– are not discussed here and can be found in the Appendix of Hamilton (2000).

The expressions for $\mathrm{F}[\hat{\mathrm{K}}](k)$ corresponding to thesis relevant kernels $K(x)$ are summarised in the following table. The kernel in the first row is required for the actual Hankel transformation, while the kernel in the second row was required for working out the Eqs. (3.14) for the polynomial filter (3.86); the third row is simply a generalisation of this kernel. $\Gamma(z)$ denotes the complex Gamma function.

$\mathrm{K}(x)$	$\mathrm{F}[\hat{\mathrm{K}}](k)$
$x^q\;J_\mu(x)$	$2^{\mathrm{i}x+q}\;\frac{\Gamma\left[\frac{1}{2}(1+\mu+q+\mathrm{i}k)\right]}{\Gamma\left[\frac{1}{2}(1+\mu-q-\mathrm{i}k)\right]}$
$x^q\;[J_\mu(x)]^2$	$\frac{1}{2\sqrt{\pi}}\frac{\Gamma\left[-\frac{1}{2}(\mathrm{i}k+q)\right]\Gamma\left[\frac{1}{2}(1+\mathrm{i}k+2\mu+q)\right]}{\Gamma\left[\frac{1}{2}(1-\mathrm{i}k-q)\right]\Gamma\left[\frac{1}{2}(1-\mathrm{i}k+\mu-q)\right]}$
$x^q\;J_\mu(x)\,J_\nu(x)$	$\frac{2^{\mathrm{i}k+q}\Gamma[\mathrm{i}k-q]\Gamma\left[\frac{1}{2}(1+\mathrm{i}k+\mu+\nu+q)\right]}{\Gamma\left[\frac{1}{2}(1-\mathrm{i}k+\mu-\nu-q)\right]\Gamma\left[\frac{1}{2}(1-\mathrm{i}k-\mu+\nu-a)\right]\Gamma\left[\frac{1}{2}(1-\mathrm{i}k+\mu+\nu-q)\right]}$

A.2. Least-square template fitting

Consider the following problem: a set of $N_{\rm sample}$ joint data points y_i and $\vec{x}_i$, where $\vec{x}_i$ is a $N_{\rm dim}$ dimensional vector, are to be best-fitted by a suitable linear combination of $N_{\rm fit}$ template functions $f_m(\vec{x}) : \mathbb{R}^{N_{\rm dim}} \to \mathbb{R}$:

$$y_i \approx \sum_{m=1}^{N_{\rm fit}} \alpha_m f_m(\vec{x}_i) \ , \tag{A.8}$$

where α_m denote the linear coefficients of the best-fit. In the following, we will summarise the well-known solution to this problem.

We encountered this problem in Chapter 5 where we required a transformation from the equatorial coordinates of the Edinburgh galaxy object catalogue to the pixel coordinates of the GaBoDS (Bonn). In this case, the y_i are either the x- or y-pixel coordinate and $\vec{x}_i = (\alpha_i, \delta_i)$ are the corresponding equatorial coordinates, right ascension α_i and declination δ_i . We fitted this transformation with a set of polynomial templates up to the 5th degree, thus $f_m(x_1, x_2) = x_1^{n_1} x_2^{n_2}$ with $n_1, n_2 \geq 0$ and $n_1 + n_2 \leq 5$. For every individual patch –A901, AXAF and S11– the GaBoDS lens catalogue was used to determine the best-fit coefficients α_m so that the equatorial coordinates of the Edinburgh object catalogue, including photometric redshifts, could be transformed to the GaBoDS pixel coordinate system.

In order to work out the best-fit coefficients α_m we demand that the weighted mean of the deviation, Δ, from the template fit (A.8) is small:

$$\Delta \equiv \frac{\sum_{i=1}^{N_{\rm sample}} w_i \left[y_i - \sum_{m=1}^{N_{\rm fit}} \alpha_m f_m(\vec{x}_i) \right]^2}{\sum_{i=1}^{N_{\rm sample}} w_i} \ , \tag{A.9}$$

where $w_i \geq 0$ is a statistical weight for the i-th data point. To minimise the deviations we require for each α_n that $\frac{\partial \Delta}{\partial \alpha_n} = 0$:

$$\sum_{i=1}^{N_{\rm sample}} w_i \left[y_i - \sum_{m=1}^{N_{\rm fit}} \alpha_m \, f_m(\vec{x}_i) \right] f_n(\vec{x}_i) \quad = \tag{A.10}$$

$$\sum_{i=1}^{N_{\rm sample}} w_i \, y_i \, f_n(\vec{x}_i) - \sum_{i,m=1}^{N_{\rm sample}, N_{\rm fit}} w_i \, \alpha_m \, f_m(\vec{x}_i) \ f_n(\vec{x}_i) \quad = \quad 0 \tag{A.11}$$

$$\Longleftrightarrow \quad \langle y_i \, f_n(\vec{x}_i) \rangle_i = \sum_{m=1}^{N_{\rm fit}} \alpha_m \ \langle f_m(\vec{x}_i) \ f_n(\vec{x}_i) \rangle_i \ , \tag{A.12}$$

where we, for convenience, introduced the expression

$$\langle g_i \rangle_i \equiv \sum_{i=1}^{N_{\rm sample}} w_i \, g_i \tag{A.13}$$

to denote the weighted sum of g_i over all data points in the sample. The solution to the problem is therefore finding the roots of the set of Eqs. (A.12) with respect to the α_m (one equation for each $n = 1 \ldots N_{\rm fit}$). This solution can immediately be written down due to the linearity of the equations, namely

$$\vec{A} = \mathbf{F}^{-1} \vec{Y} \ , \tag{A.14}$$

where we use

$$
\begin{aligned}
A_m &\equiv \alpha_m \, , && \text{(A.15)}\\
Y_m &\equiv \langle y_i \, f_m(\vec{x}_i) \rangle_i \, , && \text{(A.16)}\\
F_{mn} &\equiv \langle f_m(\vec{x}_i) \, f_n(\vec{x}_i) \rangle_i \, . && \text{(A.17)}
\end{aligned}
$$

The procedure is therefore to compute $\mathbf{F}$ and $\vec{Y}$ from the set of data points and template functions and then to numerically invert $\mathbf{F}$, finally working out $\mathbf{F}^{-1}\vec{Y}$.

A.3. Probability theory in a nutshell

In cosmology, one studies the statistical properties of cosmic fields and relates them to physics, like, for instance, the correlations in the spatial galaxy distribution or the anisotropies of the cosmic microwave background. The basic language that is used to describe their characteristics as random fields is briefly summarised here. A much more detailed account can be found in *e.g.* Bernardeau *et al.* (2002), Bardeen *et al.* (1986) or Adler *et al.* (1981).

One dimensional probability distributions

Let x' be the outcome of an experiment, an observation, *etc.* The probability of obtaining a certain value $x \le x' < x + \mathrm{d}x$ from a continuous set of possible values X is described by the probability density, *probability distribution function* (PDF) $P(x)$, in the sense that $P(x')\,\mathrm{d}x$ is the probability of finding the value x'. The probability density is normalised:

$$\int_X \mathrm{d}x \; P(x) = 1 \, . \tag{A.18}$$

The *ensemble average* or expectation $\langle f(x) \rangle$ denotes the average of $f(x')$ that would one get by performing an infinite number of trials

$$\langle f(x) \rangle = \int_X \mathrm{d}x \; P(x) \; f(x) \, . \tag{A.19}$$

Moments

One special important example of $f(x)$ are the so-called n-th (raw) *moments* of $P(x)$ defined as $m_n \equiv \langle x^n \rangle$ with n being an integer. For $n = 1$, thus $m_1 = \langle x \rangle$, we have the *mean* of the PDF. The *central moments* defined as $\mu_n \equiv \langle (x - m_1)^n \rangle$ describe the scatter x' about the mean $\langle x \rangle$; $\sigma_x^2 \equiv \mu_2$ is called the *variance* of $P(x)$. The raw and central moments are related to each other by the following binomial transformation

$$\mu_n = \sum_{i=1}^{n} \binom{n}{i} (-1)^{n-i} \, \mu_i \, m_{n-i} \, . \tag{A.20}$$

Often we use the moments of a PDF as a characterisation of the PDF itself because they capture important properties of the PDF, or because we do not know the complete PDF. For example, take the Tschebycheff inequality

$$P(|x - m_1| > k) \le \frac{\sigma_x^2}{k^2} \, , \tag{A.21}$$

where $k > 0$ and $P(|x - m_1| > k)$ denotes the probability to obtain a value x' with $|x' - m_1| > k$. This shows that the average and the variance of a PDF already determines the fraction of trials x' that can be expected to be found within the interval $\langle x\rangle - k \leq x' \leq \langle x\rangle + k$, regardless of how the PDF in detail looks like.

Finite dimensional probability distributions

We go one step further by introducing events that do not have just one outcome x but a *finite* set of outcomes x_i with $i \in \{1, 2, \ldots, N\}$. Each of the x_i is considered as an individual random variable. As before we have the *joint probability density* $P(x_1, x_2, \ldots, x_N)$, or simply $P(x_i)$, describing the statistics of the set x_i. The ensemble average of $f(x_i)$ is now:

$$\langle f(x_i)\rangle \equiv \int \mathrm{d}^N x \; P(x_i)\; f(x_i) \;. \tag{A.22}$$

Similarly, we can define moments of $P(x_i)$ of the order $|n| \equiv n_1 + n_2 + \ldots + n_N$:

$$\begin{aligned} m_{n_1, n_2, \ldots, n_N} &\equiv \left\langle x_1^{n_1} x_2^{n_2} \ldots x_N^{n_N} \right\rangle && \text{raw moments ,} \quad \text{(A.23)} \\ \mu_{n_1, n_2, \ldots, n_N} &\equiv \left\langle (x_1 - \langle x_1\rangle)^{n_1} (x_2 - \langle x_2\rangle)^{n_2} \ldots (x_N - \langle x_N\rangle)^{n_N} \right\rangle && \text{central moments .} \end{aligned}$$

Monte Carlo techniques

Monte Carlo methods approximate the integral (A.22) by

$$\langle f(x_i)\rangle \approx \frac{1}{N} \sum_{j=1}^{N} f(x_i^{(j)}) \tag{A.24}$$

using a synthetically produced large chain of $1 \leq j \leq N$ different random numbers, $x_i^{(j)}$, employing a simulated random process obeying $P(x_i)$. Monte Carlo integrations are applied if one is interested in $\langle f(x)\rangle$ but is either unable to perform the integral (A.22), or because one does not know $P(x)$ analytically. The latter is the case for the Monte Carlo sampler in Chapter 3 where a realisation of random fields x_i is performed by a series of well-defined steps without the need to explicitly write down or use $P(x)$; the "$\langle f(x)\rangle$" are in this specific application, for example, the covariances and averages of estimates for 2-point correlation functions (galaxy clustering and cosmic shear). The art of Monte Carlo techniques is to build a random number generator for x_i. Common generators are Gibbs sampler and Markov chains. Random number generators are also a clever way to evaluate integrals numerically, in particular higher-dimensional integrals.

Bayes' theorem

Let us say, we consider events that consist of the outcomes, (x_i, y_i), of two sets of random variables x_i and y_j. If we select just those x_i for some fixed y_j and focus on this subset of conditional events, $x_i|y_j$, then we are considering the so-called *conditional* PDF written as $P(x_i|y_j)$. *Bayes' theorem* states that

$$P(x_i|y_j)\,\mathrm{d}x_i\; P(y_j)\,\mathrm{d}y_j = P(y_j|x_i)\,\mathrm{d}y_j\; P(x_i)\,\mathrm{d}x_i = P(x_i, y_j)\,\mathrm{d}x_i\mathrm{d}y_j \;, \tag{A.25}$$

where $P(y_j)$ is the PDF of y_j ignoring the values of x_i,

$$P(y_j) = \int \mathrm{d}x_i \, P(x_i, y_j) \ , \tag{A.26}$$

while $P(x_i)$ is the PDF ignoring the values of y_j,

$$P(x_i) = \int \mathrm{d}y_j \, P(x_i, y_j) \ . \tag{A.27}$$

The function $P\left(x_i, y_j\right)$ is the PDF for both x_i and y_j to occur at the same time, their *joint PDF*. For uncorrelated variables x and y, we always have $P\left(x|y\right)\mathrm{d}x = P\left(x\right)\mathrm{d}x$ and $P\left(y|x\right)\mathrm{d}y = P\left(y\right)\mathrm{d}y$, meaning that x and y do not care about the outcomes of the other event y and x, respectively.

Moment generating function

As to the calculus in probability theory, it is very convenient to introduce the (raw) *moment generating function* ϕ_P of $P\left(x_i\right)$ defined as

$$\phi_P\left(J_i\right) \equiv \left\langle \mathrm{e}^{\mathrm{i}\sum_j x_j J_j} \right\rangle = \int \mathrm{d}^N x \, P\left(x_i\right) \, \mathrm{e}^{+\mathrm{i}\sum_j x_j J_j} \tag{A.28}$$

$$\Longleftrightarrow \quad P\left(x_i\right) = \int \mathrm{d}^N J \, \phi_P\left(J_i\right) \, \mathrm{e}^{-\mathrm{i}\sum_j x_j J_j} \ , \tag{A.29}$$

where J_i is the conjugate variable of x_i. If ϕ_P is known, the raw moments of $P\left(x_i\right)$ are simply

$$m_{n_1,n_2,\dots,n_N} = -\mathrm{i}^{|n|} \left[\frac{\mathrm{d}^{|n|}}{\mathrm{d}J_1^{n_1} \mathrm{d}J_2^{n_2} \dots \mathrm{d}J_N^{n_N}} \, \phi_P\left(J_i\right) \right]_{\vec{J}=0} \ . \tag{A.30}$$

The power of this representation lies in the fact that we can easily write down the moment generating function of a PDF, $P'(y_i)$, of random variables y_i that are transformations of x_i:

$$\phi_{P'}\left(J_i\right) = \int \mathrm{d}^N x \ P\left(x_i\right) \, \mathrm{e}^{+\mathrm{i}\, f(\vec{x})\vec{J}} \ . \tag{A.31}$$

The vector of random variables $\vec{y} = f\left(\vec{x}\right)$ denotes such a transformation of the random variables $\vec{x} = \left(x_1\, x_2 \, \dots \, x_N\right)$, and $f\left(\vec{x}\right)\vec{J}$ indicates its scalar product with $\vec{J} = \left(J_1\, J_2 \, \dots \, J_N\right)$. The new generating function $\phi_{P'}$ allows us to express the moments of $P'\left(y_i\right)$ in terms of the moments of $P\left(x_i\right)$. The explicit knowledge of $P'(y_i)$ is not necessary for that task.

As one illustrative example, consider the generating function of a random variable $z = ax + by + c$. It is assumed to be a linear combination of two uncorrelated random variables x and y, thus $\langle xy \rangle = 0$. The coefficients a, b, c are just constants. Let $P_z(z)$ be the PDF of z. It follows from (A.31) that

$$\phi_{P_z}\left(J\right) = \int \mathrm{d}x \, \mathrm{d}y \, P(x,y) \, \mathrm{e}^{\mathrm{i}J(ax+by+c)} \tag{A.32}$$

$$= \mathrm{e}^{\mathrm{i}cJ} \int \mathrm{d}x \, P_x(x) \, \mathrm{e}^{\mathrm{i}aJx} \int \mathrm{d}y \, P_y(y) \, \mathrm{e}^{\mathrm{i}bJy} \tag{A.33}$$

$$= \mathrm{e}^{\mathrm{i}cJ} \phi_{P_x}\left(aJ\right) \phi_{P_y}\left(bJ\right) \ . \tag{A.34}$$

The generating function of $P_z(z)$ is hence a product of the generating functions of $P_x(x) = P(x)$ and $P_y(y) = P(y)$. This decomposition is due to the fact the the joint PDF of x and y, $P(x, y)$, separates into $P(x, y) = P_x(x) P_y(y)$. According to (A.30) the n-th moment of P_z is the n-th derivative of ϕ_{P_z} with respect to J at $J = 0$. As ϕ_{P_z} is a product of three functions, this n-th derivative will produce a polynomial in the individual moments of P_x and P_y with orders less or equal n.

One may ask whether a more natural definition of the moments can be found that is linear for a linear combination of uncorrelated random variables and does not mix moments of different orders in that case? Such a definition is introduced in the following.

Cumulants

Quantities related to the moments but with nicer properties are the *cumulants*, $\kappa_{n_1,n_2,\ldots,n_N}$, or semi-invariants of a PDF; they are defined like the moments in Eq. (A.30) as derivatives of some generating function $Z_P(J_i)$:

$$\kappa_{n_1,n_2,\ldots,n_N} = -\mathrm{i}^{|n|} \left[\frac{\mathrm{d}^{|n|}}{\mathrm{d}J_1^{n_1} \mathrm{d}J_2^{n_2} \ldots \mathrm{d}J_N^{n_N}} Z_P(J_i) \right]_{\vec{J}=0} , \tag{A.35}$$

where

$$Z_P(J_i) \equiv \ln \phi_P(J_i) = \sum_{n_1,\ldots n_N=0}^{\infty} \kappa_{n_1,\ldots,n_N} \frac{(\mathrm{i}J_1)^{n_1} (\mathrm{i}J_2)^{n_2} \ldots (\mathrm{i}J_N)^{n_N}}{n_1! n_2! \ldots n_N!} \tag{A.36}$$

is the *cumulant generating function* of $P(x_i)$. It follows from this definition that the cumulants are polynomials of the moments, like, for example, in the case of a one-dimensional PDF

$$\kappa_1 = m_1 \tag{A.37}$$

$$\kappa_2 = m_2 - m_1^2 = \mu_2 \tag{A.38}$$

$$\kappa_3 = 2m_1 - 3m_1 m_2 + m_3 = \mu_3 \tag{A.39}$$

$$\kappa_4 = -6m_1^4 + 12m_1^2 m_2 - 3m_2^2 - 4m_1 m_3 + m_4 = \mu_4 - 3\mu_2^2 . \tag{A.40}$$

In many respects, the cumulants are like the moments. In fact, they are identical to the central moments for $0 < |n| < 4$. However, they are more basic in other respects: the cumulants, $\kappa_n[P_z]$, of the PDF P_z in the last section are

$$\kappa_n[P_z] = a^n \kappa_n[P_x] + b^n \kappa_n[P_y] , \tag{A.41}$$

where $\kappa_n[P_x]$ and $\kappa_n[P_y]$ are the cumulants of $P_x(x)$ and $P_y(y)$ respectively. This means that the cumulants are “linear” to all orders n which is clearly not the case for the moments. If we consider sums of uncorrelated random variables, the moments of different orders in the individual P_x and P_y mix in the sum-P_z. As this is not the case for the cumulants they are also called *unconnected moments* or reduced moments of a PDF.

One defines the *skewness* of a one-dimensional PDF $P(x)$ by $S_3 \equiv \mu_3/\mu_2^{3/2}$ and the *kurtosis* by $S_4 \equiv \mu_4/\mu_2^2 - 3$ which are the third- and fourth-order cumulants of the normalised PDF $P(x/\sigma_x)$. A non-vanishing skewness indicates an asymmetry about the mean, while the kurtosis is a measure of the spread of the distribution relative to a normal Gaussian distribution.

Multivariate Gaussian probability distribution

From the point of view of the cumulants, the simplest PDF has all cumulants vanishing beyond second-order, thus $\kappa_{n_1,n_2,\ldots,n_N} = 0$ for $|n| > 2$. According to Eq. (A.29) and the definition (A.36) we can work out this specific PDF:

$$\begin{aligned} P_{\text{Gauss}}\left(x_i\right) &= \int \mathrm{d}^N J \exp\left(\mathrm{i}\langle\vec{x}\rangle\vec{J} - \frac{1}{2}\vec{J}^{\,\mathrm{t}}\mathbf{C}\vec{J}\right)\mathrm{e}^{-\mathrm{i}\vec{x}\vec{J}} && \text{(A.42)} \\ &= \frac{1}{(2\pi)^{N/2}}\frac{1}{\sqrt{\det\mathbf{C}}}\exp\left(-\frac{1}{2}\left(\vec{x}-\langle\vec{x}\rangle\right)^{\mathrm{t}}\mathbf{C}^{-1}\left(\vec{x}-\langle\vec{x}\rangle\right)\right) , && \text{(A.43)} \end{aligned}$$

where $C_{ij} \equiv \langle(x_i - \langle x_i\rangle)(x_j - \langle x_j\rangle)\rangle$ denotes the matrix of the second-order cumulants of $P(x_i)$; it is the so-called *covariance matrix*. The PDF $P_{\text{Gauss}}(x_i)$ is the well known multivariate Gaussian probability function. Therefore, the Gaussian PDF is in some sense the simplest of all PDFs. Note that each x_i individually obeys a Gaussian distribution.

For PDFs whose other cumulants are not vanishing but negligible with respect to the second order, *i.e.*

$$\lambda_{n_1,n_2,\ldots,n_N} \equiv \frac{\kappa_{n_1,n_2,\ldots,n_N}}{\left[\sigma_{x_1}\right]^{n_1}\left[\sigma_{x_2}\right]^{n_2}\ldots\left[\sigma_{x_N}\right]^{n_N}} \ll 1 , \qquad \text{(A.44)}$$

one can find a useful asymptotic expansion of $P\left(x_i\right)$ about a Gaussian by expressing the cumulant generating function as a Taylor series in $\sigma_{x_i}^2 = \left\langle x_i^2\right\rangle - \left\langle x_i\right\rangle^2$. This expansion is known as the Edgeworth expansion (Blinnikov & Moessner 1998; Juszkiewicz *et al.* 1995).[1]

Estimators

In practice, we usually would like to evaluate the moments, cumulants or, in general, $f(x)$ from our subject of observation. However, we never have the opportunity to actually "see" the ensemble average, $\langle f(x)\rangle$, over all possible realisations of the stochastic process. Instead, we have one or a finite set of realisations that we can use to estimate the, say, cumulants κ. Applying the same estimators to a different realisation gives us in general a different estimate $\hat{\kappa}$. Therefore, the outcomes of estimators are random variables on their own obeying their own PDF $P\left(\hat{\kappa}\right)$.

We call an estimator *unbiased* if $\langle\hat{\kappa}\rangle = \kappa$. Note that a biased estimator can still converge towards κ with the number of realisations taken into account for the estimation becoming large. The theory of estimators tries to find unbiased estimators with as small as possible variance $\left\langle\hat{\kappa}^2\right\rangle - \langle\hat{\kappa}\rangle^2$. An important quantity in this context is the maximum likelihood estimator (*cf.* Tegmark *et al.* 1997).

Random fields

Consider a continuous field of random variables. We attribute to every point $\vec{x}$ in our N dimensional index space a random variable or a vector of random variables which is denoted

---

[1] The Edgeworth expansion is a special case of the Charlier series by which a PDF, P', can be expressed as a series of derivatives of another PDF, P, if the difference between the cumulants of both is known. Charlier series are used to approximate PDFs P' which are only slightly differing from a well known P. For Edgeworth expansions of P' one assumes a multivariate Gaussian for P which has the same mean and covariance than P'.

by $\delta(\vec{x})$. A random number generator is attached to every point in the field, so to say. We call this continuous field of random variables a random field. For our applications, the index space is usually the four dimensional space-time or a position on the sky, and the random variables are, for instance, the density contrast of the dark matter or the aperture mass. We will assume in the following that the average $\langle\delta(\vec{x})\rangle$ at any point vanishes. This can always be achieved by a local transformation of the random field, namely by $\delta(\vec{x}) \to \delta'(\vec{x}) = \delta(\vec{x}) - \langle\delta(\vec{x})\rangle$.

We can picture a random field as being described by a PDF depending on an infinite set of variables $\delta(\vec{x})$. Instead of describing the whole PDF, we can pick out a set of n values $\delta(\vec{x}_i)$ from the random field and study the moments of their joint PDF $P(\delta(\vec{x}_i))$, independent from all the other (infinitely many) variables:

$$\xi^{(n)}(\vec{x}_1, \vec{x}_2, \dots, \vec{x}_n) \equiv \langle\delta(\vec{x}_1)\,\delta(\vec{x}_2)\,\dots\,\delta(\vec{x}_n)\rangle\ , \tag{A.45}$$

where $\xi^{(n)}$ is a so-called n-point correlation function of the random field[2].

An important sub-class are random fields that are statistically homogeneous and isotropic (see Sect. 1.2.1). These symmetries greatly simplify the correlation functions that in the general definition above are functions of the absolute positions of the $\delta(\vec{x}_i)$.

Random fields in which every individual $\delta(\vec{x_i})$ has a Gaussian PDF (or multivariate Gaussian PDF if δ is a vector), are called *Gaussian random fields.* Gaussian fields obey the *Wick theorem* that (in this case) states that all n-point correlators with $n > 2$ decompose into sums of products of two two-point correlators or vanish otherwise. Gaussian random fields are therefore completely determined by their second-order correlators $\xi^{(2)}(\vec{x}_1, \vec{x}_2)$. In particular, all moments of multivariate Gaussian PDFs decompose into the sum of products of second-order moments.

In the same manner as above the finite PDF moments, we can express the random field correlations $\xi^{(n)}$ in terms of a generating function, which is then a generating functional since we now integrate over a infinite continuous set of random variables (see *e.g.* Bernardeau *et al.* 2001; Matsubara 1995). The correlations $\xi^{(n)}$ are expressed as functional derivatives of the generating functional. Logically, we can –in analogy to the finite PDF– introduce cumulants or *connected correlations* $\xi^{(n)}_c$ of random fields. It turns out that, as for the finite PDFs, the connected n-th order correlations are polynomials in the correlators $\xi^{(m)}$ with $m \le n$. For Gaussian random fields, higher-order connected correlations with $n > 2$ vanish in analogy to the finite multivariate Gaussian PDF.

Polyspectra of random fields

An alternative way other than $\xi^{(n)}$ to quantify coherent structure in a random field are the polyspectra; they are completely equivalent to the real space correlators. In comparison to $\xi^{(n)}$ the polyspectra $\lambda^{(n)}$ quantify the correlations of the Fourier coefficients $c(\vec{k})$ of the random field:

$$\begin{aligned}\lambda^{(n)}\left(\vec{k}_1, \vec{k}_2, \dots, \vec{k}_n\right) &\equiv \left\langle c(\vec{k}_1)c(\vec{k}_2)\dots c(\vec{k}_n)\right\rangle \qquad\qquad (\text{A.46})\\ &= \int \mathrm{d}^N x_1 \mathrm{d}^N x_2 \dots \mathrm{d}^N x_n\ \xi^{(n)}(\vec{x}_1, \vec{x}_2, \dots, \vec{x}_n)\,\mathrm{e}^{+\mathrm{i}\sum_j \vec{x}_j \vec{k}_j}\ ,\end{aligned}$$

---

[2] If δ is actually a vector of random variables, then the definition of ξ should be understood as a tensor product of the δ's.

where we are using the following convention

$$c(\vec{k}) = \int \mathrm{d}^N x\, \delta(\vec{x})\, e^{+\mathrm{i}\,\vec{k}\cdot\vec{x}} \quad ; \quad \delta(\vec{x}) = \int \frac{\mathrm{d}^N k}{(2\pi)^N}\, c(\vec{k})\, e^{-\mathrm{i}\,\vec{k}\cdot\vec{x}}\ . \tag{A.47}$$

The Fourier coefficients $c(\vec{k})$ are linear combinations of the random field variables $\delta(\vec{x})$. Therefore, if we have a random Gaussian field in real space we automatically also have a random Gaussian field in Fourier space since linear combinations of Gaussian random variables are Gaussian as well.

Effect of filters on random fields

Frequently, either on purpose or as a consequence of the means by which we investigate the statistics of random fields, we smooth or convolve the random field with some filter before we look at the correlations in the field. The effect of the smoothing with a real filter F by

$$\delta'(\vec{x}) = (\delta * F)(\vec{x}) = \int \mathrm{d}^N x'\, \delta(\vec{x}\,' - \vec{x})F(\vec{x}\,') \tag{A.48}$$

is that we attenuate or amplify fluctuations (correlations) on characteristic scales, *i.e.* for particular $\vec{k}$, defined by the filter. The smoothing effectively modifies the polyspectra as follows from the convolution theorem:

$$\bar{\lambda}^{(n)}(\vec{k}_1, \ldots, \vec{k}_n) = \left[\prod_{i=1}^{n} \tilde{F}^*(\vec{k}_i)\right] \times \lambda^{(n)}(\vec{k}_1, \ldots, \vec{k}_n)\ , \tag{A.49}$$

where $\tilde{F}^*$ denotes the complex conjugate Fourier transform of the filter F. In particular, we modify the power spectrum and bispectrum (for a definition see Sect. 1.2.2):

$$\bar{P}(\vec{k}) = |\tilde{F}(\vec{k})|^2 P(|\vec{k}|) \tag{A.50}$$

$$\bar{B}(\vec{k}_1, \vec{k}_2) = \tilde{F}^*(\vec{k}_1)\tilde{F}^*(\vec{k}_2)\tilde{F}(\vec{k}_1 + \vec{k}_2)B(|\vec{k}_1|, |\vec{k}_2|, \sphericalangle \vec{k}_1, \vec{k}_2)\ . \tag{A.51}$$

Aperture statistics

Yet another way, apart from n-point correlation functions or polyspectra, of characterising random fields or cross-correlations between different random fields is to use aperture statistics. That is one considers correlations between values in the random field(s), δ_i, *at the same position*, $\vec{x}$, obtained by convolving the fields with some, usually isotropic, kernel $F_i(x)$; thus one considers the *aperture moment*

$$A(\vec{x}, \theta_{\rm ap}) \equiv \left\langle \delta_1'(\vec{x}) \ldots \delta_N'(\vec{x}) \right\rangle\ , \tag{A.52}$$

where $\delta_i'(\vec{x}) = (\delta_i * F_i)(\vec{x})$; N is the order of the aperture moment. The values δ_i' are broadly speaking weighted averages of values δ_i in the neighbourhood of the aperture centre $\vec{x}$. The convolution kernels or aperture filter F_i have a free parameter, $\theta_{\rm ap}$ say, that parametrises the typical size of the "neighbourhood"; it is called the aperture radius. For higher-order aperture moments the aperture radii may be different for different δ_i'. This is, however, not the case in this thesis. Note that the difference to the n-point correlation functions is that A expresses correlations between values of smoothed random fields in the same point, while $\xi^{(n)}$ expresses correlations of field values at, in general, different points. Moreover, A explicitly depends on the specific definition of the aperture filter; it quantifies moments of the (one-dimensional) joint PDF, $P(\delta_1', \ldots, \delta_N')$, of values at $\vec{x}$ of random fields smoothed out to a certain spatial scale. For concrete examples of random fields, think of galaxy densities, dark matter densities, gas temperature *etc.* whose relation between each other may be characterised by the aperture statistics. In practise, the field quantities, such as the galaxy number density for the aperture number count or the convergence for the aperture mass (Chapter 3), are averaged over the aperture area, and the moments (A.52) of many differently placed apertures are averaged making use of the fair sample theorem. Counts-in-Cell statistics of galaxies (*e.g.* Wild *et al.* 2004) is another example of aperture statistics often employed in astronomy to study the clustering of galaxies.

In the following discussion we restrict ourselves to statistically homogeneous and isotropic random fields which are the only relevant for cosmology (Sect. 1.2.1). Moreover, $F_i(x) \equiv F_i(|\vec{x}\,|)$ is assumed to be isotropic (and real). In adopting these symmetries, A does not depend on $\vec{x}$ so that in calculations we are allowed to set $\vec{x} = \vec{0}$ without loss of generality. Using the fact that due to the symmetries we can express the n-point correlation function as[3]

$$\langle \delta(\vec{x}_1) \ldots \delta(\vec{x}_N) \rangle \equiv \xi^{(N)}(|\vec{x}_1 - \vec{x}_2|, |\vec{x}_2 - \vec{x}_3|, \ldots, |\vec{x}_N - \vec{x}_1|) \tag{A.53}$$

one can show with some algebra that in a two dimensional index space $\vec{x}$ A can be calculated from $\xi^{(N)}$ according to the integral transformation

$$\begin{aligned} A(\theta_{\rm ap}) &= \int_0^\infty \mathrm{d}^2\theta_1 \ldots \mathrm{d}^2\theta_N \, F_N(|\sum_{i=1}^{N} \vec{\theta}_i|) \prod_{i=1}^{N-1} F_i(|\vec{\theta}_i + \vec{\theta}_{i+1}|) \, \xi^{(N)}(|\vec{\theta}_1|, \ldots, |\vec{\theta}_N|) \\ &= \int_0^\infty \mathrm{d}x_1 \, x_1 \ldots \mathrm{d}x_N \, x_N \, K(x_1, x_2, \ldots, x_N) \, \xi^{(N)}(x_1, x_2, \ldots, x_N) \,, \end{aligned} \tag{A.54}$$

where $K(x_i)$ is the following integral kernel with $\hat{F}_i[x] \equiv F_i(\sqrt{x})$

$$K(x_1, \ldots, x_N) = \int_0^{2\pi} \mathrm{d}\phi_1 \ldots \mathrm{d}\phi_N \times \tag{A.55}$$

$$\hat{F}_N[\sum_{i=1}^{N} x_i^2 + 2 \sum_{i \neq j = 1}^{N} x_i x_j \cos{(\phi_i - \phi_j)}] \times \tag{A.56}$$

$$\prod_{i=1}^{N-1} \hat{F}_i[x_i^2 + x_{i+1}^2 + 2 x_i x_{i+1} \cos{(\phi_i - \phi_{i+1})}] \tag{A.57}$$

A similar integral relation between A and the polyspectra $\lambda^{(n)}$ can be worked out using the fact that A are the values of the n-point correlators of the filtered random fields at $\vec{x} = \vec{0}$, using the polyspectra of the filtered fields, Eq. (A.49), the relation between polyspectra and n-point correlators, Eq. (A.46), and, finally, the statistical homogeneity of the random fields:

$$A(\theta_{\rm ap}) = \int \frac{\mathrm{d}^2 k_1}{(2\pi)^2} \ldots \frac{\mathrm{d}^2 k_{N-1}}{(2\pi)^2} \, \tilde{F}_N(\sum_{i=1}^{N-1} \vec{k}_i) \prod_{i=1}^{N-1} \tilde{F}_i^*(\vec{k}_i) \, P^{(N)}(\vec{k}_1, \ldots, \vec{k}_{N-1}) \,, \tag{A.58}$$

where $P^{(N)}$ is defined in (1.33).

---

[3] This means that $\xi^{(n)}$ is only a function of the side lengths of the polygon spanned by the points $\vec{x}_i$.

A.4. Non-linear stochastic bias through higher-order statistics

Two-point statistics without any further constraints allow only for the measurement of the linear stochastic bias parameters, Eqs. (1.49). As already pointed out in Sect. 1.4.3 this parametrisation cannot discriminate between non-linear and stochastic effects in the relation between two random fields. For that reason, Dekel & Lahav (1999) introduced the non-linear biasing scheme that consists of three (scale-dependent) bias parameters, $\hat{b}$, $\tilde{b}$ and σ_b (Sect. 1.4.3). They are a specific way to quantify the probability, $P(\delta_{\rm g},\delta_{\rm m})$, to find a pair of random field values, $\delta_{\rm g}$ and $\delta_{\rm m}$, at a point in the fields. In the following, we will focus on the question of how the non-linear stochastic bias can be estimated.

The non-linear stochastic bias scheme is based on the very general assumption that the density contrast of galaxies, $\delta_{\rm g}$, is a function, $f(\delta_{\rm m})$, of the dark matter density contrast, $\delta_{\rm m}$, plus a random component $\epsilon(\delta_{\rm m})$:

$$\delta_{\rm g}=f(\delta_{\rm m})+\epsilon(\delta_{\rm m})\;, \tag{A.59}$$

with $\langle\epsilon(\delta_{\rm m})\rangle=0$. It follows from the definition of the density contrast that we also must have $\langle f(\delta_{\rm m})\rangle=0$. One can show that

$$f(\delta_{\rm m})=\langle\delta_{\rm g}|\delta_{\rm m}\rangle=\int{\rm d}\delta_{\rm g}\,\delta_{\rm g}\,P(\delta_{\rm g}|\delta_{\rm m})\;. \tag{A.60}$$

The expression $P(\delta_{\rm g}|\delta_{\rm m})$ is the conditional PDF of $\delta_{\rm g}$ for a fixed $\delta_{\rm m}$. The function $f(\delta_{\rm m})$ is thus the average value that one should expect to obtain at places where the dark matter density contrast is $\delta_{\rm m}$; in absence of any stochasticity, $\epsilon(\delta_{\rm m})=0$, this is exactly the value one obtains for $\delta_{\rm g}$. Non-linearity is indicated by deviations of $f(\delta_{\rm m})$ from a linear function. In the Dekel & Lahav *Ansatz*, $\hat{b}$ is the slope of a linear regression fitted to $f(\delta_{\rm m})$, namely

$$\begin{aligned}
\hat{b}\equiv\frac{\langle f(\delta_{\rm m})\delta_{\rm m}\rangle}{\langle\delta_{\rm m}^2\rangle} &= \frac{1}{\langle\delta_{\rm m}^2\rangle}\int{\rm d}\delta_{\rm m}\,f(\delta_{\rm m})\,\delta_{\rm m}\,P(\delta_{\rm m}) && \text{(A.61)}\\
&= \frac{1}{\langle\delta_{\rm m}^2\rangle}\int{\rm d}\delta_{\rm m}{\rm d}\delta_{\rm g}\,\delta_{\rm g}\,\delta_{\rm m}\,P(\delta_{\rm g}|\delta_{\rm m})\,P(\delta_{\rm m}) && \text{(A.62)}\\
&= \frac{1}{\langle\delta_{\rm m}^2\rangle}\int{\rm d}\delta_{\rm m}{\rm d}\delta_{\rm g}\,\delta_{\rm g}\,\delta_{\rm m}\,P(\delta_{\rm g},\delta_{\rm m}) && \text{(A.63)}\\
&= \frac{\langle\delta_{\rm g}\delta_{\rm m}\rangle}{\langle\delta_{\rm m}^2\rangle}=b\,r\;, && \text{(A.64)}
\end{aligned}$$

where we applied Bayes' theorem, $P(\delta_{\rm g}|\delta_{\rm m})\,P(\delta_{\rm m})=P(\delta_{\rm g},\delta_{\rm m})$, and used Eq. (A.60). The variables b and r are the linear stochastic bias parameters, Eqs. (1.49). In particular, note from this small exercise that $\langle f(\delta_{\rm m})\delta_{\rm m}\rangle=\langle\delta_{\rm g}\delta_{\rm m}\rangle$. The linear regression slope, $\hat{b}$, is thus different from the "linear" bias factor, b, but can easily be computed from b and r.

A decorrelation, $r<1$, of two random fields can have two causes, both non-linearity and stochasticity:

$$r=(1+\epsilon_{\rm scatt}^2+\epsilon_{\rm nl}^2)^{-1/2}\;, \tag{A.65}$$

where $\epsilon_{\rm scatt}^2$ and $\epsilon_{\rm nl}^2$ are sensitive to stochasticity and non-linearity, respectively. They are defined by Eqs. (1.59) and Eqs. (1.60), yielding[4]

$$\epsilon_{\rm nl}^2 \equiv \frac{\tilde{b}^2}{\hat{b}^2} - 1 = \frac{\left\langle [f(\delta_{\rm m})]^2 \right\rangle \left\langle \delta_{\rm m}^2 \right\rangle}{\left\langle f(\delta_{\rm m})\delta_{\rm m} \right\rangle^2} - 1 = \frac{\left\langle [f(\delta_{\rm m})]^2 \right\rangle \left\langle \delta_{\rm m}^2 \right\rangle}{\left\langle \delta_{\rm g}\delta_{\rm m} \right\rangle^2} - 1 \tag{A.66}$$

$$\Longrightarrow \quad \epsilon_{\rm nl}^2 = \frac{1}{r^2}\frac{\left\langle [f(\delta_{\rm m})]^2 \right\rangle}{\left\langle \delta_{\rm g}^2 \right\rangle} - 1\,, \tag{A.67}$$

$$\epsilon_{\rm scatt}^2 \equiv \frac{\sigma_{\rm b}^2}{\hat{b}^2} = \frac{\left\langle \delta_{\rm m}^2 \right\rangle \left\langle [\delta_{\rm g} - f(\delta_{\rm m})]^2 \right\rangle}{\left\langle f(\delta_{\rm m})\delta_{\rm m} \right\rangle} = \frac{\left\langle \delta_{\rm m}^2 \right\rangle \left\langle \delta_{\rm g}^2 - [f(\delta_{\rm m})]^2 \right\rangle}{\left\langle \delta_{\rm g}\delta_{\rm m} \right\rangle} \tag{A.68}$$

$$\Longrightarrow \quad \epsilon_{\rm scatt}^2 = \frac{1}{r^2}\left(1 - \frac{\left\langle [f(\delta_{\rm m})]^2 \right\rangle}{\left\langle \delta_{\rm g}^2 \right\rangle}\right)\,. \tag{A.69}$$

Without any further assumptions on $P(\delta_{\rm g}, \delta_{\rm m})$ there is no way to disentangle $\epsilon_{\rm scatt}$ and $\epsilon_{\rm nl}$ from b and r only. The key quantity in this context is obviously $\left\langle [f(\delta_{\rm m})]^2 \right\rangle$ because it determines the contributions to $\epsilon_{\rm scatt}$ and $\epsilon_{\rm nl}$:

$$\begin{aligned}
\left\langle [f(\delta_{\rm m})]^2 \right\rangle &= \int {\rm d}\delta_{\rm m}\, [f(\delta_{\rm m})]^2\, P(\delta_{\rm m}) && \text{(A.70)}\\
&= \int {\rm d}\delta_{\rm m} \left[\int {\rm d}\delta_{\rm g}\, \delta_{\rm g}\, P(\delta_{\rm g}|\delta_{\rm m})\right]^2 P(\delta_{\rm m}) && \text{(A.71)}\\
&= \int {\rm d}\delta_{\rm m}{\rm d}\delta_{\rm g}{\rm d}\delta_{\rm g}'\, \delta_{\rm g}\, \delta_{\rm g}'\, P(\delta_{\rm g}|\delta_{\rm m})\, P(\delta_{\rm g}'|\delta_{\rm m})\, P(\delta_{\rm m}) && \text{(A.72)}\\
&= \int {\rm d}\delta_{\rm m}{\rm d}\delta_{\rm g}{\rm d}\delta_{\rm g}'\, \delta_{\rm g}\, \delta_{\rm g}'\, \frac{P(\delta_{\rm g}, \delta_{\rm m})}{P(\delta_{\rm m})}\frac{P(\delta_{\rm g}', \delta_{\rm m})}{P(\delta_{\rm m})}\, P(\delta_{\rm m}) && \text{(A.73)}\\
&= \int {\rm d}\delta_{\rm g}\, \delta_{\rm g} \int {\rm d}\delta_{\rm g}'\, \delta_{\rm g}' \int {\rm d}\delta_{\rm m}\, \frac{P(\delta_{\rm g}, \delta_{\rm m})P(\delta_{\rm g}', \delta_{\rm m})}{P(\delta_{\rm m})} && \text{(A.74)}
\end{aligned}$$

$$\Longrightarrow \quad \left\langle [f(\delta_{\rm m})]^2 \right\rangle = \int {\rm d}\delta_{\rm m} \left[\int {\rm d}\delta_{\rm g}\, \delta_{\rm g}\, P(\delta_{\rm g}, \delta_{\rm m})\right]^2 [P(\delta_{\rm m})]^{-1}\,. \tag{A.75}$$

If the joint PDF $P(\delta_{\rm g}, \delta_{\rm m})$ is a bivariate Gaussian, Eq. (3.73), the integral becomes $\left\langle [f(\delta_{\rm m})]^2 \right\rangle = r^2 \left\langle \delta_{\rm g}^2 \right\rangle$ and, therefore, $\epsilon_{\rm nl} = 0$ and $\epsilon_{\rm scatt}^2 = 1/r^2 - 1$ which shows that a Gaussian model is a linear model in the non-linear stochastic bias scheme. On the other hand, if $\delta_{\rm g}$ is a purely deterministic function of $\delta_{\rm m}$, $\delta_{\rm g} = f(\delta_{\rm m})$, we have automatically $\left\langle [f(\delta_{\rm m})]^2 \right\rangle = \left\langle \delta_{\rm g}^2 \right\rangle$ and therefore $\epsilon_{\rm scatt}^2 = 0$ and $\epsilon_{\rm nl}^2 = 1/r^2 - 1$.

Bivariate lognormal model for $P(\delta_{\rm m}, \delta_{\rm g})$

How can we determine $\left\langle [f(\delta_{\rm m})]^2 \right\rangle$ in practice? The most convenient way is, of course, to estimate the full $P(\delta_{\rm g}, \delta_{\rm m})$ from the observed set of pairs $(\delta_{\rm g}, \delta_{\rm m})$. This is difficult, however, if

---

[4] Note that we have in the notation of Sect. 1.4.3: $f(\delta_{\rm m}) \equiv b(\delta_{\rm m})\delta_{\rm m}$. Moreover, the original Dekel & Lahav parameter $-\hat{b}$, $\tilde{b}$ and $\sigma_{\rm b}-$ are in terms of the linear bias parameter $-b$ and $r-$ and the here used expressions $\epsilon_{\rm scatt}$, $\epsilon_{\rm nl}$: 1. $\hat{b} = b\,r$, 2. $\tilde{b} = b\,r\,(1 + \epsilon_{\rm nl}^2)^{1/2}$, and 3. $\sigma_{\rm b} = b\,r\,\epsilon_{\rm scatt}$.

the number of pairs is small and/or the estimates for $\delta_{\rm m}$ and $\delta_{\rm g}$ are very noisy. This is usually the case.

Wild *et al.* (2004) assume that $P(\delta_{\rm g},\delta_{\rm m})$ is a bivariate lognormal distribution and fit this template PDF to the counts-in-cell statistics of galaxies, where $\delta_{\rm m}$ and $\delta_{\rm g}$ are here the density contrasts of two different galaxy types. Their particular bivariate lognormal distribution is the bivariate Gaussian distribution in Eq. (3.73), $P(\delta_1,\delta_2)$, that is transformed according to the relations

$$\delta_{\rm m}=\exp\left(\delta_1-\frac{1}{2}\left\langle\delta_1^2\right\rangle\right)-1\,;\qquad \delta_{\rm g}=\exp\left(\delta_2-\frac{1}{2}\left\langle\delta_2^2\right\rangle\right)-1\,. \tag{A.76}$$

For more information on lognormal fields, see Sect. 3.3.4. The bivariate lognormal PDF seems to be a realistic assumption to measure the relative bias between galaxies. The authors show that the non-linear stochastic bias parameters are in this case directly related to the 2nd-order cumulants of the PDF. Taking the authors' results of $\sigma_{\rm b}^2$ and $\hat{b}$ for a bivariate lognormal PDF (see their Appendix) we obtain:

$$\frac{\left\langle[f(\delta_{\rm m})]^2\right\rangle}{\left\langle\delta_{\rm g}^2\right\rangle}=1-r^2\epsilon_{\rm scatt}^2=1-r^2\frac{\sigma_{\rm b}^2}{\hat{b}^2}=\frac{1}{\left\langle\delta_{\rm g}^2\right\rangle}\left(\exp\left[\frac{\ln^2\left(\langle\delta_{\rm g}\delta_{\rm m}\rangle+1\right)}{\ln\left(\langle\delta_{\rm m}^2\rangle+1\right)}\right]-1\right)\,. \tag{A.77}$$

For small dispersions, $\left\langle\delta_{\rm g}^2\right\rangle\ll 1$ and $\left\langle\delta_{\rm m}^2\right\rangle\ll 1$, this expression is approximately r^2 as in the bivariate Gaussian case. This should be expected because lognormal distributions asymptotically reach Gaussian distributions if dispersions becomes small. Two-point statistics are, for a lognormal model, therefore sufficient to constraint $\epsilon_{\rm ln}$ and $\epsilon_{\rm scatt}$– however for the price that we have to assume a particular PDF.

Edgeworth expansion of $P(\delta_{\rm m},\delta_{\rm g})$

Another way different to assuming a template PDF is to measure the cumulants of the PDF to increasingly higher orders $n+m$,

$$\lambda_{n,m}\equiv\frac{\left\langle\delta_{\rm m}^n\delta_{\rm g}^m\right\rangle_{\rm c}}{\left\langle\delta_{\rm m}^2\right\rangle^{n/2}\left\langle\delta_{\rm g}^2\right\rangle^{m/2}}\,, \tag{A.78}$$

where n and m are positive integers, and to express $P(\delta_{\rm g},\delta_{\rm m})$ as a series in terms of $\lambda_{i,j}$, $\left\langle\delta_{\rm m}^2\right\rangle$ and $\left\langle\delta_{\rm g}^2\right\rangle$. This is, however, only feasible in the linear or weakly non-linear regime where $\langle\delta_{\rm m,g}^2\rangle<1$ (Blinnikov & Moessner 1998; Juszkiewicz *et al.* 1995); such an expansion is called Edgeworth expansion. Using the Edgeworth expansion,

$$P(\delta_{\rm m},\delta_{\rm g})=\left(1+\sum_{N=3}^{\infty}\sum_{n=0}^{N}(-1)^N\,\frac{n!\,(N-n)!}{N!}\lambda_{n,N-n}\,\frac{\partial^n\partial^{(N-n)}}{\partial\delta_{\rm m}\partial\delta_{\rm g}}\right)P_{\rm gauss}(\delta_{\rm m},\delta_{\rm g})\,, \tag{A.79}$$

up to third order, *i.e.* truncating this series beyond $N>3$, we can approximate a slightly skewed PDF $P(\delta_{\rm m},\delta_{\rm g})$ parametrised by its third-order cumulants $\lambda_{n,m}$, $n+m=3$; the PDF $P_{\rm gauss}$ denotes a bivariate Gaussian PDF, Eq. (3.73). Using this approximation, we calculate from (A.75):

$$\frac{\left\langle[f(\delta_{\rm m})]^2\right\rangle}{\left\langle\delta_{\rm g}^2\right\rangle}=\int_{-\infty}^{\infty}\frac{{\rm d}\delta_{\rm m}}{\sqrt{2\pi}}\,\frac{\left[(\delta_{\rm m}^2-1)\lambda_{1,2}+3r(\delta_{\rm m}+3\lambda_{0,3}-6\delta_{\rm m}^2\lambda_{0,3}+\delta_{\rm m}^4\lambda_{0,3})\right]^2}{9(1-3\delta_{\rm m}\lambda_{0,3}+\delta_{\rm m}^3\lambda_{0,3})}\,{\rm e}^{-\frac{1}{2}\delta_{\rm m}^2}\,. \tag{A.80}$$

Unfortunately, due to the expression in the denominator of the integrand we are unable to evaluate this integral analytically. In order to obtain an approximate result, we make a Taylor expansion of the denominator up to second order in $\lambda_{0,3}$ taking for granted that the skewness is small, $\lambda_{0,3} \ll 1$; this assumption is made in the Edgeworth expansion anyway. Employing this, we finally get:

$$\frac{\left\langle [f(\delta_{\rm m})]^2 \right\rangle}{\left\langle \delta_{\rm g}^2 \right\rangle} = r^2 + \frac{2}{9}\lambda_{1,2}^2(1 + 186\lambda_{0,3}^2) + 18\lambda_{0,3}^2\, r^2 - 4r\lambda_{1,2}\lambda_{0,3} + \mathcal{O}(\lambda_{0,3}^3)\ , \tag{A.81}$$

where $r \equiv \lambda_{1,1}$ is the linear correlation factor.

The technique outlined and applied in this thesis determines the second-order cumulants, *i.e.* $n+m=2$, $\left\langle N^n M_{\rm ap}^m \right\rangle$ and relates them to $\left\langle \delta_{\rm g}^n \delta_{\rm m}^m \right\rangle$. On this level, the terms including third-order $\lambda_{n,m}$ are undetermined (zero) and we cannot distinguish, as in Gaussian case, between non-linearity and stochasticity since $\left\langle [f(\delta_{\rm m})]^2 \right\rangle = r^2 \left\langle \delta_{\rm g}^2 \right\rangle$. This degeneracy can, however, be broken if we do the next logical step and go over to third-order statistics.

APPENDIX B

Appendix: Bias model

B.1. Correlations of convolved fields with a third field

Here we calculate the ensemble average $\langle [\tilde{f} * \tilde{g}](\vec{k})\tilde{h}^*(\vec{k}')\rangle'$, which is the correlator between the convolution of two random fields with a third random field. We have $\tilde{h}^*(\vec{k}') = \tilde{h}(-\vec{k}\,')$, since we are exclusively working with real number fields. Writing out explicitly the convolution of $\tilde{f}$ and $\tilde{g}$ gives

$$
\begin{aligned}
&\langle \left[\tilde{f} * \tilde{g}\right](\vec{k})\tilde{h}(-\vec{k}')\rangle' \\
=\;& \left\langle \tilde{h}(-\vec{k}') \int \frac{\mathrm{d}k''}{(2\pi)^3}\; \tilde{f}(\vec{k}'')\tilde{g}(\vec{k} - \vec{k}'') \right\rangle \\
=\;& \int \frac{\mathrm{d}k''}{(2\pi)^3} \;\left\langle \tilde{h}(-\vec{k}')\tilde{f}(\vec{k}'')\tilde{g}(\vec{k} - \vec{k}'') \right\rangle \\
=\;& \int \mathrm{d}k' \int \mathrm{d}k''\; \delta_D(\vec{k} - \vec{k}')B_{123}(-\vec{k}', \vec{k}'', \vec{k} - \vec{k}'') \\
=\;& \int \mathrm{d}k'\; B_{123}(-\vec{k}, \vec{k}', \vec{k} - \vec{k}')\;, \qquad \text{(B.1)}
\end{aligned}
$$

where B_{123} is the bispectrum of f, g and h. The only assumption that has been made here is that the considered random fields are homogeneous, for which holds

$$
\langle \tilde{h}(\vec{k})\tilde{f}(\vec{k}')\tilde{g}(\vec{k}'')\rangle = (2\pi)^3\delta_D(\vec{k} + \vec{k}' + \vec{k}'')B_{123}(\vec{k}, \vec{k}', \vec{k}'')\;.
$$

For Gaussian fields the bispectrum vanishes, so that on linear scales contributions from these correlators can be neglected.

B.2. From power spectra evolution to linear stochastic bias evolution

Here we are using the definitions (2.29) of the linear stochastic bias parameter, the model Eqs. (2.27), (2.28) and (2.7) to explicitly write down differential equations for the linear stochastic bias.

We start with the bias factor b_i relative to the dark matter field:

$$\begin{aligned}\frac{\partial b_i}{\partial t} &= \frac{\partial}{\partial t}\sqrt{\frac{P_{\mathrm{ii}}}{P_{\mathrm{m}}}} = \frac{1}{2\sqrt{P_{\mathrm{ii}}P_{\mathrm{m}}}}\frac{\partial P_{\mathrm{ii}}}{\partial t} - \frac{1}{2}\sqrt{\frac{P_{\mathrm{ii}}}{P_{\mathrm{m}}}}\frac{1}{P_{\mathrm{m}}}\frac{\partial P_{\mathrm{m}}}{\partial t} \\ &= \frac{b_i}{2}\left(\frac{1}{P_{\mathrm{ii}}}\frac{\partial P_{\mathrm{ii}}}{\partial t} - \frac{1}{P_{\mathrm{m}}}\frac{\partial P_{\mathrm{m}}}{\partial t}\right) , \end{aligned} \tag{B.2}$$

where the definition of $R(t)$ in Eq. (2.26) has been used. From Eq. (2.28) we obtain

$$\frac{1}{P_{\mathrm{ii}}}\frac{\partial P_{\mathrm{ii}}}{\partial t} = R(t)\frac{r_i}{b_i} + \frac{2}{\bar{n}_i}\left[\frac{\mathrm{Re}\,\langle\tilde{\Phi}_i\tilde{\delta}_i^*\rangle'}{P_{\mathrm{ii}}} - \langle\Phi_i\rangle\right] , \tag{B.3}$$

where $\mathrm{Re}\,[x] \equiv \frac{1}{2}(x+x^*)$ denotes the real part of x. Plugging in this expression into the previous equation we get

$$\begin{aligned}\frac{\partial b_i}{\partial t} &= R(t)\frac{r_i - b_i}{2} + I_i^1 , \\ I_i^1 &\equiv \frac{1}{\bar{n}_i}\left[\frac{\mathrm{Re}\,\langle\tilde{\Phi}_i\tilde{\delta}_i^*\rangle'}{P_{\mathrm{m}}}\frac{1}{b_i} - \langle\Phi_i\rangle b_i\right] . \end{aligned} \tag{B.4}$$

We proceed in a similar fashion for the correlation r_i to the dark matter field:

$$\begin{aligned}\frac{\partial r_i}{\partial t} &= \frac{\partial}{\partial t}\frac{P_{\mathrm{i}}}{\sqrt{P_{\mathrm{ii}}P_{\mathrm{m}}}} \qquad \text{(B.5)} \\ &= \frac{1}{\sqrt{P_{\mathrm{ii}}P_{\mathrm{m}}}}\frac{\partial P_{\mathrm{i}}}{\partial t} - \frac{P_{\mathrm{i}}}{2\sqrt{P_{\mathrm{ii}}P_{\mathrm{m}}}}\left[\frac{1}{P_{\mathrm{ii}}}\frac{\partial P_{\mathrm{ii}}}{\partial t} + \frac{1}{P_{\mathrm{m}}}\frac{\partial P_{\mathrm{m}}}{\partial t}\right] \\ &= \frac{1}{b_i}\frac{1}{P_{\mathrm{m}}}\frac{\partial P_{\mathrm{i}}}{\partial t} - \frac{r_i}{2}\frac{1}{P_{\mathrm{ii}}}\frac{\partial P_{\mathrm{ii}}}{\partial t} - R(t)\frac{r_i}{2} . \end{aligned}$$

Now we need Eq. (2.27) to go further:

$$\begin{aligned}\frac{1}{P_{\mathrm{m}}}\frac{\partial P_{\mathrm{i}}}{\partial t} &= R(t)\frac{1+r_ib_i}{2} + \frac{1}{\bar{n}_i}\frac{\langle\tilde{\Phi}_i\tilde{\delta}_m^*\rangle'}{P_{\mathrm{m}}} - \frac{P_{\mathrm{i}}}{P_{\mathrm{m}}}\frac{\langle\Phi_i\rangle}{\bar{n}_i} \qquad \text{(B.6)} \\ &= R(t)\frac{1+r_ib_i}{2} + \frac{1}{\bar{n}_i}\left[\frac{\langle\tilde{\Phi}_i\tilde{\delta}_m^*\rangle'}{P_{\mathrm{m}}} - b_ir_i\langle\Phi_i\rangle\right] . \end{aligned}$$

Plugging these in yields for the correlation parameter

$$\begin{aligned}\frac{\partial r_i}{\partial t} &= \frac{R(t)}{2}\frac{1-r_i^2}{b_i} + I_i^2 , \\ I_i^2 &\equiv \frac{1}{\bar{n}_i}\left[\frac{\langle\tilde{\Phi}_i\tilde{\delta}_m^*\rangle'}{P_{\mathrm{m}}}\frac{1}{b_i} - \frac{\mathrm{Re}\,\langle\tilde{\Phi}_i\tilde{\delta}_i^*\rangle'}{P_{\mathrm{m}}}\frac{r_i}{b_i^2}\right] . \end{aligned} \tag{B.7}$$

Now we turn to the evolution of the linear bias parameter between two galaxy populations, starting off with the bias b_{ij}:

$$\frac{\partial b_{ij}}{\partial t} = \frac{\partial}{\partial t}\frac{b_i}{b_j} = b_{ij}\left[\frac{1}{b_i}\frac{\partial b_i}{\partial t} - \frac{1}{b_j}\frac{\partial b_j}{\partial t}\right] . \tag{B.8}$$

The expressions in the bracket are worked out using Eq. (B.4) so that we therefore obtain

$$\frac{\partial b_{ij}}{\partial t} = \frac{R\left(t\right)}{2}\,\frac{r_i b_j - r_j b_i}{b_i b_j} b_{ij} + \frac{b_{ij}}{b_i} I^1_i - \frac{b_{ij}}{b_j} I^1_j \; . \tag{B.9}$$

The correlation r_{ij} between two galaxy populations is derived in the same way but is in the end a bit lengthy:

$$\frac{\partial r_{ij}}{\partial t} = \frac{\partial}{\partial t}\frac{P_{\mathrm{ij}}}{\sqrt{P_{\mathrm{ii}}P_{\mathrm{jj}}}} = r_{ij}\frac{1}{P_{\mathrm{ij}}}\frac{\partial P_{\mathrm{ij}}}{\partial t} - \frac{1}{2} r_{ij}\left[\frac{1}{P_{\mathrm{ii}}}\frac{\partial P_{\mathrm{ii}}}{\partial t} + \frac{1}{P_{\mathrm{jj}}}\frac{\partial P_{\mathrm{jj}}}{\partial t}\right] \; . \tag{B.10}$$

The expressions in the bracket have been worked out before, so that the only remaining unknown expression is (uses Eq. 2.28)

$$\frac{1}{P_{\mathrm{ij}}}\frac{\partial P_{\mathrm{ij}}}{\partial t} = \frac{R\left(t\right)}{2}\,\frac{b_i r_i + b_j r_j}{b_i b_j r_{ij}} + \frac{1}{\bar{n}_i}\left[\frac{\langle\tilde{\Phi}_i\tilde{\delta}^*_j\rangle'}{P_{\mathrm{ij}}} - \langle\Phi_i\rangle\right] + \frac{1}{\bar{n}_j}\left[\frac{\langle\tilde{\Phi}^*_j\tilde{\delta}_i\rangle'}{P_{\mathrm{ij}}} - \langle\Phi_j\rangle\right] \; . \tag{B.11}$$

Taking this into account, we finally get

$$\begin{aligned}
\frac{\partial r_{ij}}{\partial t} &= \frac{R\left(t\right)}{2}\,\frac{\left(r_i - r_{ij}r_j\right)b_i + \left(r_j - r_{ij}r_i\right)b_j}{b_i b_j} + I^3_{ij} + \left[I^3_{ji}\right]^* \; , \\
I^3_{ij} &\equiv \frac{1}{\bar{n}_i}\left[\frac{\langle\tilde{\Phi}_i\tilde{\delta}^*_j\rangle'}{P_{\mathrm{m}}}\frac{1}{b_i b_j} - \frac{\mathrm{Re}\,\langle\tilde{\Phi}_i\tilde{\delta}^*_i\rangle'}{P_{\mathrm{m}}}\frac{r_{ij}}{b_i^2}\right] \; .
\end{aligned} \tag{B.12}$$

The interaction rates Φ_i and the density contrasts δ_{X} are real numbers, so that the correlators $\langle\tilde{\Phi}_i\tilde{\delta}^*_{\mathrm{X}}\rangle'$ have to be real numbers too. For that reason, we are allowed to omit the real part operator "Re " in the interaction terms I^1_i, I^2_i and I^3_{ij} as has been done in Eqs. (2.35).

B.3. Interaction correlators for first and second order Φ_i

As we are working with the density contrasts δ_i instead of the densities n_i itself, we rewrite the above expression for Φ_i in Eq. (2.40) using the relations $\rho_{\mathrm{m}} = \bar{\rho}_{\mathrm{m}}(1+\delta_{\mathrm{m}})$ and $n_i = \bar{n}_i(1+\delta_i)$:

$$\begin{aligned}
\Phi_i &= A_i + B^r_i\bar{n}_r + \hat{C}_i\bar{\rho}_{\mathrm{m}} \\
&+ D^{rs}_i\bar{n}_r\bar{n}_s + \hat{E}_i\bar{\rho}^2_{\mathrm{m}} + \hat{F}^r_i\bar{n}_r\bar{\rho}_{\mathrm{m}} \\
&+ B^r_i\bar{n}_r\delta_r + \hat{C}_i\bar{\rho}_{\mathrm{m}}\delta_{\mathrm{m}} + D^{rs}_i\bar{n}_r\bar{n}_s\left(\delta_r + \delta_s\right) \\
&+ 2\hat{E}_i\bar{\rho}^2_{\mathrm{m}}\delta_{\mathrm{m}} + \hat{F}^r_i\bar{\rho}_{\mathrm{m}}\bar{n}_r\left(\delta_{\mathrm{m}} + \delta_r\right) \\
&+ D^{rs}_i\bar{n}_r\bar{n}_s\delta_r\delta_s + \hat{E}_i\bar{\rho}^2_{\mathrm{m}}\delta^2_{\mathrm{m}} + \hat{F}^r_i\bar{n}_r\bar{\rho}_{\mathrm{m}}\delta_{\mathrm{m}}\delta_r \; .
\end{aligned} \tag{B.13}$$

Where possible, we absorb for convenience all $\bar{\rho}_{\mathrm{m}}$ inside the associated coupling constant, removing the previously introduced hat "ˆ". This absorption makes sense, because $\bar{\rho}_m$ is supposed to be a constant and therefore produces in this formalism a degeneracy between $\bar{\rho}_m$ and its associated coupling constant. This results in

$$\begin{aligned}
\Phi_i &= A_i + C_i + E_i + \left(B^r_i + F^r_i\right)\bar{n}_r + D^{rs}_i\bar{n}_r\bar{n}_s \\
&+ B^r_i\bar{n}_r\delta_r + C_i\delta_{\mathrm{m}} + D^{rs}_i\bar{n}_r\bar{n}_s\left(\delta_r + \delta_s\right) + 2E_i\delta_{\mathrm{m}} \\
&+ F^r_i\bar{n}_r\left(\delta_{\mathrm{m}} + \delta_r\right) + D^{rs}_i\bar{n}_r\bar{n}_s\delta_r\delta_s + E_i\delta^2_{\mathrm{m}} + F^r_i\bar{n}_r\delta_{\mathrm{m}}\delta_r \; .
\end{aligned} \tag{B.14}$$

The Fourier transform of the interaction term is thus, throwing away the terms contributing only at $\vec{k} = 0$:

$$\begin{aligned}
\tilde{\Phi}_i &= B_i^r \bar{n}_r \tilde{\delta}_r + C_i \tilde{\delta}_\mathrm{m} + D_i^{rs} \bar{n}_r \bar{n}_s (\tilde{\delta}_r + \tilde{\delta}_s) + 2E_i \tilde{\delta}_\mathrm{m} \\
&+ F_i^r \bar{n}_r (\tilde{\delta}_\mathrm{m} + \tilde{\delta}_r) + D_i^{rs} \bar{n}_r \bar{n}_s (\tilde{\delta}_r * \tilde{\delta}_s) \\
&+ E_i (\tilde{\delta}_\mathrm{m} * \tilde{\delta}_\mathrm{m}) + F_i^r \bar{n}_r (\tilde{\delta}_\mathrm{m} * \tilde{\delta}_r) \; . \qquad \text{(B.15)}
\end{aligned}$$

The model equations (2.20) and (2.23) require the interaction correlators $\langle \tilde{\Phi}_i \tilde{\delta}_m^* \rangle'$, $\langle \tilde{\Phi}_j \tilde{\delta}_i^* \rangle'$ and $\langle \tilde{\Phi}_i \tilde{\delta}_j^* \rangle'$ to be evaluated. The last two are, of course, the same up to an exchange of the indices, so that we only have to determine the first two. Using the definition of the correlation power spectra in (2.16) and the restriction to Gaussian fields (bispectra emerging according to Appendix B.1 are zero), we obtain:

$$\begin{aligned}
\langle \tilde{\Phi}_i \tilde{\delta}_\mathrm{m}^* \rangle' &= B_i^r \bar{n}_r P_r + C_i P_\mathrm{m} + D_i^{rs} \bar{n}_r \bar{n}_s \left(P_r + P_s \right) \qquad \text{(B.16)} \\
&+ 2E_i P_\mathrm{m} + F_i^r \bar{n}_r \left(P_\mathrm{m} + P_r \right) \; , \\
\\
\langle \tilde{\Phi}_i \tilde{\delta}_j^* \rangle' &= B_i^r \bar{n}_r P_{rj} + C_i P_j + D_i^{rs} \bar{n}_r \bar{n}_s \left(P_{rj} + P_{sj} \right) \\
&+ 2E_i P_j + F_i^r \bar{n}_r \left(P_j + P_{rj} \right) \; , \\
\\
\langle \tilde{\Phi}_j^* \tilde{\delta}_i \rangle' &= B_j^r \bar{n}_r P_{ri} + C_j P_i + D_j^{rs} \bar{n}_r \bar{n}_s \left(P_{ri} + P_{si} \right) \\
&+ 2E_j P_i + F_j^r \bar{n}_r \left(P_i + P_{ri} \right) \; .
\end{aligned}$$

Eq. (2.34) for the mean density evolution, however, needs the ensemble average of the interaction term in *real space*, $\langle \Phi_i \rangle$. Doing so and removing terms linear in the density contrasts due to $\langle \delta_i \rangle = 0$, results in

$$\begin{aligned}
\langle \Phi_i \rangle &= A_i + C_i + E_i + \left(B_i^r + F_i^r \right) \bar{n}_r + D_i^{rs} \bar{n}_r \bar{n}_s \qquad \text{(B.17)} \\
&+ D_i^{rs} \bar{n}_r \bar{n}_s \left\langle \delta_r \delta_s \right\rangle + E_i \left\langle \delta_\mathrm{m}^2 \right\rangle + F_i^r \bar{n}_r \left\langle \delta_\mathrm{m} \delta_r \right\rangle \; .
\end{aligned}$$

B.4. Fields with fixed bias

Here we consider a new class of density fields –*static fields*– that may serve as a model source for producing galaxies within the model. Their difference to the already described fields δ_i in Sect. 2.2 is that they are supposed to have a constant bias with respect to the dark matter *for all time*; they are therefore some sort of random component $\delta_\perp$ as in Tegmark & Peebles (1998, TP98). They are introduced therein in order to serve as a source for creating new galaxies with a certain fixed bias at the time of there formation. In contrast to the random component in TP98, the static fields here do not necessarily have to be totally uncorrelated to the dark matter field and do not have to be coupled linearly only; hence the static fields are a bit more general.

As we force this class of fields to have a constant bias relative to the dark matter, they certainly do not obey Eq. (2.10) and hence have to be treated differently compared to the common galaxy fields. As before, we restrict ourselves to the linear regime. To avoid confusion with the already studied fields, we use Greek letters as indices, like for example δ_α and $\tilde{\delta}_\alpha$ for its Fourier coefficients.

Demanding the linear bias parameter b_α and r_α to be constant, immediately fixes the equations for the correlation power spectra $P_{\alpha\alpha}$ and P_α by virtue of the definition (2.29):

$$\begin{aligned} \frac{\partial b_\alpha}{\partial t} = 0 \quad &\Rightarrow \quad \frac{\partial P_{\alpha\alpha}}{\partial t} = b_\alpha^2 \frac{\partial P_{\mathrm{m}}}{\partial t} \\ \frac{\partial r_\alpha}{\partial t} = 0 \quad &\Rightarrow \quad \frac{\partial P_{\alpha}}{\partial t} = b_\alpha r_\alpha \frac{\partial P_{\mathrm{m}}}{\partial t} \; . \end{aligned} \tag{B.18}$$

The cross-correlation of δ_α with one of the conventional galaxy number density fields δ_i (Sect. 2.2) is not equally obvious to the eye. But is generally needed to work out the bias evolution of galaxies coupled to static fields. Since the bias relative to the dark matter stays constant, we know that fluctuations of the static fields have to grow with the same rate as the dark matter fluctuations

$$\frac{\partial \delta_\alpha}{\partial t} = \frac{R\,(t)}{2} \delta_\alpha \; , \tag{B.19}$$

where $R\,(t)$ is the rate of structure growth on linear scales (Eq. 2.26). This relation yields

$$\begin{aligned} \frac{\partial P_{\mathrm{i}\alpha}}{\partial t} &= \frac{\partial}{\partial t} \langle \tilde{\delta}_i \tilde{\delta}_\alpha^* \rangle' = \langle \frac{\partial \tilde{\delta}_i}{\partial t} \tilde{\delta}_\alpha^* \rangle' + \langle \tilde{\delta}_i \frac{\partial \tilde{\delta}_\alpha^*}{\partial t} \rangle' \\ &= \frac{R\,(t)}{2} \left(P_\alpha + P_{\mathrm{i}\alpha} \right) + \frac{1}{\bar{n}_i} \left[\langle \tilde{\Phi}_i \delta_\alpha^* \rangle' - P_{\mathrm{i}\alpha} \left\langle \Phi_i \right\rangle \right] \; , \end{aligned} \tag{B.20}$$

where Eq. (2.10) for $\frac{\partial \tilde{\delta}_i}{\partial t}$ has been used (as usual bispectra terms have been neglected: Appendix B.1).

Analogue to Appendix B.2 we then have

$$\frac{\partial b_{i\alpha}}{\partial t} = \frac{\partial}{\partial t} \frac{b_i}{b_\alpha} = \frac{1}{b_\alpha} \frac{\partial b_i}{\partial t} = \frac{R\,(t)}{2} \, \frac{r_i - b_i}{b_\alpha} + \frac{1}{b_\alpha} I_i^1 \; , \tag{B.21}$$

and

$$\frac{\partial r_{i\alpha}}{\partial t} = r_{i\alpha} \frac{1}{P_{\mathrm{i}\alpha}} \frac{\partial P_{\mathrm{i}\alpha}}{\partial t} - \frac{1}{2} r_{i\alpha} \left[\frac{1}{P_{\mathrm{ii}}} \frac{\partial P_{\mathrm{ii}}}{\partial t} + \frac{1}{P_{\alpha\alpha}} \frac{\partial P_{\alpha\alpha}}{\partial t} \right] = \frac{R\,(t)}{2} \, \frac{r_\alpha - r_i r_{i\alpha}}{b_i} + I_{i\alpha}^3 \; ,$$

where the definitions of $I_{i\alpha}^3 = I_{ij}^3 \Big|_{j=\alpha}$ and I_i^1 are used.

Setting $b_\alpha = r_\alpha = 1$ and $r_{i\alpha} = r_i$ reduces $\frac{\partial r_{i\alpha}}{\partial t}$ and $\frac{\partial b_{i\alpha}}{\partial t}$ to $\frac{\partial b_i}{\partial t}$ (Eq. 2.30) and $\frac{\partial r_i}{\partial t}$ (Eq. 2.32) respectively. This tells us that the dark matter field is just a special case of the here introduced static fields, since it (trivially) stays unbiased with respect to itself all the time.

APPENDIX C

Appendix: Shear tomography

C.1. Switching from a finer to a coarser redshift binning

Here we show how the auto- and cross-correlations of the cosmic shear from a finer redshift binning are related to the auto- and cross-correlations obtained from a coarser redshift binning (by combining the finer bins). The relations of this section ensure that we only have to make simulated data of the finest redshift binning, since the corresponding data with less redshift information can always be related to the 3D-correlations of the cosmic shear of this case.

In a first step, we turn to the auto-correlation $\xi_\pm$ of a new redshift bin, neglecting for a moment the cross-correlations to the other new redshift bins. $\xi_\pm$ is according to the Eqs. (6.1) and (6.5) a function that linearly depends on $\bar{W}^2(w)$

$$\xi_\pm(\theta) = \frac{9H_0^4\Omega_m^2}{4c^4}\int\frac{\mathrm{d}\ell\,\ell}{2\pi}\int_0^{w_h}\mathrm{d}w\,\frac{\bar{W}^2(w)}{a^2(w)}\,J_{0,4}(\ell\theta)\;P_\delta\left(\frac{\ell}{f(w)},w\right)\;. \tag{C.1}$$

If we split the redshift distribution $p(w)$ of the source galaxies into disjunct parts, like

$$\begin{aligned} p(w) &= \sum_i q^{(i)}(w) \\ q^{(i)}(w) &\equiv \begin{cases} p(w) & \text{for } w\in[w_{i-1},w_i] \\ 0 & \text{else} \end{cases} \end{aligned} \tag{C.2}$$

with $w_i(z_i)$ in the sense of Fig. 6.2, we expand with the notation of Eqs. (6.3) the function $\bar{W}$ in the following manner

$$\begin{aligned} \bar{W}^2(w) &= \sum_{ij} n_i n_j\,\bar{W}^{(i)}(w)\,\bar{W}^{(j)}(w) \qquad \text{(C.3)} \\ &= \sum_i n_i^2\left[\bar{W}^{(i)}(w)\right]^2 + 2\sum_{i>j} n_i n_j \bar{W}^{(i)}(w)\,\bar{W}^{(j)}(w)\;. \end{aligned}$$

As the $q^{(i)}$ defined here are not normalised, but the corresponding redshift distributions $p^{(i)}$ in the definition for $\bar{W}^{(i)}(w)$ are, we introduce the *normalisation factors*

$$n_i \equiv \int_{w_{i-1}}^{w_i}\mathrm{d}w\;q^{(i)}(w) \tag{C.4}$$

telling us what fraction of the distribution inside the new bin is contained in its subdivisions $q^{(i)}$. Translating Eq. (C.3) to the power spectra gives, leaving out the arguments in ℓ:

$$P_\kappa = \sum_i n_i^2 \, P_\kappa^{(ii)} + 2 \sum_{i>j} n_i n_j \, P_\kappa^{(ij)} \; . \tag{C.5}$$

Similarly, we get for the cosmic shear auto-correlation $\tilde{\xi}$ (actually for all linear functions of $P_\kappa^{(ij)}$; hence the dropped index "±"):

$$\tilde{\xi} = \sum_i n_i^2 \, \xi_{ii} + 2 \sum_{i>j} n_i n_j \, \xi_{ij} \; , \tag{C.6}$$

where ξ_{ii} are the auto-correlations for the sub-bins, ξ_{ij} are the cross-correlations of the cosmic shear between the sub-bins. This equation tells us, therefore, how we have to combine the cosmic shear correlations of the sub-bins when we are switching from a finer to a coarser redshift binning of the data.

What about the cross-correlations between the new redshift bins if we decide to switch to a binning with more than one redshift bin? This case is treated like the foregoing one, except that it is slightly more general. Assume we focus on two new redshift bins k and l consisting of data from a finer redshift binning:

$$p_k\,(w) = \sum_i q_k^{(i)}\,(w) \;\; ; \;\; p_l\,(w) = \sum_j q_l^{(j)}\,(w) \;\; , \tag{C.7}$$

where p_k is the redshift distribution inside the new bin k and p_l the same for the new bin l. Bin k combines $q_k^{(i)}$ and the bin l combines $q_l^{(j)}$ from a finer binning, respectively. Using the same arguments as before, we obtain the following relation between the cosmic shear cross-correlation between the new redshift bins $\tilde{\xi}_{kl}$, and the cross-correlations $\xi_{ij}^{(kl)}$ between their components:

$$\tilde{\xi}_{kl} = \sum_{ij} n_i^{(k)} n_j^{(l)} \xi_{ij}^{(kl)} \; . \tag{C.8}$$

$n_i^{(k)}$ and $n_j^{(l)}$ are the normalisations for the sub-bins. This equation is, of course, the generalisation of Eq. (C.6).

BIBLIOGRAPHY

[1] Adelberger, K.L., Steidel, C.C., Giavalisco, M., *et al.*, 1998, ApJ, 505, 18

[2] Adler, R.J., *The Geometry of Random Fields*, 1981, Wiley, London

[3] Bacon, D.J., Refregier, A.R., Ellis, R.S., 2000, MNRAS, 318, 625

[4] Balian, R., Schaeffer, R., 1989, A&A, 220, 1

[5] Bardeen, J.M., Bond, J.R., Kaiser, N., Szalay, A.S., 1986, ApJ, 304, 15

[6] Bartelmann, M., Schneider P., 2001, Phys. Rev., 340, 291

[7] Bagla, J.S., 1998, MNRAS, 299, 417

[8] Baker, J.E., Davis, M., Strauss, M. A., Lahav, O., Santiago, B.X., 1998, ApJ, 508, 6

[9] Basilakos, S., Plionis, M., 2001, ApJ, 550, 522

[10] Baugh, C.M., Efstathiou, G., 1993, MNRAS, 265, 145

[11] Bell, E., Wolf, Ch., Meisenheimer, K., *et al.*, 2004, ApJ, 608, 752

[12] Benoist, C., Maurogordato, S., da Costa, L.N., *et al.*, 1996, ApJ, 472, 452

[13] Blinnikov, S. Moessner, R., 1998, A&A Suppl. Ser., 130, 193

[14] Budavari, T., Connelly, A.J., Szalay, A.S., *et al.*, 2003, ApJ, 595, 59

[15] Bernardeau, F. 1994, A&A, 291, 697

[16] Bernardeau, F., Colombi, S., Gaztańaga, E., Scoccimarro, R., 2002, PhR, 367, 1

[17] Bernardeau, F., van Waerbeke, L., Mellier, Y., 1997, A&A, 322, 1

[18] Benson, A.J., Cole, S., Frenk, C.S., Baugh, C.M., Lacey, C.G., 2000, MNRAS, 311, 793

[19] Benson, A.J., Baugh, C.M., Cole, S., Frenk, C.S., Lacey, C.G., 2000b, MNRAS, 316, 107

[20] Benson, A.J., Cole, S., Frenk, C.S., Baugh, C.M., Lacey, C.G., 2001, MNRAS, 327, 1041

[21] Bennett, C. *et al.*, 2003, ApJS, 148, 1

[22] Berlind, A.A., Weinberg, D.H., 2002, ApJ, 575, 587

[23] Berlind, A.A., Weinberg, D.H., Benson, A.J, *et al.*, 2003, ApJ, 593, 1

[24] Bertin, E., Arnouts, S., 1996, A&A, 117, 393

[25] Blandford, R.D., Saust, A.B., Brainerd, T.G. Villumsen, J.V., 1991, MNRAS, 251, 600

[26] Blanton, M.R., Cen, R., Ostriker, J.P., Strauss, M.A., 1999, ApJ, 522, 590

[27] Blanton, M.R., Cen, R., Ostriker, J.P., *et al.*, 2000, ApJ, 531, 1

[28] Blanton, M.R., 2000, ApJ, 544, 63

[29] Blanton, M.R., Dalcanton, J., Eisenstein, D., *et al.*, 2001, AJ, 121, 235

[30] Blanton, M.R., Eisenstein, D., Hogg, D.W., Schlegel, D.J., Brinkmann, J., 2003, submitted to ApJ, `astro-ph/0310453`

[31] Blanton, M.R., Eisenstein, D., Hogg, D.W., Zehavi, I., 2004, submitted to ApJ, `astro-ph/0411037`

[32] Bolzonella, M., Miralles, J.-M., Pelló, R., 2000, A&A, 363, 476

[33] Bradač, M., 2004, PhD thesis, "*Exploring Dark Matter Properties from the Smallest to the Largest Scales*", University of Bonn, Germany

[34] Brainerd, T.G., Blandford, R.D., Smail, I., 1996, Apj, 466, 623

[35] Brown, M.L., Taylor, A.N., Hambly, N.C., Dye, S., 2002, MNRAS, 333, 501

[36] Brown, M.L., Taylor, A.N., Bacon, D.J., *et al.*, 2003, MNRAS, 341, 100

[37] Carlberg, R.G., Yee, H.K.C., Morris, S.L., *et al.*, 2000, ApJ, 538, 29

[38] Carlberg, R.G., Yee, H.K.C., Morris, S.L., *et al.*, 2000b, ApJ, 542, 57

[39] Carroll, S.M., Press, W.H., Turner, E.L., 1992, ARAA, 30, 499

[40] Catelan, P., Lucchin, F., Matarrese, S., Porciani, C., 1998, MNRAS 297, 692

[41] Catelan, P., Porciani, C., Lamionkowski, M., 2000, MNRAS, 318, L39

[42] Catelan, P., Kamionkowski, M., Blandford, R.D., 2001, MNRAS, 320, L7

[43] Cen, R., Ostriker, J.P., 1992, ApJ, 399, 11

[44] Cen, R., Ostriker, J.P., 2000, ApJ, 583, 38

[45] Christensen, N., Meyer, R., Know, L., Luey, B., 2001, Class.Quant.Grav., 18, 2677

[46] Coles, P., Jones, B., 1991, MNRAS, 248, 1

[47] Coles, P., 1993, MNRAS, 262, 1065

[48] Coles, P., Melott, A.L., Munshi, D., 1999, ApJ, 521, L5

[49] Cole, S., Lacey, C., Baugh, C.M., Frenk, C.S., 2000, MNRAS, 319, 168

[50] Colinn, P. Klypin, A.A., Kravtsov, A.V., Khokhlov, A.M., 1999, ApJ, 523, 32

[51] Colless, M.M., *et al.* (the 2dFGRS team), 2001, MNRAS, 328, 1039

[52] Colombi, S., 1994, ApJ, 435, 536

[53] Cooray, A., Sheth, R., 2002, Phys.Rept., 372, 1

[54] Crittenden, R.G., Natarajan, P., Pen, U.-L., Theuns, T., 2001, ApJ, 559, 552

[55] Croft, R.A.C., Dalton, G.B., Efstathiou, G., 1999, MNRAS, 305, 547

[56] Croft, R.A.C., Metzler, C.A., 2001, ApJ, 545, 561

[57] Croton, D.J, Farrar, G.R., Norberg, P., *et al.*, 2005, MNRAS, 356, 1155

[58] Davis, M., Geller, M.J., 1976, ApJ, 208, 13

[59] Davis, M., Groth, E.J., Peebles, P.J.E., 1977, ApJ, 212, 107

[60] da Costa, L.N., *et al.*, 1988, ApJ, 327, 544

[61] Davis, M., Peebles, P.J.E., 1983, ApJ, 267, 465

[62] Davis, M., Efstathiou, G., Frenk, C.S., White, S.D.M., 1985, ApJ, 292, 371

[63] Davis, M., Meiksin, A., Strauss, M.A., da Costa, L.N., Yahil, A., 1988, ApJ, 333, 9

[64] Dekel, A., Bertschinger, E., Yahil, A., Strauss, M.A., Davis, M., Huchra, J.P., 1993, ApJ, 412, 1

[65] Dekel, A., Lahav, O., 1999, ApJ, 520, 24

[66] Dressler, A., 1980, ApJ, 236, 351

[67] Dressler, A., Oemler, A., Couch, W.I., *et al.*, 1997, ApJ, 490, 577

[68] Efstathiou, G., Kaiser, N., Saunders, W., *et al.*, 1990, MNRAS, 247, 10

[69] Efstathiou, G., Ellis, R.S., Peterson, B.A., 1988, MNRAS, 232, 431

[70] Efstathiou, G., Bond, J.R., White, S.D.M., 1992, MNRAS, 258, 1

[71] Efstathiou, G., Bond, J.R., 1999, MNRAS, 304, 75

[72] Eisenstein, D.J., Hu, W., 1999, ApJ, 511, 5

[73] Erben, T., van Waerbeke, L., Bertin, E., Mellier, Y., Schneider, P., 2001, A&A, 366, 717

[74] Erben, T., Schirmer, M., Dietrich, J.P., *et al.*, 2005, submitted to A&A, `astro-ph/0501144`

[75] Fan, Z., 2003, ApJ, 594, 33

[76] Feldmann, H.A., Kaiser, N., Peacock, J.A., 1994, ApJ, 426, 23

[77] Firth, A.E., Somerville, R.S., McMahon, R.G., *et al.*, 2002, MNRAS, 332, 617

[78] Fry, J.N., 1984, ApJ, 279, 499

[79] Fry, J.N., Gaztańaga, 1993, ApJ, 413, 447

[80] Fry, J.N., 1996, ApJ, 461, L65

[81] Fisher, R.A., 1935, J. Roy. Stat. Soc., 98, 39

[82] Fischer, P., McKay, T.A., Sheldon, E., *et al.*, 2000, AJ, 120, 1198

[83] Fixsen, D.J., Cheng, E.S., Gales, J.M., *et al.*, 1996, ApJ, 473, 576

[84] Fruchter, A.S., Hook, R.N., 2002, PASP, 114, 144

[85] Gaztańaga, E.,Frieman, J.A., 1994, ApJ, 437, 13

[86] Gladders, M.D., Yee, H.K.C., `astro-ph/0011073`

[87] Goto, T., Yamauchi, C., Fujita, Y., *et al.*, 2003, MNRAS, 346, 601

[88] Gott, J.R., Melott, A.L., Dickinson, M., 1986, ApJ, 306, 341

[89] Goroff, M. H., Grinstein, B., Rey, S.-J., Wise, M. B. 1986, ApJ, 311, 6

[90] Gray, M.E., Taylor, A.N., Meisenheimer, K., Dye, S., Wolf, C., Thommes, E., 2002, ApJ, 282, 1159

[91] Groth, E.J., Peebles, P.J.E., 1977, ApJ, 217, 385

[92] Guth, A.H., 1981, Phys. Rev. D, 23, 347

[93] Guzik, J., Seljak, U., 2001, MNRAS, 321, 439

[94] Guzzo, L., Strauss, M.A., Fisher, K.B., Giovanelli, R., Haynes, M.P., 1997, ApJ, 489, 37

[95] Hamilton, A.J.S., Gott, J.R. III, Weinberg, D.H., 1986, ApJ, 309, 1

[96] Hamilton, A.J.S., 1988, ApJ, 331, 59

[97] Hamilton, A.J.S., Kumar, P., Matthews, A., Lu, E., 1991, ApJ, 374, 1

[98] Hamilton, A.J.S., 2000, MNRAS, 312, 257

[99] Hasegawa, T., Umemura, M., 1993, MNRAS, 263, 191

[100] Hawkins, E., Maddox, S.J., Branchini, E., Saunders, W., 2001, MNRAS, 325, 589

[101] Hawkins, E., Maddox, S.J., Cole, S., *et al.*, 2003, MNRAS, 346, 78

[102] Heavens, A.F., Refregier, A., Heymans, C.E.C., 2000, MNRAS, 319, 649

[103] Hoekstra, H., Yee, H.K.C., Gladders, M.D., 2001, ApJ, 558, 11

[104] Hoekstra, H., van Waerbeke, L., Gladders, M.D., Mellier, Y., Yee, H.K.C., 2002, ApJ, 577, 604

[105] Hoekstra, H., Franx, M., Kuijken, K., Carlberg, R.G., Yee, H.K.C., 2003, MNRAS, 340, 609

[106] Hermit, S., Santiago, B.X., Lahav, O., *et al.*, 1996, MNRAS, 283, 709

[107] Heymans, C., Heavens, A., 2003, MNRAS, 339, 711

[108] Heymans, C.E.C., Brown, M., Heavens, A., Meisenheimer, K., Taylor, A., Wolf, C., 2004, MNRAS, 347, 895

[109] Higham, N.J., 1997, Numerical Algorithms, 15, 227

[110] Hildebrandt, H., Erben, T., Bomans, D.J., *et al.*, 2005, submitted to A&A, `astro-ph/0412375`

[111] Hoyle, F., Baugh, C.M., Shanks, T., Ratcliffe, A., 1999, MNRAS, 309, 659

[112] Hu, W., Tegmark, M., 1999, ApJ, 514, L65

[113] Hu, W., 1999, ApJ, 522, L21

[114] Hu, W., White, M., 2001, ApJ, 554, 67

[115] Hubble, E.P., 1936, The Realm of the Nebulae, Oxford University Press: Oxford, 79

[116] Hudson, M.J., Gwyn, S.D.J., Dahle, H., Kaiser, N., 1998, ApJ, 503, 531

[117] Huterer, D., 2002, Phys.Rev. D, 65, 06f3001H

[118] Iovino, A., Giovanelli, Haynes, M., Chincarini, G., Guzzo, L., 1993, MNRAS, 265, 21

[119] Jain, B., Seljak, U., White, S.D.M., 2000, ApJ, 530, 547

[120] Jarvis, M., Bernstein, G.,Jain, B., 2004, MNRAS, 352, 338

[121] Jenkins, A., Frenk, C.S., Pearce, F.R., *et al.*, 1998, ApJ, 499, 20

[122] Jing, Y.P., Mo, H.J., Börner, G., 1998, ApJ, 494, 1

[123] Juszkiewicz, R., Weinberg, D.H., Amsterdamski, P., Chodorowski, R., Bochet, F.R., 1995, ApJ, 442, 32

[124] Kaiser, N., 1984, ApJ, 284, L9

[125] Kaiser, N., 1987, MNRAS, 227, 1

[126] Kaiser, N., 1992, ApJ, 388, 272

[127] Kaiser, N., Squires, G., Broadhurst, T., 1995, ApJ, 449, 460

[128] Kaiser, N., 1998, ApJ, 498, 26

[129] Kaiser, N., Wilson, G., Luppino, G., 2001, ApJ, 556, 601

[130] Katz, N., Hernquist, L., Weinberg, D. 1999, ApJ, 523, 463

[131] Kauffmann, G., Colberg, J.M., Diaferio, A., White S.D.M., 1999a, MNRAS, 303, 188

[132] Kauffmann, G., Colberg, J.M., Diaferio, A., White S.D.M., 1999b, MNRAS, 307, 529

[133] Kayo, I., Taruya, A., Suto, Y., 2001, ApJ, 561, 22

[134] Kayo, I., Suto, Y., Nichol, R.C., *et al.*, 2004, PASJ, 56, 415

[135] Kleinheinrich, M., 2003, PhD thesis, "*Dark matter halos of galaxies studied with weak gravitational lensing*", University of Bonn, Germany

[136] Kleinheinrich, M., Schneider, P., Rix, H.-W., *et al.*, submitted to A&A, `astro-ph/0412615`

[137] Kilbinger, M., Schneider, P., 2004, A&A, 413, 465

[138] King, J.L., Schneider, P., 2003, A&A, 398, 23

[139] Kolb, E.W., Turner, M.S., 1990, *The early universe*, Frontiers in Physics, Reading, MA: Addison-Wesley, 1990

[140] Kravtsov, A.V., Klypin, A., 1999, ApJ, 520, 437

[141] Kruse, G., Schneider, P., 1999, MNRAS, 302, 821

[142] Lacey, C., Cole, S., 1993, MNRAS, 262, 627

[143] Lahav, O., Nemiroff, R.J., Piran, T., 1990, ApJ, 350, 119

[144] Lahav, O., Saslaw, W.C., 1992, ApJ, 396, 430

[145] Lahav, O., Bridle, S.L., Percival, W.J., *et al.*, 2002, MNRAS, 333, 961

[146] Landy, S.D., Szalay, A.S., 1993, 412, 64

[147] Le Fèvre, O., Hudon, D., Lilly, S.J., *et al.*, 1996, ApJ, 461, 534

[148] Liddle, A.R., Lyth, D., 1993, Phys. Rep., 231, 1

[149] Lewis, A., Bridle, S., 2002, Phys. Rev. D, 66, 103511

[150] Loveday, J., Maddox, S.J., Efstathiou, G., Peterson, B.A., 1995, ApJ, 442, 457

[151] Loveday, J., Efstathiou, G., Maddox, S.J., Peterson, B.A., 1996, ApJ, 468, 1

[152] Loveday, J., Tresse, L., Maddox, S., 1999, MNRAS, 310, 281

[153] Maddox, S.J., Efstathiou, G., Sutherland, W.J., Loveday, J., 1990, MNRAS, 242, 43

[154] Madgwick, D.S., 2002, MNRAS, 338, 197

[155] Madgwick, D.S., Hawkins, E., Lahav, O., *et al.*, 2003, MNRAS, 344, 847

[156] Magliocchetti, M., Bagla, J.S., Maddox, S.J., Lahav, O., 2000, MNRAS, 314, 546

[157] Mann, R.G., Peacock, J.A., Heavens, A.F., 1998, MNRAS, 293, 209

[158] Marzke, R.O., Geller, M.J., Huchra, J.P., Corwin, H.G.J., 1994a, AJ, 108, 437

[159] Marzke, R.O., Huchra, J.P., Geller, M.J., 1994b, ApJ, 428, 43

[160] Matarrese, S., Coles, P., Lucchin, F., Moscardini, L., 1997, MNRAS, 286, 115

[161] Matsubara, T., 1995, ApJS, 101, 1

[162] Matsubara, T., 1999, ApJ, 525, 543

[163] McKay, T.A., Sheldon, E.S., Racusin, J., *et al.*, 2001, submitted to ApJ, `astro-ph/0108013`

[164] Mecke, K.R., Buchert, T., Wagner, H., 1994, A&A, 288, 697

[165] Meszaros, P., 1974, A&A, 37, 225

[166] Mo, H.J., White, S.D.M., 1996, MNRAS, 282, 347

[167] Moore, A.W., *et al.*, *Fast Algorithms and efficient statistics: N-Point Correlation Functions*, misk.conf. 71

[168] Miralda-Escudé, J., 1991, ApJ, 380, 1

[169] Narayanan, V.K., Berlind, A.A., Weinberg, D.H., 2000, ApJ, 528, 1

[170] Norberg, P., Baugh, C.M., Hawkins, E., *et al.*, 2001, MNRAS, 328, 64

[171] Norberg, P., Baugh, C.M., Hawkins, E., *et al.*, 2002a, MNRAS, 332, 827

[172] Nusser, A., Davis, M., 1994, ApJ, 421, L1

[173] Olive, K.A., Steigman, G., Walker, T.P., 2000, PhR, 333, 389

[174] Park, C., Vogeley, M.S., Geller, M.J., Huchra, J.P., 1994, ApJ, 431, 569

[175] Peacock, J.A., Dodds, S.J., 1996, MNRAS, 280, L19

[176] Peacock, J.A., 1997, MNRAS, 284, 885

[177] Peacock, J.A., 1998, `astro-ph/9805208`

[178] Peacock, J.A., Smith, R.E., 2000, MNRAS, 318, 1144

[179] Peacock, J.A., 2001, *Cosmological Physics*, Cambridge University Press

[180] Peacock, J.A., Cole, S., Norberg, P., *et al.*, 2001, Nature, 410, 169

[181] Pearce, F.R, Jenkins, A., Frenk, C.S., White, S.D.M., *et al.*, 2001, MNRAS, 326, 649

[182] Pen, U.-L., 1998, ApJ, 504, 601

[183] Pen, U.-L., Zhang, L.L., 2003, `astro-ph/0305447`

[184] Pen, U.-L., Lun, T., van Waerbeke, L., Mellier, Y., 2003, MNRAS, 346, 994

[185] Perlmutter, S., Aldering, G., Goldhaber, G., *et al.*, 1999, ApJ, 517, 565

[186] Phleps, S., Meisenheimer, K., 2003, A&A, 407, 855

[187] Philips, S., Shanks, T., 1987, MNRAS, 229, 621

[188] Postman, M., Lauer, T.R., Szapudi, I., Oegerle, W., 1998, ApJ, 506, 33

[189] Press, W.H., Tokolsky, S.A., Vetterling, W.T., Flannery, B.P., 1992, Numerical Recipes, Cambridge University Press

[190] Rix, H.-W., Barden, M., Beckwith, S.V.W., *et al.*, 2004, ApJS, in press, `astro-ph/0401427`

[191] Santiago, B.X., Strauss, M.A., 1992, ApJ, 387, 9

[192] Scherrer, R.J., Weinberg, D.H., 1998, ApJ, 504, 607

[193] Schirmer, M., Erben, T., Schneider, P., *et al.*, 2003, A&A, 407, 869

[194] Schneider, P., 1996, MNRAS, 283, 837

[195] Schneider, P., 1998, ApJ, 498, 43

[196] Schneider, P., van Waerbeke, L., Jain, B., Kruse, G., 1998, MNRAS, 296, 873

[197] Schneider, P., van Waerbeke, L., Kilbinger, M., Mellier, Y., 2002a, A&A, 396, 1

[198] Schneider, P., van Waerbeke, L., Mellier, Y., 2002b, A&A 389, 729

[199] Schneider, P., Lombardi, M., 2003, A&A, 367, 809

[200] Schneider, P., Kilbinger, M., Lombardi, M., 2004, submitted to A&A, `astro-ph/0308328`

[201] Schneider, P., Saas-Fee lecture on weak gravitational lensing, 2004

[202] Schneider, P., Watts, P., 2005, A&A, 432, 3

[203] Seitz, C., Schneider, P., 1995, A&A, 318, 687

[204] Seljak, U., 2000, MNRAS, 318, 203

[205] Seljak, U., Makarov, A., Mandelbaum, R., *et al.*, 2004a, submitted to PRD, `astro-ph/0406594`

[206] Seljak, J., Makarov, A., McDonald, P., *et al.*, 2004b, submitted to PRD, `astro-ph/0407372`

[207] Shectman, S.A., Landy, S.D., Oemler, A., *et al.*, 1996, ApJ, 470, 172

[208] Sheldon, E.S., Johnston, D.E., Frieman, J.A., *et al.*, 2004, AJ, 127, 2544

[209] Shepherd, C.W., Carlberg, R.G., Yee, H.K.C., *et al.*, 2001, ApJ, 560, 72

[210] Sheth, R.K., Lemson, G., 1999, MNRAS, 767

[211] Siegmann, A.E., 1977, Opt. Lett., 1, 13

[212] Sigad, Y., Branchini, E., Dekel, A., 2000, ApJ, 540, 62

[213] Sigad, Y., Eldar, A., Dekel, A., Strauss, M., Yahil, A., 1998, ApJ, 495, 516

[214] Silk, J., 1968, ApJ, 151, 459

[215] Simon, P., King, J.L., Schneider, P., 2004, A&A, 417, 873

[216] Simon, P., 2004a, A&A, in press, `astro-ph/0409435`

[217] Simon, P., Schneider, P., Erben, T., Schirmer, M., Wolf, C., Meisenheimer, K., 2004b, conference Proceedings of Science (SISSA), *Baryons in Dark Matter Halos*, 5-9 October 2004, Novigrad (Croatia), in press, `astro-ph/0412139`

[218] Smail, I., Hogg, D., Yan, L., Cohen, J., 1995, ApJ, 449, 105L

[219] Small, T.A., Ma, C.-P., Sargent, W.L.W., Hamilton, D., 1999, ApJ, 524, 31

[220] Smith, R.E., Peacock, J.A., White, S.D.M., *et al.*, 2003, MNRAS, 341, 1311

[221] Somerville, R.S., Lemson, G., Sigad, Y., Dekel, A., Kauffmann, G., White, S.D.M., 2001, MNRAS, 320, 289

[222] Spergel, D.N., Verde, L., Peiris, V.H., *et al.*, 2003, ApJS, 148, 175

[223] Steidel, C.C., Adelberger, K.L., Dickinson, M., *et al.*, 1998, ApJ, 492, 428

[224] Sugiyama, N., 1995, ApJS, 100, 281

[225] Szapudi, I., Branchini, E., Frenk, C.S., Maddox, S., Saunders. W., 2000, MNRAS, 318, 45

[226] Taruya, A., Koyama, K., Soda, J., 1999, ApJ, 510, 541

[227] Taruya, A., Soda, J., 1999, ApJ, 522, 46

[228] Taruya, A., Suto, Y., 2000, ApJ, 542, 559

[229] Taruya, A., Takada, M., Hamana, T., Kayo, I., Futamase, T., 2002, ApJ, 571, 638

[230] Tegmark, M., Taylor, A.N., Heavens, A.F., 1997, ApJ, 480, 22

[231] Tegmark, M., Peebles, P.J.E., 1998, ApJ, 500, L79

[232] Tegmark, M., Bromley, B., 1999, ApJ, 518, L69

[233] Tegmark, M., Strauss, M.A., Blanton, M.R., *et al.*, 2004a, PhysRevD, 69, 103501

[234] Tegmark, M., Blanton, M.R., Strauss, M.A., 2004b, ApJ, 606, 702

[235] Tereno, I., Dorè, O., van Waerbeke, L., Y. Mellier, 2004, `astro-ph/0404317`

[236] Totsuji, H., Kihara, T., 1969, PASJ, 21, 221

[237] Tucker, D.L., Oemler, J.A., Kirshner, R.P., *et al.*, 1997, MNRAS, 285, 1335

[238] van Dokkum, P.G., Franx, M., 2001, ApJ, 553, 90

[239] van Waerbeke, L., 1998, A&A, 334, 1

[240] van Waerbeke, L., Mellier, Y., Erben, T., *et al.*, 2000, A&A, 358, 30

[241] van Waerbeke, L., Mellier, Y., Radovich, M., et al., 2001, A&A, 374, 757

[242] van Waerbeke, L., *et al.*, 2001b, A&A, 374, 757

[243] van Waerbeke, L., Mellier, Y., Pell/o, R., et al., 2002, A&A, 393, 369

[244] van Waerbeke, L., Mellier, Y., 2003, Gravitational Lensing by Large Scale Structures: A Review, lecture given at Aussois Winter School, 01/2003, `astro-ph/0305089`

[245] Verde, L., Heavens, A.F., Percival, W.J., 2002, MNRAS, 335, 432

[246] Wagoner, R.V., Fowler, W.A., Hoyle, F., 1967, ApJ, 148, 3

[247] Wambsganss, J., Cen, R., Ostriker, J.P., 1998, ApJ, 494, 29

[248] Wechsler, R.H., Gross, M.A.K, Primack, J.R., *et al.*, 1998, ApJ, 506, 19

[249] Weinberg, D.H., Dave, R., Katz, N., Hernquist, L., 2004, ApJ, 60, 1

[250] Weinberg, S., 1972, *Gravitation and Cosmology: Principles and Applications of the General Theory of Gravitation*, Wiley (Publisher)

[251] White, S.D.M., Rees, M.J., 1978, MNRAS, 183, 341

[252] White, S.D.M., Davis, M., Efstathiou, G., Frenk, C.S., 1987, Nature, 330, 451

[253] White, S.D.M., Tully, R.B., Davis, M., 1988, ApJ, 333, 45

[254] White, S.D.M., Frenk, C.S., 1991, ApJ, 379, 52

[255] White, S.D.M., Efstathiou, G., Frenk, C.S., 1993, MNRAS, 1023

[256] White, M., Hu, W., 2000, ApJ, 537, 1

[257] Wild, V., Peacock, J.A., Lahav, O., *et al.*, 2004, MNRAS, 606

[258] Willmer, C.N.A., da Costa, L.N., Pellegrini, P.S., 1998, AJ, 115, 869

[259] Wilson, G., Kaiser, N., Luppino, G.A., 2001, ApJ, 556, 601

[260] Wilson, G., 2003, ApJ, 585, 191

[261] Wittman, D.M., Tyson, J.A., Kirkman, D., Dell'Antonio, I., Bernstein, G., 2000, Nature, 405, 143

[262] Wolf, C., Dye, S., Kleinheinrich, M., Rix, H.-W., Wisotzki, L., 2001a, A&A, 365, 681

[263] Wolf, C., Meisenheimer, K., Röser, H.-J., 2001b, A&A, 365, 660

[264] Wolf, C., Meisenheimer, K., Rix, H.-W., Borch, A., Dyse, S., Kleinheinrich, M., 2003, A&A, 401, 73

[265] Wolf, C., Meisenheimer, K., Kleinheinrich, M., *et al.*, 2004, A&A, 421, 913

[266] York, D.G., *et al.* (the SDSS team), AJ, 120, 1579

[267] Yoshikawa, K., Taruya, A., Jing, Y.P., Suto, Y., 2001, ApJ, 558, 520

[268] Zaldarriaga, M., Seljak, U., 2000, ApJS, 129, 431

[269] Zehavi, I., Blanton, M.R., Frieman, J.A., *et al.*, 2002, ApJ, 571, 172

[270] Zehavi, I., Weinberg, D.H., Zheng, Z., *et al.*, 2004, ApJ, 608, 16

[271] Zwicky, F., Herzog, E., Wild, P., Karpowicz, M., Kowal, C., 1961–1968, *Catalog of Galaxies and the Clusters of Galaxies*, Vols. 1–6, Pasadena: California Institute of Technology

INDEX

Acknowledgements

Many people supported me during my work on this thesis. First of all, I would like to thank Peter Schneider for his supervision and for having always time for me when necessary. I am especially grateful for the helpful discussions and comments on my thesis manuscript.

Many thanks for offering charge-free editor services also go to my office-mate Peter Watts, to Lindsay King and Marc Thormeier. I also thank my collaborators who made contributions to various chapters of this thesis: Peter Schneider (Chapter 3 and 6), Mischa Schirmer and Thomas Erben (Chapter 4 and 5), Christian Wolf (Chapter 4 and 5), Klaus Meisenheimer (Chapter 4 and 5), and, moreover, Lindsay King who contributed much to Chapter 6 and who kindly invited me to Cambridge to give a lunch talk on my work.

Not to forget Marco Hetterscheidt who shared with me his knowledge on “real” cosmic shear data. Without him I probably would still endlessly run my evaluation scripts wondering what might be wrong with the lensing catalogues.

Nowadays nobody gets along with a helping hand from a computer expert next door. I luckily happened to know even two particularly helpful species of this kind in our institute. Thank you very much Ole Marggraf and Oliver Cordes.

Furthermore, I would like to thank Pavel Kroupa for agreeing to be the co-corrector of my thesis, and I would like to thank all the participants of the exam panel for their time.

This work was supported by the Deutsche Forschungsgemeinschaft under the Graduiertenkolleg 787 (GRK787). I really would like to thank the board for the tremendous work they are doing for the GRK787.